An experimental study on adhesive or antiadhesiveand strong bio-inspired nanomaterials

Emiliano Lepore

An experimental study on adhesive or anti-adhesive and strong bio-inspired nanomaterials

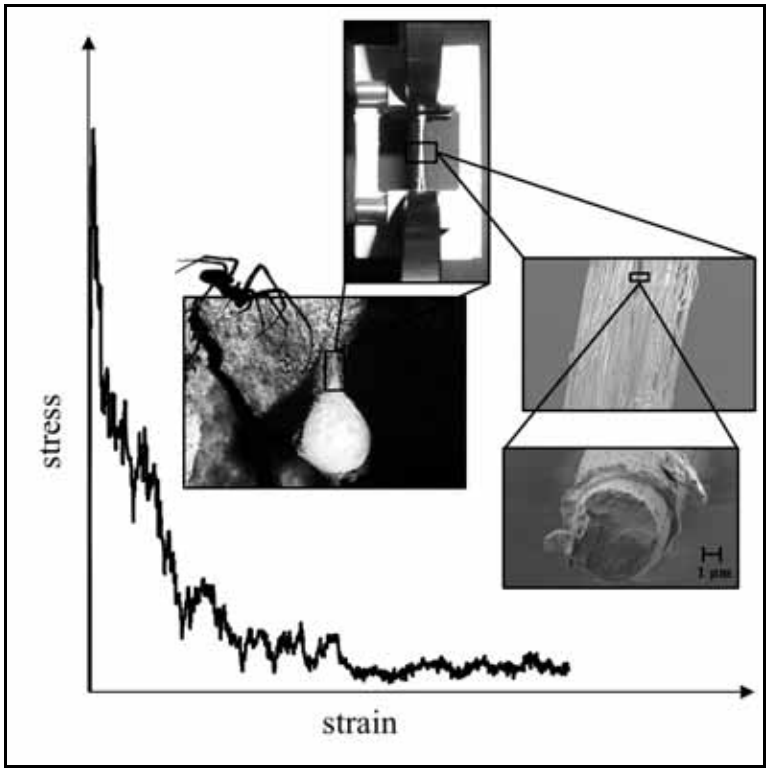

Dottorato di Ricerca in Ingegneria delle Strutture
Politecnico di Torino

Emiliano Lepore

An experimental study on adhesive or anti-adhesive and strong bio-inspired nanomaterials

Tesi per il conseguimento del titolo di Dottore di Ricerca
XXIV Ciclo (A.A. 2009/10, 2010/11, 2011/12)

Dottorato di Ricerca in Ingegneria delle Strutture
Politecnico di Torino

Dicembre 2011

Dottorato di Ricerca in Ingegneria delle Strutture
Politecnico di Torino
10129 Torino, Italia

Tutore: Prof. Nicola M. Pugno (ICAR/08)

Coordinatore: Prof. Alberto Carpinteri

Acknowledgements

First and foremost, I would like to express my deep gratitude to my tutor Prof. Nicola Pugno for his theoretical rigour and fascinating scientific approach. I thank Nature for its continuous stimulus and inspiration to optimization.

I wish to sincerely thank Maria, who has always encouraged me and believed in my abilities, showing me every day how small wonderful things could become great, only with passion.

I am very thankful to my mother Marilena and my father Vittorino who, when I was a child, taught me how only honesty and respect for the others are the two milestones in human relationships, thus also in work. Unfortunately, these are not common human values.

“The only way to do great work is to love what you do. If you haven't found it yet, keep looking. Don't settle. As with all matters of the heart, you'll know when you find it. And, like any great relationship, it just gets better and better as the years roll on. So keep looking until you find it. Don't settle. [...] Stay hungry. Stay foolish”

(S. Jobs, an American computer entrepreneur and innovator)

"Genius is one percent inspiration, ninety-nine percent perspiration"

(T. Edison, an American inventor and entrepreneur)

“Poor is the pupil who does not surpass his master”

(L. da Vinci, an Italian Renaissance polymath)

“I seek not the answer but to understand the question”

(H. Kroto, a British Nobel Prize Winner)

Dedicated to
small things which become great

CONTENTS

GENERAL INTRODUCTION

This experimental PhD thesis presents the results of research performed in five different facilities: in the Laboratory of Bio-inspired Nanomechanics "Giuseppe Maria Pugno" at the Politecnico of Torino, the "Nanofacility Piemonte" at the INRIM Institute in Torino, the Division of Dental Sciences and Biomaterials of the Department of Biomedicine at the University of Trieste, the Physics Department of the Politecnico of Torino, the Toscano-Buono Veterinary Surgery in Torino and the Department of Human and Animal Biology at the University of Torino.

The adhesive abilities of insects, spiders and reptiles have inspired researchers for a long time. All these organisms present outstanding performance particularly for force, adhesion and climbing abilities, especially considering their size and weight. Scientists have focused attention on the gecko's adhesive paw system and climbing abilities, and its adhesion mechanism has been an important topic of research for nearly 150 years. However, certain phenomena about geckos are still not completely understood and nowadays these still represent the main challenge of several scientific discussions which aim to better understand the gecko's adhesive ability.

This thesis deals first with the influence of surface roughness on the gecko's adhesion on the inverted surface of Poly(methyl meth-acrylate) (PMMA) and glass in **Chapter 1**, of PMMA with different surface roughness in **Chapter 2**, while **Chapter 3** deals with the gecko's maximum normal adhesive force and **Chapter 4** looks at the optimal adhesion angle at different hierarchical levels. The gecko's moult (Appendix 1) is examined in a preliminary way.

The Tokay gecko (*Gekko gecko*) is the most studied gecko among more than 1050 Gekkonid lizard species in the world, due to its strong adhesive ability. Because this thesis reports clear experimental measurements on two living Tokay geckos, it is comparable to scientific results reported in the literature.

It is well known how small insects can carry many times their own weight and can walk quickly, but their most interesting ability is their extremely high adhesion. In recent decades, many scientists have studied a number of insects in order to understand and measure their adhesive abilities. Biological adhesion can be obtained through different adhesive mechanisms (*e.g.* claw, clamp, sucker, glue, friction). In particular, this thesis focuses on living specimens of the non-climbing cockroach (*Blatta Orientalis*

Linnaeus) by evaluating its maximum shear safety factor on artificial surfaces using a centrifuge machine, see **Chapter 5**.
In general, the adhesive structure and mechanism of an animal could be connected to the micro-structured roughness of natural substrata (*e.g.* plant surfaces), which animals usually find when they move around in the natural environment.
In nature, plants show an extraordinary variety of morphologies and surface structures. Some plants possess two special properties; superhydrophobicity (or water-repellency) and self-cleaning (or dirt-freedom). These two related phenomena were observed for the first time by Aristotle more than 2,000 years ago but it was only in the 20th century that scientists examined them accurately on some natural leaves, *e.g.* the lotus (*Nelumbo nucifera*) on which "raindrops take a clear, spherical shape without spreading, which probably has to be ascribed to some kind of evaporated essence", as Goethe described in 1817. Accordingly to scientific literature, a strong influence of surface roughness on wettability and self-cleaning behaviour clearly emerges. This well-defined problem was of particular interest (for the Indesit Company) since we wanted to find an industrial solution which would leave the internal sides of refrigerators clean from condensed water or dirt. For this reason, a collaborative project started. Two industrial processes, plasma and thermoforming treatments, were applied to polystyrene surfaces. The Indesit refrigerator box is made of polystyrene. The influence of these industrial treatments on the surface wettability were analysed, see **Chapter 6**. The focus of the Indesit Company was to understand the role of roughness and to produce a superhydrophobic and self-cleaning surface. Thus, this thesis reports the method which we developed in order to design an artificial biomimetic superhydrophobic polystyrene surface, copying the natural lotus leaf (**Chapter 7**). In addition, surface roughness implies a modification of the tribological and frictional properties, so it assumes a crucial role when designing two contacting surfaces, in particular at nano-scale (**Chapter 8**).
The nanometer scale characterises this thesis and is involved in everything from gecko spatulae to the waxy nanotubules of the lotus leaf, to the fibroin protein materials which constitute spider silks. In general, spider silks display superior mechanical properties but, only in the last few decades, reserachers have studied various types of silks and have evaluated their very different mechanical properties. The fact that the mechanical behaviour of spider silks varies accordingly to their type is well-known, since silk properties have been demonstrated to be species-specific and are linked to

silk-based peptide fibrils or protein aggregates, with different structural and mechanical properties. The dragline silk (or radial silk) and the flag silk (or circumferential silk) of orb weaving spiders have been characterized in scientific literature while, to our knowledge, few studies have been conducted on bundles, which connect the cocoons of *Meta menardi* to the ceiling of caves. These were tested to determine their mechanical properties in terms of stress, strain and toughness (**Chapter 9**).

ADHESIVE MATERIALS

1. THE WEIBULL STATISTICS APPLIED TO THE ADHESION TIMES OF LIVING TOKAY GECKOS ON NANOROUGH SURFACES

Abstract

In this paper we demonstrate that living tokay geckos (*Gekko gecko*) display adhesion times following Weibull Statistics. We have considered two different geckos, male or female, adhering on different surfaces, glass or Poly(methyl meth-acrylate) (PMMA) with different roughness. We have performed detailed surface topography characterizations by means of a three-dimensional optical profilometer. The analysis suggests the existence of a "weakest link" in the gecko's adhesion and is able to quantify its degree of brittleness in different systems.

1.1. Introduction

In the world, there are more than 1050 species of geckos divided into 50 families. The Tokay gecko (*Gekko gecko*) is the second largest gecko species: an individual can weigh up to 150-200 grams. The gecko's climbing ability has attracted human attention for more than two millennia. The gecko's ability to "run up and down a tree in any way, even with the head downwards" has been observed since the time of Aristotle [1], who mentioned these curious creatures in his manuscript, *Historia Animalium*, written four centuries before Christ.

Until the mid-twentieth century, scientific observations have not permitted a good understanding of the capacity of the gecko to stay stuck motionless or running on vertical or inverted surfaces [2-5]. Only after the electron microscopy's development, in the 1950s, were researchers able to note the hierarchical, from the nano- to the macro-scale, morphology of the gecko's feet [6-10]. A Tokay gecko's typical foot consists of hierarchical structures (Fig. 1.1) starting with macroscopic lamellae (soft ridges ~1 mm in length), from which branch off setae (30-130 μm in length and 5-10 μm in diameter). Each setae terminates with 100-1000 substructures such as

spatulae (0.1-0.2 μm wide and 15-20 nm thick), responsible for the gecko's adhesion. More recently, numerous studies (see [11-22] and related references) bring out the factors that allow the gecko to adhere and detach from surfaces. Very recently, van der Waals attraction [21] and capillarity [22] have been recognized as the key mechanisms in the gecko's adhesion.
Like geckos, many other creatures such as beetles, flies and spiders possess the remarkable ability to move on vertical surfaces and ceilings (*e.g.* see [23, 24] and related references). Their adhesive ability arises from the micro/nanostructures of which their attachment pads are composed. It is noteworthy that as the mass of the creature increases, the size of the terminal attachment elements decreases and their density increases [15], in order to enhance the adhesion strength. Thus, more than insects and spiders, geckos exhibit the most versatile and effective dry adhesion known in nature, as imposed by their larger mass. The mimicry of the gecko's adhesion could lead to a revolution in material science [25-27] and Spiderman suits are also envisioned [27].
In this paper we report new observations on the adhesion times of living tokay geckos following two different *in vivo* experiments. We have considered two different geckos, male or female, adhering on different surfaces, glass or Poly(methyl meth-acrylate) (PMMA) with different roughness. Previously, all these surfaces were analysed with a three-dimensional (3D) optical profilometer. The data have been treated using Weibull statistics, showing a relevant statistical correlation.
Although the measurement of failure time is an interesting parameter, it cannot be directly correlated with the force and energy values of prior studies. Moreover, since our data were from live geckos, the role of the animal's behaviour in failure time cannot be *a priori* excluded and the adhesion times have to be considered as indicative of the entire biosystem, *i.e.*, not only of the animal's adhesive ability but, for example, also of muscular fatigue (it is well-known that geckos must produce shear forces to maintain adhesive forces [19]: given the long attachment times, it is reasonable that the geckos became fatigued, limiting their clinging ability). Nevertheless, the extraordinary adhesive ability that we have observed after the moult suggests to us that the adhesion times that we have measured are mainly linked to the adhesive ability and scarcely influenced by other factors, such as muscular fatigue.

1.2. Surface characterization

The characterization of PMMA and glass surfaces was performed with a three-dimensional (3D) optical profilometer, Talysurf CLI 1000, equipped with the CLA Confocal Gauge 300 HE (300 μm range and 10 nm vertical resolution), both from Taylor Hobson, Leicester, UK. The parameters tuned during the analysis were the measurement speed (50 μm/s), the sampling rate (100 Hz), the measured area (0.1 x 0.1 mm^2), the resolution in "*xy*" plane (0.5 μm), leading to a final resolution of 201 points/profile. All parameters were referred to a 25 μm cut-off.

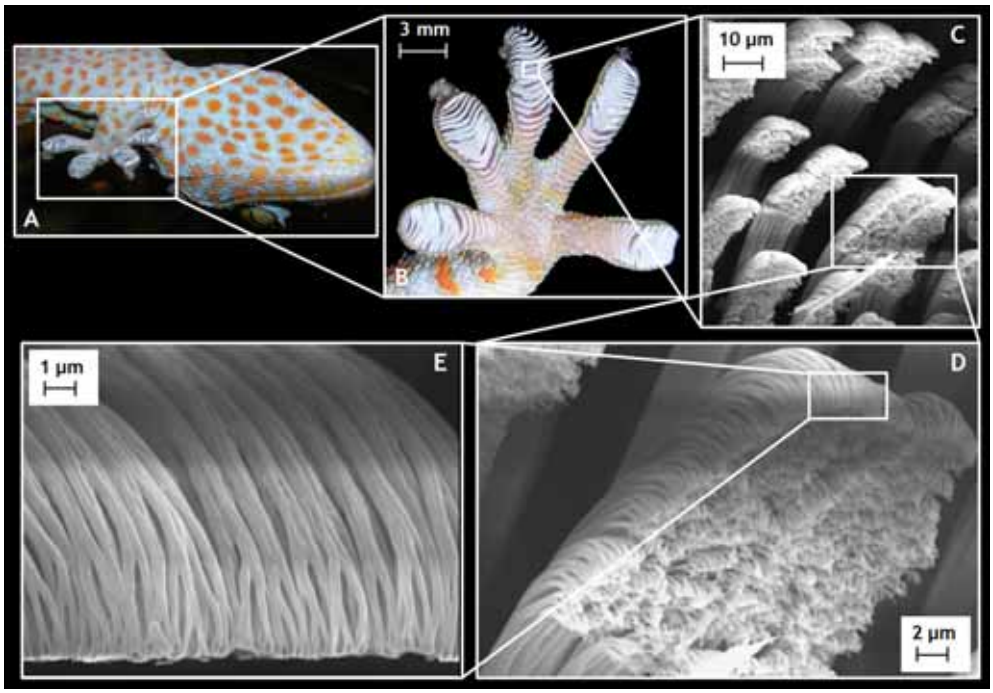

Fig. 1.1 The gecko's hierarchical adhesive apparatus. (A) Ventral view of the Tokay gecko (*Gekko gecko*). (B) Gecko's foot. Scanning electron microscope (SEM) micrographs of (C) the setae, (D) at higher magnification, (E) terminating in hundreds of spatula.

The roughness parameters of interest were: the standard amplitude parameters R_a, R_q, R_p, R_v, S_{sk} and the hybrid parameters S_{dr} (for details, see Fig. 1.2). R_a represents the arithmetical average roughness

($R_a = \frac{1}{l_n}\int_0^{l_n} |y(x)|dx$); R_q is the mean square roughness and represents the mean square deviation of the profile from the middle line ($R_q = \sqrt{\frac{1}{l_n}\int_0^{l_n} y^2(x)dx}$); R_p and R_v are, respectively, the height of the highest peak and the depth of the deepest valley (absolute values). The parameters S_{sk} and S_{dr} offer a comprehensive overview of the surface's characteristics, indicating, respectively, the surface skewness and the surface complexity. When S_{sk} is close to 0, the surface is equally distributed on the middle plane (p_m), when lower than 0 the surface is characterized by plateaus and several deep thin valleys, whereas when higher than 0 the surface is characterized by plateaus and several peaks. The parameter S_{dr} compares the effective surface (l_e) with the nominal one (l_n): when close to 0%, the surface is smooth, when higher the surface is characterized by a specific superficial complexity.

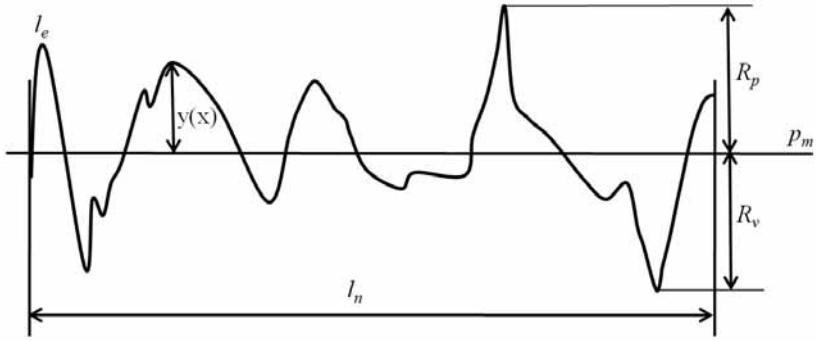

Fig. 1.2 General scheme of a profile for the definition of the roughness parameters.

Virgin PMMA and glass surfaces, tested in the first experiment, nearly present homogeneous roughness without significant anomalous alterations, apart from small isolate bubbles on the surface of glass derived from melting during the fabrication process. Figs. 1.3 and 1.4 show the virgin PMMA and glass surface (A) three-dimensional topographies and (B) two-dimensional profiles. PMMA surfaces with different roughness, namely PMMA2400 or PMMA800, have been also considered. PMMA2400/800

surfaces are obtained by a manual process that consists in doing clockwise circular movement for 2 minutes on the material sample using sandpaper 2400/800. Figs. 1.5 and 1.6 show the PMMA2400/800's surface (A) topographies and (B) profiles. We note that the roughness parameters allow us to appreciate the differences between virgin PMMA and glass surfaces and more importantly become nearly one order of magnitude greater for machined PMMA surfaces (with the exception of the skewness that however changes its sign). Table 1.1 summarizes average roughness parameters of the characterized surfaces.

	Glass	**PMMA**	**PMMA2400**	**PMMA800**
S_a (μm)	0.031 ± 0.0019	0.033 ± 0.0034	0.481 ± 0.0216	0.731 ± 0.0365
S_q (μm)	0.041 ± 0.0034	0.042 ± 0.0038	0.618 ± 0.0180	0.934 ± 0.0382
S_p (μm)	0.366 ± 0.1649	0.252 ± 0.0562	2.993 ± 0.1845	4.62 ± 0.8550
S_v (μm)	0.434 ± 0.2191	0.277 ± 0.1055	2.837 ± 0.5105	3.753 ± 0.5445
S_{sk}	-0.381 ± 0.4630	-0.122 ± 0.1103	0.171 ± 0.1217	0.192 ± 0.1511
S_z (μm)	0.609 ± 0.2791	0.432 ± 0.1082	4.847 ± 0.2223	6.977 ± 0.2294
S_{dr} (%)	0.574 ± 0.0724	0.490 ± 0.0214	15.1 ± 1.6093	28.367 ± 2.2546

Table 1.1 Roughness parameters of the characterized surfaces.

For the first experiment, the roughness parameters S_a and S_q did not allow to appreciate significant differences between virgin PMMA and glass surfaces. In particular, the parameter S_a represents the area between the middle line and the roughness profile, but it is a measurement which cannot distinguish the difference between solid areas and voids. For this reason it could not provide information about the superficial design and the skewness of the surface. However, in the second experiment the roughness parameters S_a and S_q of PMMA2400 and PMMA800 revealed the first important difference between machined PMMA surfaces and virgin PMMA: these two surface parameters present a value one order of magnitude higher than those of virgin PMMA.

For our focus, the parameters S_p, S_v and S_z, combined with the parameter S_{sk}, and the roughness parameter S_{dr} have a particular interest because they are significant in surface characterization. The roughness parameters S_p and S_v

denotes that both virgin PMMA and glass have a similar value for the highest peak and deepest valley and this value is in the magnitude order of hundreds of nm. The same observation can be made for PMMA2400 and PMMA800, but for the latter surfaces the value of S_p and S_v is of few μm (~3 and ~4 μm, respectively), one order of magnitude higher than that of virgin PMMA and glass.

When we consider the S_p and S_v parameters, the virgin PMMA surface shows lower values than glass and, as expected, PMMA2400 presented lower values compared to PMMA800. However, both virgin PMMA and glass had a higher value for the S_v parameter compared to the respective value of S_p. This indicates a surface characterized by higher depth (absolute value) of valleys compared with the height of peaks; as a consequence of the manual process of surface manufacture, both PMMA2400 and PMMA800 denotes a reverse trend, showing a surface with higher height of peaks in comparison with the depth (absolute value) of valleys.

Moreover, an analysis of the S_z parameter reveals the spatial distribution of the five highest peaks and five deepest valleys. The virgin PMMA surface is characterized by less marked peaks and valleys compared to the glass surface ($S_{p\text{-SmPMMA}} < S_{p\text{-Glass}}$, $S_{v\text{-SmPMMA}} < S_{v\text{-Glass}}$), but on the virgin PMMA surface the five highest peaks are nearer one to another ($S_{z\text{-SmPMMA}} = 0.432$ μm) than those of the glass surface ($S_{z\text{-Glass}} = 0.609$ μm). Both the virgin PMMA surface and glass surface show a negative parameter S_{sk}, which indicates a trend of plateau and several deep thin valleys, and therefore supports our findings about the S_p and S_v parameter. This trend is more marked on the glass surface than on the virgin PMMA surface. Instead, PMMA2400 and PMMA800 possess a positive S_{sk} parameter value, which indicates a trend of plateau and several peaks, in agreement with the previously reported results of the S_p and S_v parameters.

In conjunction with the S_{sk} parameter, the S_{dr} parameter gives an idea of the complexity of the surfaces. Both virgin PMMA and glass are characterized by a small value of the S_{dr} parameter ($S_{dr} < 1$ %) and this means that both surfaces have a reduced superficial complexity: the maximum value, obtained for the glass surface, indicates that the measured area of curvilinear surface exceeds the area of the support surface of a maximum factor of 0.574%.

In contrast, the two machined surfaces (PMMA2400 and PMMA800) present a high superficial complexity, so the real measured area exceeds the support scanning area by a factor of ~15 % and ~28 %, respectively.

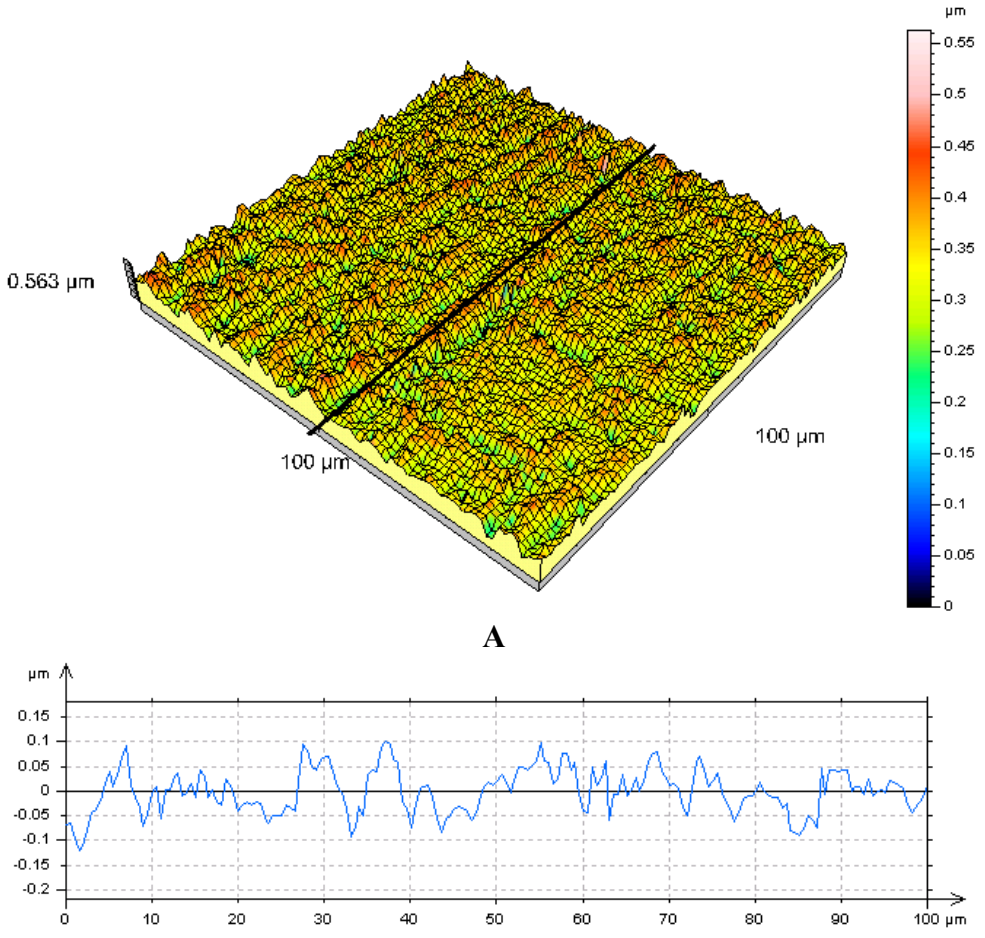

A

B

Fig. 1.3 PMMA virgin surface. (A) Three-dimensional topography. (B) Two-dimensional profile (extracted at 50 µm from the edge of the square measured area).

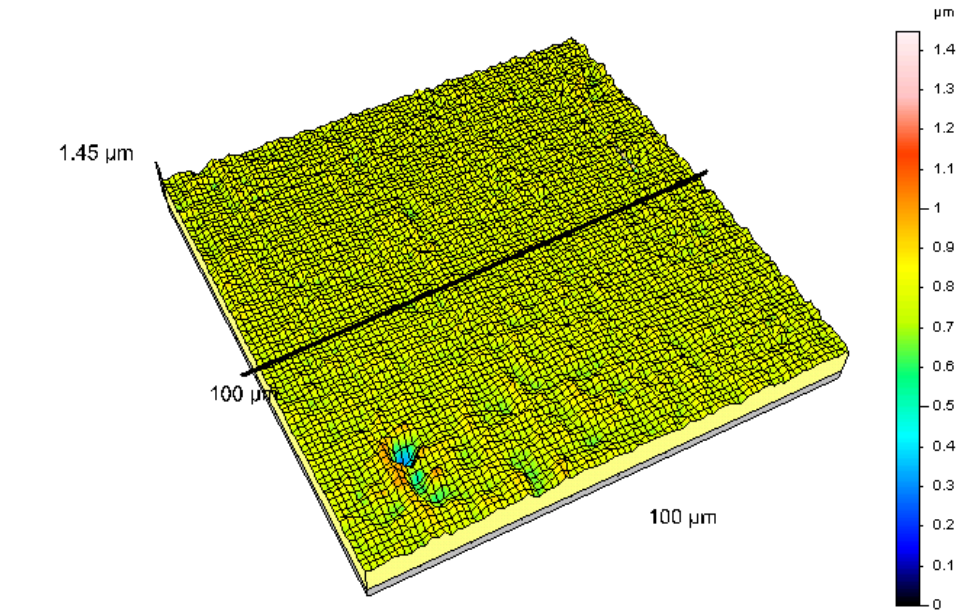

A

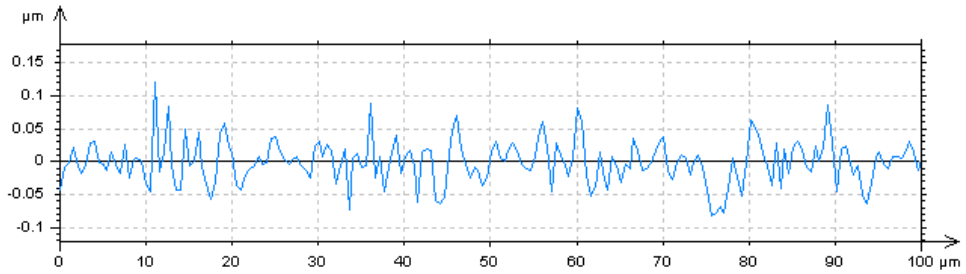

B

Fig. 1.4 Glass surface. (A) Three-dimensional topography. (B) Two-dimensional profile (extracted at 50 µm from the edge of the square measured area).

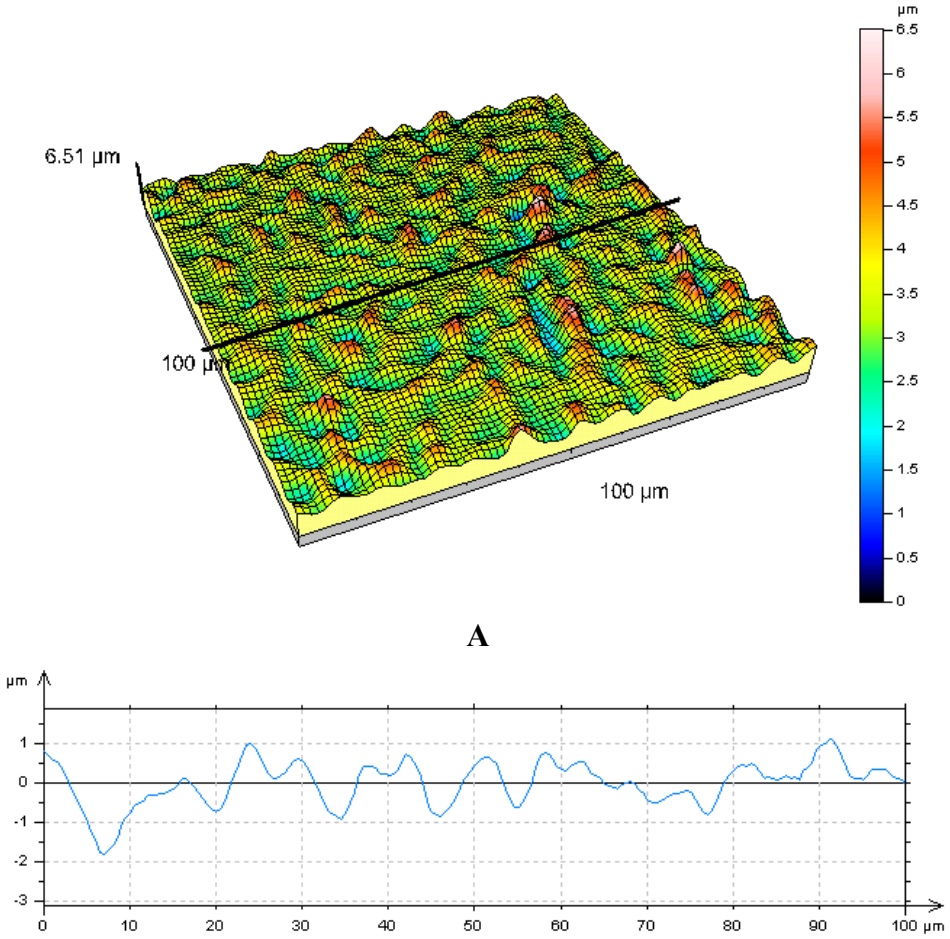

A

B

Fig. 1.5 PMMA2400 surface. (A) Three-dimensional topography. (B) Two-dimensional profile (extracted at 50 µm from the edge of the square measured area).

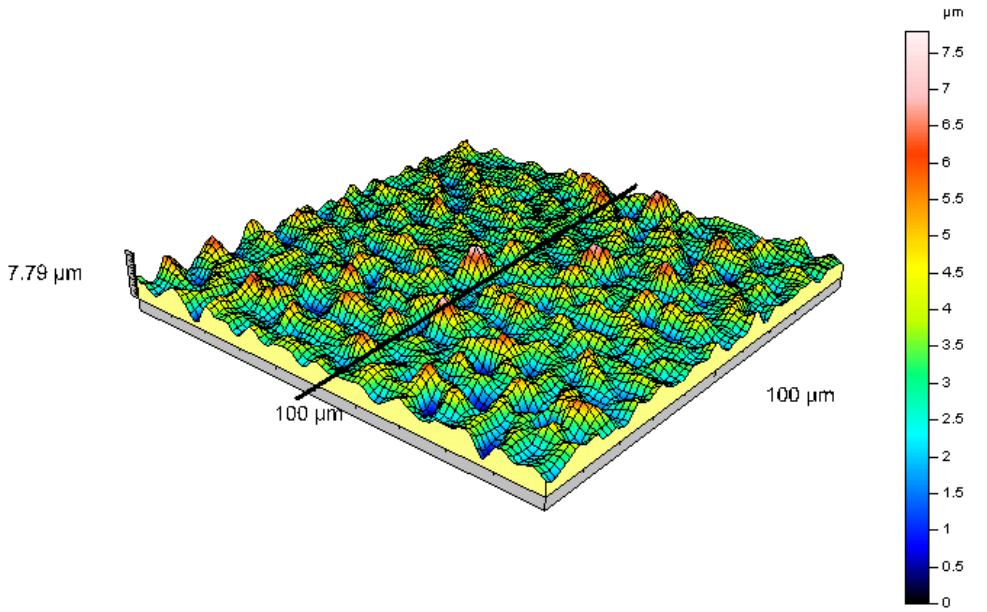

A

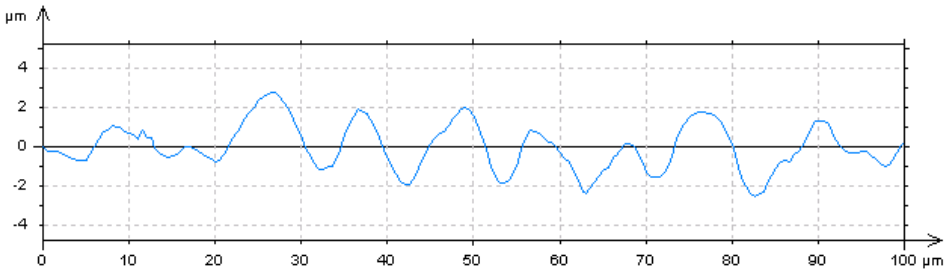

B

Fig. 1.6 PMMA800 surface. (A) Three-dimensional topography. (B) Two-dimensional profile (extracted at 50 µm from the edge of the square measured area).

Figs. 1.3B and 1.4B present the characteristic profiles of virgin PMMA and glass, analysed in the first set of experiments. First of all, these profiles confirm what our previously reported findings in that both surfaces have mainly plateau and several deep thin valleys. This feature seems to be more marked on the glass profile than on the virgin PMMA profile. During our analysis, extracted profiles enabled us to make some further observations.

The glass profile is characterized by a higher irregularity compared to the PMMA profile: it shows very deep thin valleys close to very marked peaks; on the contrary, in the distribution of valleys and peaks, virgin PMMA presents a profile that is nearer to the middle line: the height of peaks and valleys is of the same order of magnitude compared to the glass profile's height, while the lateral width is almost one order of magnitude higher than that of the glass profile.
Figs. 1.5B and 1.6B present the characteristic profiles of machined surfaces (PMMA2400 and PMMA800), analysed in the second set of experiments and compared to the virgin PMMA. The superficial profile is similar for both surfaces and with a regular spatial design: in the PMMA2400 profile a wavelength $\lambda_{PMMA2400} \approx$ 7-8 μm with some scattered irregularities can be recognized, while PMMA800 revealed a wavelength $\lambda_{PMMA800} \approx$ 10-12 μm and a semi regular sinusoidal superficial profile. The quantitative difference to emphasize between these two surfaces is the height of the peaks and valleys: the PMMA800 surface presents an absolute height $h_{PMMA800} \approx 2$ μm, that is double compared to the height of the peaks and valleys for PMMA2400 ($h_{PMMA2400} \approx 1$ μm).

1.3. Weibull statistics

We analysed the gecko's adhesion times using the well-known Weibull statistics. It is usually applied to describe the strength and fatigue life of solids, since it is based on the weakest link concept. Thus, we treat the gecko's detachment as an interfacial failure. The discovered significant statistical correlation suggests the existence of a weakest link in the animal's adhesion, rigorously quantified by the Weibull shape and scale parameters by data fitting.
Accordingly, the distribution of failure (F) describing the cumulative probability for the gecko's detachment is expected to be:

$$F(t;m;t_0) = 1 - e^{-\left(\frac{t}{t_0}\right)^m} \quad (1)$$

where t is the measured adhesion time, m is the shape parameter (governing the standard deviation), or Weibull modulus, and t_0 is the scale parameter (governing the mean value) of the distribution of failure.
The cumulative probability $F_{\mathrm{i}}(t_{\mathrm{i}})$ can be obtained experimentally as

$$F_{\mathrm{i}}(t_{\mathrm{i}}) = \frac{\mathrm{i} - 1/2}{N}, \tag{2}$$

where N is the total number of measured adhesion times t_{i} and $t_1, \ldots,$ t_{N}, are ranked in an ascending order.

All experiments were performed at room temperature (~23 °C) and humidity (~75 %). Each set of measurements was performed during different days. The time between one measurement and the following, pertaining to the same set, is only the time needed to rotate the box (~14 s), in order to place the gecko again in its downwards position.

1.3.1. The first set of experiments

We considered a female gecko (G1) adhering on inverted virgin PMMA or glass surfaces under only its weight (~46 g). The animal was placed in its natural position on the horizontal bottom of the box (50 x 50 x 50 cm^3) composed of the characterized surfaces. Then, slowly, we rotated the box, so that the gecko reached its downwards position; at that time we started to measure the gecko's adhesion time. We excluded any trial in which the gecko walked on the inverted surface; the time measurement was stopped when gecko broke loose from the inverted surface and jumped on the bottom of the box. A similar analysis was carried out with a male gecko (G2, weight of ~72 g), but in this case the time was stopped at the first detachment movement of the gecko's feet. The different measurement strategies do not significantly affect the statistics of the results, confirming their robustness.
Fig. 1.7 presents the Weibull statistics applied to the results of the five measurements of the adhesion of G1 on a virgin PMMA surface; only one set is taken during the moult (X-dots). Similarly, Fig. 1.8 shows the Weibull interpretation of four sets of G1 and two of G2 (dashed lines) on the glass surface.

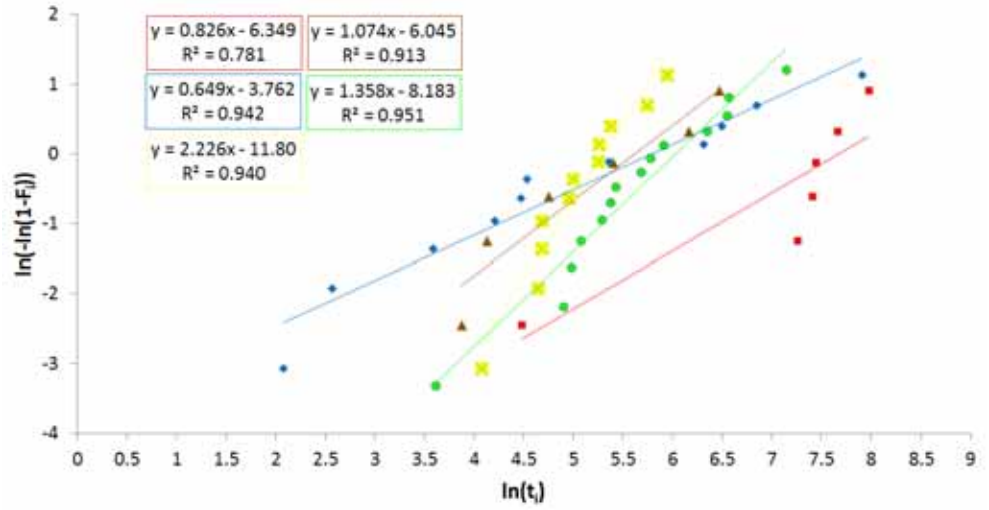

Fig. 1.7 Weibull statistics on G1 applied to the four data sets and in case of moult (X-dots), on virgin PMMA.

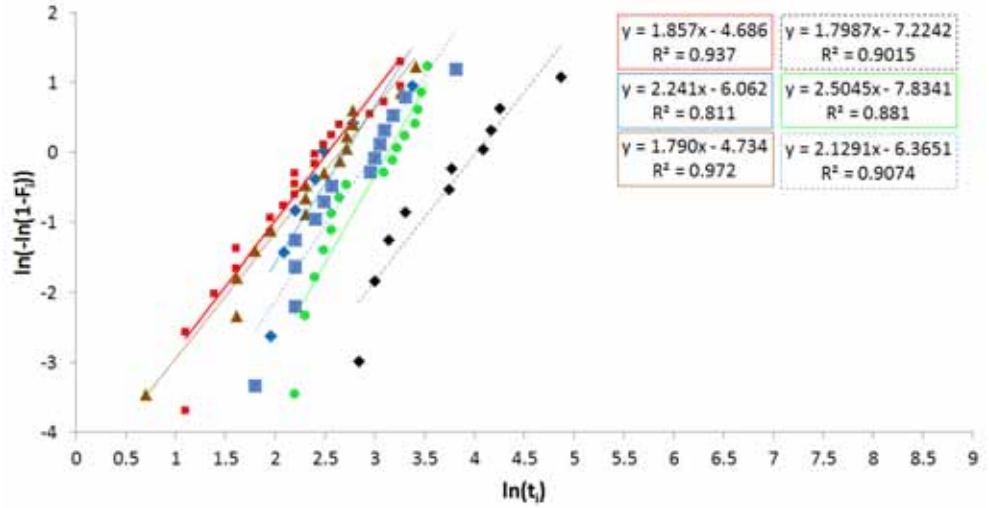

Fig. 1.8 Weibull statistics applied to the four data sets of G1 and the two data sets of G2 (dashed lines), on glass.

Table 1.2 summarizes the value of the Weibull modulus, m (shape parameter), and of the scale parameter, t_0, for each set on virgin PMMA (m_{PMMA} and t_{0PMMA}) or glass (m_{Glass} and t_{0Glass}).

		Virgin PMMA		Glass	
		Scale parameter m_{PMMA}	Shape parameter t_{0PMMA} (s)	Scale parameter m_{Glass}	Shape parameter t_{0Glass} (s)
Gecko G1	1 set	0.826	2178.6	1.857	12.5
	2 set	1.074	278.2	1.79	14.1
	3 set	0.649	329.2	2.241	15.0
	4 set	1.358	413.9	2.504	22.8
Gecko G2	1 set	\	\	1.798	55.6
	2 set	\	\	2.129	19.9
Average value		**0.977**	**800.0**	**2.053**	**23.3**

Table 1.2 Weibull Modulus m (shape parameter) and the scale parameter t_0 for each gecko and set, on virgin PMMA (m_{PMMA} and t_{0PMMA}) and on glass (m_{Glass} and t_{0Glass}).

We continued to observe the adhesive ability of G1 during the phase following the moult; we observed an extraordinary increase of the time of adhesion, of about 1000 % for PMMA and 20000 % for glass, corresponding to adhesion times of hours. This again confirms that the predominant cause of the gecko's detachment is its adhesive ability and that such an ability is limited by pollutant factors, efficiently removed by the moult.

Considering the average values for the virgin PMMA surface, the Weibull modulus is found to be $m_{PMMA} \approx 1$ and the scale parameter t_{0PMMA} is exactly 800 s, corresponding to 13 minutes and 20 s. In each set of measurements on the PMMA surface, the correlation R^2 is high, showing a coefficient of correlation $R^2 > 0.7$ only in the first set, while the coefficient of correlation is $R^2 > 0.9$ in the other three sets. When the average values for the glass surface is considered, the Weibull modulus is found to be $m_{Glass} \approx 2$ and the scale parameter t_{0Glass} is ≈ 23 s, one order of magnitude less than the value of the scale parameter found for the virgin PMMA. In each set of measurements on the glass surface, the correlation R^2 is high, showing a coefficient of correlation $R^2 > 0.9$ in the first two sets with G1 and in the

two sets with G2, and a coefficient of correlation $R^2 > 0.8$ in the other two sets with G1.

The Weibull statistics were also applied to the set of failure times (Fig. 1.7) represented by the yellow dotted line set. These were gathered during the gecko's moulting process on the virgin PMMA surface. Its capacity of adhesion is reduced to a few minutes. In this case, the Weibull modulus ($m_{\text{PMMA-M}}$) is found to be ~2.2 and the correlation is $R^2 = 0.94$. The scale parameter $t_{0\text{PMMA-M}}$ is ~200 s, corresponding to 3 minutes and 20 s. As the failure shape parameter m suggests, in this set the values of failure times have a tendency to be closer to one another. When the shape parameter m is high, very high or very low adhesion times become less probable. The probability distribution is less spread over all possible values and becomes symmetric to the scale parameter value t_0. The time failure process becomes an almost deterministic process. The failure times have a magnitude of a hundreds of seconds (Table 1.3, Test 1).

The adhesion tests on glass demonstrate a similar trend in the distribution probability function. In this case, the averaged value (m_{Glass}) emerges to be equal to 2 and this shows an inferior dispersion of measured data of adhesion time, that have a magnitude of tens of seconds (Table 1.3, Test 2). The virgin PMMA adhesion tests instead present a shape parameter value (m_{PMMA}) equal to 1. The lower the parameter m, the more variable the failure time. In this case, the values are strongly variable between over two orders of magnitude (Table 1.3, Test 3).

As our results confirm, on the PMMA surface the gecko shows higher times of failure. Thus, we can form the hypothesis that, on PMMA surfaces during these high time intervals, different causes of detachment can be introduced and be very variable, linked to the external factors of the experimental box, *e.g.* sound, light and movement, or physiological factors of the gecko, *e.g.* hunger, cooling, disinterest and muscular fatigue. On the other hand, on the glass surface and on the virgin PMMA surface during moulting, the ability of the gecko to remain attached drastically decreases. The gecko realizes adhesion with several difficulties, so detachment only occurs when it is unable to remain attached any longer. This is the explanation for the narrower spread of values obtained from these test measurements. As a consequence, we can suppose that, on glass surfaces and on virgin PMMA surface during moulting, the failure of the gecko's adhesive system certainly occurs at the instant of detachment and so the shape parameter m_{Glass}, $m_{\text{PMMA-M}}$ and the scale parameter $t_{0\text{Glass}}$, $t_{0\text{PMMA-M}}$ have been correctly

estimated. m_{Glass} and t_{0Glass} correspond to the real adhesive capabilities and characteristics of the Tokay gecko's foot system on glass surfaces.

Test 1		Test 2		Test 3	
Test n°	Time (s)	Test n°	Time (s)	Test n°	Time (s)
1	59	1	9	1	8
2	104	2	10	2	13
3	108	3	11	3	36
4	108	4	12	4	67
5	142	5	13	5	87
6	148	6	13	6	93
7	190	7	14	7	212
8	192	8	15	8	550
9	216	9	22	9	660
10	310	10	24	10	936
11	380	11	25	11	2703
		12	27		
		13	30		
		14	31		
		15	32		
		16	34		

Table 1.3 Adhesion times on virgin PMMA (Test 1) during the moult, (Test 2) on glass surface, and (Test 3) on virgin PMMA not during the moult.

According to the above-mentioned causes for detachment on PMMA surfaces, the gecko's detachment can also be linked to a limited number of variable physiological and external factors. Moreover, the test condition plans to use only two geckos. In both our experiments, we certainly tried to check firm values of m_{PMMA} and t_{0PMMA} for the Tokay gecko on PMMA surfaces and the subsequent relation between the failure of the gecko's

adhesive system and the surface roughness. We start from two basic concepts: two different methods used for the measurement of failure time and the observed repeatability of trials of two geckos on different and successive days. The two methods used for G1 and G2 evaluated completely and conceptually different intervals of time of failure. We can form the hypothesis that our two measurement methods allowed us to exclude that the physiological factors, linked to the will and to the decisional capability of geckos, deeply influenced the results of our study. Furthermore, by repeating the experiments on different days the negative influence on results due to external factors was limited. We performed several trials during the same day and on the next days. The obtained results confirm those already obtained and permits us to suppose that estimated values for the shape parameter m_{PMMA} and the scale parameter t_{0PMMA} are correctly linked to the failure of the gecko's adhesive system.

Moreover, the greater difficulty noted for the gecko's adhesion on the glass surface could be explained through the observation of the glass profile (Fig. 1.4B). It is characterized by a higher irregularity compared to the virgin PMMA profile (Fig. 1.3B). The height of peaks and valleys is of the same order of magnitude compared to the virgin PMMA profile height ($h_{Glass} = h_{PMMA} \approx 0.5\text{-}1$ μm), but the lateral width ($w_{Glass} \approx 2\text{-}3$ μm) is almost one order of magnitude lower than that of the virgin PMMA profile ($w_{PMMA} \approx 8\text{-}9$ μm). This feature determines a considerable closeness of one peak to the next. Thus, considering this superficial conformation, we can interpret our results in the following way. At the interface gecko toe-surface, considering the glass surface with thin, marked peaks and valleys, it could not represent the complementary surface to the gecko's toe, which is unable to cling to the surface by each nanometric contact of each singular lamella. As a consequence, the gecko's adhesion ability drastically decreases. On the other hand perhaps thanks to the presence of larger hollows and peaks, the virgin PMMA surface guarantees a good adhesion despite this unfavorable situation for our two geckos before the moulting process.

The totality of the above mentioned polluting substances trapped at the interface foot-surface clearly disappears in the days that follow moulting and in which we registered the extraordinary increase of the gecko's adhesive ability.

1.3.2. The second set of experiments

We have also tested machined PMMA2400/800 surfaces. Fig. 1.9 presents the Weibull statistics applied to the results of one set of gecko G1 on the PMMA2400 surface and two sets of gecko G2 on both PMMA2400 and PMMA800. Table 2.4 summarizes the value of the Weibull modulus m (shape parameter) and the value of the scale parameter t_0 for each set on PMMA2400 surface ($m_{PMMA2400}$ and $t_{0\text{-}PMMA2400}$) and on PMMA800 surface ($m_{PMMA800}$ and $t_{0\text{-}PMMA800}$). On PMMA2400, the Weibull modulus is basically the same for both G1 and G2 and corresponds to $m_{PMMA2400\text{-}G1} \approx m_{PMMA2400\text{-}G2} \approx 1.2$, with a statistical correlation $R^2 = 0.95$. For gecko G1, the scale parameter is $t_{0\text{-}PMMA2400\text{-}G1} \approx 1618$ s (corresponding to almost 27 minutes); the scale parameter for gecko G2 is $t_{0\text{-}PMMA2400\text{-}G2} \approx 886$ s (approximately corresponding to 15 minutes). On PMMA800, the identified Weibull modulus is $m_{PMMA800\text{-}G2} = 1.1$ and the correlation is $R^2 = 0.83$. The scale parameter of gecko G2 is $t_{0\text{-}PMMA800\text{-}G2} \approx 108$ s (corresponding approximately to 1 minute and 48 s).

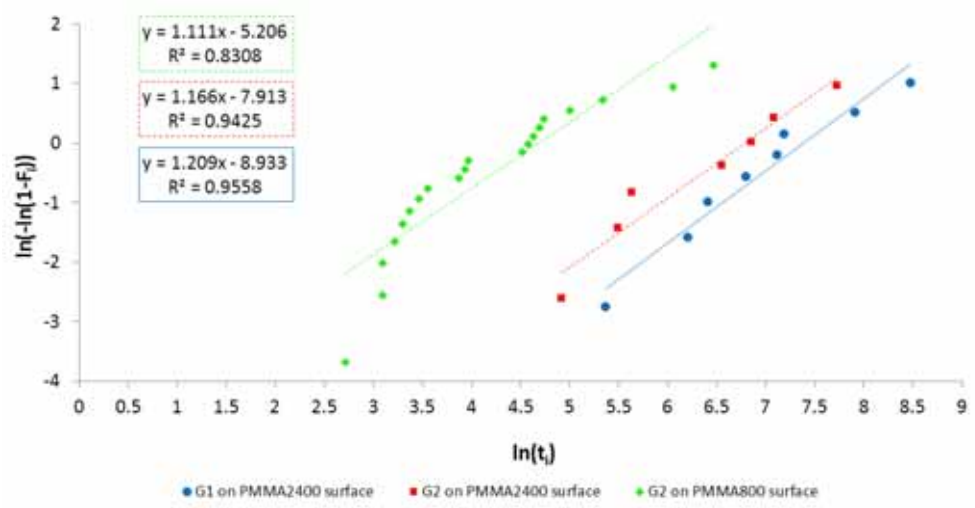

Fig. 1.9 Weibull statistics applied to the data set of G1 on PMMA2400 and to the two data sets of G2 on PMMA2400 and PMMA800.

		PMMA2400		PMMA800	
		Scale parameter $m_{PMMA2400}$	Shape parameter $t_{0PMMA2400}$ (s)	Scale parameter $m_{PMMA800}$	Shape parameter $t_{0PMMA800}$ (s)
Gecko G1	1 set	1.209	1617.7	\	\
Gecko G2	1 set	1.166	885.8	\	\
	2 set	\	\	1.111	108.4
Average value		**1.188**	**1251.7**	**1.111**	**108.4**

Table 1.4 Weibull Modulus m (shape parameter) and the scale parameter t_0 for each gecko and set, on PMMA2400 ($m_{PMMA2400}$ and $t_{0\text{-}PMMA2400}$) and on PMMA800 ($m_{PMMA800}$ and $t_{0\text{-}PMMA800}$).

Considering all of the analysed PMMA surfaces, both the virgin and machined ones, we have found a value of the Weibull modulus (m_{PMMA}) in the restricted range of 1-1.2, suggesting that this value could be a characteristic of the PMMA/gecko system. Moreover, comparing PMMA2400 and PMMA800, we note that $t_{0\text{-}PMMA800}$ is one order of magnitude lower than $t_{0\text{-}PMMA2400}$ and eight times lower than t_{0PMMA}.
Through the analysis of our results and the characteristics of the surfaces, we have demonstrated how an inverse relationship exists between the gecko's adhesive ability and the grade of roughness. Geckos show a weakening of adhesion on PMMA surfaces as roughness increases. When roughness is very high the adhesive abilities drastically decrease. These observations contradict those reported in the interesting paper by Huber et al. [26]. Our hypothesis concerns 3D complexity of PMMA surfaces and the capability of deformation and adaptability of the gecko's feet. For our focus, the S_{sk} parameter is less significant since it demonstrates a clear difference between virgin PMMA surfaces and machined ones, but it does not provide further factors to use when distinguishing between machined PMMA surfaces (PMMA2400 and PMMA800). Therefore, S_{sk} does not justify the evident decrease in the adhesive ability of geckos between PMMA2400 and PMMA800 measurement tests. In discussion of our results the S_{dr} parameter is shown to be more significant. The roughness parameter doubles between PMMA2400 and PMMA800. On the gecko's foot, the lamellae, and also its

setae, can presumably adapt well to the interacting substrates, but these lamellae have shown a physiological limit. When the PMMA surface is smooth (S_{dr} < 1 %), the gecko's setae (represented in blue in Fig. 1.10), and also its spatulae, can adapt to the surface and permit van der Waals forces to act. However, extraordinary capabilities of nanocontact hairs (spatulae) are not exploited at the top. Virgin PMMA shows that the values of the S_a and S_q parameter are lower than the spatula contact area, approximated as a circle of 100-200 nm radius [5, 24, 26, 27]. In this case the spatulae cannot follow the roughness of the surface and so cannot penetrate the characteristic valleys of virgin PMMA and adhere to the side of each individual one (Fig. 1.10A). An increase in the gecko's adhesive abilities was observed for PMMA2400 with an intermediate S_{dr} value ($S_{dr} \approx 15$ %). This surface is characterized by a higher superficial complexity compared to virgin PMMA and so the real area of contact with the gecko's foot is greater. The gecko's setae, and also its spatulae, have demonstrated a superior ability to adapt to the PMMA2400 surface roughness, adhering this time to the top and the side of single peaks of the surface. In this way the effective number of spatulae-surface nanocontacts increases and, as a direct consequence, also the adhesion ability of the gecko increases (Fig. 1.10B). Adhesion time drastically decreases on an high complexity surface ($S_{dr} \approx 30$ %). We suppose that in this case the waviness characterizing the superficial roughness ($\lambda_{PMMA800} \approx$ 10-12 μm and $h_{PMMA800} \approx 2$ μm) is superior compared to the capabilities of adaptability of the gecko's lamellae. As a consequence we observed a decrease of the %-number of setae and spatulae that, in fact, interact performing a real nanocontact with the surface (Fig. 1.10C).
Our interpretation of the results also explains the presence of claws on the tip of each gecko toe. These claws are a fundamental additional help for geckos on the surface with high superficial complexity where its lamellae, and so all its sub-hierarchical-micro and sub-hierarchical-nano structures (setae and spatulae), show not to be able to guarantee a secure adhesion. These surfaces have to possess a level of roughness that permits claws to cling to (presumably S_q of tens or hundreds of μm as order of magnitude) and to perform a more secure attachment of the gecko.

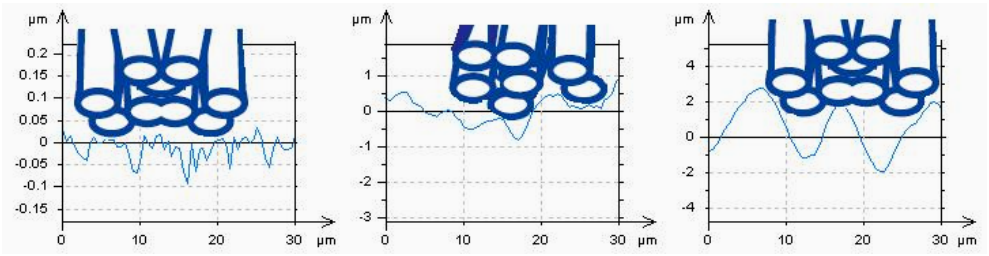

A **B** **C**

Fig. 1.10 Interpretation of experimental results of adhesion tests on different-roughness PMMA surfaces. (A) Setae (represented in blue) and its sub-hierarchical structures (spatulae) can adapt well on virgin PMMA; (B) on PMMA2400 surface the adhesion is better because of the higher interactions spatulae-substrates; (C) on PMMA800 only partial contact interactions are achieved.

1.4. Conclusions

In this paper we have demonstrated that living geckos display adhesion times following Weibull statistics, by performing three-dimensional surface topography characterizations and time of adhesion measurements. The Weibull shape (*i.e.*, modulus) and scale parameters can be used to describe quantitatively the statistics of the adhesion times of different geckos (male or female), materials (glass or PMMA), and interfaces (virgin or machined PMMA surfaces).

ACKNOWLEDGMENTS

The authors would like to thank M. Biasotto of the Department of Special Surgery of the University of Trieste for experimental instruments of surface measurements, and F. Antoniolli of the Department of Biomedicine, Unit of Dental Sciences and Biomaterials of the University of Trieste, for the helpful scientific discussion. The authors are grateful to M. Buono and S. Toscano, DVM and SIVAE member, for the technical and veterinary aid and also for the fundamental support for experimental studies. We gratefully acknowledge the “2I3T Scarl - Incubatore dell'Università di Torino” for SEM imaging instruments and M. G. Faga, CNR-ISTEC member, Chemical Department IFM and NIS Centre of Excellence, University of Torino for the

fundamental help performing the SEM micrographs. The authors thanks Margaret Pate for the final English grammar supervision.
NMP is supported by the "Bando Ricerca Scientifica Piemonte 2006" - BIADS: Novel biomaterials for intraoperative adjustable devices for fine tuning of prostheses shape and performance in surgery.

REFERENCES

[1] Aristotle, *Historia Animalium*, 343 B.C. See Book IX, Part 9, translated by Thompson DAW, http://classics.mit.edu/Aristotle/history_anim.html.
[2] Simmermacher, G., *Zeitschr. Wiss. Zool.* **40**, 481-556 (1884).
[3] Schmidt, H. R., *Jena. Z. Naturwiss.* **39**, 551-563 (1904).
[4] Dellit, W. D., *Jena. Z. Naturwiss.* **68**, 613-658 (1934).
[5] Ruibal, R., and Ernst, V., *J. Morphol.* **117**, 271-293 (1965).
[6] Autumn, K., *Biological Adhesives* (ed. A. Smith and J. Callow), 225-255. Berlin Heidelberg: Springer Verlag (2006).
[7] Russell, A. P., *J. Zool.* **176**, 437-476 (1975).
[8] Russell, A. P., *Can. J. Zool.* **64**, 948-955 (1986).
[9] Schleich, H. H., and Kästle, W., *Amphib. Reptil.* **7**, 141-166 (1986).
[10] Gennaro, J. G. J., *J. Nat. Hist.* **78**, 36-43 (1969).
[11] Hiller, U., *Z. Morphol. Tiere* **62**, 307-362 (1968).
[12] Autumn, K. and Peattie, A. M., *Int. Comp. Biol.* **42**, 1081-1090 (2002).
[13] Autumn, K., *MRS Bulletin* **32**, 473-478 (2007).
[14] Autumn, K. and Gravish, N., Philosophical Transactions of the Royal Society of London, Series A: Mathematical, Physical, and Engineering Sciences **366**, 1575-1590 (2008).
[15] Arzt, E., Gorb, S., and Spolenak, R., *Proc. Natl. Acad. Sci. USA* **100**, 10603-10606 (2003).
[16] Autumn, K., Sitti, M., Peattie, A., Hansen, W., Sponberg, S., Liang, Y. A., Kenny, T., Fearing, R., Israelachvili, J., and Full, R. J., *Proc. Natl. Acad. Sci. USA* **99**, 12252-12256 (2002).
[17] Bergmann, P. J., and Irschick, D. J., *J. Exp. Zoology A*, **303**, 785-791 (2005).
[18] Huber, G., Mantz, H., Spolenak, R., Mecke, K., Jacobs, K., Gorb, S. N., and Arzt, E., *Proc. Natl. Acad. Sci. USA* **102**, 16293-16296 (2005).
[19] Autumn, K., Dittmore, A., Santos, D., Spenko, M., and Cutkosky, M., *J. Exp. Biol.* **209**, 3569-3579 (2006).

[20] Autumn, K., Hsieh, S. T., Dudek, D. M., Chen, J., Chitaphan, C., and Full, R. J., *J. Exp. Bio.*, **209**, 260-272 (2006).
[21] Autumn, K., Liang, Y. A., Hsieh, S. T., Zesch, W., Chan, W.-P., Kenny, W. T., Fearing, R., and Full, R. J., *Nature* **405**, 681-685 (2000).
[22] Huber, G., Gorb, S. N., Spolenak, R., and Arzt, E., *Biology Letters* **1**, 2-4 (2005).
[23] Stork, N. E., *J. Exp. Biol.* **88**, 91-107 (1980).
[24] Dai, Z., Gorb, S. N., and Schwarz, U., *J. Exp. Biol.* **205**, 2479-2485 (2002).
[25] Yurdumakan, B., Raravikar, N. R., Ajayan, P. M., and Dhinojwala, A., *Chemical Communications* **30**, 3799-3801 (2005).
[26] Haeshin, L., Bruce, P. L., and Phillip, B. M., *Nature* **448**, 338-341 (2007).
[27] Pugno, N. M., *J. Phys.: Condens. Matter* **19**, 395001, pp. 1-17 (2007).

2. THE GECKO'S OPTIMAL ADHESION ON NANOROUGH SURFACES

Abstract

In this letter we report experimental observations on the times of adhesion of living Tokay geckos on Poly(methyl meth-acrylate) (PMMA) inverted surfaces. Two different geckos (male and female) and three surfaces with different root mean square (RMS) roughness (RMS = 42 nm, 618 nm and 931 nm) have been considered, for a total of 72 observations. The measured data are proved to be statistically significant, following the Weibull statistics with coefficients of correlation between 0.78 and 0.96. The unexpected result is the observation of the gecko's maximum adhesion on the surface with intermediate roughness of RMS = 618nm, that we note has waviness comparable to the seta size.

2.1. Introduction

The Tokay gecko's (*Gekko gecko*) ability to "run up and down a tree in any way, even with the head downwards" was first observed by Aristotle, almost 25 centuries ago, in his *Historia Animalium*. However, the pioneer study on the gecko's adhesion has been done by Hiller [1], who first provided Scanning Electron Microscope (SEM) pictures of the setae, showing their hierarchical ultrastructure and high density of terminal spatulae; he first did a very careful experiment on living geckos, showing adhesion dependence on surface energy of the substrate. The structure of the digital setae of lizards was accurately discussed [2]. In spite of this, only recently, the adhesive force of a single foot-hair of geckos has been measured [3]. Like geckos, a comparable adhesive mechanism and adhesive ability, resulting in an extraordinary ability to move on vertical surfaces and ceilings, can be found in other creatures, such as beetles, flies and spiders. A comparison between the gecko and spider nanostructured feet is reported in Fig. 2.1.

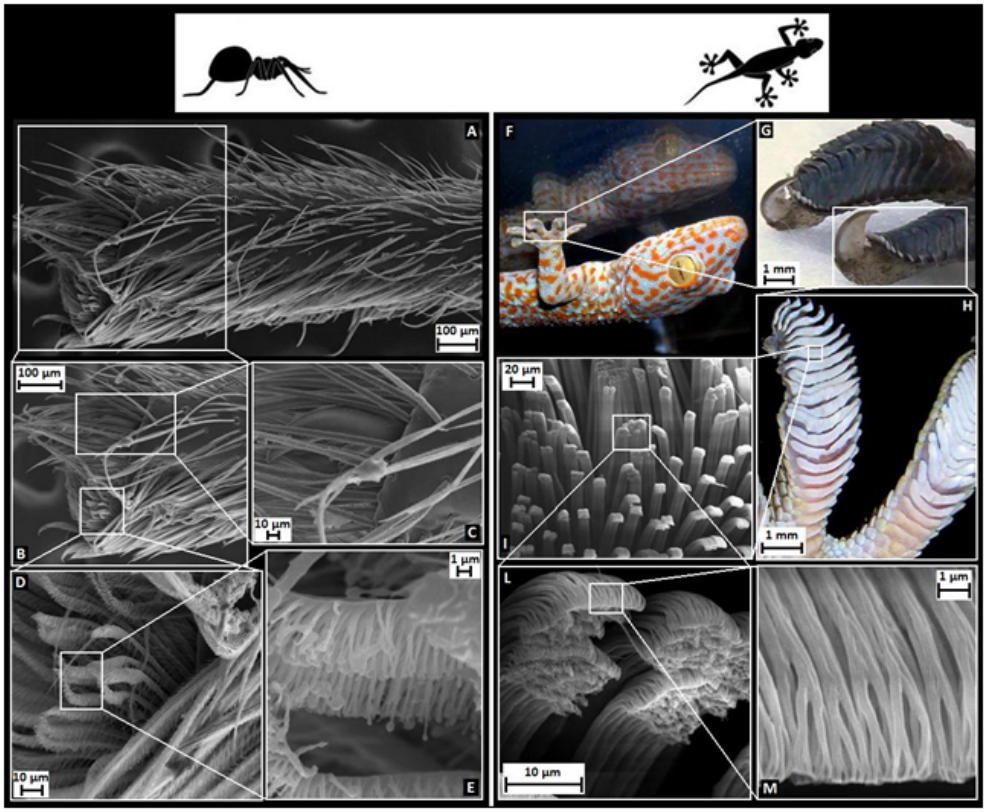

Fig. 2.1 Spider and gecko feet showed by SEM (Zeiss EVO 50). In the Tokay gecko (Fig. 2.1F) the attachment system is characterized by a hierarchical hairy structures, which starts with macroscopic lamellae (soft ridges ~1 mm in length, Fig. 2.1H), branching in setae (30-130 µm in length and 5-10 µm in diameter, Fig. 2.1I, 2.1L [1, 2, 4, 5]). Each seta consists of 100-1000 substructures called spatulae, the contact tips (0.1-0.2 µm wide and 15-20 nm thick, Fig. 2.1M; [1, 2]) responsible for the gecko's adhesion. Terminal claws are located at the top of each singular toe (Fig. 2.1G). Van der Waals and capillary forces are responsible for the generated adhesive forces [6, 7], whereas claws guarantee an efficient attachment system on surfaces with very large roughness. Similarly, in spiders (*e.g. Evarcha arcuata* [8]) an analogous ultrastructure is found. Thus, in addition to the tarsal claws, which are present on the tarsus of all spiders (Fig. 2.1C), adhesive hairs can be distinguished in many species (Fig. 2.1D, 2.1E). Like for insects, these adhesive hairs are specialised structures that are not restricted only to one particular area of the leg, but may be found either

distributed over the entire tarsus, as for lycosid spiders, or concentrated on the pretarsus as a tuft (scopula) situated ventral to the claws (Fig. 2.1A, 2.1B), as in the jumping spider *Evarcha arcuata* [8].

Surface roughness strongly influences the animal's adhesion strength and ability. Its role was shown in different measurements on flies and beetles, walking on surfaces with well-defined roughness [9-11], on the chrysomelid beetle *Gastrophysa viridula* [12], on the fly *Musca domestica* [11] as well as on the Tokay geckos [13]. In papers [11, 12], a minimum of the adhesive/frictional force, spanning surface roughness from 0.3 μm to 3 μm, was reported. The experiments on the reptile Tokay gecko [13] showed a minimum in the adhesive force of a single spatula at an intermediate root mean square (RMS) surface roughness around 100-300 nm, and a monotonic increase of adhesion times of living geckos by increasing the RMS, from 90 to 3000 nm. There are several observations and models in the literature, starting with the pioneer paper by Fuller and Tabor (1975), in which roughness was seen to decrease adhesion monotonically. But there is also experimental evidence in the literature, starting with the pioneer paper [14], which suggests that roughness need not always reduce adhesion. For example, in the framework of a reversible model in papers [15, 16], it has been shown that for certain ranges of roughness parameters, it is possible for the effective surface energy to first increase with roughness amplitude and then eventually decreasing. Including irreversible processes, due to mechanical instabilities, it has been demonstrated [17], under certain hypotheses, that the pull-out force must increase by increasing the surface wave amplitude. We suggest here that roughness alone could not be sufficient to describe the three-dimensional topology of a complex surface and additional parameters have to be considered for formulating a well-posed problem.
Accordingly, we have machined and characterized three different Poly(methyl meth-acrylate) (PMMA) surfaces (PMMA 1, 2, 3; surface energy of ~41 mN/m) with a full set of roughness parameters, as reported in Table 2.1 (see paragraph 1.2 for a detailed explanation of the classical roughness parameters extracted (S_a, S_q, S_p, S_v, S_z, S_{sk}, S_{dr})).

2.2. Materials and Methods

Two different Tokay geckos, female (G1, weight of ~46 g) and male (G2, weight of ~72 g), have been considered. The gecko was placed in its natural position on the bottom of a box (50 x 50 x 50 cm^3). Then, slowly, we rotated the box up to the gecko reaches a natural downwards position and, at that time, we started the measurement of the gecko's adhesion time. We excluded any trial in which the gecko walked on the inverted surface. The time measurement was stopped when gecko broke loose from the inverted surface and fell on the bottom of the box (for G1) or at the first detachment movement of the gecko's foot (for G2). The time between one measurement and the next, pertaining to the same set, was only the time needed to rotate the box (~14 s) and replace the gecko again on the upper inverted surface. The experiments were performed at room temperature (~22 °C) and humidity (~75 %). The measured adhesion times are summarized in Table 2.2 and confirmed to be statistically significant by applying Weibull statistics, see Fig. 2.2.

2.3. Results and conclusions

We have observed a maximum in the gecko's adhesion times on PMMA 2, having an intermediate roughness of RMS = 618 nm. An oversimplified explanation could be the following. For PMMA 1 ($S_{q\text{-PMMA1}}$ = 42 nm, $S_{dr\text{-PMMA1}}$ < 1 % and waviness of $\lambda_{PMMA1} \approx$ 3-4 μm, $h_{PMMA1} \approx$ 0.1 μm), the gecko's seta (diameter of ~10 μm, represented in blue in Fig. 2.3, that must not be confused with the terminal nearly two dimensional spatulae) cannot penetrate in the characteristic smaller valleys and adhere on the side of each single one (Fig. 2.3A), thus cannot optimally adapt to the surface roughness. For PMMA 2 ($S_{q\text{-PMMA2}}$ = 618 nm, $S_{dr\text{-PMMA2}} \approx$ 15 % and $\lambda_{PMMA2} \approx$ 7-8 μm, $h_{PMMA2} \approx$ 1 μm) the gecko's setae are able to adapt better to the roughness, adhering this time on the top of and on the side of a single asperity: in this way the effective number of setae in contact increases and, as a direct consequence, also the adhesive ability of the gecko increases (Fig. 2.3B). On PMMA 3 ($S_{q\text{-PMMA3}}$ = 931 nm, $S_{dr\text{-PMMA3}} \approx$ 30 % and $\lambda_{PMMA3} \approx$ 10-12 μm, $h_{PMMA3} \approx$ 2 μm) the waviness characterizing the roughness is larger than the seta's size: as a consequence, a decrease in the number of setae in contact is

expected (Fig. 2.3C). As a result, on PMMA 2 an adhesion increment, of about 45 %, is observed. According to [14], an increment of 40 %, thus close to our observation, is expected for an adhesion parameter α equal to 1/3. Such a parameter was introduced as the key parameter in governing adhesion as [20]:

$$\alpha = \frac{4\sigma}{3}\left(\frac{4E}{3\pi\sqrt{\beta}\gamma}\right)^{2/3} \quad (1)$$

where σ is the standard deviation of the asperity height distribution (assumed to be Gaussian), β is the mean radius of curvature of the asperity, γ is the surface energy and E is the Young modulus of the soft solid (the gecko's foot). Even if the value of E of the entire foot cannot be simply defined, as a consequence of its non-compact structure, we note that considering it to be of the order of 10 MPa (thus much smaller than that of the keratin material), with $\gamma \approx 0.05$ N/m (Autumn et al., 2000), $\sigma \approx S_q$, $\beta \approx \lambda$ would correspond to values of α close to 0.5.

The reported maximum adhesion was not observed by [13]. Note that their tested polished surfaces were of five different types, with a nominal asperity size of 0.3 μm, 1 μm, 3 μm, 9 μm and 12 μm, which correspond to RMS values of 90 nm, 238 nm, 1157 nm, 2454 nm and 3060 nm respectively. The sliding of geckos on polishing paper with a RMS value of 90 nm for slopes larger than 135° was observed [13]. On a rougher substrate, with a RMS value of 238 nm, two individual geckos were able to cling to the ceiling for a while, but the foot-surface contact had to be continuously renewed because gecko toes slowly tend to slid off the substrate. Finally, on the remaining tested rougher substrates, animals were able to adhere stably to the ceiling for more than 5 minutes.

These different observations (assuming that the influences of claws and moult were minimized also by [13]) suggest that the RMS parameter is not sufficient alone to describe the aspects of the surface roughness. The use of a "complete" set of roughness parameters could help in better understanding the animal's adhesion.

	PMMA1	PMMA2	PMMA3
S_a (μm)	0.033 ± 0.0034	0.481 ± 0.0216	0.731 ± 0.0365
S_q (μm)	0.042 ± 0.0038	0.618 ± 0.0180	0.934 ± 0.0382
S_p (μm)	0.252 ± 0.0562	2.993 ± 0.1845	4.620 ± 0.8550
S_v (μm)	0.277 ± 0.1055	2.837 ± 0.5105	3.753 ± 0.5445
S_{sk}	-0.122 ± 0.1103	0.171 ± 0.1217	0.192 ± 0.1511
S_z (μm)	0.432 ± 0.1082	4.847 ± 0.2223	6.977 ± 0.2294
S_{dr} (%)	0.490 ± 0.0214	15.100 ± 1.6093	28.367 ± 2.2546

Table 2.1 Roughness parameters for the three different PMMA (1, 2, 3) surfaces.

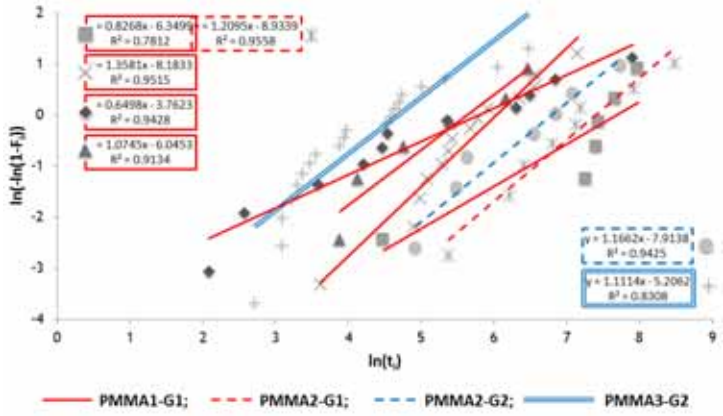

Fig. 2.2 Weibull statistics (F is the cumulative probability of detachment/failure and t_i are the measured adhesion times) applied to the measured adesion times on PMMA surfaces. PMMA 1 (red lines, for which we made the 4 sets of measurements in four different days with gecko G1), PMMA 2 (dotted lines, for which we made the 2 sets of measurements in two different days, one with gecko G1 (red) and one with gecko G2 (blue)) and PMMA 3 (blue double-line, for which we made the measurements in a single day with gecko G2).

Test No.	PMMA 1	PMMA 2	PMMA 3
1	8	137	15
2	13	215	22
3	36	243	22
4	37	280	25
5	48	498	27
6	62	610	29
7	67	699	32
8	87	900	35
9	88	945	48
10	93	1194	51
11	116	1239	53
12	134	1320	91
13	145	2275	97
14	160	2740	102
15	197	4800	109
16	212		114
17	215		148
18	221		207
19	228		424
20	292		645
21	323		
22	369		
23	474		
24	550		
25	568		
26	642		
27	660		
28	700		
29	707		
30	936		
31	1268		
32	1412		
33	1648		
34	1699		
35	2123		
36	2703		
37	2899		
Scale Parameter t_0 (s)	**800**	**1251.7**	**108.4**
Sq (μm)	**0.042 ± 0.0038**	**0.618 ± 0.0180**	**0.934 ± 0.0382**

Table 2.2 The gecko's adhesion times on PMMA 1, 2, 3 surfaces. Note that, as an index of the gecko's adhesive ability, we use here the Weibull scale

parameter t_0 (in seconds) of the distribution of the detachment/failure F (closely related to its mean value).

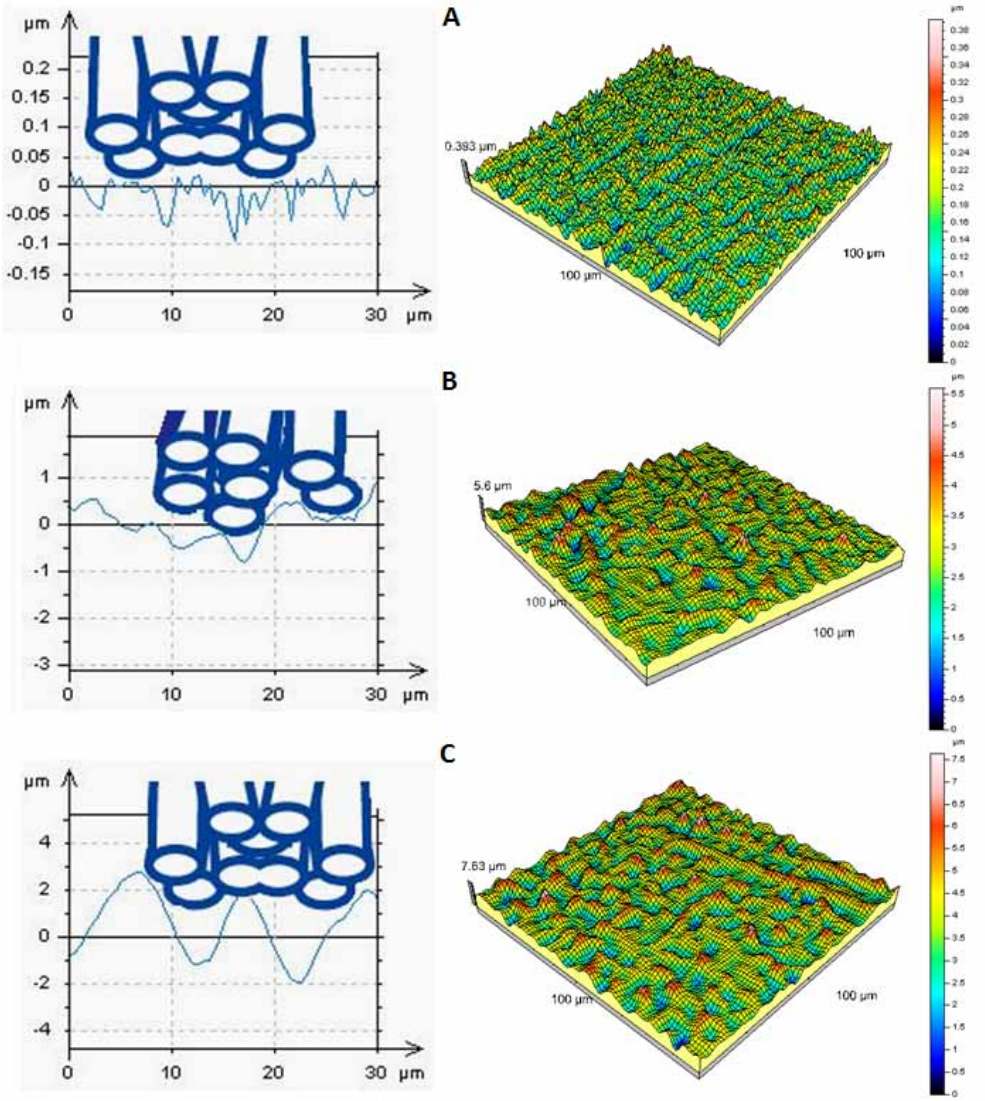

Fig. 2.3 A simple interpretation of our experimental results on the adhesion tests of living geckos on PMMA surfaces having different roughness. (A) Setae cannot adapt well on PMMA 1; (B) on PMMA 2 the adhesion is enhanced thanks to the higher compatibility in size between setae and roughness; (C) on PMMA 3 only partial contact is achieved. On the right,

we report the analysed three-dimensional profiles of the roughness for all of the three investigated surfaces (from the top: PMMA 1, 2 and 3).

ACKNOWLEDGMENTS

The authors would like to thank M. Buono and S. Toscano, DVM and SIVAE member, for the technical and veterinary aid and also for the support on the experimental measurements. We gratefully acknowledge the "2I3T Scarl - Incubatore dell'Università di Torino" for SEM imaging instruments and M. G. Faga, CNR-ISTEC member, Chemical Department IFM and NIS Centre of Excellence, University of Torino for the fundamental help performing the SEM micrographs. NMP is supported by the "Bando Ricerca Scientifica Piemonte 2006" - BIADS: Novel biomaterials for intraoperative adjustable devices for fine tuning of prostheses shape and performance in surgery.

REFERENCES

[1] Hiller, U., *Z. Morphol. Tiere* **62**, 307-362 (1968).
[2] Ruibal, R., and Ernst, V., *J. Morphol.* **117**, 271-293 (1965).
[3] Autumn, K., Liang, Y. A., Hsieh, S. T., Zesch, W., Chan, W. -P., Kenny, W. T., Fearing, R., and Full, R. J., *Nature* **405**, 681-685 (2000).
[4] Russell, A. P., *J. Zool.* **176**, 437-476 (1975).
[5] Williams, E. E., and Peterson, J. A., *Science* **215**, 1509-1511 (1982).
[6] Autumn, K. and Peattie, A. M., *Int. Comp. Biol.* **42**, 1081-1090 (2002).
[7] Sun, W., Neuzil, P., Kustandi, T. S., Oh, S., and Samper, V. D., *Biophysical Journal* **89**, L14-L17 (2005).
[8] Kesel, A. B., Martin, A., and Seidl, T., *J. Exp. Biol.* **206**, 2733-2738 (2003).
[9] Dai, Z., Gorb, S. N., and Schwarz, U.,. *J. Exp. Biol.* **205**, 2479-2485 (2002).
[10] Persson, B. N. J., and Gorb S., *J. Phys. Chem.* **119**, 11437-11444 (2003).
[11] Peressadko, A. G., and Gorb, S. N., Surface profile and friction force generated by insects. In: Boblan I, Bannasch R, editors. Bionik 2004, **15**, 237 (2004).
[12] Gorb, S. N., Dordrecht: Kluwer Academic Publishers (2001).

[13] Huber, G., Gorb, S. N., Hosoda, N., Spolenak, R., and Arzt, E., *Acta Biomaterialia* **3**, 607-610 (2007).
[14] Briggs, G. A. D., and Briscoe, B. J., *J. Phys. D: Applied Physics.* **10**, 2453-2466 (1977).
[15] Persson, B. N. J., and Tosatti, E., *J. Phys. Chem.* **115**, 5597-5610 (2001).
[16] Persson, B. N. J., *European Physical Journal E* **8**, 385-401 (2002).
[17] Guduru, P. R., *J. Mech. Phys. Solids* **55**, 445-472 (2007).
[18] Lepore, E., Antoniolli, F., Brianza, S., Buono, M., Carpinteri, A., and Pugno, N., *J. Nanomat.* **194524**, pp. 1-5 (2008).
[19] Pugno, N. M., *J. Phys.: Condens. Matter* **19**, 395001 (17pp) (2007).
[20] Fuller, K. N. G., and Tabor, D., *Proc. Royal Soc. London, Series A* **345**, 327-342 (1975).

3. NORMAL ADHESIVE FORCE-DISPLACEMENT CURVES OF LIVING TOKAY GECKOS

Abstract

In this paper, we report experimental measurements of normal adhesive force *versus* body displacement for living tokay geckos (*Gekko gecko*) adhered to Poly(methyl meth-acrylate) (PMMA) or glass surfaces. We have measured the normal adhesive force needed for reaching the gecko's detachment. Atomic force and scanning electron microscopies are used to characterize the surfaces and feet topologies. The measured safety factors (maximum adhesive force divided by the body weight) are 10.23 on PMMA surfaces or 9.13 on glass surfaces. We have observed minor and reversible damage of the gecko feet caused by our tests, as well as the self-renewal of the gecko adhesive abilities after the moult.

3.1. Introduction

The ability of a gecko to stay stuck motionless to a vertical surface or even to a ceiling seems to defy gravity. Since the 4th century B.C. geckos have been observed to "run up and down a tree in any way, even with their head downwards [1]" by Aristotele. Scientific researchers have focused their attention on the gecko's adhesive foot architecture, adhesive abilities and related mechanisms [2-20]. Scanning electron microscopy (SEM) has brought about new opportunities to go under the length-scale limitations given by the wavelength of visible light and to study the sub-micrometric hierarchical architecture of gecko toes.

The Tokay gecko (*Gekko gecko*) is the second largest Gekkonid lizard species (1050 species in the world), attaining lengths of approximately 0.3-0.4 m or 0.2-0.3 m for males or females, respectively. The weight of an adult gecko ranges from ~30 up to ~300 g [21]. A previously published study on Tokay geckos [2] revealed a strong shear adhesive force of ~20 N when placed with its front feet contacting a nearly vertical (85°) acetate

sheet attached to a stiff PMMA plate. As a consequence, if we assume the gecko's weight of ~100 g, we estimate a shear safety factor (SF) of approximately 40. This SF is comparable with that of *Hemisphaerota cyanea* beetle (SF ~ 60; measured for a force applied perpendicularly to the vertically-oriented attachment surface, generated either electronically or by hanging weights [22]), of *Chrysolina Polita* leaf beetle (SF ~ 50; attached to a force transducer [17]), but lower than the SF of the jumping spider *Evarcha arcuata* (SF ~ 160; theoretically extracted *via* atomic force microscopy (AFM) analysis [23]) and of *Crematogaster* cocktail ants (SF~146; measured using a centrifuge technique [24]). Thus, not only for insects, spiders [2, 17, 22-25], but also for geckos, several studies have been carried out with the aim of quantifying the maximum adhesive force by direct *in vivo* [2, 19, 26-33] or *in vitro* measurements [19, 26-30].
In this paper, we report measurements of the normal adhesive force *versus* body displacement of living Tokay geckos, up to the detachment. We are also interested in comparing the effects of surface roughness on the gecko's maximum normal safety factor. The influence of the damage of the gecko's feet, caused by our experimental tests, on the adhesive abilities is also discussed. The surfaces topography of PMMA or glass was analysed by AFM, whereas we have used SEM to characterize the hierarchical architecture of the gecko's feet.

3.2. Materials and Methods

3.2.1. Gecko's feet architecture

Considering Figs. 3.1-3.3, the investigations of the hierarchical structure of the gecko's toe were possible by means of SEM (Zeiss EVO 50) equipped with a lanthanum hexaboride cathode and FESEM (Zeiss SUPRA 40) equipped with a field emission tungsten cathode. About SEM analysis, three frozen and formaldehyde fixed samples of toes retrieved from two geckos died naturally were unfrozen at room temperature, 5h-dehydrated with ethanol increasing its percentage at every hour (10 %, 30 %, 50 %, 70 %, 100 %). Thus, samples were fixed to aluminium stubs by double-sided adhesive carbon conductive tape (Agar Scientific), 30-min air-dried and gold-coated (approx. 40 nm) in a SCD 050 sputter coater (BalTec). About

FESEM analysis, the procedure of sample preparation is the same but the samples are chrome-coated (approx. 20 nm).

3.2.2. PMMA and glass surface characterization

The roughness of the adhering surfaces, PMMA and glass, was nanocharacterized by AFM Perception (Assing, Rome, Italy) using the contact mode with a silicon nitride tip. A surface area of 10 × 10 μm^2 for each material was evaluated with a final resolution of 200 points/profile.

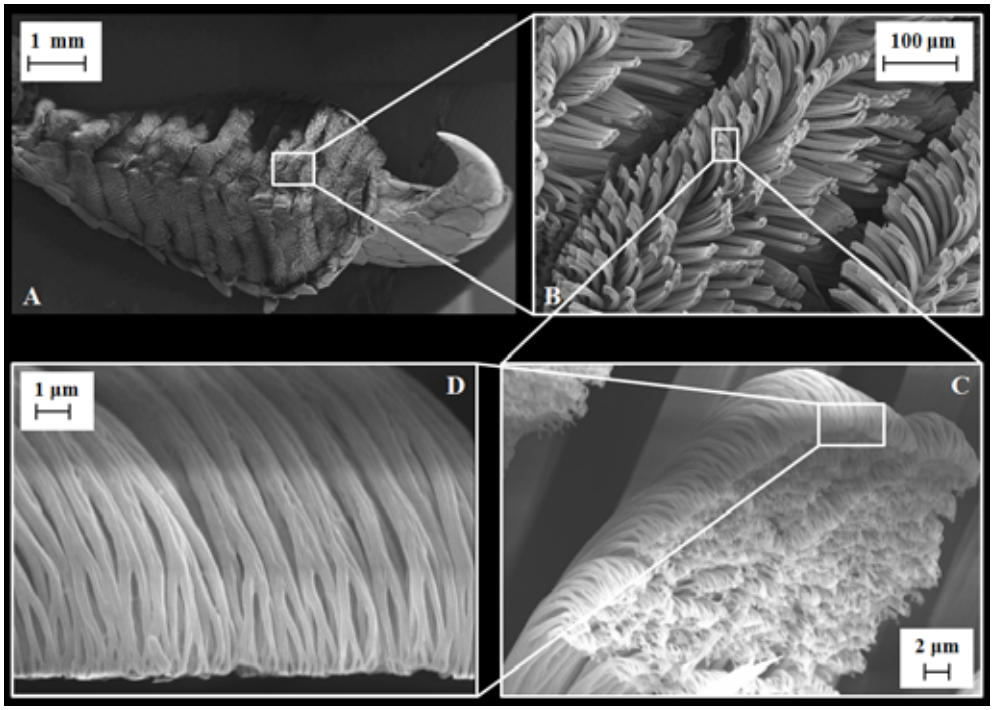

Fig. 3.1 The Tokay gecko's adhesive system is observed by FESEM (Zeiss SUPRA 40) (A, B) and by SEM (Zeiss EVO 50) (C, D). (A) Toe and FESEM micrograph of the setae (B). SEM micrograph of the setae (C) and a nanoscale array of hundreds of spatulae (D).

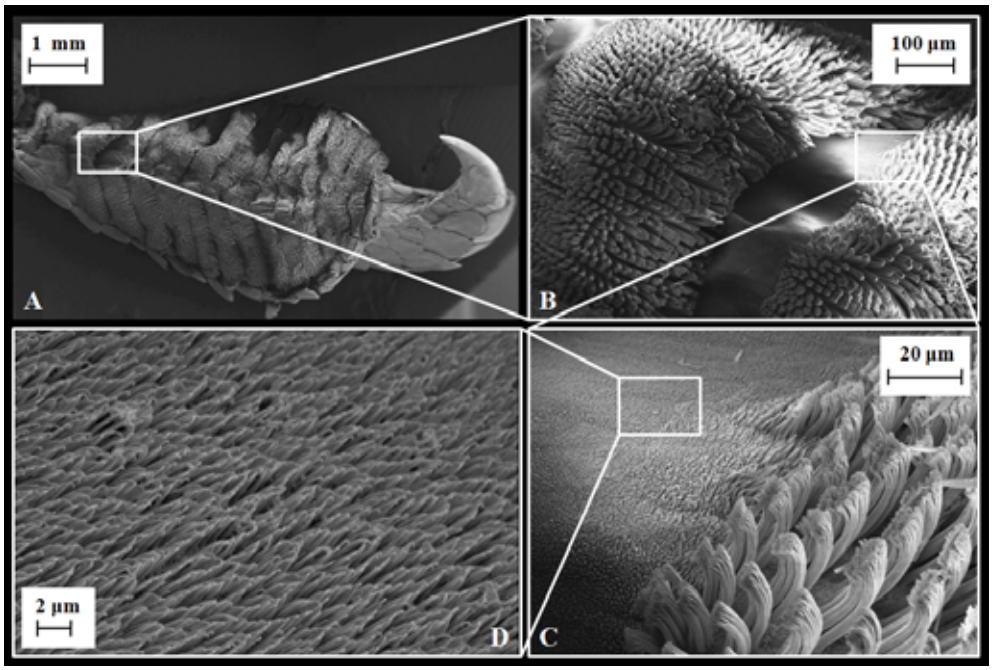

Fig. 3.2 The Tokay gecko's adhesive system is observed by FESEM (Zeiss SUPRA 40). (A) The Tokay gecko's toe. (B, C) The connection area between adjacent lamellae, that are localized perpendicular to the longitudinal axis of each digit, is covered by nanostructured hairy units; (D) at high magnification.

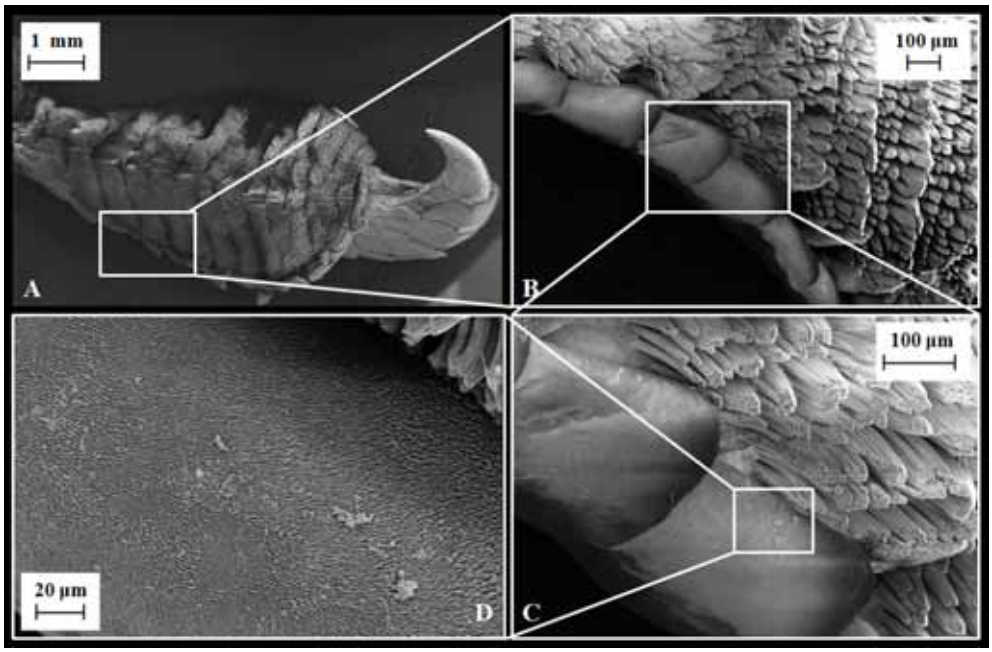

Fig. 3.3 The Tokay gecko's adhesive system is observed by FESEM (Zeiss SUPRA 40). (A) The Tokay gecko's toe. (B, C) The edge of the gecko's toe is covered by nanostructured hairy units; (D) at high magnification.

3.2.3. The gecko's normal adhesive force *versus* displacement curves

We used a single male adult Tokay gecko (authorized by Ministerial Decree n° 73/2010-B). The gecko was maintained in its terrarium at ~28 °C. The temperature of the experimental room, in which the force-displacement were measured, was ~22 °C. The gecko was fed moths and water *ad libitum* and crickets one time a week. The animal did not show any particular discomfort being manipulated, segregated in the box and bound with adherent elastic cloth bandaging.

Force-displacement measurements were conducted as follows. The gecko was prepared and placed in the PMMA-Glass (Vetronova, Varese, Italy) box 10 minutes before each set of tests. We took the gecko from its terrarium and we fixed to it an adherent cloth bandaging; a metallic hook was inserted within the bandage on the gecko's back. After this preliminary operation, the gecko was connected, by means of a plastic wire tied to the metallic hook, to the measurement platform, and it was placed gently on the

bottom of the measurement box (Fig. 3.4). The force-displacement measurement platform was built outside the box (Fig. 3.5). We applied the force using an increasing amount of mass (16, 48, 98, 148, 198, 273, 348, 423, 498, 573, 648 and 723 g). The displacements of the point of applied force on the gecko's body were recorded during the test. The measured displacement corresponds to the stretching of the front and rear legs of gecko without slipping of its feet.

Fig. 3.4 Our tested Tokay gecko: adherent elastic cloth bandaging and metallic hook of connection with the outside measurement platform.

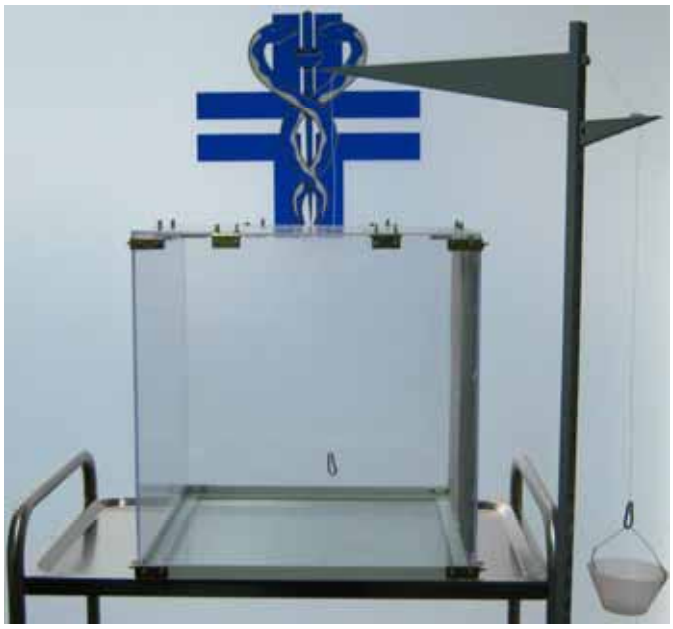

Fig. 3.5 Force-displacement measurements platform.

The procedure of increasing hung weights was conducted as follows. We started with the application of 16 g. We waited 10 seconds for a stabilized value of the gecko's displacement and read it on a millimetric scale. Similarly, we continued with the next applied weights up to 198 g. For larger weights we allowed a relaxing time of about 15 s after each weight application to try to avoid the gecko's muscular fatigue. When the detachment occurred, the gecko was pulled upwards but immediately reached a secure point, approximately 42 cm from the top of the box and then was slowly taken back to the bottom. Each force-displacement curve was obtained in ~3 minutes. During a single test, the only allowed action was the renewal of the foot contact and hyperextension [2].

We have accordingly measured the normal adhesive force-displacement curves of a gecko adhered to the interior surface of a box (50 x 50 x 50 cm^3). One wall of the box was made of glass and the other walls were made in PMMA. We realized fiftheen tests on PMMA and three tests on glass after a first moulting process and three tests on PMMA and four tests on glass after the next moulting.

After the first moult, in the first test-day that was 50 days from the moult, we realized only one force-displacement curve, both on PMMA and glass

(blue line, Figs. 3.6 and 3.7 respectively). After 62 days from the moult, we performed the second day of tests: we carried out four tests on PMMA (cyan line, Fig. 3.6) and two tests on glass (cyan line, Fig. 3.7). The third test-day took place the day after and we realized ten tests on PMMA (green line, Fig. 3.6). After the second moult, we only conducted experiments in one day, 7 days after moult, due to the damage imposed by this first day of tests on the gecko's feet. We started on glass, performing four tests (red line, Fig. 3.7), and then on PMMA measuring three force-displacement curves (red line, Fig. 3.6).

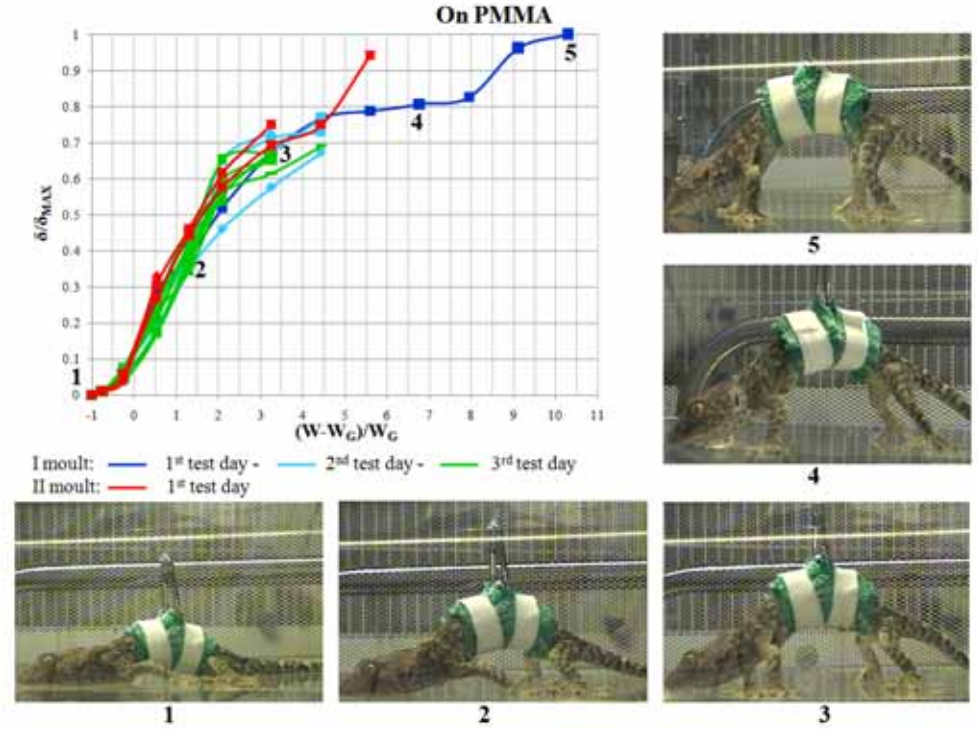

Fig. 3.6 Normal adhesive force-displacement curves on PMMA surfaces after the first and second moults. Snapshots show five specific instants of the gecko's displacement at 0, 148, 273, 423 and 723 g of hung weight (W is the applied weight, W_G is the gecko's weight, δ is the gecko's displacement, δ_{MAX} is the gecko's maximum displacement).

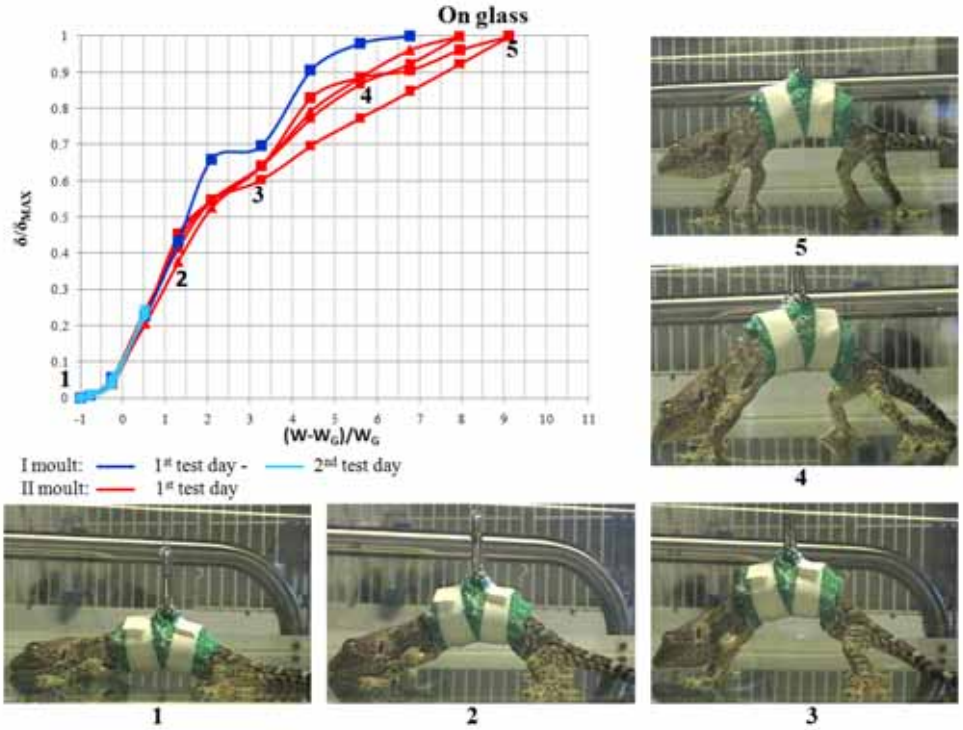

Fig. 3.7 Normal adhesive force-displacement curves on glass surface after the first and second moults. Snapshots show five specific instants of the gecko's displacement at 0, 148, 348, 423 and 648 g of hung weight (W is the applied weight, W_G is the gecko's weight, δ is the gecko's displacement, δ_{MAX} is the gecko's maximum displacement).

3.3. Results

3.3.1. The gecko's feet architecture

The Tokay gecko foot consists of five digits (Fig. 3.1A) covered with macroscopic hairy structures called lamellae (~0.5-3 mm in width and 200-500 μm in length, Fig. 3.1B). These lamellae are organized in a series of multi-arrays localized perpendicular to the longitudinal axis of each digit; the lamellae are separated one from another. Nanostructured hairy units (~2-5 μm in length and ~200 nm in diameter, Figs. 3.1C, 3.1D) have been identified on the connection areas between adjacent lamellae (Fig. 3.1C) and

on the edge of each single digit (Figs. 3.2B, 3.2C, 3.2D). Each lamella is covered with several thousand setae (10-130 μm in length and 3-10 μm in diameter, density of ~0.014 setae/μm^2 [12, 34], Figs. 3.1B, 3.1C), which in turn contain at their tips hierarchical substructures called spatulae (0.1-0.2 μm wide and 15-20 nm thick, Fig. 3.3D). Terminal claws are located at the top of each single toe (~500 μm in diameter and ~1 mm in length, Fig. 3.1A) and guarantee a secure mechanical interlocking on surfaces with high roughness, *i.e.* where the diameter of the gecko's claw tip is smaller than the roughness [35-40].

3.3.2. PMMA and glass surface characterization

Table 3.1 summarizes roughness parameters of the considered PMMA and glass surfaces. The PMMA (Fig. 3.8) and glass (Fig. 3.9) surfaces are different in terms of roughness. In addition on the glass surface isolated bubbles of ~1 μm in diameter are recognizable.

	PMMA	**Glass**
R_a (nm)	3.81 ± 0.085	0.80 ± 0.214
R_q (nm)	5.88 ± 0.778	1.41 ± 0.796
R_v (nm)	52.74 ± 14.938	16.88 ± 13.895
R_p (nm)	90.06 ± 28.736	21.61 ± 16.943
S_{sk}	1.41 ± 0.997	0.79 ± 0.461
S_{dr} (%)	0.60 ± 0.046	0.02 ± 0.007

Table 3.1 Roughness parameters of the considered PMMA or glass surfaces.

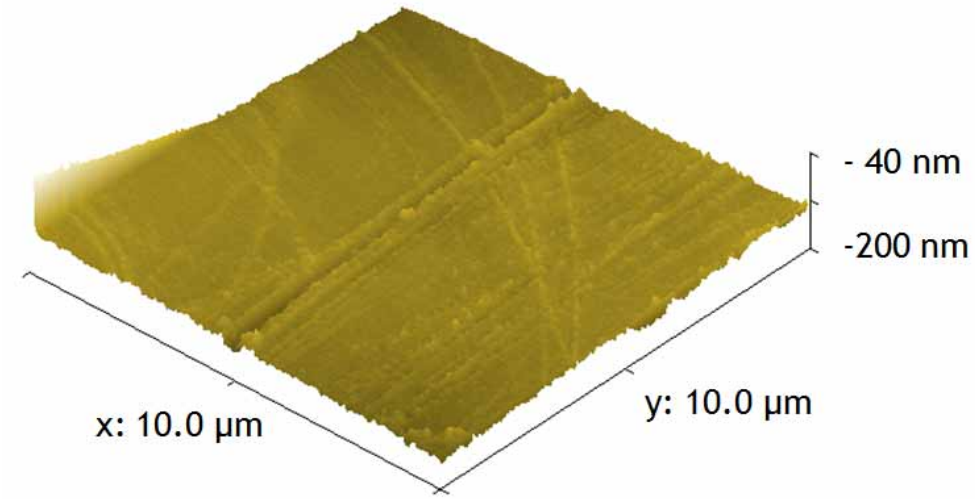

Fig. 3.8 AFM characterization of the PMMA surface.

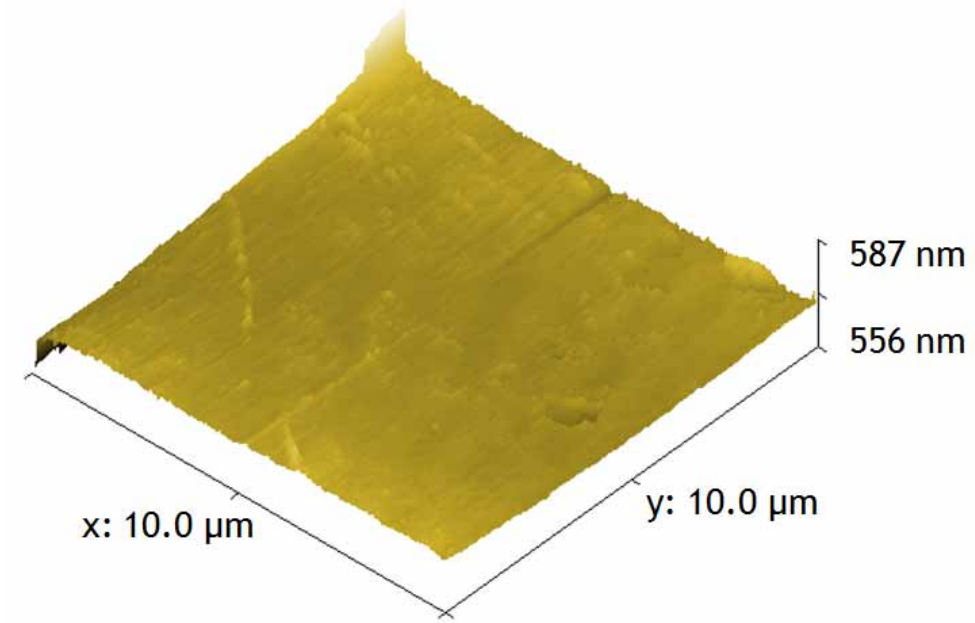

Fig. 3.9 AFM characterization of the glass surface.

3.3.3. The gecko's normal adhesive force *versus* displacement curves

After the first moult on the PMMA surface, we obtained a maximum SF $\lambda_{PMMA(I)\text{-}1Day} = 10.23$ in the first test-day. Note that to compute this value we have considered the animal's weight (64 g) and the final hung weight of 723 g (Fig. 3.6, snapshot 5). In the second test-day, the gecko reached an average SF reduced by 60% ($\lambda_{PMMA(I)\text{-}2Day} \approx 4.1$), in comparison with the maximum value. Finally, the SF reaches a minimum value equal to $\lambda_{PMMA(I)\text{-}3Day} \approx 2.1$ during the third test-day. Analogously, on the glass surface, the final hung weight of 498 g and the gecko's same weight correspond to a maximum SF $\lambda_{Glass(I)\text{-}1Day} \approx 6.8$ in the first test-day. In the second test-day, it is reduced to less than 1 ($\lambda_{Glass(I)\text{-}2Day} \approx 0.5$). In the first test-day after the second moult, the final maximum hung weight of 648 g and the gecko's same weight correspond to a maximum SF $\lambda_{Glass(II)\text{-}1Day} = 9.13$ (Fig. 3.7, snapshot 5). After four tests on the glass surface, we performed three tests on the PMMA surface, reaching a SF that gradually decreases starting from a value $\lambda_{PMMA(II)\text{-}1Day} \approx 5.6$ up to a final minimum value $\lambda_{PMMA(II)\text{-}1Day} \approx 0.5$. In summary, the final maximum SF is found to be $\lambda_{PMMA} = \lambda_{PMMA(I)\text{-}1Day} = 10.23$ on the PMMA surface and $\lambda_{Glass} = \lambda_{Glass(II)\text{-}1Day} = 9.13$ on the glass surface.

3.4. Discussion

Figs. 3.6 and 3.7 report our results of force-displacement curves and five snapshots of gecko's specific configurations on PMMA or glass respectively. We condensed all of the obtained force-displacement curves, measured during the gecko's best condition (first test-day after moulting) and in course of the period after the gecko's moult (second and third test-day). In the first test-day after the first moult, we found the gecko's maximum SF on the PMMA surface, while in the first test-day after the second moult, the maximum SF on the glass surface was found. The SF of ~10 that we measured for Tokay geckos is coherent with previously reported observations. In particular, in [2], the shear adhesive force was measured. Each gecko was gently placed with its front feet contacting a nearly vertical acetate sheet (85°) and then slowly pulled in a downward direction. Our experimental set, instead, permitted us to evaluate the normal force to detach the Tokay gecko from a horizontal surface (PMMA and

glass). Thus, the maximum shear force can be estimated to be ~40 N for the living Tokay gecko [2] and now we have calculated the maximum normal adhesive force equal to 7.1 N on PMMA and 6.4 N on glass.
Considering a setae density of 14.000 setae/mm^2 [27, 28, 34] and the gecko's total pad area of 450 mm^2, the shear adhesive force of ~40 N [2] as well as our normal adhesive force of ~6.7 N, imply for a single seta a shear adhesive force equal to 6.2 μN [28] and a normal adhesive force equal to 1.1 μN. These top-down computations are underestimated, due to the unavoidable presence of defects at the macroscale of the pads. Indeed, the maximum shear adhesive force of a single seta was directly measured equal to ~200 μN [19, 28, 31], leading to a theoretical shear adhesive force for the gecko of 1250 N [28]; similarly, the maximum normal adhesive force of a single setae is ~40 μN [27, 31], leading to a theoretical normal adhesive force for the gecko of 250 N [28]. At the size of the spatulae, only the normal adhesive force has been determined, equal to ~10 nN [29, 30, 32], which leads to a final adhesive force for the gecko of 65 N (if we consider that the gecko has 6.5 billions of spatulae [2, 28, 34]).
From the results at different characteristic sizes, we should conclude that the force estimated at the macroscale (*i.e.* of the whole gecko) leads to an underestimation of nearly 32 times the microscale (setae) shear adhesive force and of nearly 36 times the microscale normal adhesive force; thus 'smaller is stronger' [41, 42]. Similarly, at the nanoscale (spatulae) the normal adhesive strength is nearly 10 times that at the macro-scale [43]. As a consequence of the presence of defects [26, 31] at the level of the entire body, a normal safety factor of ~10 has to be expected, in order to have a safe attachment and an easy detachment, as we have measured.
Summarizing, the shear adhesive force is equal to ~200 μN [19, 28, 31] for a single seta and ~40 N [2] for the whole gecko, while the normal adhesive force is equal to ~10 nN [29, 30, 32] for a single spatula, ~40 μN [27, 31] for a single seta and ~7.1 (~6.4) N on PMMA (glass) for the whole gecko, as here determined. Thus, our result of the normal adhesive force for the whole gecko gives a contribution to the characterization of the functionality of the hierarchical adhesive system of Tokay gecko [44] and confirms the ratio of 5:1 between the shear and normal adhesive forces for the whole animal, as observed by Autumn [33] for a different climbing gecko (*Hemidactylus garnotii*, ~2 g of body mass); interestingly, note that, for Tokay gecko, such a ratio of 5:1 of the shear to normal adhesive forces is verified both at macro and micro scales.

In addition, we observed the self-renewal of the gecko's adhesive system after the gecko's moulting process and a negative effect of the previously executed experimental tests, leading to a reduction of the maximum adhesive force.

3.4.1. Feet damage

During the first test-day after the second moult, we observed evident feet damage. As above-mentioned, we started by performing four tests on the glass surface and then on the PMMA surface we performed three tests, which showed that the gecko's detachment force drastically decreases from one test to the next. In particular, on the PMMA surface, we have noted a decrement of the SF corresponding to 40% from the first to the second test and to ~85 % from the second to the third test. After the end of these three tests, the gecko could no longer stay attached with the hind feet. Fig. 3.10 shows the negative effects of our seven consecutive tests, photographed one day after the first test-day subsequent to the second moult. A diffused inflammation of gecko toes and the presence of small thin wound, located on the gecko's skin between one toe and the next, were observed.
Regarding the self-renewal of the gecko's adhesive system and abilities after the gecko's moulting process, we measured an increase of the gecko's SF from $\lambda_{\text{Glass(I)-2Day}} \approx 0.5$ before the second moult to $\lambda_{\text{Glass(II)-1Day}} = 9.13$ after the second moult. The increment of SF is also appreciable on the PMMA surface: from a SF $\lambda_{\text{PMMA(I)-3Day}} \approx 2.1$, before the second moult, up to $\lambda_{\text{PMMA(II)-1Day}} \approx 5.6$ after the second moult.

Fig. 3.10 Damage on the feet imposed by the adhesive tests: (A) diffused inflammation of gecko toes; (B) the gecko's healthy foot is here reported for comparison; (C) small thin wound located on the gecko's skin between one toe and the next.

3.5. Conclusions

We have measured normal adhesive force-displacement curves of a live gecko. Thus, the gecko's maximum SF was determined to be $\lambda_{PMMA} = 10.23$ on PMMA surface, that showed in general higher roughness and index S_{dr} (25 times greater than that of glass), and $\lambda_{Glass} = 9.13$ on the glass surface. We observed a clear trend of the adhesive ability during the period after the moulting: normal adhesive forces drastically decrease at each subsequent test as a consequence of the damage of the gecko's feet caused by our previously executed experimental tests. Finally, we documented the

observed self-renewal of the gecko's adhesive system and abilities after the moulting. The analysis here reported could have also implications in the design of bio-inspired smart adhesive materials.

ACKNOWLEDGMENTS

The authors would like to thank M. Buono, DVM and SIVAE member, and M. Nervo for the technical and veterinary aid. Also the authors are grateful to M. Biasotto of the Department of Special Surgery and F. Antoniolli of the Department of Biomedicine at the University of Trieste for their help in using the AFM. We gratefully acknowledge A. Chiodoni, Department of Physics, Politecnico of Torino, for the help in performing the FESEM micrographs. We thank the "2I3T Scarl - Incubatore dell'Università di Torino" for SEM imaging instruments and M. G. Faga, CNR-ISTEC member, Chemical Department IFM and NIS Centre of Excellence, University of Torino, for the help in performing the SEM micrographs. NMP is supported by "Metrology on a cellular and macromolecular scale for regenerative medicine" - METREGEN (2009-2012).

REFERENCES

[1] Aristotle, *Historia Animalium*, 343 B.C. See Book IX, Part 9, translated by Thompson DAW, http://classics.mit.edu/Aristotle/history_anim.html.
[2] Irschick, D. J., Austin, C. C., Petren, K., Fisher, R. N., Losos, J. B., and Ellers, O., *Biol. J. Linn. Soc*. **59**, 21-35 (1996).
[3] Cartier, O., *Verhandl. Würz Phys-med Gesell* **1**, 83-96 (1872).
[4] Haase, A., *Archiv. Naturgesch* **66**, 321-345 (1900).
[5] Gadow, H., Amphibia and Reptiles (Macmillan & Company, Ltd., London, 1902).
[6] Weitlaner, F., *Verhdl. Zool. Bot. Ges. Wien.* **52**, 328-332 (1902).
[7] Schmidt, H. R., *Jena. Z. Naturwiss* **39**, 551-580 (1904).
[8] Hora, S. L., *J. Proc. Asiat. Soc. Beng.* **9**, 137-145 (1923).
[9] Dellit, W. D., *Jena. Z. Naturwiss* **68**, 613-658 (1934).
[10] Mahendra, B. C., *Proc. Indian. Acad. Sci.* **13**, 288-306 (1941).
[11] Maderson, P. F. A., *Nature* **203**, 780-781 (1964).
[12] Ruibal, R., and Ernst, V., *J. Morph.* **117**, 271-294 (1965).
[13] Hiller, U., *Z. Morphol Tiere* **62**, 307-362 (1968).
[14] Hiller, U., *Forma et functio* **1**, 350-352 (1969).

[15] Gennaro, J. G. J., *Nat. Hist.* **78**, 36-43 (1969).
[16] Williams, E. E., and Peterson, J. A., *Science* **215**, 1509-1511 (1982).
[17] Stork, N. E., *J. Exp. Biol.* **88**, 91-107 (1980).
[18] Liang, Y. A., Autumn, K., Hsieh, S. T., Zesch, W., Chan, W. P., Fearing, R., Full, R. J., and Kenny, T. W., *Technical Digest of the 2000 Solid-State Sensor and Actuator Workshop* 200033, 38 (2000).
[19] Autumn, K., Liang, Y. A., Hsieh, S. T., Zesch, W., Chan, W. P., Kenny, T. W., Fearing, R., and Full, R. J., *Nature* **405**, 681-685 (2000).
[20] Autumn, K., Ryan, M. J., and Wake, D. B., *Q. Rev. Biol.* **77**, 383-408 (2002).
[21] Tinkle, D. W., *Encyl. Amer. Grolier.* **12**, 359 (1992).
[22] Eisner, T., and Aneshansley, D. J., *Proc. Natl. Acad. Sci. USA* **97**, 6568-6573 (2000).
[23] Kesel, A. B., Martin, A., and Seidl, T., *J. Exp. Biol.* **206**, 2733-2738 (2003).
[24] Federle, W., Rohrseitz, K., and Hölldobler, B., *J. Exp. Biol.* **203**, 505-512 (2000).
[25] Walker, G., *Int. J. Adhes. Adhes.* **13**, 3-7 (1993).
[26] Pugno, N. M., *J. Phys.: Condens. Matter* **19**, 395001, pp. 1-17 (2007).
[27] Autumn, K., Sitti, M., Liang, Y. A., Peattie, A. M., Hansen, W. R., Sponberg, S., Kenny, T. W., Fearing, R., Israelachvili, J. N., and Full, R. J., *Proc. Natl. Acad. Sci. USA* **99**, 12252-12256 (2002).
[28] Autumn, K., and Peattie, A. M., *Int. J. Comp. Biol.* **42**, 1081-1090 (2002).
[29] Huber, G., Gorb, S. N., Spolenak, R., and Arzt, E., *Biol. Lett.* **1**, 2-4 (2005).
[30] Huber, G., Gorb, S. N., Hosoda, N., Spolenak, R., and Arzt, E., *Acta. Biomater.* **3**, 607-610 (2007).
[31] Autumn, K., Dittmore, A., Santos, D., Spenko, M., and Cutkosky, M.,. *J. Exp. Bio.* **209**, 3569-3579 (2006).
[32] Huber, G., Mantz, H., Spolenak, R., Mecke, K., Jacobs, K., Gorb, S. N., and Arzt, E., *Proc. Natl. Acad. Sci. USA* **102**, 16293-16296 (2005).
[33] Autumn, K., Hsieh, S. T., Dudek, D. M., Chen, J., Chitaphan, C. and Full, R. J., *J. Exp. Bio.* **209**, 260-272 (2006).
[34] Schleich, H. H. and Kästle, W., *Amphib. Reptil.* **7**, 141-166 (1986).
[35] Lepore, E., Antoniolli, F., Brianza, S., Buono, M., Carpinteri, A., and Pugno, N., *J. Nanomat.* **194524**, pp. 1-5 (2008).
[36] Pugno, N., and Lepore, E., J. *Adhesion* **84**, 949-962 (2008).
[37] Pugno, N., and Lepore, E., *Biosystems* **94**, 218-222 (2008).

[38] Pugno, N., *Nano Today* **3**, 35-41 (2008).
[39] Varenberg, M., Pugno, N., and Gorb, S., *Soft Matter* **6**, 3269-3272 (2010).
[40] Lepore, E., Chiodoni, A., and Pugno, N., *Rev. Adv. Mat. Sci.* **24**, 69-80 (2010).
[41] Buehler, M. J., Yao, H., Gao. H., and Ji, B., *Modelling. Simul. Mater. Sci. Eng.* **14**, 799-816 (2006).
[42] Keten, S., Xu, Z., Ihle, B., and Buehler, M. J., *Nature Materials* **9**, 359-367 (2010).
[43] Gorb, S., Gorb, E., and Kastner, V., *J. Exp. Bio.* **204**, 1421-1431 (2001).
[44] Buehler, M. J., *Nano Today* **5**, 379-383 (2010).

4. OPTIMAL ANGLES FOR MAXIMAL ADHESION IN LIVING TOKAY GECKOS

Abstract

In this paper, we report experimental measurements of the adhesion angles of living Tokay geckos (*Gekko gecko*) at two different characteristic sizes of the feet and toes. In particular, we have determined the adhesion angles between the opposing front and rear feet and between the first and fifth toe of each foot on different inverted surfaces (steel, aluminium, copper, Poly(methyl meth-acrylate) and glass). We explained the experimental results with the multiple peeling theory, recently derived, and found an interesting agreement; previous reported observations on the architecture of the gecko adhesive system, even when considering the size scale of the single seta, suggest the validity of the approach at different hierarchical levels.

4.1. Introduction

Geckos and lizards in general usually climb in complex three-dimensional habitats and this necessitates the development of such a sophisticated dry adhesive system on their pads. During the last century, many of the secrets of the gecko's adhesion were explained [1-30], although some crucial problems still remain unsolved [14, 19, 21, 31-34]. Such open questions include function, molecular mechanism, morphological characteristics of the nano-hierarchical structures, mechanism of frictional adhesion, tail function during climbing or aerial descent and interactive effects of size and loading on kinematics. The millisecond controllable attachment/detachment mechanism in geckos with negligible forces has assumed a huge importance from a technological point of view, *e.g.* fabrication of dry adhesives, robotic systems, artificial adhesive suits and gloves for astronauts [21, 23, 30, 35-41]. The uniqueness of the gecko's adhesive system, in terms of repeatable high-strong feet contacts combined with temporary and reversible weak bonds, is based on intermolecular van der Waals forces [14, 30, 33, 42-45].

In order to maintain the necessary shear/frictional adhesive forces and avoid toe detachment [12], the gecko's adhesive mechanism is based on the use of opposing feet and toes making a V-shaped geometry. Gecko attachment is achieved only proximally along the toe axis of the gecko, which pulls its feet inwards towards the center of mass (COM) and its toes inwards towards the foot to engage adhesion [14, 21, 30, 31, 34, 45, 46], as schematically reported in Fig. 4.1A.

The key factor that governs the gecko's mechanism of attachment/detachment is the adhesion angle α which is formed between the terminal structure attached to the surface and the surface itself. Several scientific studies have been developed to establish the value of the angle α from an experimental [12, 21, 31, 32], computational [14, 19, 31, 41, 47] or theoretical [19, 29, 34, 41, 46, 48-58] point of view and at different characteristic levels of the hierarchical adhesive system. From the literature, the angle α of Tokay geckos (*Gekko gecko*) is equal to ~25.5° for a single toe, ~24.6° (or ~30°) for isolated setae arrays and ~30.0° (or ~31°) for a single seta [21] (or [31]).

In this paper, we evaluated experimentally the adhesion angles of living Tokay geckos at two different hierarchical characteristic sizes of the feet and toes. We measured the angles between the opposing front and rear feet and between the first and fifth toe of each foot on five different surfaces (steel, aluminium, copper, Poly(methyl meth-acrylate), *i.e.* PMMA, and glass). Then, we compared them with the new theory of multiple peeling [48] and other previously published experimental results, finding interesting evidence. This finding could be useful for the industrial fabrication of dry adhesives, robotic systems, artificial adhesive suits and gloves for astronauts or designing bio-inspired smart adhesive nanomaterials in general.

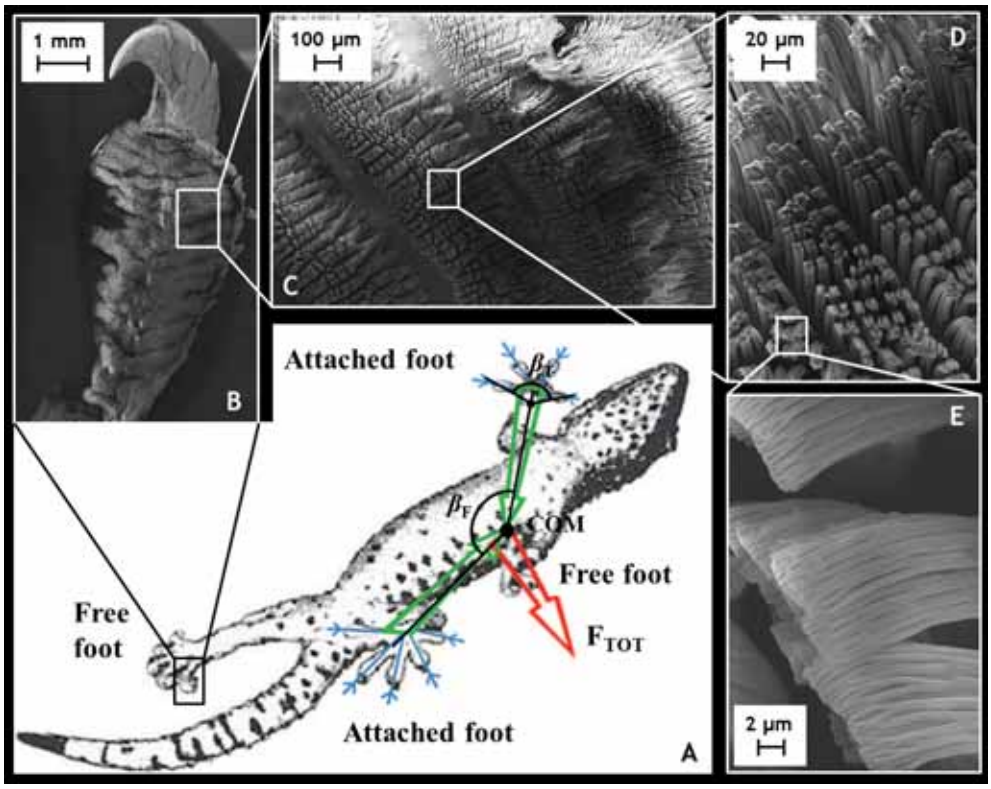

Fig. 4.1 (A) A schematic 3D representation of the measured angle between the opposing front and rear feet (β_F) and between the first and fifth toe (β_T) of each foot on inverted surfaces; inset adapted from Y. Tian, N. Pesika, H. Zeng, K. Rosenberg, B. Zhao, P. M., K. Autumn, and J. Israelachvili, Adhesion and friction in gecko toe attachment and detachment, 19320-19325, PNAS, December 19, 2006, vol. 103, no. 51; Copyright (2006) National Academy of Sciences, U.S.A. The adhesive system of Tokay geckos showed by FESEM (Zeiss SUPRA 40) (B, C, D) and by SEM (Zeiss EVO 50) (E). The gecko's toe (B), FESEM micrograph of setae arraies (C), SEM micrograph of several setae (D) and nanoscale array of hundreds of spatula tips (E).

4.2. Materials and methods

We used a single male adult Tokay gecko maintained in its terrarium at ~28 °C. The gecko was provided with food (moths and crickets with a calcium

supplement) and water *ad libitum*. The animal and the experimental procedures were authorized by the Ministerial Decree n° 73/2010-B.
The animal was placed in its natural position on the bottom of a box (50 x 50 x 50 cm^3). Each surfaces of the box was made of a different material (steel, aluminium, copper, PMMA and glass) (Vetronova, Varese, Italy).
composed of the analyzed surfaces. Then, we slowly rotated the box so that the gecko reached its downwards position under its own weight (~88 g) only. At this time, we recorded the adhesion angle between the opposing front and rear feet (β_F) and between the first and fifth toe (β_T) of each foot on the inverted surfaces in the box. Each leg was named as follows: front right (FR), front left (FL), rear right (RR), rear left (RL). Experiments were performed at a room (experimental box) temperature of ~21 °C (~25 °C) and humidity of ~50 % (~30 %). Figs. 4.2 and 4.3 show the photos which were used to calculate the adhesion angles between the opposing front and rear foot (Fig. 4.2), and on the same substratum (Fig. 4.3A) or of the same leg (Fig. 4.3B). The angle β_T was determined between the first and fifth toe by taking the foot-forearm joint as the vertex of the resulting triangle. Similarly, the angle β_F was determined between the opposing front and rear feet by using the center of the gecko's mass (COM) as the vertex of the resulting triangle, as defined in [21]. The resulting angle α was computed as $\alpha = (180° - \beta)/2$.

Fig. 4.2 The measured angle β_F between the opposing front and rear feet on different surfaces (steel, aluminium, copper, PMMA and glass).

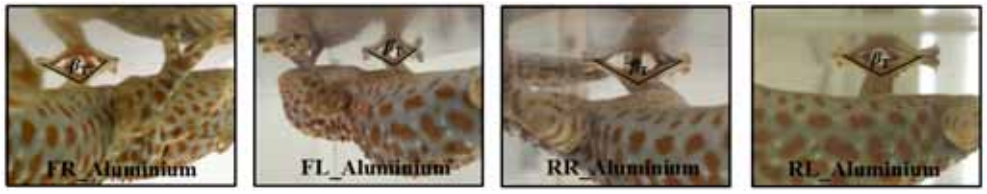

A

B

Fig. 4.3 The measured angle β_T between the first and fifth toe: on the aluminium surface for all legs (A), or for the FR leg on different surfaces (steel, aluminium, copper, PMMA and glass).

4.3. Results

The experimental measurements of the adhesion angles are summarized in Table 4.1.

α_F (°)	FR-RL	FL-RR	MEAN ± s.d.	λ_F
Steel	28 ± 4.7 (N=21)	29 ± 4.6 (N=39)	29 ± 0.6	0.013
Aluminium	31 ± 4.5 (N=33)	31 ± 4.2 (N=57)	31 ± 0.3	0.018
Copper	31 ± 8.0 (N=25)	33 ± 3.8 (N=37)	32 ± 0.8	0.023
PMMA	22 ± 4.5 (N=19)	26 ± 6.9 (N=33)	24 ± 2.8	0.007
Glass	28 ± 3.7 (N=22)	31 ± 3.8 (N=28)	30 ± 1.6	0.016
MEAN ± s.d.	28 ± 3.7	30 ± 2.4		

A

α_T (°)	FR	FL	RR	RL	MEAN ± s.d.	λ_T
Steel	28 ± 2.9 (N=24)	31 ± 4.3 (N=22)	31 ± 4.8 (N=44)	28 ± 4.4 (N=40)	30 ± 1.7	0.016
Aluminium	28 ± 3.9 (N=39)	30 ± 4.1 (N=50)	29 ± 4.3 (N=14)	28 ± 4.8 (N=28)	29 ± 0.8	0.013
Copper	24 ± 3.4 (N=30)	32 ± 6.1 (N=35)	28 ± 4.5 (N=43)	29 ± 4.7 (N=45)	28 ± 3.4	0.013
PMMA	21 ± 2.4 (N=24)	23 ± 2.7 (N=23)	21 ± 3.5 (N=27)	19 ± 2.0 (N=27)	21 ± 1.8	0.003
Glass	27 ± 3.7 (N=56)	32 ± 2.5 (N=37)	30 ± 3.3 (N=33)	27 ± 5.7 (N=18)	29 ± 2.5	0.015
MEAN ± s.d.	26 ± 3.0	29 ± 3.8	28 ± 4.3	26 ± 4.3		

B

Table 4.1 Experimental values (and the number N of measurements) of the adhesion angles α_F (A) and α_T (B) on different surfaces.

It is clear that the FR value of α_T is lower than the FL for each surface and, similarly, RL leg shows a lower value of α_T than the RR leg, with the exception of the copper surface. Moreover, the opposing FR and RL legs show the smallest values of α_T if compared to the other ones (FL and RR). The determined values of α_F and α_T in Tokay geckos are in agreement with previously obtained results reported by Autumn et al. [21], which

indicated the range of 25°-30° as the values of α for toes, isolated setae arrays or a single seta. This suggests a maximum of the gecko's attachment force when α reaches values of around 30° [36, 41].

4.4. Discussion

We found a good correlation between the experimental results and the theory of multiple peeling [48], according to which, the dimensionless detachment force of a V-shaped system is:

$$f = \frac{F_C(\alpha)}{F_C(\pi/2)} = \frac{\sin\alpha\left(\cos\alpha - 1 + \sqrt{(1-\cos\alpha)^2 + 4\lambda}\right)}{-1+\sqrt{1+4\lambda}} \qquad (1)$$

where α is the adhesion angle and

$$\lambda = \frac{\gamma}{tE}, \qquad (2)$$

where γ is the surface energy, t is the tape thickness and E is the Young modulus. Thus, when we use our data (so the mean values of α_F and α_T for each surface) with Eq. 1, we were able to determine the dimensionless adhesion strength λ for the five surfaces at each hierarchical level (of foot and toe), as graphically shown in Fig. 4.4 and reported in the right column of Table 4.1. Note that λ_T is smaller than λ_F (except for the steel surface). Thus, as suggested by the multiple peeling theory, the smaller the parameter λ ($\lambda_T < \lambda_F$), the smaller the optimal adhesion angle ($\alpha_T < \alpha_F$), which corresponds to the peak value of the function f as in Fig. 4.4.

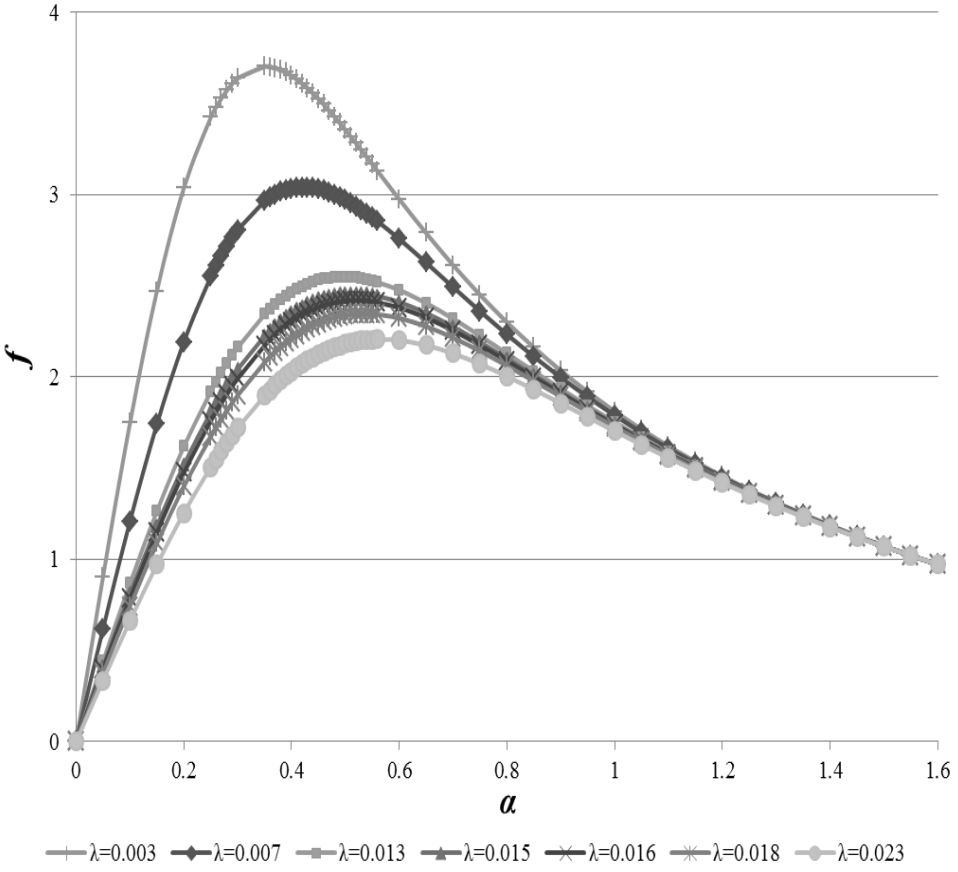

-

Fig. 4.4 From the multiple peeling theory [51], the dimensionless force f *versus* the adhesion angle α using the experimental mean values α_{F} and α_{T} (fitting parameters λ reported in Table 4.1).

Following [53], we expect at each hierarchical level n the validity of the following equation:

$$\frac{8}{\left(1-\nu_{\mathrm{f}}^{2}\right)\pi}\frac{\gamma_{\mathrm{n}}\left(E_{\mathrm{n}}/\phi_{\mathrm{n-1}}\right)}{\left(\sigma_{\mathrm{th}}\phi_{\mathrm{n-1}}\right)^{2}R_{\mathrm{n}}}=1 \qquad (3)$$

where $\gamma_n = W_n^{ad}$ is the work of adhesion, $E_n / \phi_{n-1} = E_f$ is the elastic modulus of a fiber, ν_f is the Poisson's ratio of a fiber, $\sigma_{th}\phi_{n-1} = S_n = E_n\varepsilon$ is the effective adhesion strength and $\phi_{n-1} = \prod_{i=1}^{n-1}\varphi_i$, where φ_i is the area fraction. Thus, according to Eq. 3, Eq. 2 can be rewritten for each hierarchical level n as:

$$\lambda_n = \phi_{n-1}, \tag{4}$$

finding a weak dependence of the parameter λ on the number n of hierarchical levels, so the parameter λ decreases as n increases.
We defined the Young modulus $E_T = E_F = 1$ GPa and the hierarchical level n and the thickness t of feet ($n_F = 4$ (four feet per gecko), $t_F = 10$ mm) and toes ($n_T = 5$ (five toes per each foot), $t_T = 4$ mm). Thus, using the work of adhesion γ of [53] (varying in the range of 10^3-10^6 J/m^2), we found the theoretical range of λ ($10^{-4} \div 10^{-1}$), which confirms the values of the parameter λ ($10^{-2} \div 10^{-1}$), computed in [53], and also the experimental range of λ ($10^{-3} \div 10^{-2}$) here determined.
A further consideration concerns the critical angle α_c, which corresponds to the inclination of the force vector (F_{TOT} in Fig. 4.1) just before the gecko's detachment and is governed by the normal (F_n) and shear (F_s) adhesive forces as follows:

$$\alpha_c = arctg\left(\frac{F_n}{F_s}\right) \leq \alpha\,. \tag{5}$$

The experimental value of the critical angle α_c is equal to ~11.3° for the *Hemidactylus garnotii* gecko (calculated with F_n = 0.006 N and F_s = 0.03 N [21]). Referring to Tokay geckos, the critical angle α_c is ~9.5° at the level of the entire animal (calculated with F_n = 6.7 N [42] and F_s = 40.2 N [2]) or ~11.3° at the level of setae (calculated with F_n = 40 μN [15] and F_s = 200 μN [12]). Note that the experimental values of the critical angle α_c confirm the range of 5.2°-11.3° for the whole insect, previously reported in

[21], and are in line with Eq. 5 so are coherently smaller than the optimal adhesion angle α, as experimentally here determined.
A final consideration regards the linear equation which fits the experimental data of the perpendicular adhesive force F_n of the gecko's seta and the adhesion angle α, reported in [12]:

$$\alpha = \frac{0.22}{1N} \cdot F_n + 28.2 . \quad (6)$$

Interestingly, when the normal adhesive force F_n = 6.7 N for the whole Tokay gecko [42] in Eq. 6 was used, we obtain the value α of 28.6° (or 28.9°) between the opposing first and fifth toe (or between the opposing front and rear feet), by roughly dividing F_n by 4 for the number of the gecko's feet (or by 2 for the number of couples of opposing front and rear feet), and this resulted in an agreement with the experimental results of the gecko's adhesion angles here reported.

4.5. Conclusions

Summarizing, the gecko's adhesion angles α have been estimated for a single toe (~25.5° [21]), for isolated setae arrays (~24.6° [21], ~30° [31]) and for a single seta (~30.0° [21], ~31° [12]). In this study, they are calculated for the angles between the opposing front and rear feet ($\alpha_{F\_FR\text{-}RL}$ = 28°, $\alpha_{F\_FL\text{-}RR}$ = 30°) and between the first and fifth toe of each foot (α_{T_FR} = 26°, α_{T_FL} = 29°, α_{T_RR} = 28°, α_{T_RL} = 26°), directly for the whole gecko [48]. Thus, such angles in the range from ~26° to ~30° seems to be optimized to maximize the adhesion of living Tokay geckos. The agreement between theoretical calculations of the multiple peeling theory and the experimental results at the level of foot and toe here extracted, also with those already reported in the literature about the gecko adhesive system (single toe, isolated setae arrays and single seta), support the validity of the approach at different hierarchical levels and provides an important contribution to the literature. In general, the presented findings could be useful for the industrial fabrication of bioinspired dry adhesives tapes, robotics systems, artificial adhesive suits and gloves for astronauts or

designing bio-inspired smart adhesive nanomaterials and especially they can have significant biomedical applications.

ACKNOWLEDGMENTS

The authors would like to thank A. Chiodoni, Physical Department, Politecnico di Torino for the fundamental help performing the FESEM micrographs. We thank the "2I3T Scarl – Incubatore dell'Università di Torino" for the SEM imaging instruments and M.G. Faga, CNR-ISTEC member, Chemical Department IFM and NIS Centre of Excellence, University of Torino for the fundamental help performing the SEM micrographs. NMP is supported by "Metrology on a cellular and macromolecular scale for regenerative medicine" - METREGEN (2009-2012).

REFERENCES

[1] Wagler, J. J. *G.*, *Cotta'schen Buchhandlung*, Munich, Germany (1830).
[2] Simmermacher, G., *Zeitschr. Wiss. Zool.* **40**, 481-556 (1884).
[3] Schmidt, H. R., *Jena. Z. Naturwiss.* **39**, 551-563 (1904).
[4] Dellit, W. D., *Jena. Z. Naturwiss.* **68**, 613-658 (1934).
[5] Ruibal, R., and Ernst, V., *J. Morphol.* **117**, 271-293 (1965).
[6] Hiller, U., *Z. Morphol. Tiere* **62**, 307-362 (1968).
[7] Gennaro, J. G. J., *J. Nat. Hist.* **78**, 36-43 (1969).
[8] Russell, A. P., *J. Zool.* **176**, 437-476 (1975).
[9] Russell, A. P., *Can. J. Zool.* **64**, 948-955 (1986).
[10] Schleich, H. H., and Kästle, W., *Amphib. Reptil.* **7**, 141-166 (1986).
[11] Irschick, D. J., Austin, C. C., Petren, K., Fisher, R., Losos, J. B., and Ellers, O., *Biol. J. Linn. Soc.* **59**, 21-35 (1996).
[12] Autumn, K., Liang, Y. A., Hsieh, S. T., Zesch, W., Chan, W. -P., Kenny, W. T., Fearing, R., and Full, R. J., *Nature* **405**, 681-685 (2000).
[13] Gorb, S.N., Dordrecht: Kluwer Academic Publishers (2001).
[14] Autumn, K. and Peattie, A. M., *Int. Comp. Biol.* **42**, 1081-1090 (2002).
[15] Autumn, K., Sitti, M., Peattie, A., Hansen, W., Sponberg, S., Liang, Y. A., Kenny, T., Fearing, R., Israelachvili, J., and Full, R. J *Proc. Natl. Acad. Sci. USA* **99**, 12252-12256 (2002).
[16] Arzt, E., Gorb, S., and Spolenak, R., *Proc. Natl. Acad. Sci. USA* **100**, 10603-10606 (2003).

[17] Bergmann, P. J., and Irschick, D. J., *J. Exp. Zool. A* **303**, 785-791 (2005).
[18] Huber, G., Gorb, S. N., Spolenak, R., and Arzt, E., *Biol. Lett.* **1**, 2-4 (2005).
[19] Gao, H. J., Wang, X., Yao, H., Gorb, S., and Arzt, E., *Mech. Mater.* **37**, 275-285 (2005).
[20] Hansen, W. R., and Autumn, K., *Proc. Natl. Acad. Sci. USA* **102**, 385-389 (2005).
[21] Autumn, K., Dittmore, A., Santos, D., Spenko, M., and Cutkosky, M., *J. Exp. Biol.* **209**, 3569-3579 (2006).
[22] Huber, G., Gorb, S. N., Hosoda, N., Spolenak, R., and Arzt, E., *Acta Biomaterialia* **3**, 607- 610 (2007).
[23] Pugno, N. M., *J. Phys.: Condens. Matter* **19**, 395001 (17pp) (2007).
[24] Lepore, E., Antoniolli, F., Buono, M., Brianza, S., Carpinteri, A., and Pugno N., *J. Nanomat.* **194524** (5 pp) (2008).
[25] Pugno, N. M., and Lepore, E., *J. Adhesion* **84**, 949-962 (2008).
[26] Pugno, N. M., and Lepore, E., *Biosystems* **94**, 218-222 (2008).
[27] Lepore, E., Chiodoni, A., Pugno, N., *Rev. Adv. Mater. Sci.* **24**, 69-80 (2010).
[28] Russell, A. P., *Integr. Comp. Biol.* **42**, 1154-1163 (2002).
[29] Autumn, K., Majidi, C., Groff, R., Dittmore, A. and Fearing, R. *J. Exp. Biol.* **209**, 3558-3568 (2006).
[30] Autumn, K., Hsieh, S. T., Dudek, D. M., Chen, J., Chitaphan, C., and Full, R. J., *J. Exp. Biol.* **209**, 260-272 (2006).
[31] Gravish, N., Wilkinson, M., and Autumn, K., *J. R. Soc. Interface.* **6**, 339-348 (2008).
[32] Jusufi, A., Goldman, D. I., Revzen, S., and Full, R. J., *Proc. Natl. Acad. Sci. USA* **105**, 4215-4219 (2008).
[33] Irschick, D. J., Vanhooydonck, B., Herrel, A., and Andronescu, A., *J. Exp. Biol.* **206**, 3923-3934 (2003).
[34] Tian, Y., Pesika, N., Zeng, H., Rosenberg, K., Zhao, B., McGuiggan, P., Autumn, K., and Israelachvili, J., *Proc. Natl. Acad. Sci. USA* **103**, 19320-19325 (2006).
[35] Lee, J., Fearing, R. S., and Komvopoulos, K., *App. Phys. Lett.* **93**, 191910 (2008).
[36] Santos, D., Spenko, M., Parness, A., Kim, S., and Cutkosky, M., *J. Adhes. Sci. Technol.* **21**, 1317 (2007).
[37] Aksak, B., Murphy, M. P., and Sitti, M., *Langmuir* **23**, 3322 (2007).

[38] Murphy, M. P., Aksak, B., and Sitti, M., *J. Adhes. Sci. Technol.* **21**, 1281 (2007).
[39] Yao, H., Rocca, G. D., Guduru, P. R., and Gao, H., *J. R. Soc. Interface* **5**, 723 (2008).
[40] Schubert, B., Lee, J., Majidi C., and Fearing, R. S., *J. R. Soc. Interface* **5**, 845-853 (2008).
[41] Shah, G. J., and Sitti, M., *Proceedings of the 2004 IEEE, International Conference on Robotics and Biomimetics*, August 22 - 26, Shenyang, China (2004).
[42] Pugno N., Lepore, E., Toscano, S., and Pugno, F., *J. Adhesion* **87**, 1059-1072 (2011).
[43] Zaaf, A., Van Damme, R., Herrel, A., and Aerts, P., *J. Exp. Biol.* **204**, 1233-1246 (2001).
[44] Russell A. P., and Higham, T. E., *Proc. Biol. Sci.* **276**, 3705-3709 (2009).
[45] Haase, A., *Arch. Naturgesch.* **66**, 321-345 (1900).
[46] Pesika, N.S., Tian, Y., Zhao, B., Rosenberg, K., Zeng, H., McGuiggan, P., Autumn, K., and Israelachvili, J.N., *J. Adhesion* **83**, 383-401 (2007).
[47] Kim, T. W., and Bhushan, B., *Ultramicroscopy* **107**, 902-912 (2007).
[48] Pugno, N., *Int. J. Fracture*, ICF XII Special Issue on Nanoscale Fracture, Guest Editor Nicola M. Pugno (2011). In Print. (published as arXiv: 0903.0935 cond-mat, 5 march 2009). Available online from the 14 November 2011
http://www.springerlink.com/content/um36255632007747/fulltext.pdf
[49] Bhushan, B., and Sayer, R., *Applied Scanning Probe Methods Vol. VII - Biomimetics and Industrial Applications*, Springer-Verlag, Heidelberg, Germany, 41-76 (2007).
[50] Autumn, K., *Biological Adhesives* (ed. A. Smith and J. Callow), 225-255. Berlin Heidelberg: Springer Verlag (2006).
[51] Sitti, M., and Fearing, R. S., *J. Adhes. Sci. Tech.* **17**, 1055-1073 (2003).
[52] Spolenak, R., Gorb, S. and Arzt, E., *Acta Biomater.* **1**, 5-13 (2005).
[53] Yao, H., and Gao, H., *J. Mech. Phys. Solids* **54**, 1120-1146 (2006).
[54] Pugno, N., *Nano Today* **3**, 35-41 (2008).
[55] Varenberg, M., Pugno, N., and Gorb, S., *Soft Matter* **6**, 3269-3272 (2010).
[56] Buehler, M. J., Yao, H., Ji, B., and Gao, H., *Modelling and Simulation in Materials Science and Engineering* **14**, 799-816 (2006).
[57] Sen, D., Novoselov, K., Reis, P., and Buehler, M. J., *Small* **6**, 1108-1116 (2010).

[58] Buehler, M. J., *Nano Today* **5**, 379-383 (2010).

5. OBSERVATIONS OF SHEAR ADHESIVE FORCE AND FRICTION OF *BLATTA ORIENTALIS* ON DIFFERENT SURFACES

Abstract

The shear adhesive force of four non-climbing living cockroaches (*Blatta Orientalis* Linnaeus) was investigated using a centrifugal machine with the determination of the shear safety factor on six surfaces (steel, aluminium, copper, two sand papers and a common paper sheet). The adhesive system of *Blatta Orientalis* was characterized by means of a field emission scanning electron microscope and the surface roughness was determined by an atomic force microscope. It is highlighted an interesting correlation between cockroach shear adhesion and the surface roughness with a threshold mechanism dictated by the competition between claw tip radius and roughness.

5.1. Introduction

The adhesive abilities of insects, spiders and reptiles have inspired scientists and researchers for a long time. All these organisms present outstanding performance particularly for frictional and adhesive forces and related climbing abilities, especially considering their weight. In particular, it is well known how small insects can carry many times their own weight and simultaneous walk quickly.

During the last decades, many authors have studied a multitude of insects, especially thanks to the availability of microscopy instruments (Scanning Electron Microscope (SEM) and Atomic Force Microscope (AFM)), in order to understand and measure their adhesive abilities such as common beetles [1-6], flies [7-13], ants [14-17], cockroaches [18-22], spiders [23-25] and geckos [26-36].

Biological adhesion can be obtained through different mechanisms (*e.g.* claws, clamp, sucker, glue, friction), even if insect attachment pads have evolved in two main types, those which are hairy (thousands of flexible

hairs, as fly pulvilli and beetle pads) or those which are smooth (a high deformable material, as for grasshoppers and cockroaches) [37, 38]. For example, geckos present a dry adhesive surface, organized in a hierarchical structure [26], like anoles, skinks and spiders; while other animals present secretion aided fibrillas or pads, which are common in some insects, especially hexapods [39] like ants [15] and cockroaches [18]. The adhesive organs of these insects consist of smooth pads and the adhesion is mediated by a small volume of fluid which is secreted into the contact zone and influences the attachment performance [40]. In general, the adhesive structure and mechanism could be correlated with the micro-structured roughness of substrata (*e.g.* plant surfaces), which usually interacts with such animals in nature [41, 42] and has a strong influence on their adhesive abilities [43].

The normal and shear adhesive forces of several animals have been determined in order to assess their climbing ability. As a matter of fact, to run and climb animals have to deal not only with perpendicular but also with shear forces. For example, during the last decades the adhesion of the Tokay gecko (*Gekko gecko*, ~100 g), which has the most widely studied biological adhesive system, was measured in terms of the normal force [27], the shear force [28], the adhesion time [29] and the influence of surface roughness on the adhesive properties [30, 32].

The shear adhesive force, and so the shear safety factor (sSF) obtained by dividing the shear adhesive force by the body weight, thus an apparent friction coefficient was determined for some living animals through different techniques [20]: with a centrifuge machine the sSF was estimated to be ~70 or ~60 for male or female of the Colorado potato beetle *Leptinotarsa decemlineata* (mass ~121 mg or ~168 mg, respectively) [3], ~43 for syrphid flies (mass ~62 mg) [11], ~843 for the ant *Oecophylla smaragdina* (mass ~4 mg) [17], ~18 or ~14 for male or female of the codling moth *Cydia pomonella* (mass ~19 mg or ~30 mg, respectively) [42], ~70 for the bug *Coreus marginatus* (mass ~80 mg) [44]; with the application of weights or force transducer the sSF is equal to ~40 for the beetle *Pachnoda marginata* (mass ~1 g) [4], ~109 and ~3 for the leaf beetle *Gastrophysa viridula* and the stick insect *Carausius morosus* (mass ~10.4 mg and ~898 mg, respectively) [5], ~28 for the blowfly *Calliphora vomitoria* (mass ~72 mg) [12], ~100 for geckos (mean mass ~10 g), ~60 for anoles (mean mass ~9 g) and ~18 for skinks (mean mass ~9 g) [33], ~317 and ~81 for male or female of the leaf beetle *Gastrophysa viridula* (mass

~10.8 mg and ~19.7 mg, respectively) [45], and finally $<<1$ for the green bushcricket *Tettigonia viridissima* (mass ~1 g, on polished silicon substratum) [38].
We have focused on the shear adhesive force of living cockroaches (*Blatta Orientalis* Linnaeus), which are a species of the Blattodea order. There are thousands of species of cockroaches and only a few of these species live in human environments. The species of Blattodea are distinguished between climbing (*i.e. Blattella Germanica*) and non-climbing (*i.e. Blatta Orientalis*), if they show the ability of climbing on smooth vertical surfaces, like Poly(methyl meth-acrylate) (PMMA), Poly(ethylene terephthalate) (PET), sheet metals, even upside down.
In this study, we present the measurement of the sSF using a centrifuge technique of non-climbing living cockroaches (*Blatta Orientalis* Linnaeus) on six surfaces (two different sandpapers, common paper, steel, aluminium and copper) with different roughnesses. Four cockroaches were used to assess the sSF with three measurements, per individual, on each surface. This procedure guarantees to get consistent biomechanical data which are correlated to the surface roughness, that is quantified by the AFM. The adhesive system of *Blatta Orientalis* was characterized by a field emission scanning electron microscope (FESEM) at the end of the experimental session.

5.2.Experimental set-up

A self-built centrifuge device was used to directly measure the sSF of cockroaches. The centrifuge machine allowed us to avoid any prior treatment of cockroaches, which are left free of motion and of assuming a natural attachment position inside the experimental box. In addition, looking at previously data [14], the centrifuge device probably yields higher values of adhesive forces than any other procedure of force measurement.
The sSF measurement just depends on the angular speed, since the radius is constant (the position of cockroaches is far from the rotational axis). The experimental configuration is shown in Fig. 5.1.
The box was built in order to have an interchangeable floor and carry out tests on different surfaces. The machine is made of an electric motor (named M_1 in Fig. 5.1), which is used as a shaft, and another electric motor (M_2), which forces the system to rotate. M_1 and M_2 are connected through a belt

transmission. M_2 is connected to the 220 V (50 Hz, AC) and it is controlled through a frequency controller (VFD004L21E, Delta Electronics, named FC), which modulates the current frequency in the range of 1-400 Hz. Two aluminum bars are attached to the shaft and support the box B_1 of 25 x 25 x 25 cm^3 on one side and the counterweight (CW) on the other side. The camera (C) is put on the rotational axis (RA) of the system and records the cockroach's movement. Inside B_1, we have another small box B_2 of 7(w) x 4(l) x 3(h) cm^3, where we put the animals (so the uncertainty on the insect's radial position is reduced to ± 2.0 cm). The angular speed was measured with a standard bicycle computer (BCP-01, BBB company, named BC) by a magnetic sensor and a LCD screen, which is fixed to the radially external wall of B_1. Thus, in the movie (in Fig. 5.1, the blue lines identify the video shot) we recorded both the cockroach and the speed measurement, so that the correct speed which corresponds to the cockroach's detachment is determined. The BC was calibrated with the reference distance (51 cm) between the rotational axis and the middle (M) of B_2. The reference distance is known and the angular speed is calculated from the linear speed read on the LCD screen of BC, which gives the speed value in the range of 0.0-199.9 km/h with an accuracy of ± 1 % over the read value.

To minimize the cockroach experience of the rotation, we decided to insulate the box from the environment by using a dark paper to obscure the box and adding an artificial light (L) inside B_1.

Experiments were conducted upon four adult cockroaches (B_1, B_2, B_3 and B_4) of the species *Blatta Orientalis*. They were kept alone and were fed chicken feed *ad libitum*. The insects were maintained at a room temperature of ~25 °C and humidity of ~50 %, which corresponds also to the experimental conditions.

The sSF measurements were conducted as follows. Four cockroaches were used to assess the sSF with three measurements, per individual, on each surface. During the biomechanical experiments, we provided a slow speed-up to avoid high acceleration, which can determine an early detachment, and to satisfy the hypothesis of a constant angular speed in order to correctly evaluate the sSF. Every time the cockroach was put on the bottom of the box, we waited two minutes in order for it to familiarize with the room. During an acceptable test, at low speeds the animal can still run on the bottom of B_2, while it walks more slowly when the centrifuge speeds up; finally it stands still until it detaches by contacting the substratum with all legs and assuming the 'freezing' position which is advantageous to the

insect's attachment, also reported in [14]. By standing motionless with all legs spread out, the cockroach assumes a position that maximizes its adhesive ability and so the detachment is not caused by its natural movement but just by the shear force which acts on the animal. During an unacceptable test, the animals tend to go in a corner or against a wall and this represents the aborting condition of an experimental test. We didn't test an animal over more than two surfaces per day. We measured the body weight of the four insects (equal to 405.9 ± 22.9 mg) by a balance (EB200, Orma) with a precision of ± 0.1 mg.

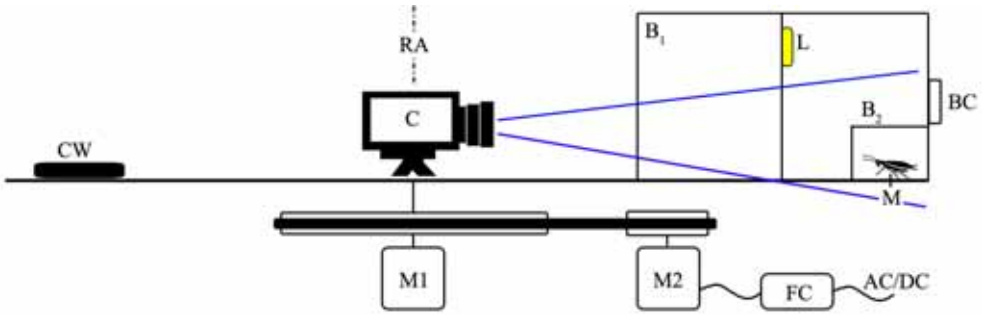

Fig. 5.1 The centrifuge machine for the measurement of the insects sSF.

5.3. Video output

Fig. 5.2 shows an example of two subsequent frames extracted from a single test video. The cockroach's detachment and tangential speed on the LCD screen are clearly visible. Before the detachment, the cockroach stands on the surface until it detaches and goes immediately against the back wall due to the centrifuge force.

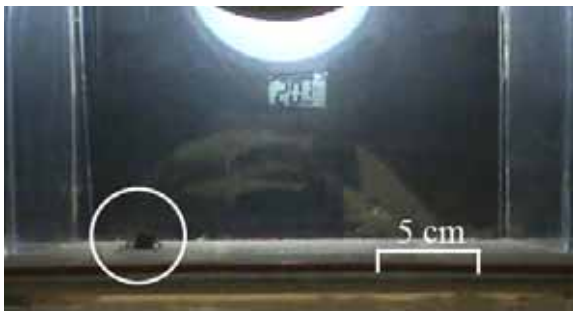

A

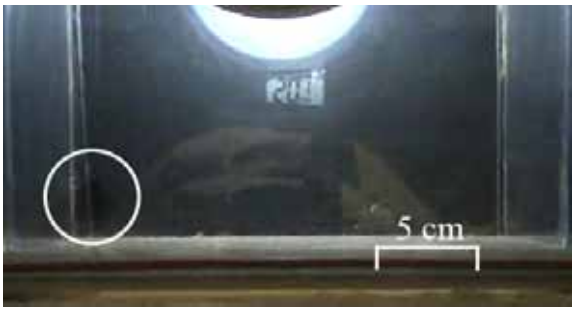

B

Fig. 5.2 Two subsequent frames from a video: before detachment the insect stands still on the surface (A) and, one frame later, it is in the box corner (B). These frames are extracted from a preliminary video without the use of the small box (B_2).

5.4. AFM characterization of surfaces

The characterization of surfaces (sheet of common office paper (80 g/m², named Cp), steel, aluminum and copper) was performed in 'contact mode' with an AFM (Solver Pro M) with NSG01 tips, from NT-MDT, Moscow, Russia (Fig. 5.3). The parameters tuned during the analysis are the measurement speed (14.2 μm/s), the measured area (100 x 100 μm^2 for 3 tests on metals and 50 x 100 μm^2 for 6 tests on Cp) with a final resolution of 512 points/profile. All parameters were referred to a 100 μm cut-off. The cut-off length defines the length on which the roughness parameters are calculated and therefore it strongly influences the roughness values. The roughness parameters were determined with NOVA software from NT-MDT, Moscow, Russia. No roughness data was obtained for the two types of sandpaper (Sp50 and Sp150) because their roughness is beyond the working ranges of the AFM, so the mean nominal diameter of surface asperities was used to compare them with the AFM measured surfaces. See [27, 29-31] for a detailed explanation of the classical roughness parameters (S_a, S_q, S_p, S_v, S_z, S_{sk}). S_{ka} is the kustosis parameter and indicates the distribution of surface heights: when close to 0 the distribution of surface heights is like a Gaussian distribution; when higher than 0 the height distribution is more sharp than a Gaussian distribution (so peak heights are close to the mean height), when lower than 0 the height distribution is more spread.

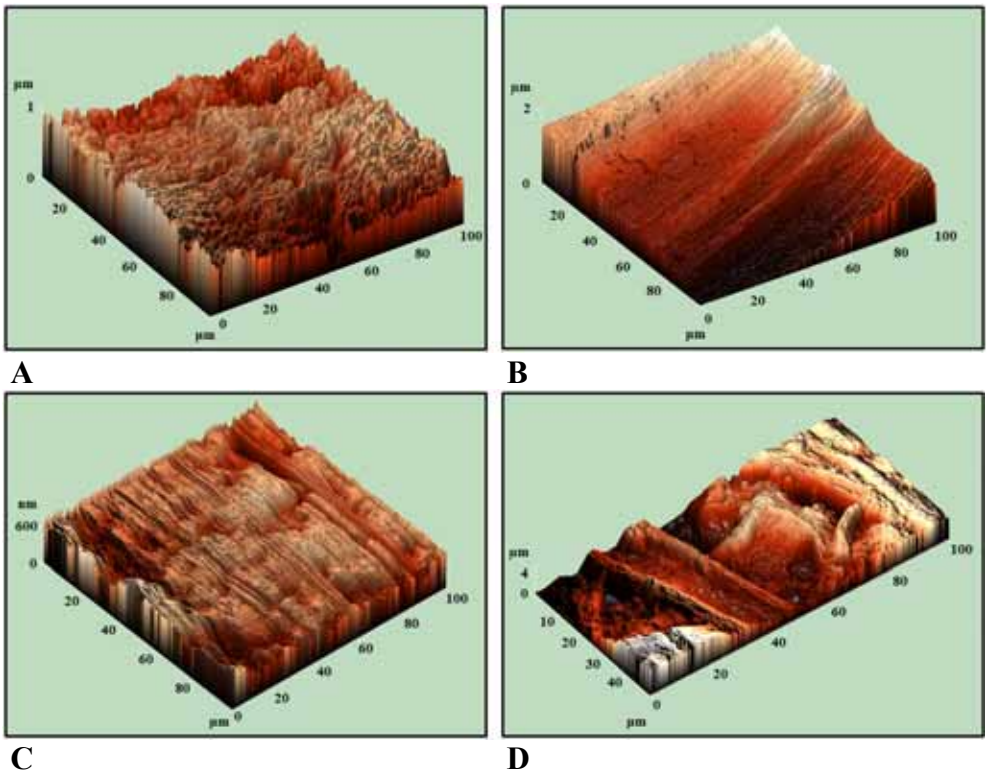

Fig. 5.3 The AFM characterization of the (A) steel, (B) aluminium, (C) copper and (D) Cp surfaces.

5.5. FESEM characterization of *Blatta Orientalis*

We observed the adhesive system of *Blatta Orientalis* by means of a FESEM (FEI-Inspect^{TM} F50) equipped with a field emission tungsten cathode at 1 kV. Samples were amputated from naturally dead adult cockroaches and maintained in 70 % ethanol solution, 12 h dehydrated, fixed to aluminium stubs by a double-sided adhesive carbon conductive tape (Nisshin EM Co. Ltd.) and scanned without metallization.
Fig. 5.4 confirms the adhesive system description recently reported in [19]: a sub-obsolete nonfunctional arolium (no better adapted for climbing a smooth vertical surface) with two claws for each of the six legs of *Blatta Orientalis*. The claw tip diameter is equal to 12.3 ± 4.73 μm and is determined by using the ImageJ 1.41o software.

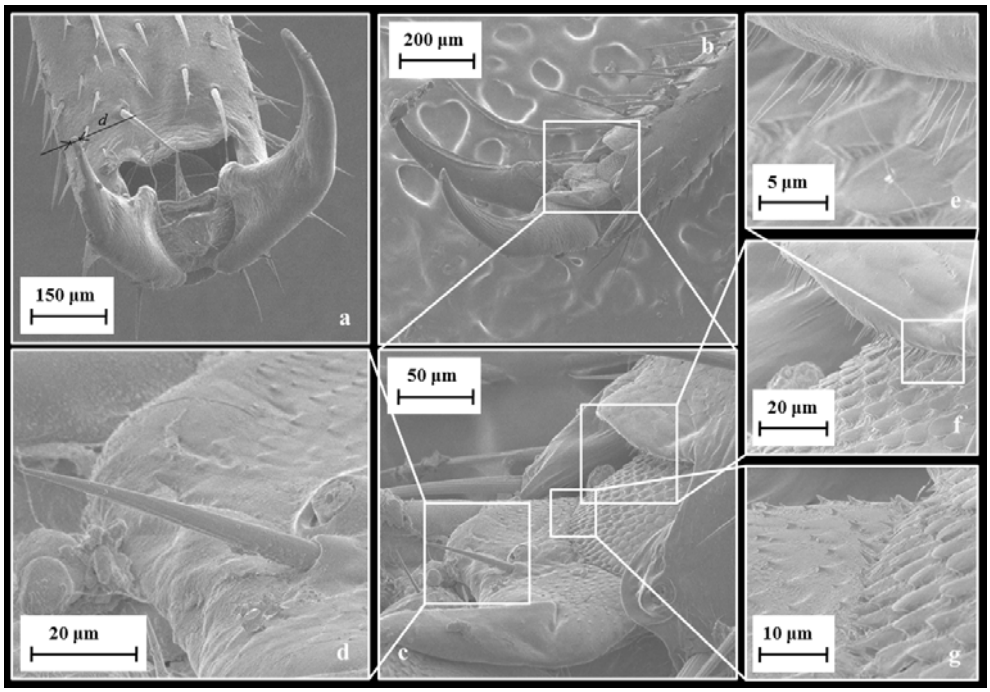

Fig. 5.4 The adhesive structures of the legs of *Blatta Orientalis*. (a) Frontal and (b) lateral view of a leg and some detailed micrographs (c, d, e, f, g) (*d* is the claw tip diameter).

5.6. sSF evaluation

Our goal is to measure the sSF, which is defined as the ratio between the shear detachment force ($F_{\text{detachment}}$) and the mass (m) multiplied by the gravity acceleration (g), so it is dimensionless and represents also the apparent friction coefficient:

$$sSF = \frac{F_{\text{detachment}}}{m \cdot g} \tag{1}$$

We focused on the shear adhesive force and thus we just considered the radial force (F_{radial}) which acts on the insect, thus in our case $F_{\text{detachment}} = F_{\text{radial}}$. A constant angular speed (ω) is considered, so the radial force is

proportional to the insect distance from the axis (the radius, R = 51 cm), the square of the angular speed and the insect mass:

$$F_{\text{radial}} = m \cdot \omega^2 \cdot R \tag{2}$$

Thus, we can easily determine the sSF as:

$$sSF = \frac{\omega^2 \cdot R}{g} \tag{3}$$

that does not depend on the body weight of the insect. Knowing the radius (constant) and neglecting the drag force, since the insects are in a closed box, we measured the sSF just from the value of the angular speed, that we get from the BC.

5.6. Experimental results

Fig. 5.5 shows that there is not any significant difference among the sSF of different insects. Thus, we could simply average the results of the four tests on each surface. Table 5.1 reports the sSF and the F_{radial} for each surface (mean ± st.dev.) and shows a clear separation between rough (Sp50, Sp150, Cp) and smooth (steel, aluminium, copper) surfaces.

5.7. Discussion

In general, claw-mediated adhesive insects can attach to a horizontal or vertical surface just by interlocking and so the adhesive abilities increase with the surface roughness [5, 20], in agreement with our observations. In particular, the claw-mediated adhesion occurs when the surface asperity size is comparable or larger than the claw tip diameter [3, 4, 42], which is estimated to be 12.3 μm for *Blatta Orientalis*. Table 5.1 summarizes the calculated or estimated roughness parameters.
The unmeasured asperity diameter (*Ad*) for Cp, steel, aluminium and copper (marked with $^{(*)}$ in Table 5.1) is estimated by multiplying the parameter S_q by the value of 3.6, which is computed as the mean value S_q/Ad for

sandpapers (Sp) from previously published papers (the value of *Ad* is known for sandpapers on which the roughness parameter S_q was calculated). It is here reported as Sp_{Ad}-S_q, thus $Sp_{30\mu m}$-6.66 µm, $Sp_{16\mu m}$-3.75 µm, $Sp_{12\mu m}$-3.25 µm, $Sp_{0.5\mu m}$-0.13 µm and $Sp_{1\mu m}$-0.4 µm [46], $Sp_{12\mu m}$-3.06 µm, $Sp_{9\mu m}$-2.45 µm, $Sp_{3\mu m}$-1.16 µm, $Sp_{1\mu m}$-0.24 µm and $Sp_{0.3\mu m}$-0.09 µm [32], $Sp_{12\mu m}$-3.0603 µm, $Sp_{9\mu m}$-2.4537 µm, $Sp_{3\mu m}$-1.1567 µm, $Sp_{1\mu m}$-0.2384 µm and $Sp_{0.3\mu m}$-0.09 µm [3]. Looking at the results, the assumptions are confirmed: the claws of *Blatta Orientalis* would hardly be able to grip surfaces with *Ad* smaller than ~12 µm. As a matter of fact, if compared with the shear adhesive force on Sp50 and Sp150, a decrement of the shear adhesive forces of about 35 % on the Cp surface and of more than 80 % on metals is recorded.

Referring to the roughness analysis of steel, aluminium, copper and Cp (Fig. 5.3 and Table 5.1), it is clear that the Cp surface is characterized by the parameters S_a, S_q, S_p, S_v, S_z one order of magnitude higher than those of metal surfaces with a spread distribution of peak heights ($S_{ka} < 0$), whose number is overtaken by the number of valleys ($S_{sk} < 0$), which are deep, wide and so probably complementary to the geometry of the claw tip.

Looking at the metal surfaces, the noteworthy difference clearly emerges between copper and aluminium if compared with steel (on which we recorded the lowest sSF). The steel surface is denoted by a higher number of valleys than peaks ($S_{sk} < 0$), whose heights are very close to the mean value ($S_{ka} > 0$) and which are usually at a distance lower than 1 µm. Thus, the lowest performance of *Blatta Orientalis* on the steel surface could be explained by the objective impossibility of the cockroach to interlock its claws inside the peak to peak distance.

The aluminium and copper surfaces are comparable for all of the roughness parameters, with the exception of S_{sk}, which allow us to highlight that the cockroach *Blatta Orientalis* performs higher sSF on surfaces with a lower number of peaks than valleys, which probably become the fundamental interlocking for its claws.

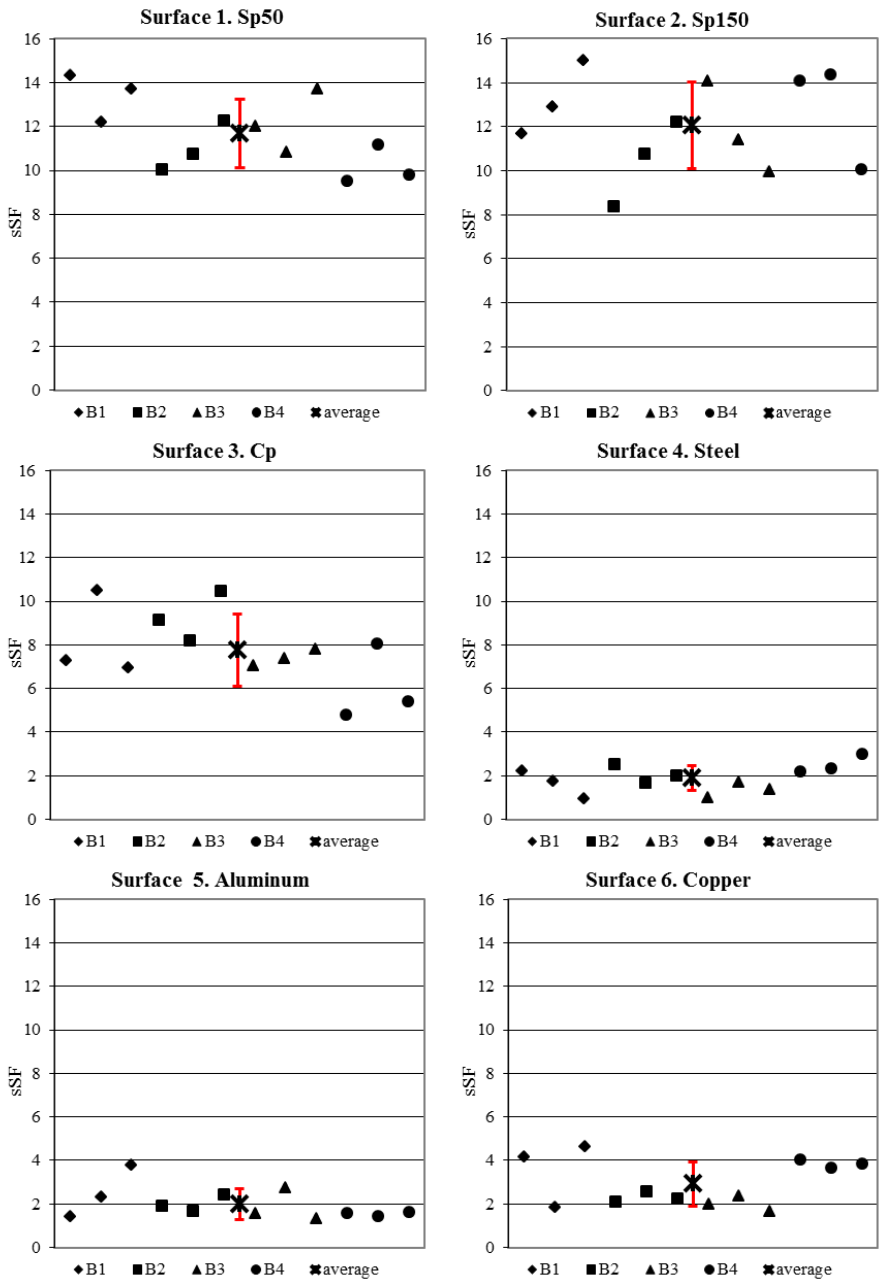

Fig. 5.5 The sSF of each individual are grouped by surfaces.

	Sp50	Sp150	Cp	Steel	Aluminium	Copper
Ad (μm)	336	100	$4.5^{(*)}$	$0.7^{(*)}$	$0.6^{(*)}$	$0.8^{(*)}$
S_a (μm)	-	-	1.044 ± 0.228	0.145 ± 0.041	0.141 ± 0.026	0.178 ± 0.125
S_q (μm)	-	-	1.248 ± 0.255	0.190 ± 0.053	0.173 ± 0.026	0.215 ± 0.145
S_p (μm)			2.727 ± 0.433	0.801 ± 0.176	0.626 ± 0.045	0.496 ± 0.258
S_v (μm)			3.132 ± 0.112	0.885 ± 0.353	0.434 ± 0.105	0.670 ± 0.237
S_z (μm)	-	-	2.927 ± 0.233	0.838 ± 0.190	0.521 ± 0.051	0.584 ± 0.228
S_{sk}	-	-	-0.31 ± 0.143	-0.78 ± 0.472	0.41 ± 0.331	-0.48 ± 0.590
S_{ka}	-	-	-0.66 ± 0.327	1.31 ± 0.485	-0.08 ± 0.820	-0.04 ± 1.139
sSF	11.7 ± 1.6	12.1 ± 2.0	7.7 ± 1.7	1.9 ± 0.6	2.0 ± 0.7	2.9 ± 1.0
F_{radial} (mN)	46.8 ± 8.5	48.1 ± 9.0	30.9 ± 7.2	7.4 ± 2.1	7.9 ± 3.2	11.6 ± 4.3

Table 5.1 The roughness parameters, sSF and F_{radial} of the characterized insect/surface systems. The values $^{(*)}$ are computed multiplying the parameter S_q by the value of 3.6, which is calculated as S_q/Ad for sandpapers (Sp) from previously published papers with known Ad on which the roughness parameter S_q has been observed.

5.8. Conclusions

We measured the sSF of four non-climbing living cockroaches (*Blatta Orientalis* Linnaeus) using a centrifuge technique on six surfaces (two different sandpapers, common paper, steel, aluminium and copper). The cockroach's maximum sSF, or apparent friction coefficient, is determined to be 12.1 on Sp150 ($Ad \approx 100$ μm, $F_{\text{radial}} = 48$ mN), while the minimum sSF is equal to 1.9 on a steel surface ($Ad \approx 0.7$ μm, $F_{\text{radial}} = 7.4$ mN). An interesting threshold mechanism is demonstrated between the cockroach's shear adhesive force and the surface roughness. It is clear that the best adhesion is obtained for roughness larger than the claw tip radius; also surfaces with a higher number of valleys than peaks ($S_{sk} < 0$) and a spread distribution of peak heights ($S_{ka} < 0$) allow large adhesion.

ACKNOWLEDGMENTS

The authors would like to thank the entomologist Franco Casini for his advice and for providing the insects, Maddalena Binda of the LabSamp of Politecnico di Milano for her helpfulness in surface analysis, Alessandro Pero of Politecnico di Torino for his help in order to build the centrifuge machine. We thank NanoFacility Piemonte, INRiM, a laboratory supported by Compagnia di San Paolo for the FESEM imaging instruments and E. Enrico, INRIM Institute, for the fundamental help by performing the FESEM micrographs. NMP is supported by "Metrology on a cellular and macromolecular scale for regenerative medicine" - METREGEN (2009-2012).

REFERENCES

[1] Stork, N. E., *J. Exp. Biol.* **88**, 91-107 (1980).
[2] Eisner, T., and Aneshansley, D. J., *Proc. Natl. Acad. Sci. USA* **97**, 6568-6573 (2000).
[3] Voigt, D., Schuppert, J. M., Dattinger, S., and Gorb, S. N., *J. Insect Physiol.* **54**, 765-776 (2008).
[4] Dai, Z., Gorb, S. N., and Schwarz, U., *J. Exp. Biol.* **205**, 2479-2488 (2002).
[5] Bullock, J. M. R., Drechsler, P., and Federle, W., *J. Exp. Biol.* **211**, 3333-3343 (2008).
[6] Eigenbrode, S. D., and Jetter, R., *Integr. Comp. Biol.* **42**, 1091-1099 (2002).
[7] Wigglesworth, V. B., *J. Exp. Biol.* **129**, 373-376 (1987).
[8] Dixon, A. F. G., Croghan, P. C., and Gowing, R. P., *J. Exp. Biol.* **152**, 243-253 (1990).
[9] Lees, A. D., and Hardie, J., *J. Exp. Biol.* **136**, 209-228 (1988).
[10] Dixon, A. F. G., Croghan, P. C. and Gowing, R. P., *J. Exp. Biol.* **152**, 243-253 (1990).
[11] Gorb, S. N., Gorb, E. V., and Kastner, V., *J. Exp. Biol.* **204**, 1421-1431 (2001).
[12] Walker, G., Yue, A. B., and Ratcliffe, J., *J. Zool., Lond. A* **205**, 297-307 (1985).
[13] Voigt, D., Dissertation. Technische Universität Dresden, Dresden, Germany, 185 pp (2005).

[14] Federle, W., Rohrseitz, K., and Holldobler, B., *J. Exp. Biol.* **203**, 505-512 (2000).
[15] Federle, W., Riehle, M., Curtis, A. S. G., and Full, R. J., *Integr. Comp. Biol.* **42**, 1100-1106 (2002).
[16] Brainerd, E. L., *Am. Zool.* **34**, 128A (1994).
[17] Federle, W., Baumgartner W., and Hölldobler, B., *J. Exp. Biol.* **206**, 67-74 (2003).
[18] Arnold, J. W., *Int. J. Insect Morph. Embryol.* **3**, 317-334 (1974).
[19] Bell, W. J., Roth, L. M., and Nalepa, C. A., Cockroaches. Ecology behavior and natural history, in *The Johns Hopkins University Press*, Baltimore (2007).
[20] Van Casteren, A., and Codd, J. A., *J. Insect Sci.* **10,** 1-11 (2008).
[21] Clemente, C. J., and Federle, W., *Proc. R. Soc. B* **275**, 1329-1336 (2008).
[22] Clemente, C. J., Dirks, J. -H., Barbero, D. R., Steiner, U., and Federle, W., *J. Comp. Physiol. A* **195**, 805-814 (2009).
[23] Niederegger, S., and Gorb, S. N., *J. Comp. Physiol. A* **192**, 1223-1232 (2006).
[24] Kesel, A. B., Martin, A., and Seidl, T., *Smart Mater. Struct.* **13**, 512-518 (2004).
[25] Kesel, A. B., Martin, A., and Seidl, T., *J. Exp. Biol.* **206**, 2733-2738 (2003).
[26] Autumn, K., and Peattie, A. M., *Integr. Comp. Biol.* **42**, 1081-1090 (2002).
[27] Pugno N., Lepore, E., Toscano, S., and Pugno, F., *J. Adhesion* **87**, 1059-1072 (2011).
[28] Autumn, K., Dittmore, A., Santos, D., Spenko, M., and Cutkosky, M., *J. Exp. Biol* **209**, 3569-3579 (2006).
[29] Pugno, N. M., and Lepore, E., *J. Adhesion* **84**, 949-962 (2008).
[30] Pugno, N. M., and Lepore, E., *Biosystems* **94**, 218-222 (2008).
[31] Lepore, E., Antoniolli, F., Buono, M., Brianza, S., Carpinteri, A., and Pugno N., *J. Nanomat.* **194524** (5 pp) (2008).
[32] Huber, G., Gorb, S. N., Hosoda, N., Spolenak, R., and Arzt, E., *Acta Biomaterialia* **3**, 607-610 (2007).
[33] Irschick, D. J., Austin, C. C., Petren, K., Fisher, R., Losos, J. B., and Ellers, O., *Biol. J. Linn. Soc.* **59**, 21-35 (1996).
[34] Pugno, N. M., *J. Phys.: Condens. Matter* **19**, 395001 (17pp) (2007).
[35] Pugno, N., *Nano Today* **3**, 35-41 (2008).

[36] Varenberg, M., Pugno, N., and Gorb, S., *Soft Matter* **6**, 3269-3272 (2010).
[37] Peattie, A.M., *J. Comp. Physiol. B* **179**, 231-239 (2009).
[38] Gorb, S. N. and Scherge, M., *Proc. Roy. Soc. London B* **267**, 1239-1244 (2000).
[39] Beutel, R. G., and Gorb, S.N., *J. Zool. Syst. Evol. Research* **39**, 177-207 (2001).
[40] Drechsler, P., and Federle, W., *J. Comp. Physiol. A* **192**, 1213-1222 (2006).
[41] Gorb, S. N., Beutel, R. G., Gorb, E. V., Jiao, Y., Kastner, V., Niederegger, S., Popov, V. L., Scherge, M., Schwarz, U., and Votsch, W., *Integr. Comp. Biol.* **42**, 1127-1139 (2002).
[42] Bitar, L. A., Voigt, D., Zebitz, C. P. W., and Gorb, S. N., *J. Insect Physiol.* **56**, 1966-1972 (2010).
[43] Persson, B.N.J., *Mrs Bulletin* **32**, 486-490 (2007).
[44] Gorb, S. N., and Gorb, E. V., *J. Exp. Biol.* **207**, 2917-2924 (2004).
[45] Bullock, J. M. R., and Federle, W., *J. Exp. Biol.* **212**, 1876-1888 (2009).
[46] Bullock, J. M. R., and Federle, W., *Insect Science* **00**, 1-7 (2010).

ANTI-ADHESIVE

MATERIALS

6. PLASMA AND THERMOFORMING TREATMENTS TO TUNE THE BIO-INSPIRED WETTABILITY OF POLYSTYRENE

Abstract

This paper shows the effects on wettability of plasma and thermoforming treatments on fourteen different polystyrene (PS) surfaces, with a comparison with a lotus leaf. Quantitative roughness analyses of PS surfaces and lotus leaf, by three-dimensional optical profilometer and scanning electron microscope, have been carried out. We characterized the water drop sliding by measuring the contact angle, sliding angle, sliding volume and sliding speed. A relevant correlation between technological treatment, surface roughness parameters and wetting measurements clearly emerges, suggesting the plasma/thermoforming treatment as a process for enhancing the hydrophilic/hydrophobic behaviour of PS surfaces. Determination of the static and resistant forces of the drop sliding on the surfaces concludes the paper.

6.1. Introduction

Water-repellent (or superhydrophobic) and dirt-free (or self-cleaning) natural surfaces were probably observed for the first time more than 2000 years ago; however, only in the 20th century scientists studied these two related phenomena on some natural leaves [1-10], *e.g.* the famous lotus *Nelumbo nucifera*, on which "raindrops take a clear, spherical shape without spreading, which probably has to be ascribed to some kind of evaporated essence", as Goethe described in 1817 [11].
In contrast to the Goethe's conjecture, the so called lotus-effect is governed more than by chemistry (Young's law [12]) by topology (Wenzel's law [13], Cassie-Baxter's law [14]) and hierarchical architectures [15, 16] (similar to what we observe on the strength and toughness of materials [17-21]). The contribution of surface roughness on superhydrophobic/self-cleaning behaviour has been extensively shown in the literature [22-34].

However, in some applications, materials should be hydrophilic more than hydrophobic, *e.g.* in order to maximize wettability.
In this paper, we study the effects of plasma or thermoforming treatments on different polystyrene (PS) surfaces. We have considered seven PS surfaces before (A_p) or after (B_p) the plasma treatment and fourteen PS surfaces before (A_t) or after (B_t) the thermoforming treatment. All these surfaces have been analysed with a three-dimensional optical profilometer and a field emission scanning electron microscope. The hydrophilic behaviour given by plasma treatment is quantified by deposing distilled water drops on PS horizontal surfaces with controlled or random volumes, showing a relevant correlation between surface roughness parameters and contact angles (CA) measurements, in accordance with Wenzel theory. The effects of the thermoforming treatment are quantified by measuring the drop contact angle, sliding angle, sliding volume and speed. Finally, we determine the static and resistant forces of a drop sliding on the surfaces.

6.2. Materials and methods

6.2.1. Plasma treatment

A commonly applied method to increase wettability and chemical reactivity of polymeric materials (by raising surface energy) is plasma discharge treatment, also known as corona treatment. Such a treatment, invented by the Danish engineer Verner Eisby in the 1950s, is particularly suitable for continuous production processes, like the extruded PS sheets constituting the subject of the present paper, being safe, economical and capable of high line speed throughput.
Corona treatment is based on a high-frequency and high-voltage electrical discharge. The discharge is generated between an electrode and a counter electrode. The corona discharge has such a powerful impact on the substance surface that the molecular structure changes in a way that improves the surface wettability. In the presence of a high voltage discharge in an air gap, air ionization occurs. If a plastic material is placed in the discharge path, the electrons generated in the discharge impact the surface with energies two or three times larger than that necessary to break the molecular bonds. This creates very reactive free radicals that, in presence of air oxygen, can react rapidly to form various chemical functional groups on

the substrate surface. An evolution of the system, particularly efficient for the higher activation potential, is the plasma jet system, where by means of high-voltage discharge (5-15 kV, 10-100 kHz) a pulsed electric arc is generated. A process gas, usually oil-free compressed air flowing past this discharge section, is excited and converted to the plasma state. This plasma then passes through a jet head to arrive on the surface of the material to be treated. The jet head is at earth potential and in this way largely holds back potential-carrying parts of the plasma stream. Corona surface and plasma jet treatment modifies only the surface characteristics without affecting material bulk properties [35-37].
Corona discharge treatment is commonly applied in cooling appliance industry: refrigerator insulation systems are typically constituted by polyurethane foam, reticulated *in situ* within cavity designed by purpose. To ensure mechanical and thermal stability of the final assembly, and thanks to the strongly modified surface topology due to the plasma treatment, adhesion of polyurethane foam over surrounding surfaces, *i.e.* PS liner surface and external case, must be maximized. For the purposes of the present paper, PS extruded slabs have been treated with the industrial "Ferrarini and Benelli" corona discharge system, integrated within refrigerators production line at Indesit Company; main characteristics of the equipment are: nominal power (7.3 kVA), corona discharge power (6.5 kW), corona discharge device working frequency (30 kHz), achievable surface energy after treatment ((4.2-5.6) · 10^{-2} N/m), material temperature in treatment area (80 °C), performance test method (ASTM Standard Test Method D2578-84, "Wetting Tension of Polyethylene and Polypropylene Film").

6.2.2. Thermoforming treatment

Thermoforming is the technology almost universally applied for refrigerator cabinet liner and door internal surface manufacturing; such a technique allows high throughput production, together with a very good net shape surface finishing. Main phases of the process are: pre-heating (100 °C), peak temperature (180 °C), final temperature (70 °C).
After thermoforming, thickness reduction can exceed 90 % in some areas: a careful control is needed to verify that sheet is kept robust (*e.g.* no breakage of aesthetic or functional layer), tuning the process and the material characteristics.

6.2.3. Surface characterization

The characterization of PS surfaces was performed with a three-dimensional optical profilometer, Talysurf CLI 1000, equipped with the CLA Confocal Gauge 300HE or a mechanical cantilever with 300 μm range and 10 nm vertical resolution or with 546 μm range and 10 nm vertical resolution from Taylor Hobson, Leicester, UK. The parameters tuned during the analysis are the measurement speed equal to 200 μm/s, the return speed equal to 1 mm/s or 500 μm/s, the sampling rate equal to 150 Hz or 40 Hz, the measured area equal to 500 x 500 μm^2 and the resolution in the "*xy*" plane equal to 2.5 μm, leading to a final resolution of 201 points/profile. All parameters were referred to a 250 μm cut-off. See paragraph 1.2 for a detailed explanation of the classical roughness parameters extracted (S_a, S_q, S_p, S_v, S_z, S_{sk}, S_{dr}).
We also observed the PS surfaces and lotus leaf by means of a field emission scanning electron microscope (FESEM, Zeiss SUPRA 40 for A_p, B_p and A_t samples and lotus leaf, or FEI-Inspect^{TM} F50 for B_t samples) equipped with a field emission tungsten cathode. Samples of ~1 cm^2 were obtained, fixed to aluminium stubs by double-sided adhesive carbon conductive tape (Nisshin EM Co. Ltd.), ethanol-cleaned (except for lotus leaf used as is) and air-dried. Samples A_p, B_p and lotus leaf or A_t and B_t were chrome or gold-coated, approximately 8 or 3.6 nm.

6.2.4. CA measurement

The wettability of PS surfaces and lotus leaf was determined by measuring the static CA of distilled water droplets over the samples, fixed to a horizontal plane by a double-sided adhesive tape and cleaned with ethanol before drop deposition, in order to reduce the negative influence of sample cleanliness on contact angle measurements [41-44]. We consider a series of ten random-volume drops, gently deposited on the substrate with a standard single use syringe, and nine controlled-volume drops (0.5, 0.7, 0.9, 1.1, 1.3, 1.5, 1.7, 1.9, 2.0 μl), deposited with a digital micropipette (Gilson, Ultra-range U2-Model, 0.2-2.0 μl). The contact angle was recorded with an OLYMPUS MJU 1010 digital photocamera, measured and statistically analysed with the software ImageJ 1.41o.

6.2.5. Sliding measurements

Two conceptually distinct procedures were used to evaluate the sliding angles on B_t samples and lotus leaf: (1) fixing the volume of the drop (~16 μl) and measuring the angle of the sample stage at sliding or (2) fixing the angle of the specimen stage (90°) and measuring the sliding volume.

6.3. Results

6.3.1. Surface characterization

Table 6.1 summarizes the extracted roughness parameters from the profilometer whereas Fig. 6.1 shows the related FESEM images (surface morphologies at the same magnification) of all PS materials. Figs. 6.2-6.4 show the plasma untreated PS surfaces, while Fig. 6.5 shows the typical topography of plasma treated samples. Fig. 6.6 shows the effects of thermoforming treatment through samples 1 and 4 considered as examples and Fig. 6.7 displays the profiles extracted at 50 mm from the edge of the square measured area. Finally, the SEM morphology of the adaxial leaf surface of the water-repellent and self-cleaning lotus is reported in Fig. 6.8.

6.3.2. CA measurement

In Table 6.2, the mean values and standard deviation of nineteen CA measurements for each PS surface are reported.

6.3.3. Sliding measurements

The results of the first applied procedure for the determination of sliding angle show that PS surfaces have a sliding angle greater than 90° (no sliding). The exception is represented by the sample $4B_t$, showing a sliding angle of 48 ± 15.7 ° (Fig. 6.9). The sliding volume V_s and the sliding speed v_s for B_t surfaces were determined by means of the second procedure. The values of V_s and v_s were calculated from five measurements per each sample, see Fig. 6.10.

	S_a (µm)	S_q (µm)	S_p (µm)	S_v (µm)	S_z (µm)	S_{sk}	S_{dr} (%)
$1A_p$=$1A_t$	0.671±0.014	0.859±0.016	4.267±0.309	5.340±1.282	8.240±0.689	-0.274±0.012	5.583±0.104
$2A_p$=$2A_t$	0.753±0.049	0.970±0.060	4.697±0.926	6.027±0.195	8.967±0.320	-0.136±0.043	5.277±0.293
$3A_p$=$3A_t$	0.205±0.006	0.266±0.004	1.907±1.025	1.803±0.550	2.790±0.649	0.217±0.181	0.273±0.036
$4A_p$=$4A_t$	0.086±0.009	0.126±0.016	2.160±0.691	1.863±0.861	2.833±0.578	0.821±0.099	0.108±0.024
$5A_p$=$5A_t$	1.197±0.120	2.143±0.159	11.500±1.179	16.500±1.969	24.867±0.723	-2.523±0.483	11.003±1.731
$6A_p$=$6A_t$	0.120±0.018	0.156±0.025	1.201±0.309	0.896±0.196	1.530±0.399	0.138±0.124	0.060±0.022
$7A_t$	0.744±0.084	0.946±0.115	3.553±1.703	4.613±0.664	6.01±0.840	-0.444±0.178	0.486±0.093
$1B_p$=$8A_t$	1.730±0.095	2.203±0.125	12.963±5.797	13.927±6.907	21.300±3.863	-0.074±0.132	20.800±1.345
$2B_p$=$9A_t$	1.330±0.056	1.693±0.078	6.960±0.259	9.353±1.021	14.167±0.808	-0.144±0.159	14.500±0.794
$3B_p$=$10A_t$	0.921±0.009	1.187±0.011	4.403±0.195	6.657±0.447	10.080±0.470	-0.331±0.099	7.090±0.157
$4B_p$=$11A_t$	1.427±0.068	1.857±0.075	8.747±0.473	9.780±0.121	16.400±0.600	-0.383±0.187	12.967±0.929
$5B_p$=$12A_t$	0.939±0.030	1.213±0.035	5.627±1.137	6.733±1.259	10.473±1.040	-0.289±0.205	6.293±0.780
$6B_p$=$13A_t$	1.273±0.136	1.653±0.182	6.657±0.631	9.553±0.624	14.367±0.924	-0.396±0.110	11.663±1.807
$14A_t$	0.745±0.132	0.953±0.166	4.555±0.912	4.425±1.365	6.365±0.502	-0.171±0.064	0.617±0.057
$7A_p$	0.313±0.016	0.403±0.023	2.647±0.894	2.383±0.365	3.913±0.682	0.076±0.118	0.629±0.120
$7B_p$	1.427±0.176	1.867±0.244	20.757±17.423	11.333±0.751	24.767±11.829	-0.306±0.449	15.533±3.060

	S_a (µm)	S_q (µm)	S_p (µm)	S_v (µm)	S_z (µm)	S_{sk}	S_{dr} (%)
$1B_t$	0.841 ± 0.201	1.059 ± 0.240	3.443 ± 1.364	3.970 ± 0.260	5.827 ± 1.064	-0.276 ± 0.165	0.572 ± 0.220
$2B_t$	0.647 ± 0.078	0.827 ± 0.096	3.910 ± 1.230	4.187 ± 2.081	4.870 ± 0.348	-0.128 ± 0.161	0.373 ± 0.081
$3B_t$	0.675 ± 0.064	0.856 ± 0.071	2.660 ± 0.547	3.320 ± 0.333	5.147 ± 0.316	-0.242 ± 0.080	0.401 ± 0.020
$4B_t$	0.235 ± 0.011	0.298 ± 0.014	1.250 ± 0.089	1.590 ± 0.560	1.850 ± 0.062	0.265 ± 0.249	0.048 ± 0.0098
$5B_t$	0.359 ± 0.065	0.463 ± 0.088	2.020 ± 0.754	2.020 ± 0.372	2.837 ± 0.721	-0.326 ± 0.157	0.101 ± 0.030
$6B_t$	0.518 ± 0.047	0.644 ± 0.055	2.123 ± 0.320	2.553 ± 0.170	3.757 ± 0.399	-0.026 ± 0.012	0.228 ± 0.065
$7B_t$	0.602 ± 0.076	0.757 ± 0.099	2.917 ± 0.815	3.133 ± 0.743	4.413 ± 0.433	-0.095 ± 0.101	0.342 ± 0.090
$8B_t$	0.933 ± 0.905	1.180 ± 0.141	5.690 ± 0.212	4.460 ± 1.343	6.580 ± 0.877	-0.044 ± 0.106	0.724 ± 0.253
$9B_t$	0.528 ± 0.024	0.672 ± 0.021	2.335 ± 0.007	2.605 ± 0.672	4.130 ± 0.113	0.166 ± 0.094	0.261 ± 0.008
$10B_t$	0.384 ± 0.064	0.476 ± 0.081	2.815 ± 1.930	1.630 ± 0.198	2.695 ± 0.233	0.061 ± 0.002	0.103 ± 0.016
$11B_t$	0.545 ± 0.075	0.700 ± 0.110	2.485 ± 0.587	2.645 ± 0.601	4.610 ± 1.103	-0.023 ± 0.063	0.368 ± 0.170
$12B_t$	0.466 ± 0.057	0.588 ± 0.064	2.085 ± 0.049	2.295 ± 0.163	3.695 ± 0.092	-0.006 ± 0.099	0.214 ± 0.008
$13B_t$	0.113 ± 0.008	0.147 ± 0.001	0.739 ± 0.397	0.518 ± 0.001	0.955 ± 0.134	0.444 ± 0.668	0.018 ± 0.001
$14B_t$	0.616 ± 0.083	0.786 ± 0.121	3.010 ± 0.764	3.275 ± 0.870	4.605 ± 1.011	0.018 ± 0.274	0.336 ± 0.085

Table 6.1 Measured roughness parameters of PS surfaces. Note that samples $7A_p$ and $7B_p$ are used only to evaluate the effects of plasma treatment, while $7A_t$ and $14A_t$ are new starting samples for the determination of the effects of thermoforming treatment.

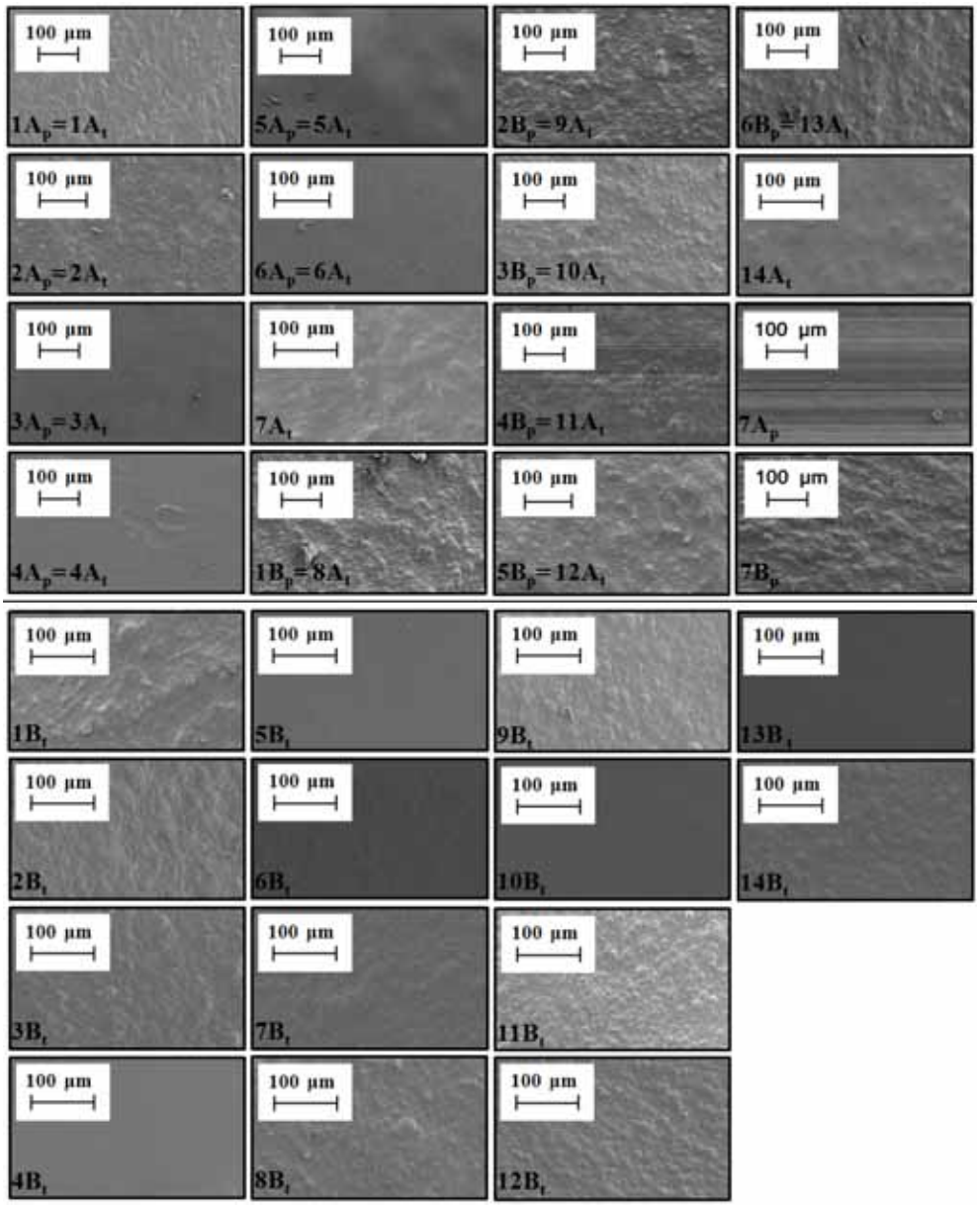

Fig. 6.1 FESEM microscopies of the tested PS surfaces.

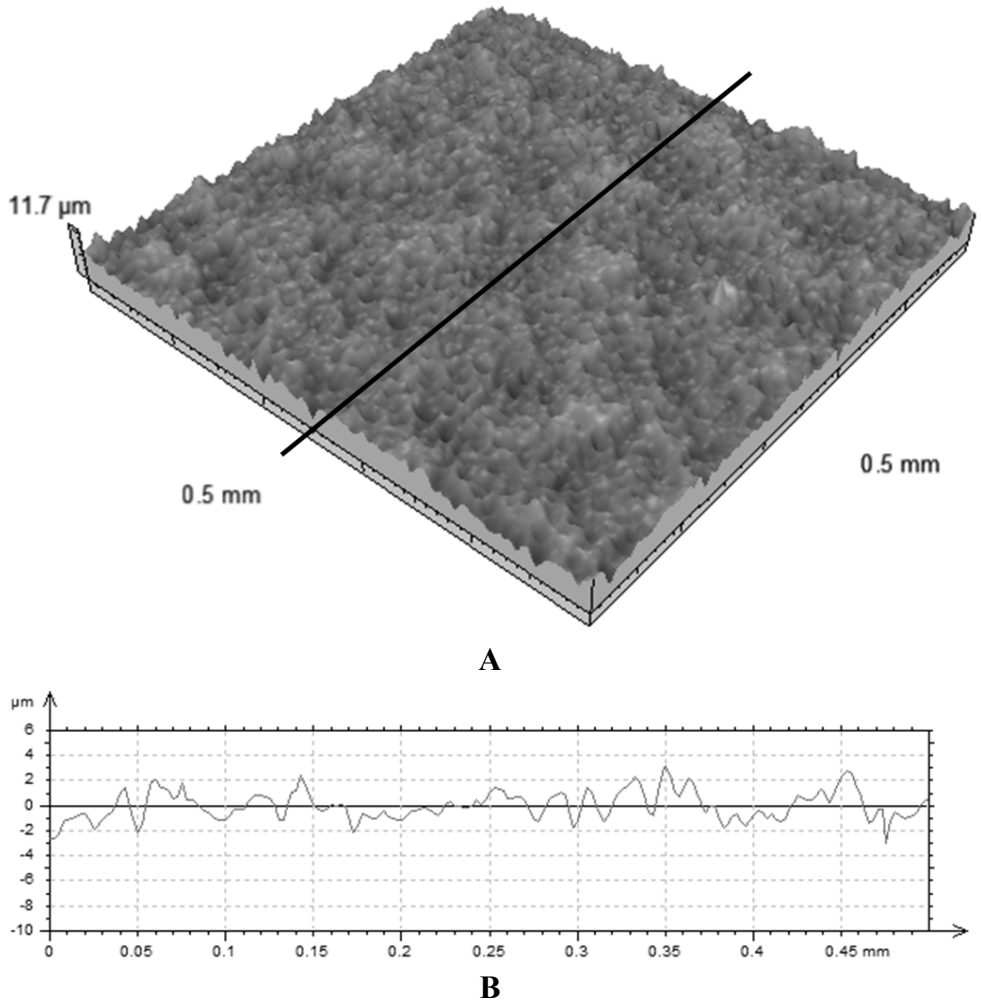

Fig. 6.2 Surface topography before plasma treatment. PS surface of sample $2A_p$, as representative of surface topography of samples $1A_p$ and $2A_p$. (A) 3D topography and (B) 2D profile (extracted at 50 mm from the edge of the square measured area).

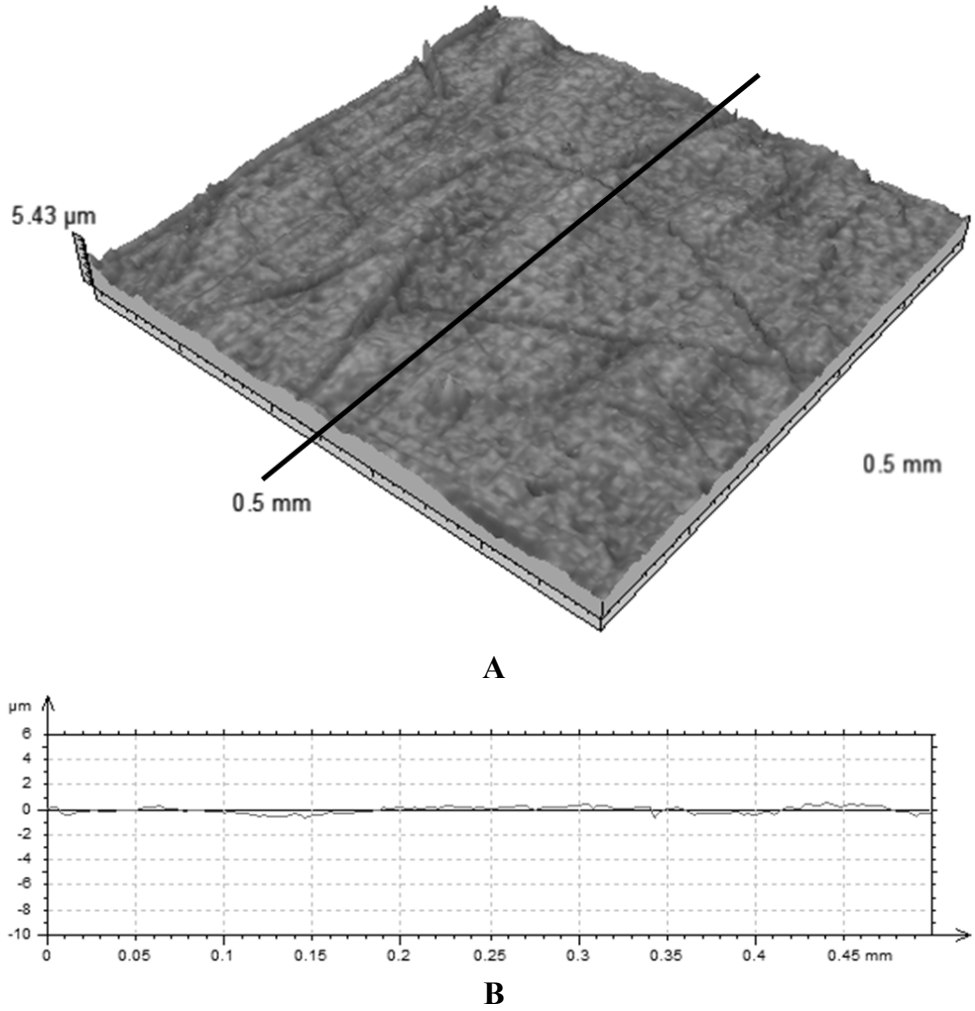

Fig. 6.3 Surface topography before plasma treatment. PS surface of sample $3A_p$, as representative of surface topography of sample $3A_p$, $4A_p$, $6A_p$ and $7A_p$. (A) 3D topography and (B) 2D profile (extracted at 50 mm from the edge of the square measured area).

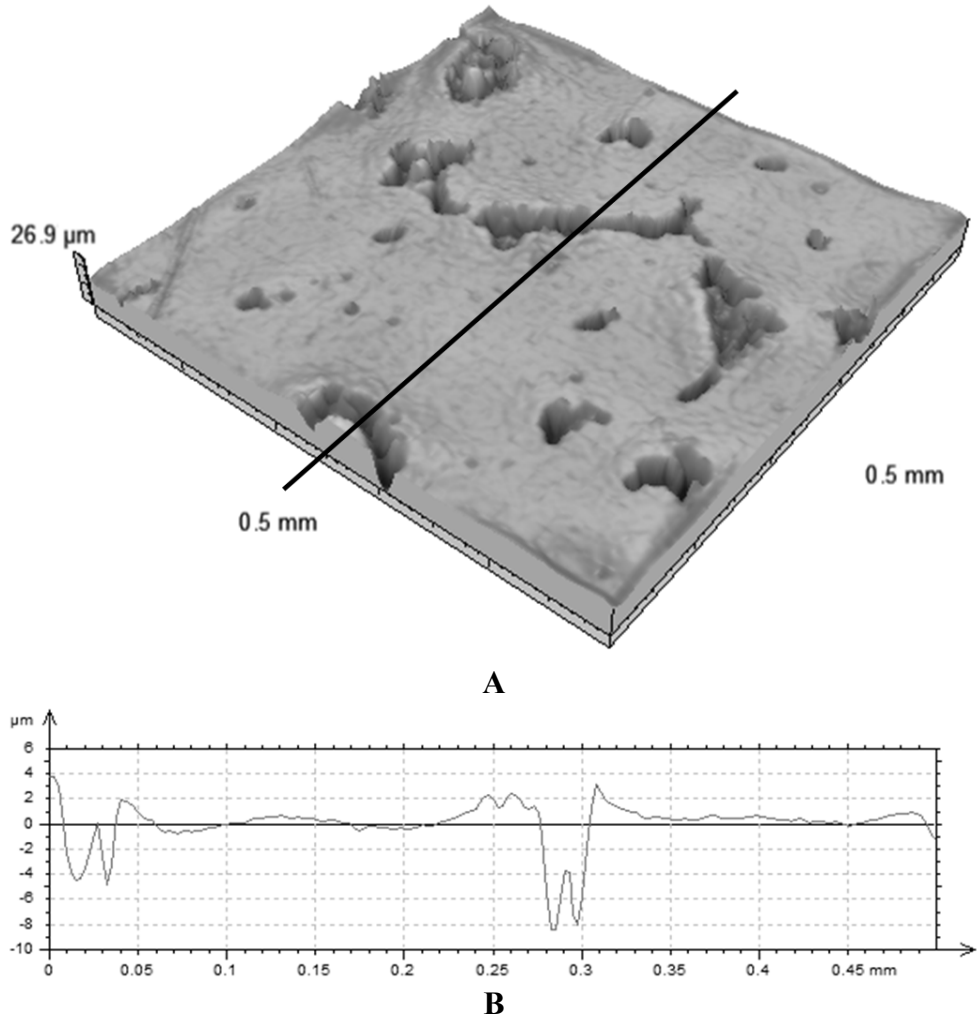

Fig. 6.4 Surface topography before plasma treatment. PS surface of sample $5A_p$. (A) 3D topography and (B) 2D profile (extracted at 50 mm from the edge of the square measured area).

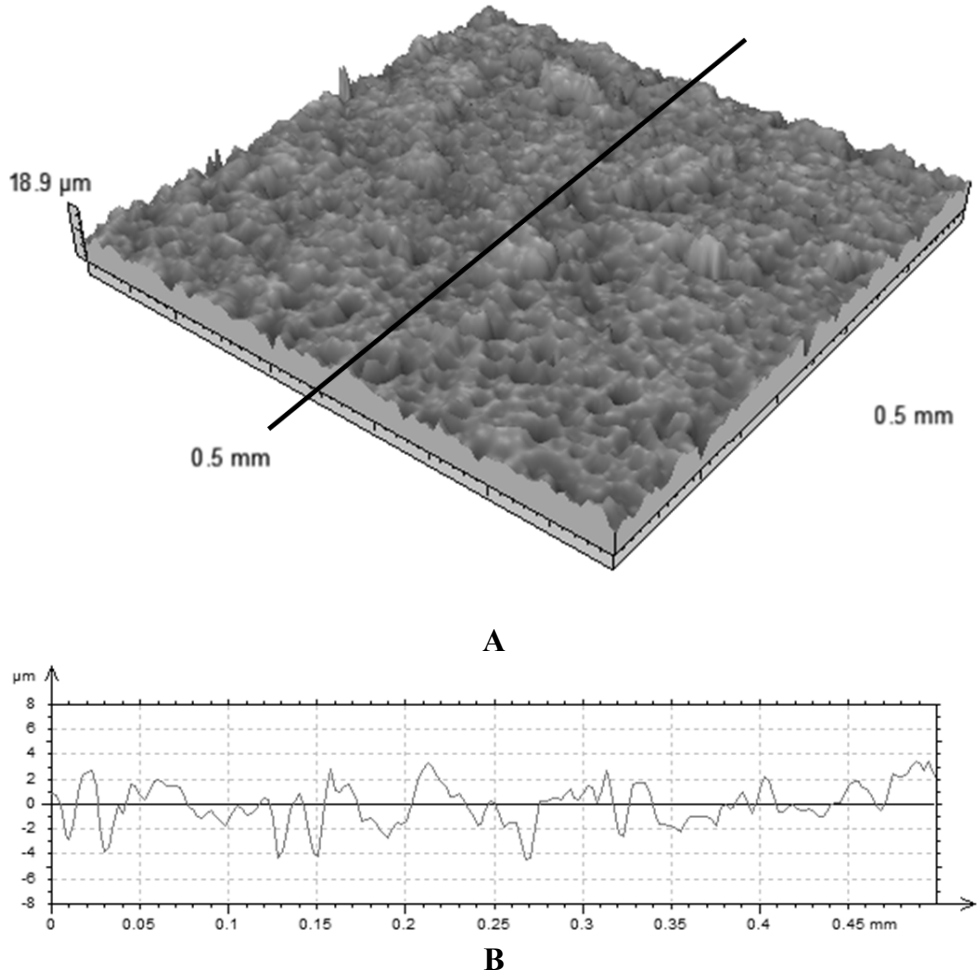

Fig. 6.5 Surface topography after plasma treatment. PS surface of sample $4B_p$, as representative of surface topography of plasma treated samples. (A) 3D topography and (B) 2D profile (extracted at 50 mm from the edge of the square measured area).

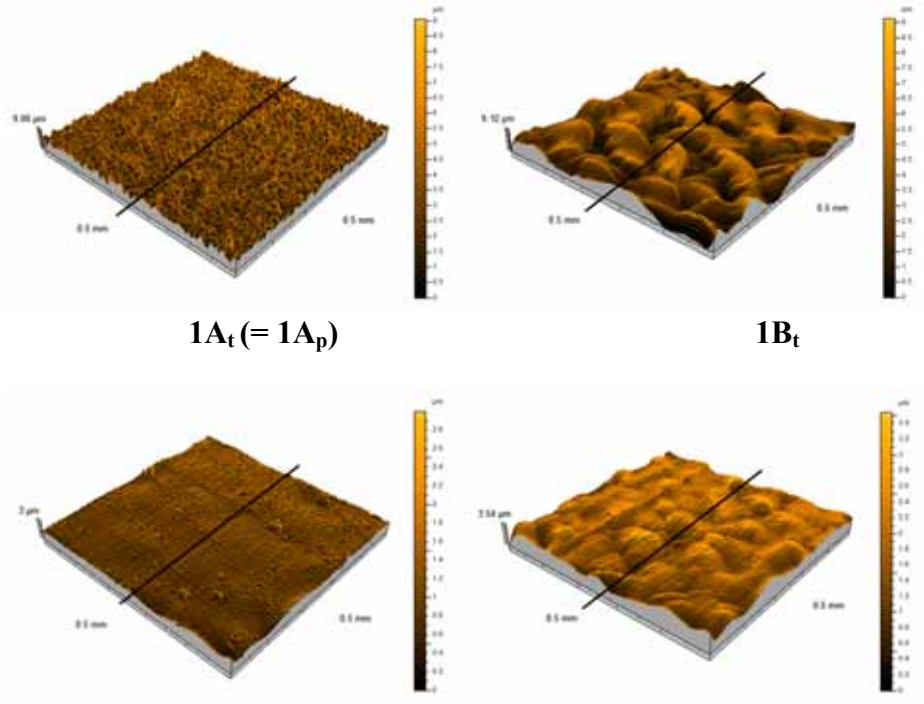

$1A_t$ (= $1A_p$) **$1B_t$**

$4A_t$ (= $4A_p$) **$4B_t$**

Fig. 6.6 3D PS surface topography of sample 1 (up) and 4 (down), before (left) and after (right) thermoforming treatment.

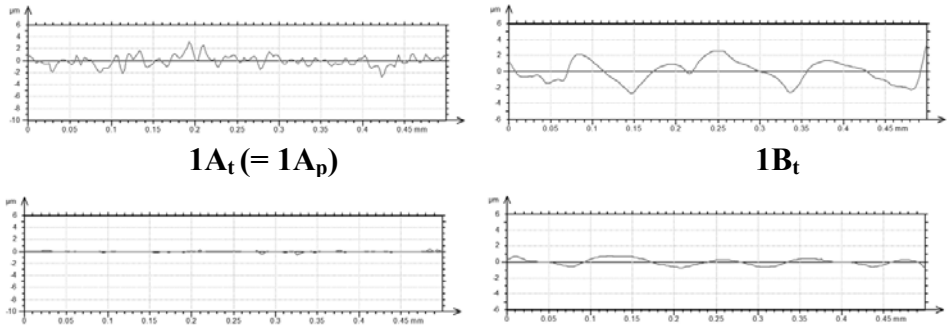

$1A_t$ (= $1A_p$) **$1B_t$**

$4A_t$ (= $4A_p$) **$4B_t$**

Fig. 6.7 2D PS profiles of sample 1 (up) and 4 (down), before (left) and after (right) thermoforming treatment. Each profile was extracted at 50 mm from the edge of the square measured area shown in Fig. 6.6.

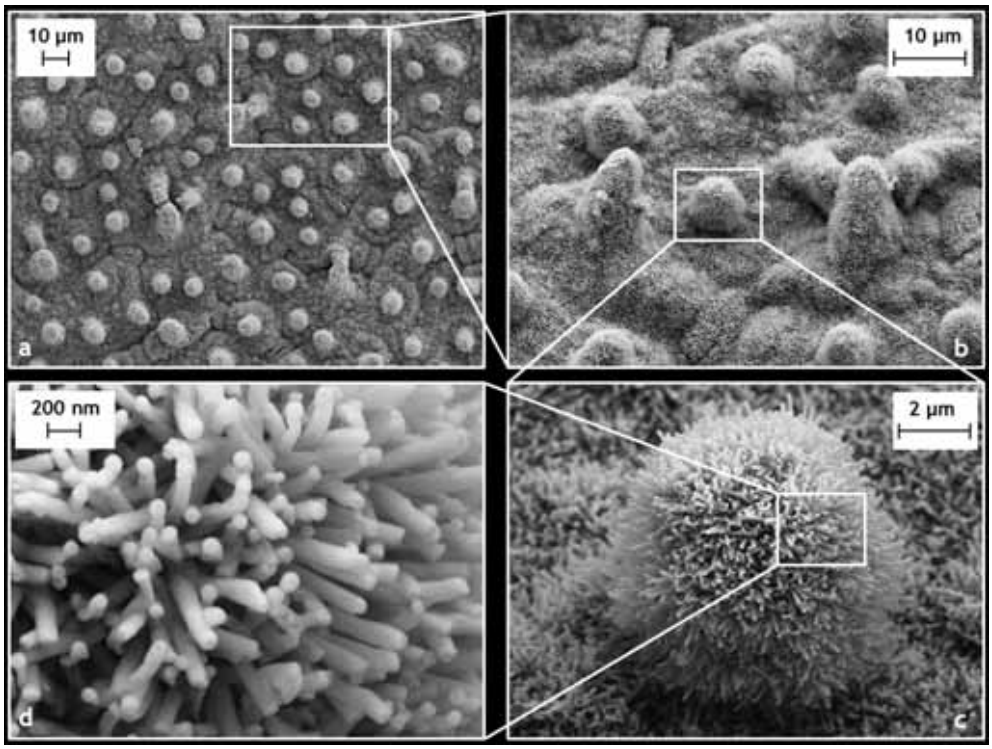

Fig. 6.8 FESEM microscopies of the lotus (*Nelumbo nucifera*) leaf: a natural 6-month dried adaxial leaf surface of lotus (a and b), the papillose cells (c) and the wax tubules (d).

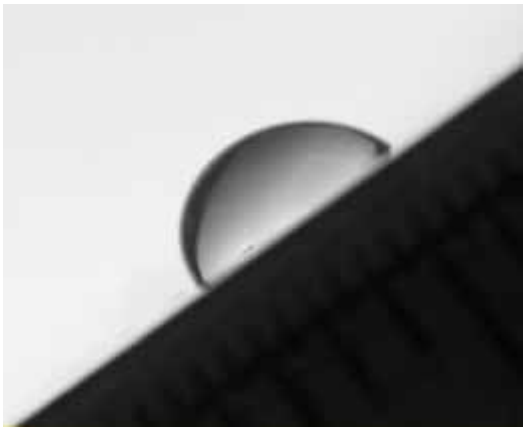

Fig. 6.9 Sample $4B_t$ at 36°, the sliding was observed at 48°.

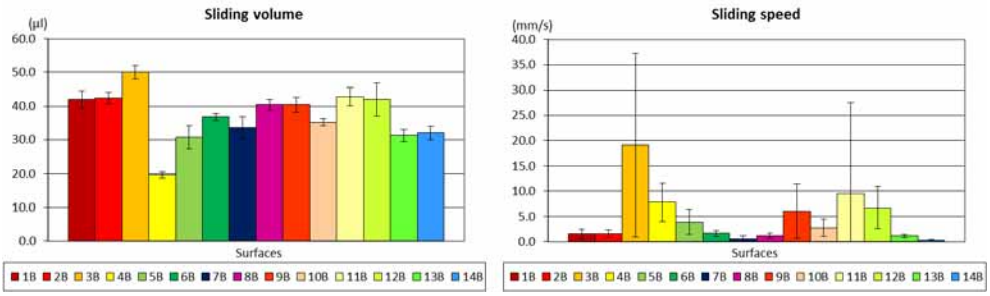

Fig. 6.10 Sliding volume or speed of B_t surfaces.

	CA (°)		CA (°)
$\mathbf{1A_p=1A_t}$	55 ± 3.2	$\mathbf{1B_t}$	93 ± 2.5
$\mathbf{2A_p=2A_t}$	80 ± 5.8	$\mathbf{2B_t}$	87 ± 3.7
$\mathbf{3A_p=3A_t}$	72 ± 6.7	$\mathbf{3B_t}$	81 ± 1.9
$\mathbf{4A_p=4A_t}$	78 ± 7.6	$\mathbf{4B_t}$	91 ± 4.2
$\mathbf{5A_p=5A_t}$	69 ± 4.0	$\mathbf{5B_t}$	82 ± 2.3
$\mathbf{6A_p=6A_t}$	88 ± 3.8	$\mathbf{6B_t}$	94 ± 2.8
$\mathbf{7A_t}$	89 ± 2.4	$\mathbf{7B_t}$	88 ± 3.2
$\mathbf{1B_p=8A_t}$	50 ± 6.7	$\mathbf{8B_t}$	82 ± 2.4
$\mathbf{2B_p=9A_t}$	84 ± 4.4	$\mathbf{9B_t}$	89 ± 3.0
$\mathbf{3B_p=10A_t}$	67 ± 3.3	$\mathbf{10B_t}$	85 ± 5.0
$\mathbf{4B_p=11A_t}$	50 ± 7.1	$\mathbf{11B_t}$	84 ± 2.8
$\mathbf{5B_p=12A_t}$	61 ± 6.1	$\mathbf{12B_t}$	78 ± 4.4
$\mathbf{6B_p=13A_t}$	87 ± 6.4	$\mathbf{13B_t}$	77 ± 5.3
$\mathbf{14A_t}$	81 ± 2.8	$\mathbf{14B_t}$	82 ± 1.9
$\mathbf{7A_p}$	78 ± 5.4		
$\mathbf{7B_p}$	83 ± 5.0		

Table 6.2 CA measurements of the tested PS surfaces.

6.4. Discussion

6.4.1. Plasma treatment

According to Wenzel $\cos\theta_A = r_{A.B} \cdot \cos\theta_B$, where $r_{A.B} = \frac{r_B}{r_A}$, r_A (1.0006 - 1.0558) and r_B (1.0629 - 1.2080) are the Wenzel roughness parameters (reported in Table 6.3), before or after the plasma treatment respectively, $\theta_{A,B}$ is the corresponding theoretical contact angle; thus, we could evaluate the effect of the plasma treatment by the increment of the superficial roughness. The comparison between theoretical predictions and experimental data is presented in Fig. 6.11.
According to the FESEM microscopies reported in Fig. 6.1, the plasma treatment increases the surface roughness. It is necessary to consider sample $5A_p$ separately, since it presents a specific initial (untreated, Fig. 6.4) situation showing several distributed valleys with greater depth than in other samples, thus implying the greatest value of the S_{dr} parameter (11 %); after plasma treatment, the S_{dr} parameter is of the same order of magnitude as for the other samples (see Table 6.1). The plasma treatment levels the surface with deep valleys, as we can see in sample 5, and by surface erosion eliminates the presence of excessive high peaks. Except for sample 5, the plasma treatment increases the roughness parameters (see S_a, S_q, S_p, S_v, S_z in Table 6.1) leading to more valleys than peaks (negative value of S_{sk}) with a greater effective area than the untreated surfaces (greater value of S_{dr}). Apart from samples $2A_p$ and $7A_p$, we observed a decrement of CA as expected from the Wenzel theory for an intrinsically hydrophilic material subjected to an increment of roughness. Thus plasma treatment is ideal for increasing the PS surface wettability.

	$1A_p$	$2A_p$	$3A_p$	$4A_p$	$5A_p$	$6A_p$	$7A_p$
r_A	1.0558	1.0528	1.0027	1.0011	1.1100	1.0006	1.0063

	$1B_p$	$2B_p$	$3B_p$	$4B_p$	$5B_p$	$6B_p$	$7B_p$
r_B	1.2080	1.1450	1.0709	1.1297	1.0629	1.1166	1.1553

Table 6.3 Wenzel roughness parameters *r* of PS surfaces.

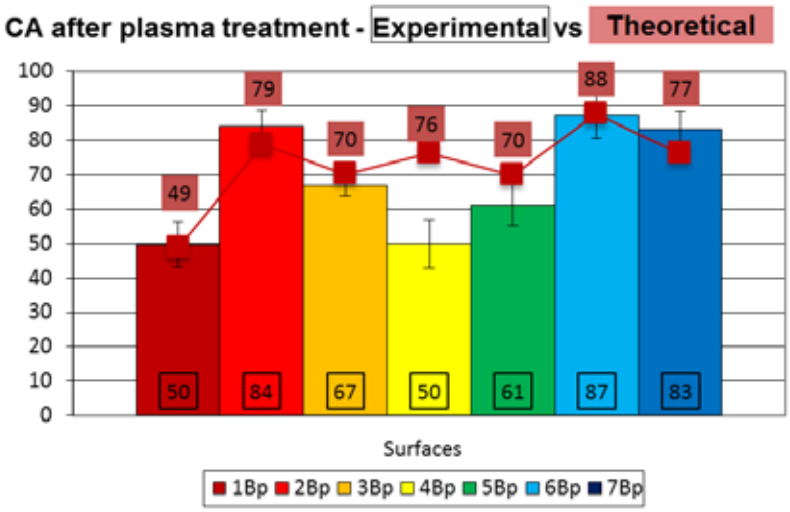

Fig. 6.11 Experimental measurements vs. theoretical predictions of CA for samples after plasma treatment.

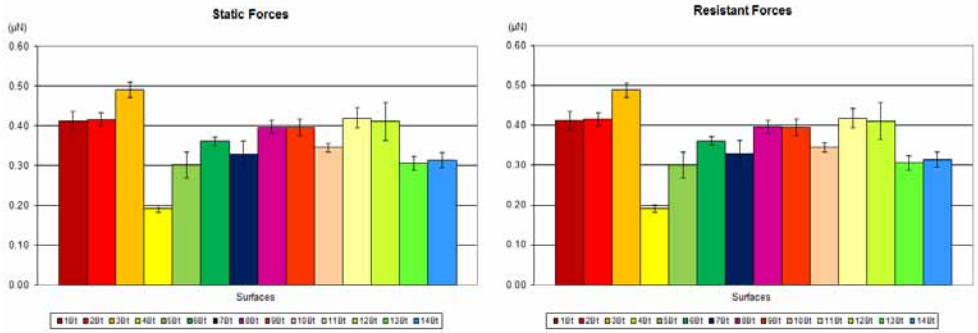

Fig. 6.12 Static and resistant forces on B_t surfaces.

6.4.2. Thermoforming treatment: adhesive static and resistant forces

Considering the roughness parameters reported in Table 6.1 and the profilometer 3D-images of Fig. 6.6, we could observe that the thermoforming treatment globally decreases the roughness parameters (see S_a, S_q, S_p, S_v, S_z in Table 6.1). Referring to the S_{dr} parameter close to 0 %, we can say that the thermoforming treatment renders the surfaces smoother. Apart from samples $13A_t$, we observed an increment of the CA as expected from the Wenzel theory for an intrinsically hydrophilic material subjected to a decrement of the roughness. Finally, we calculate the static and the resistant forces of sliding drops for B_t vertical (at 90°) surfaces and on a natural 6-month dried lotus leaf for comparison. The complete measured wettability parameters of lotus leaf are summarized in Table 6.4.
The static force (F_S) was computed as follows:

$$F_S = m \cdot g = V \cdot \rho_0 \cdot g \tag{1}$$

where V is the drop sliding volume, ρ_0 is the water density and g is the gravity acceleration. The resistant force (F_R) was obtained, assuming a resistant force during sliding on PS proportional to the low velocity observed, as:

$$F_R = F_S \cdot \left(1 - \frac{F_{RL}}{F_S}\frac{v}{v_{oL}}\right) \tag{2}$$

where F_S is the static force of the surface, F_{RL} and v_{oL} are the resistant force (0.032 ± 0.009 μN) and the sliding speed (233 ± 25.82 mm/s) for the lotus leaf, respectively, and v is the sliding speed of the surface. The resistant force of the lotus leaf was computed as proportional to the velocity square, due to the high velocity observed:

$$F_{RL} = \frac{1}{2} \cdot \rho_0 \cdot v_{oL}^2 \cdot A_r \cdot C_p \tag{3}$$

where A_r is the resistant area (2.32 ± 0.327 mm^2) and C_p is drag coefficient (equal to ~0.47 since the shape of the sliding drop is nearly a sphere),

finding $F_{RL} \approx 0.03$ μN. The resistance forces are found to be negligible, thus static and resistant force are nearly identical (Fig. 6.12).

	Lotus (*Nelumbo nucifera*)
CA (°)	153.4 ± 3.28
TA (°)	26.2 ± 3.64
SV (μl)	4.7 ± 1.15
SS (mm/s)	233.3 ± 25.82
Static force (μN)	0.043 ± 0.008
Resistant force (μN)	0.032 ± 0.009

Table 6.4 Contact angle, sliding angle, sliding volume and sliding speed of a natural 6-month dried adaxial leaf surface of lotus.

6.5. Conclusions

In this paper the effects of plasma and thermoforming treatments on the water sliding behaviour have been studied on fourteen different PS surfaces, in terms of contact angle, sliding angle, sliding volume, sliding speed, and static and resistant forces acting on the sliding drop. We compared the experimental results with those on a natural 6-month dried lotus leaf. A significant correlation between technological treatment, surface roughness parameters and wetting measurements clearly emerges. Thus, the analysis suggests that plasma/thermoforming are ideal treatments to tune the wettability and enhance the hydrophilic/hydrophobic behaviour of PS surfaces.

ACKNOWLEDGMENTS

The authors would like to thank M. Biasotto of the Department of Special Surgery and B. Codan of the Division of Dental Sciences and Biomaterials of the Department of Biomedicine at the University of Trieste for their help in using the surface profilometer. The authors wish to sincerely thank A. Chiodoni, Physical Department, Politecnico di Torino for the fundamental help performing the FESEM micrographs of A_p, B_p and A_t samples and lotus

leaf. The authors thank James Vanzo for the final English grammar supervision. NMP is supported by "Metrology on a cellular and macromolecular scale for regenerative medicine" - Metregen (2009-2012).

REFERENCES

[1] Barthlott, W., *Nord. J. Bot.* **1**, 345-55 (1981).
[2] Neinhuis, C., and Barthlott, W., *Ann. Bot.* **79**, 667-677 (1997).
[3] Barthlott, W., and Neinhuis, C., *Planta* **202**, 1-8 (1997).
[4] Herminghaus, S., *Europhysics Letters* **52**, 165-170 (2000).
[5] Wagner, P., Furstner, R., Barthlott, W., and Neinhuis, C., *J. Exp. Bot.* **385**, 1295-1303 (2003).
[6] Nosonovsky, M., and Bhushan, B., *Microsyst. Technol.* **11**, 535-549 (2005).
[7] Lu-quan, R., Shu-jie, W., Xi-mei, T., Zhi-wu, H., Lin-na, Y., and Zhao-mei, Q., *J. Bionic. Eng.* **4**, 33-40 (2007).
[8] Otten, A., and Herminghaus, S., *Langmuir* **20**, 2405-8 (2004).
[9] Zhiqing, Y., Hong, C., Jianxin, T., Huifang, G., Yuejun, L., Zhengxiang, W., Pu, S., Jide, Z., and Xin, C., J. Phys. D Appl. Phys. **40**, 3485-3489 (2007).
[10] Brushan, B., and Jung, Y. C., *J. Phys. Condens. Matt.* **20**, 225010 (24pp) (2008).
[11] Solga, A., Cerman, Z., Striffler, B. F., Spaeth, M., and Barthlott, W., *Bioinsp. Biomim.* **2**, 126-134 (2007).
[12] Young, T., *Phil. Trans. R. Soc.* **95**, 65-87 (1805).
[13] Wenzel, R.N., *Ind. Eng. Chem.* **28**, 988-94 (1936).
[14] Cassie, A. B. D., and Baxter, S., *Trans. Faraday Soc.* **40**, 546-51 (1944).
[15] Pugno, N. M., *J. Phys.: Condens. Matter* **19**, 395001 (17pp) (2007).
[16] Pugno NM. The Nanomechanics in Italy, Research signpost (IND) (2007).
[17] Bosia, F., Pugno, N., and Buehler, M., *Phys. Rev. E* **82**, 056103 (7pp) (2010).
[18] Bignardi, C., Petraroli, M., and Pugno, N., *J. Nanosci. Nanotechnol.* **10**, 6453-6460 (2010).
[19] Pugno, N., *Nanotechnology* **17**, 5480-5484 (2006).
[20] Pugno, N., and Carpinteri, A., *Phil. Mag. Lett.* **88**, 397-405 (2008).
[21] Pugno, N., Bosia, F., and Carpinteri, A., *Small* **4**, 1044-1052 (2008).

[22] Burton, Z., and Bhushan, B., *Nano Lett* **5**, 1607-13 (2005).
[23] Bhushan, B., and Jung, Y. C., *Ultramicroscopy* **107**, 1033-41 (2007).
[24] Bhushan, B., Nosonovsky, M., and Jung, Y. C., *J. R. Soc. Interface* **4**, 643-8 (2007).
[25] Jung, Y.C., and Bhushan, B., *Nanotechnology* **17**, 4970-80 (2007).
[26] Jung, Y. C., and Bhushan, B., *Scr. Mater.* **57**, 1057-60 (2007).
[27] Nosonovsky, M., and Bhushan, B., *Microsyst. Technol.* **12**, 273-81 (2006).
[28] Nosonovsky, M., and Bhushan, B., *Microelectron. Eng.* **84**, 382-6 (2007).
[29] Shibuichi, S., Onda, T., Satoh, N., and Tsujii, K., *J. Phys. Chem.* **100**, 19512-7 (1996).
[30] Hozumi, A., and Takai, O., *Thin Solid Films* **334**, 54-59 (1998).
[31] Miwa, M., Nakajima, A., Fujishima, A., Hashimoto, K., and Watanabe, T., *Langmuir* **16**, 5754-60 (2000).
[32] Oner, D., and McCarthy, T. J., *Langmuir* **16**, 7777-7782 (2000).
[33] Lau, K. K. S., Bico, J., Teo, K. B. K., Chhowalla, M., Amaratunga, G. A. J., Milne, W. L., McKinley, G. H., and Gleason K. K., *Nano Lett* **3**, 1701-5 (2003).
[34] Quéré, D., *Nat. Mater.* **1**, 14-5 (2002).
[35] Noeske, M., Degenhardt, J., Strudhoff, S., and Lommattzsch, U., *Int. J. Adhes. Adhes.* **2**, 171-177 (2004).
[36] Valeri, S., Paradisi, P., Luches, P., and Bona, A., *Thin Solid Films* **352**, 114-118 (1999).
[37] Bellucci, S., Bergamaschi, A., Bottini, M., Magrini, A., and Mustelin, T., *J. Phys.* **61**, 95-98 (2007).
[38] Lepore, E., Antoniolli, F., Buono, M., Brianza, S., Carpinteri, A., and Pugno N., *J. Nanomat.* **194524** (5 pp) (2008).
[39] Pugno, N. M., and Lepore, E., *J. Adhesion* **84**, 949-962 (2008).
[40] Pugno, N. M., and Lepore, E., *Biosystems* **94**, 218-222 (2008).
[41] Adamson, A. V., Wiley, NY (1990).
[42] Israelachvili, J. N., In: 2nd edn. Academic press, London (1992).
[43] Brushan, B., Principles and applications of tribology. Wiley, NY (1999).
[44] Brushan, B., Introduction to tribology. Wiley, NY (2002).

7. A SUPERHYDROPHOBIC POLYSTYRENE BY REPLICATING THE NATURAL LOTUS LEAF

Abstract

In this paper, we report the realization of an artificial biomimetic superhydrophobic polystyrene (PS) surface by direct copy of a natural lotus leaf, using a simple template method at room temperature and atmospheric pressure. We characterized the water sliding behaviour by measuring the contact angle (CA), sliding angle, sliding volume and sliding speed (SS) of the lotus leaf (CA = 153.4°, SS = 319.4 mm/s), copied lotus leaf, negative silicone template, flat silicone and PS control surfaces and final PS artificial leaf (CA = 149.0°, SS = 416.7 mm/s); the last one displays properties comparable with those of lotus. This template method needs neither expensive instruments nor complicated chemical treatments. An adequate optimization of this molding process into automated industrial procedures will lead to a new, innovative, cheap concept for the large-scale industrial development of superhydrophobic surfaces, also starting from their intrinsically hydrophilic counterparts, as here demonstrated for PS.

7.1. Introduction

The ability of some natural leaves to stay un-wetted (superhydrophobic) and dirt-free (self-cleaning) came to be evident more than 2,000 years ago; however, only in the twentieth century scientists studied these two correlated phenomena on some natural leaves, focusing on their natural morphologies [1-3] correlated with surface roughness [4-13], surface adhesion [14-16], friction [17] and self-cleaning [18]. The most famous is lotus (*Nelumbo nucifera*), on which "raindrops take a clear, spherical shape without spreading, which probably has to be ascribed to some kind of evaporated essence", as yet Goethe described in 1817 [19]. Superhydrophobicity and self-cleaning are said to be correlated but this correlation do not always appear in nature. For example, the water ferns of *Salvinia* reveal trichomes and waxes, as surface micro- and nano-structures,

which lead to a superhydrophobic property of the surface even if the self-cleaning is absent [13].
After a good comprehension of these underlying properties from nature, the next step was to implement them man-made technology: this process is well-known as biomimicry, from the Greek word *biomimesis* which means mimic life. As a matter of fact, micro-, nano- and micro/nano-patterned superhydrophobic surfaces have become one of the most popular research topics in engineering [20, 21]. Due to the superhydrophobicity and self-cleaning characteristics of its surfaces, the natural lotus leaf has been intensively bio-mimed [20, 22-24] and a number of methods have been applied to fabricate such artificial surfaces mimicking the natural morphology: by the fabrication of nano- (micro-) protrusion by reactive ion etching [20], creating structured coatings similar to the lotus leaves from polyelectrolyte multilayer films [25], making a nickel mold *via* electroforming and UV-nanoimprint lithography [24, 26, 27]; by adding ethanol to PS solution [28], producing Poly(dimethyl siloxane) (PDMS) replica molding with photolithographically manufactured micro-patterned masters [29], nano-casting PDMS [22]; by soft-lithography method of Poly(methyl meth-acrylate) (PMMA) replica using PDMS molds [30], developing the dental wax cast technique [31] of a replica with polyether (PE) [23], Poly(vinyl siloxane) [32], conventional lacquer [5], epoxy resin [33, 34], the artificial surface patterning [35-45], the chemical surface modification [46-48] or a combination of both morphological and chemical modifications [49-51]. On the contrary, only six patents for invention, with "self cleaning super hydrophobic" as keywords, have been duly deposited during the last 6 years at the European Patent Office, thus with a current rate of one European patent per year.
From the literature, the superhydrophobic and self-cleaning properties have been evaluated only by the measurement of the contact angle (CA) and the contact angle hysteresis (CAH), which can be more easily quantified by the tilting angle (TA) [17, 22, 28, 29]. By definition, a high CA and low CAH (or TA) denote a superhydrophobic and self-cleaning surface [13, 17, 22, 27]. However, it was highlighted that a more, than the maximum CA, important parameter to determine when a surface is superhydrophobic is TA, due to its correlation with the driving force of a liquid drop [9]. In a previously published work of our group [52], we introduce other two parameters - the sliding volume (SV) and the sliding speed (SS) - as additional indexes of the superhydrophobicity and self-cleaning property of a surface; this was motivated by the fact that SV and SS are straightforward

and direct measurements of the surface water-repellency and self-cleaning ability, in both a static and dynamic regimes. Moreover, we have defined the drop minimum volume and the corresponding sliding speed with respect to a vertical surface very close to the real condition of use (*i.e.*, glass windows, external building coverings, internal faces of refrigerators or freezers, surfaces of bathroom fittings or tiles, etc.). A high CA, low CAH (or TA), low SV and high SS denote a superhydrophobic and self-cleaning surface.
Referring to previously published scientific works on lotus leaf, only few papers deal with the replication of its surface structures (convex cell papillae but not 3D wax crystals) by molding [22, 24, 26, 27], such as the present study.
In this study, we readily obtained a biomimetic lotus-leaf-like polystyrene (PS) superhydrophobic surface by replicating the morphological surface pattern of a natural lotus leaf. The molding method used in this study is similar to that reported in previously published works [9, 22] but, to our knowledge, our method is the first capable of creating a superhydrophobic lotus-leaf-like PS surface using a template method at room temperature and atmospheric pressure (no controlled temperature/vacuum condition was necessary). We elaborate on the definition of what is a superhydrophobic and self-cleaning surface, taking into account not only the classical parameters (CA and TA), but also the SV and SS parameters of a drop rolling down, for a more complete surface characterization of the lotus leaf, copied lotus leaf, negative silicone template, flat silicone and PS control surfaces, as well as positive PS template. Compared with the other above-mentioned methods, our molding technique needs neither expensive instruments nor complicated chemical treatments and is thus a good candidate for industrial applications.

7.2. Materials and methods

7.2.1 Molding method

Upper leaf sides (adaxial) of freshly lotus plant, cultivated in the “Giardino Botanico Rea” (Turin) associated with the Natural Science Museum of Turin, were used. These leaves (diameter of ~25 cm) are cut and the first copy (C1) deposition was made within 24 h. Fig. 7.1 reported the simple

flowchart of the lotus leaf replication process composed by two steps at room temperature and atmospheric pressure.

The molding method uses a silicone elastomer (R39-2186-2, Nusil Technology), a low viscosity hydrophobic silicone, to obtain the first copy C1 (diameter of ~25 cm) of a natural lotus leaf used as the natural template (LL). The lotus leaf resulted after the copying process is named copied lotus leaf (CLL). R39-2186-2 is a two-phase silicone, mixed in the mass proportion of 1:1, when extracted from side-by-side kits through a disposable static mix tip. Both components are extruded directly onto the lotus leaf and immediately spread with a stick to form a few millimetres high silicone layer on the substratum. After polymerization, the negative mold can be easily peeled off from the surface, giving rise to C1. Without any other intermediate treatment, C1 was directly used for preparation of the positive mold, called C2. Need to say, the low viscosity of the silicone R39-2186-2 does not require any pressure to replicate the smaller structures on the leaves, contrary to the molding methods already described in the literature [24, 26, 27, 53].

A commercial hydrophilic PS sheet was reduced into small particles without any further treatment. A volume of 20 ml tetrahydrofuran solvent was added to 1 g of PS and then the solution was stirred with a magnetic stirrer (Are - Velp) for 20 min with an increasing speed (5 min at 600 rpm, 5 min at 720 rpm and 10 min at 840 rpm) to form a uniform solution at room temperature and pressure. The solution was directly cast on a 9-cm diameter subarea of the negative silicone template (C1). After solvent volatilization for 24 h in the atmosphere at room temperature, a double adhesive was applied on a rigid substratum, the PS positive template (C2) was attached on the double adhesive and then the silicone negative template was peeled off from the C2 positive one (diameter of ~9 cm). As a result, the surface micro-structure of the lotus leaf was transferred to the PS surface on the side contacting with the silicone.

Two control surfaces have been necessarily characterized to establish the reference intrinsic parameters for comparing between C1 and C2: R39-2186-2 silicone or the PS/20ml-tetrahydrofuran solution was cast on a cleaned silicon wafer in 100 % ethanol and sonicated and, after 24 h polimerization (volatilization), we obtained flat silicone or PS surfaces, called C1_control or C2_control.

7.2.2. Surface characterization

We observed the surfaces of LL, CLL, C1 and C2 by means of a field emission scanning electron microscope (FESEM, Zeiss SUPRA 40 for LL and CLL or FEI-Inspect^{TM} F50 for C1 and C2) equipped with a field emission tungsten cathode. Samples of ~0.5 cm^2 were obtained, fixed to aluminium stubs by double-sided adhesive carbon conductive tape (Nisshin EM Co. Ltd.), used as these were (except for C1, cleaned with ethanol) and air-dried. Samples LL and CLL (C1 and C2) were Cr(Au-Pd) coated, approximately 10 nm in thickness. Referring to LL and CLL, no fixation processes were made to avoid alteration of the wax crystals [2].

7.2.3. Wettability measurement

The wettability of LL, CLL, C1, C1_control, C2, C2_control surfaces was determined by measuring the static CA of distilled water droplets over the samples, fixed to a horizontal plane by a soft adhesive to keep the samples flat. We consider a series of 20 (five of them were considered in [20, 29, 52]) random volume drops, gently deposited on the LL and CLL (C1, C1_control, C2, C2_control) with a standard single-use syringe. The contact angle was recorded with an OLYMPUS MJU 1010 digital photocamera, measured and statistically analysed with the software ImageJ 1.41o. The average CA of the control surfaces was used as the intrinsic CAs of the R39-2186-2 and PS flat surfaces.
Two conceptually distinct procedures were used to evaluate the drop sliding characteristics: (1) fixing the volume of the drop (~18 μl, the diameter of the spherical droplet was ~2.2 mm) and measuring the tilted angle of the sample stage at drop sliding (TA) or (2) fixing the angle of the specimen stage vertically (90°) and measuring the minimum SV of the drop, increasing it step-by-step with 2 μl volume increment. Referring to the second procedure, the sliding speed (SS) of the drop was also determined, measuring the time of the minimum SV drop to cover the fixed distance of 10 mm. Fig. 7.2 schematically shows the step-by-step process to determine the two additional parameters, SV and SS.

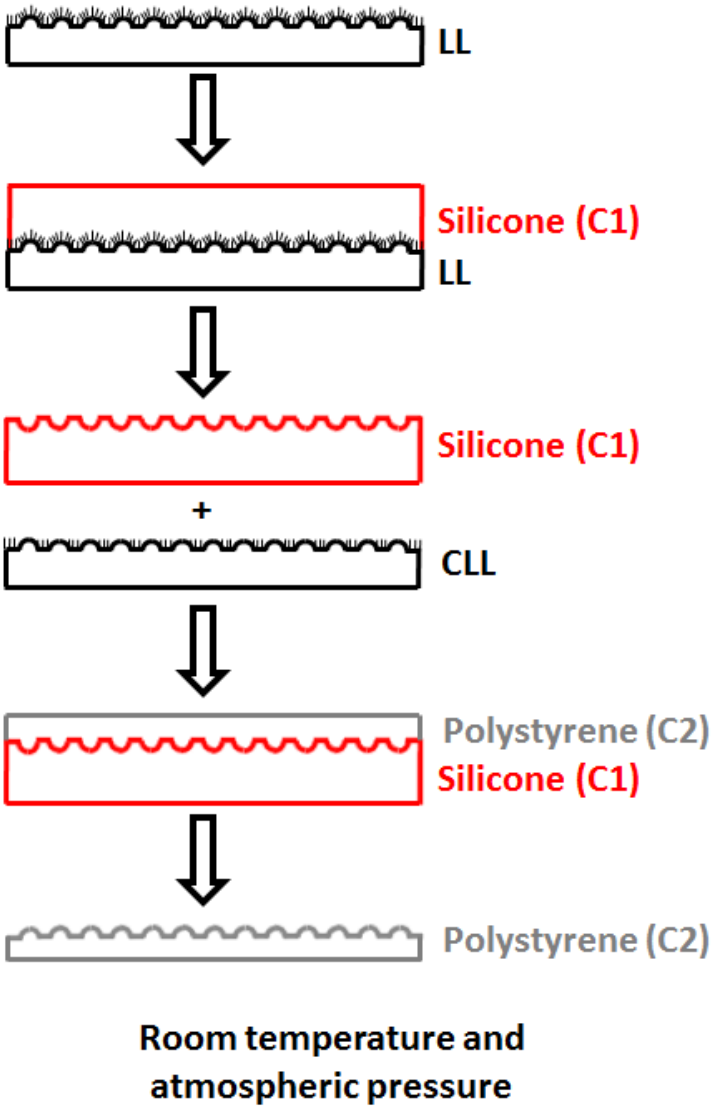

Fig. 7.1 Schematic illustration of our lotus leaf replication process, composed of two steps at room temperature and atmospheric pressure.

7.3. Results

7.3.1. Surface characterization

This technique demonstrates excellent replication ability for convex micro-structures (cell papillae) of the lotus leaf and the replication quality of these micro-structures from LL to C1 and in turn to C2 appears to be high. As shown in Fig. 7.3 (with the lack of 200-nm-scale bar micrographies for C1 and C2), the nano-tubules (superimposed layer of hydrophobic 3D wax tubules) of the lotus leaf have not been transferred, owing to their permanent removal during the C1 deposition which rules out the possibility of the nano-tubules replication, as reported in other previously published studies [5, 23, 24, 26, 27, 30, 53].

7.3.2. Wettability measurement

In Table 7.1, the mean values and standard deviation of wettability measurements are reported; correspondingly, Fig. 7.3 shows a representative water drop on each surface. The first remarkable result concerns the same CA (~150°) for LL and CLL in spite of the absence of wax nano-tubules over the cell papillae of CLL. When compared to the flat C1_control surface (~100°, intrinsically hydrophobic) and C2_control surface (~85°, intrinsically hydrophilic), the water CAs of corresponding replicas are increased by about 24° (C1 ~ 124°) and 64° (C2 ~ 149°). This finding indicates that the CA of C2 is absolutely comparable with LL, suggesting an excellent CA replication. The C2_control surface of PS has an intrinsic CA closed to the values found in literature (~92° [17], ~98° [28]), while C2 has a CA significantly higher of 45° than that (~105°) reported in [17]. Meanwhile, referring to a PE based (intrinsic CA = 102.9° ± 4.5) molding method, the CA for C2 could be comparable with those of the PE lotus replica (CA = 157.8° ± 4.2) [23].
The best (so lowest) TA belongs to CLL, 10° lower than the value recorded for LL. The silicone samples, both flat and micro-structured, display a high TA (~74° and ~81°, respectively) and an intermediate value of ~50° was measured by C2_control. The SV is similar among LL (~5 µl) and CLL (~6 µl) surfaces while increases to ~20 µl for the others. The worst result belongs to C2 (TA not observed, thus > 90°).

In spite of this, the SS highlights the goodness of the result obtained for C2, comparable with those of the surfaces LL and CLL. The SS values of C2_control, C1 and C1_control are three, two and one order of magnitude lower than those of C2, LL and CLL.

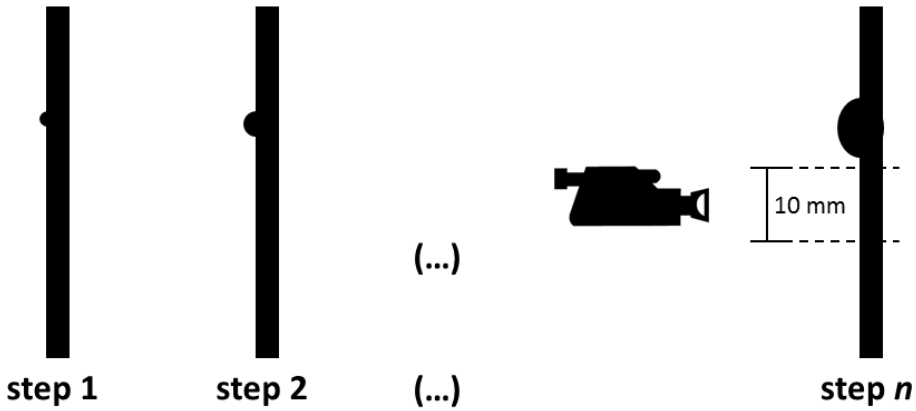

Fig. 7.2 The step-by-step process to determine the two additional parameters, SV and SS. The specimen stage is fixed vertically (90°) and the drop volume has been increased with 2-µl droplet at each step, from 2-µl up to the minimum sliding volume (SV) of the drop, which is necessary to cause the sliding of the drop (final step, *n*). At this instant, the drop starts to slide and the sliding speed (SS) was determined measuring the time to cover the fixed distance of 10 mm (mean velocity).

	CA (°)	TA (°)	SV (µl)	SS (mm/s)
LL	153.4 ± 3.28	26.2 ± 3.64	4.7 ± 1.15	319.4 ± 97.42
CLL	150.5 ± 3.70	18.0 ± 1.52	6.3 ± 0.82	319.4 ± 97.42
C1	124.2 ± 1.78	80.7 ± 1.32	19.3 ± 0.77	9.7 ± 2.95
C1_control	99.7 ± 2.27	73.9 ± 4.21	21.7 ± 3.44	15.7 ± 12.27
C2	149.0 ± 3.78	> 90°	23.0 ± 1.10	416.7 ± 91.29
C2_control	85.1 ± 2.60	48.6 ± 3.30	20.0 ± 0.00	0.1 ± 0.08

Table 7.1 Contact angle (CA), tilting angle (TA), sliding volume (SV) and sliding speed (SS) of lotus leaf (LL), copied lotus leaf (CLL), first silicone copy (C1), flat silicone control surface (C1_control), second PS copy (C2) and flat PS control surface (C2_control).

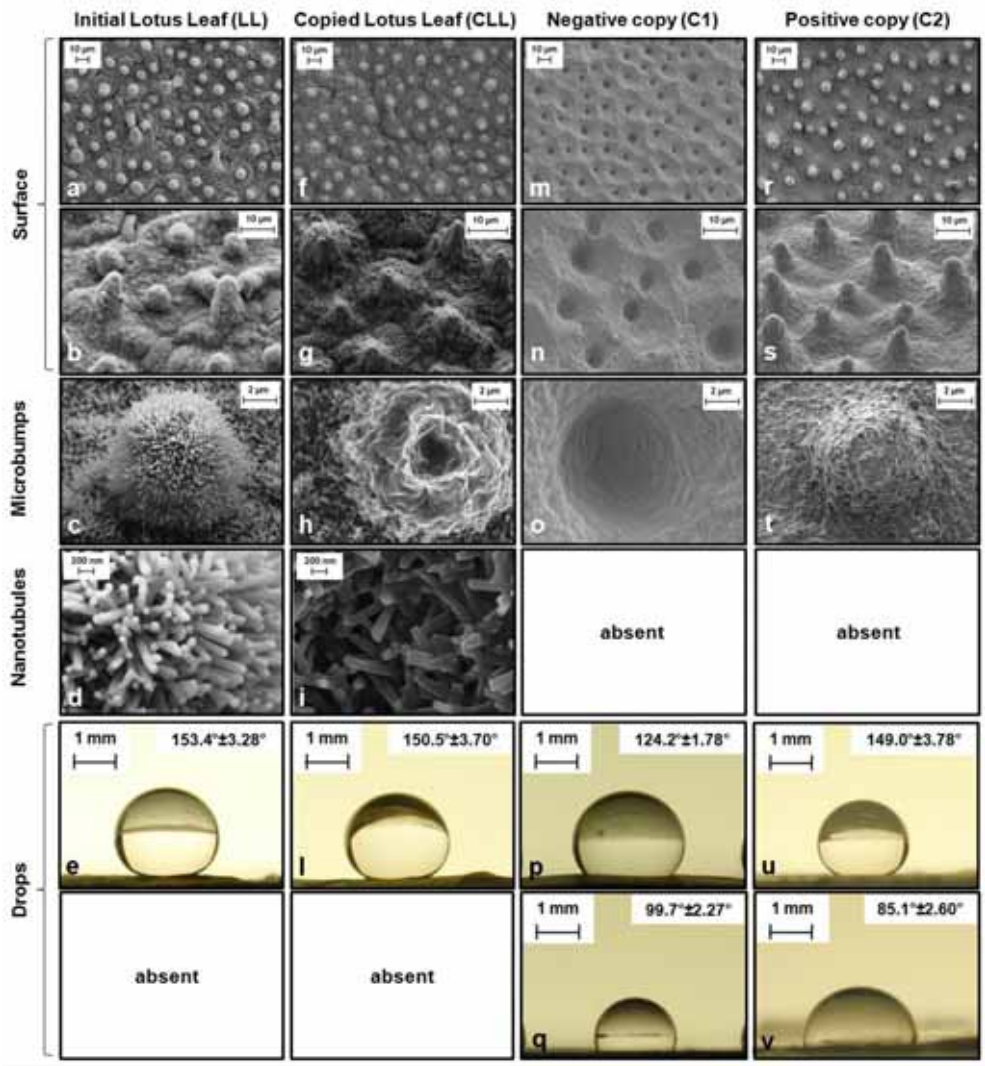

Fig. 7.3 Details of: (a) the fresh lotus leaf (LL), (f) the lotus leaf resulted after copying process (CLL), (m) the negative copy (C1) and (r) the positive copy (C2). In particular, b, g and s (n) show randomly distributed convex (concave) cell papillae; c, h and t (o) show a detail of the convex (concave) cell papilla and the wax tubules are magnified in d (natural wax tubules) and i (the wax tubules are here broken due to the C1 deposition and peeling). The nano-tubules are absent on C1 and C2. Water drop on the surface of: (e) the fresh lotus leaf (LL), (l) the lotus leaf resulted after copying process (CLL), (p) the negative copy (C1) and (u) the positive copy (C2). (q) and (v) show the shape of a water drop on C1_control and C2_control surfaces,

respectively. For LL and CLL, no control surface can be defined. The measurements reported in e, l, p, u, q, v are the average CA ± st.dev..

7.4. Discussion

The described molding technique requires a silicone polymerization time one order of magnitude longer than the fast and similar molding process presented in [53]. Considering live and dried lotus leaves, showing only a little discernible difference (cell papillae are taller on the fresh lotus leaf) in the wettability response [17, 30, 34], a longer time of polymerization is needed for an excellent morphological replication. Its resolution could be quantified into ~1 μm; thus, through this method, nano-structures could not be copied with our considered materials (silicone and PS).
The material of the positive (negative) template is here intrinsically hydrophilic (hydrophobic), while according to the experimental increment of CA, the C2 (C1) replica becomes hydrophobic (more hydrophobic). Some previously published papers reported that the hydrophobic behaviour could be achieved from hydrophilic material by increasing the surface roughness [24, 27]. A possible explanation is related to the molding process inducing modification of the topological characteristics, namely the cell papillae of PS replicas: several studies [6, 13] gave evidence that a surface with hemispherical topped asperities, like lotus convex cell papillae, should be the most appropriate to obtain an increment of the CA. On the contrary, if the classical Wenzel model [54] is taken into account, surface roughness increases the hydrophilicity (hydrophobicity) of an intrinsically hydrophilic (hydrophobic) material. As a consequence, Wenzel model could not be correctly applicable to the PS surface while agrees with the observations on C1 surfaces.
According to [26], a surface is self-cleaning if having very high CA and very low CAH, which is usually associated to the Cassie-Baxter [55] regime. We observed on C2 samples that the just-deposited drop stays in a state not conformal to the topology of substratum, in accordance with the Cassie-Baxter hypothesis: however, after only few seconds, the drop becomes conformal with surface topology and thus falls into the Wenzel state, displaying a high CAH/TA. Experimentally, we clearly observed the transition from the Cassie-Baxter to the Wenzel state for the C2 surface (intrinsically hydrophilic, high CA, high TA) as time goes by or due to any

external disturbance the specimen stage is subjected to [26] (inducing evaporation and thus pressure increment) or when depositing the droplet from some height [56]. Thus, it seems that in some cases [24, 26, 27, 57-59], including the surfaces presented in this work, the water drops seem to be sticky at high CA (Wenzel state).
Probably, superficial irregularities of micro-structures are present on the C2 surface leading to unstable air pockets under the drop which are substituted by water in few seconds. These superficial imperfections, rather than the absence of wax crystal tubules over C2, have probably determined this significant difference between C2 and LL. We suggest such an interpretation because in this case, the superimposition of the nano-scale wax tubules to the micro-scale cell papillae on the LL is not expected to supply any significant contribute: as we have verified, CLL shows the absence of wax tubules on the cell papillae and a presence of broken and numerous wax tubules in the areas between cell papillae but still shows the same results of LL in terms of CA, TA, SV and SS. This finding adds an information to previously published works, which highlighted that the complete removal of the wax tubules from the surface halved the CA value [17] while the annealing of wax tubules, keeping the wax composition and quantity nearly unchanged on the micro-patterned surface (this morphology is really close to our C2), determines a 11 % diminution of the initial CA of the lotus leaf [34] and a sticky behaviour of drops (TA > 90°, as for C2 here). However, in our case, we have reached a high CA of C2 copy, even if the hierarchical nano-tubules are absent.
According to previously published papers [6, 13], we conclude that the presence of hemispherical micro-bumps (first hierarchical level) induces an increment of CA (for C2) and the presence of additional nano-tubules (second hierarchical level) on micro-bumps decreases the TA and SV (for CLL). Therefore, such an absence of nano-tubules on C2, differently from a lotus leaf, can be supposed to be the reason of the observed high TA and SV with respect to those describing the performance of a natural leaf.

7.5. Conclusions

We have successfully fabricated a stable biomimetic lotus-leaf-like PS superhydrophobic surface. The CA and the SS of the positive PS copy of lotus leaf are 149.0° and 416.7 mm/s respectively, comparable to those of a

lotus leaf (CA = 153.4° and SS = 319.4 mm/s). As shown by the existing TA and SV limitations (relate to CAH), our method necessitates to be further improved in order to enhance also these last parameters. The replication of the nano-tubules, and thus the improvement of the molding method here presented, appears to be necessary to obtain an even more efficient superhydrophobic and simultaneously self-cleaning surface.
In spite of this, our approach remains very promising for realizing with different materials superhydrophobic synthetic lotus leaves working in static regime (contact angle). Compared to other methods of morphological replication of natural superhydrophobic leaves, this procedure involves ambient pressure and temperature and is much easier, requiring neither expensive instruments nor complicated chemical treatments.

ACKNOWLEDGMENTS

The living plant was provided by the Giardino Botanico Rea (Turin), associated with the Natural Science Museum of Turin, and the authors wish to sincerely thank R. Camoletto for this. The authors would like to thank A. Chiodoni and S. Guastalla, Physical Department, Politecnico di Torino for the fundamental help performing the FESEM micrographs of LL and CLL. We thank the “Nanofacility Piemonte” for the FESEM imaging instruments and L. Boarino, INRIM Institute, for the fundamental help performing the SEM micrographs of C1 and C2 surfaces. NMP is supported by "Metrology on a cellular and macromolecular scale for regenerative medicine" - METREGEN (2009-2012).

REFERENCES

[1] Barthlott, W., *Nord. J. Bot.* **1**, 345-55 (1981).
[2] Neinhuis, C., and Barthlott, W., *Ann. Bot.* **79**, 667-677 (1997).
[3] Barthlott, W., and Neinhuis, C., *Planta* **202**, 1-8 (1997).
[4] Herminghaus, S., *Europhysics Letters* **52**, 165-170 (2000).
[5] Wagner, P., Furstner, R., Barthlott, W., and Neinhuis, C., *J. Exp. Bot.* **385**, 1295-1303 (2003).
[6] Nosonovsky, M., and Bhushan, B., *Microsyst. Technol.* **11**, 535-549 (2005).
[7] Lu-quan, R., Shu-jie, W., Xi-mei, T., Zhi-wu, H., Lin-na, Y., and Zhao-mei, Q., *J. Bionic. Eng.* **4**, 33-40 (2007).

[8] Otten, A., and Herminghaus, S., *Langmuir* **20**, 2405-8 (2004).
[9] Zhiqing, Y., Hong, C., Jianxin, T., Huifang, G., Yuejun, L., Zhengxiang, W., Pu, S., Jide, Z., and Xin, C., J. Phys. D Appl. Phys. **40**, 3485-3489 (2007).
[10] Bhushan, B., and Jung, Y. C, *Ultramicroscopy* **107**, 1033-41 (2007).
[11] Nosonovsky, M., and Bhushan, B., *Microsyst. Technol.* **12**, 273-81 (2006).
[12] Nosonovsky, M., and Bhushan, B., *Microelectron. Eng.* **84**, 382-6 (2007).
[13] Koch, K., Bhushan, B., and Barthlott, W. *Progress in Materials Science* **54**, 137-178 (2009).
[14] Lepore, E., Antoniolli, F., Brianza, S., Buono, M., Carpinteri, A., and Pugno, N., *J. Nanomat.* **194524**, pp. 1-5 (2008).
[15] Pugno, N., and Lepore, E., J. *Adhesion* **84**, 949-962 (2008).
[16] Pugno, N., and Lepore, E., *Biosystems* **94**, 218-222 (2008).
[17] Brushan, B., and Jung, Y. C., *J. Phys. Condens. Matt.* **20**, 225010 (24pp) (2008).
[18] Quéré, D., *Nat. Mater.* **1**, 14-5 (2002).
[19] Solga, A., Cerman, Z., Striffler, B. F., Spaeth, M., and Barthlott, W., *Bioinsp. Biomim.* **2**, 126-134 (2007).
[20] Lee, S. M., Jung, I. D., and Ko, J. S., *J. Micromech. Microeng.* **18**, 125007 (7pp) (2008).
[21] Raibeck, L., Reap, J., and Bras, B., 15th CIRP International Conference on Life Cycle Engineering (2008).
[22] Sun, M., Luo, C., Xu, L., Ji, H., Ouyang, Q., Yu, D., and Chen, Y., *Langmuir* **21**, 8978-8981 (2005).
[23] Furstner, R., Barthlott, W., Neinhuis, C., and Wanzel, P., *Langmuir* **21**, 956-961 (2005).
[24] Lee, S. M., Lee, H. S., Kim, D. S., and Kwon, T. H., *Surface and Coatings Technology* **201**, 553-9 (2006).
[25] Zhai, L., Cebeci, F. C., Cohen, R. E., and Rubner, M. F., *Nano Letters* **4**, 1349 (2004).
[26] Lee, S. M., and Kwon T. H., *J. Micromech. Microeng.* **17**, 687-92 (2007).
[27] Lee, S., and Kwon, T. H., *Nanotechnology* **17**, 3189-3196 (2006).
[28] Yuan, Z., Chen, H., Tang, J., Chen, X., Zhao, D., and Wang, Z., *Surface and Coatings Technology* **201**, 7138-7142 (2007).
[29] Yeo, J., Choi, M. J., and Kim, D. S., *J. Micromech. Microeng.* **20**, 025028 (8 pp) (2010).

[30] Singh, R. A., Yoon, E., Kim, H. J., Kim, J., Jeong, H. E., and Suh, K. Y., *Materials Science and Engineering: C* **27**, 875-879 (2007).
[31] Gorb, S., *Microscopy Today* 44-46 (2007).
[32] Koch, K., Dommisse, A., Barthlott, W., and Gorb, S. N. *Acta Biomaterialia* **3**, 905-909 (2007).
[33] Schulte, A. J., Koch, K., Spaeth, M., and Barthlott, W., *Acta Biomaterialia* **5**, 1848-1854 (2009).
[34] Cheng, Y. T., Rodak, D. E., Wong, C.A., and Hayden, C. A., *Nanotechnology* **17**, 1359-1362 (2006).
[35] Oner, D., and McCarthy, T. J., *Langmuir* **16**, 7777-7782 (2000).
[36] Shibuichi, S., Onda, T., Satoh, N., and Tsujii, K., *J. Phys. Chem.* **100**, 19512-7 (1996).
[37] Miwa, M., Nakajima, A., Fujishima, A., Hashimoto, K., and Watanabe, T., *Langmuir* **16**, 5754-60 (2000).
[38] Jung, Y. C., and Bhushan, B., *Nanotechnology* **17**, 4970-80 (2006).
[39] Jung, Y. C., and Bhushan, B., *Scripta Materialia* **57**, 1057-60 (2007).
[40] Jung, Y. C., and Bhushan, B., *J. Microscopy* **229**, 127-40 (2008).
[41] Bhushan, B., Nosonovsky, M., and Jung, Y. C., *J. Royal Society Interface* **4**, 643-8 (2007).
[42] Nosonovsky, M., and Bhushan, B., *Ultramicroscopy* **107**, 969-79 (2007).
[43] Nosonovsky, M., and Bhushan, B., *Nano Letters* **7**, 2633-7 (2007).
[44] Nosonovsky, M., and Bhushan, B., *Materials Science and Engineering: R: Reports* **58**, 162-193 (2007).
[45] Nosonovsky, M., and Bhushan, B., *Langmuir* **24**, 1525-1533 (2008).
[46] Coulson, S. R., Woodward, I., and Badyal, J. P. S., *J. Phys. Chem. B* **104**, 8836-40 (2000).
[47] Hozumi, A., and Takai, O., *Thin Solid Films* **334**, 54-9 (1998).
[48] Erbil, H. Y., Demirel, A. L., and Avci, Y., *Science* **299**, 1377-80 (2003).
[49] Burton, Z., and Bhushan, B., *Nano Letters* **5**, 1607-1613 (2005).
[50] Feng, L., Li, S., Li, Y., Li, H., Zhang, L., Zhai, J., Song, Y., Liu, B., Jiang, L., and Zhu, D., *Advanced Materials* **14**, 1857-60 (2002).
[51] Lau, K. K. S., Bico, J., Teo, K. B. K., Chhowalla, M., Amaratunga, G. A. J., Milne, W. L., McKinley, G. H., and Gleason, K. K., *Nano Letters* **3**, 1701-5 (2003).
[52] Lepore, E., Faraldi, P., Boarino, L., and Pugno, N., *Composites Part B: Engineering*. doi:10.1016/j.compositesb.2011.05.028.

[53] Koch, K., Schulte, A. J., Fischer, A., Gorb, S. N., and Barthlott, W., *Bioinspiration and Biomimetics* **3**, 046002 (10 pp) (2008).
[54] Wenzel, R. N., *Industrial and Engineering Chemistry* **28**, 988-94 (1936).
[55] Cassie, A. B. D., and Baxter, S., *Trans. Faraday Society* **40**, 546-51 (1944).
[56] He, B., Patankar, N. A., and Lee, J., *Langmuir* **19**, 4999-5003 (2003).
[57] Liu, B., He, Y., Fan, Y., and Wang, X., *Macromolecular Rapid Communications* **27**, 1859-64 (2006).
[58] Cheng, Y. T., and Rodak, D. E., *Appl. Phys. Lett.* **86**, 144101-3 (2005).
[59] Wu, X., Zheng, L., and Wu, D., *Langmuir* **21**, 2665-7 (2005).

8. THE ROLE OF ROUGHNESS PARAMETERS ON THE TRIBOLOGY OF RANDOMLY NANO-TEXTURED SILICON SURFACE

Abstract

This experimental work is oriented to give a contribution to the knowledge of the relationship among surface roughness parameters and tribological properties of lubricated surfaces; it is well known that these surface properties are strictly related, but a complete comprehension of such correlations is still far to be reached. For this purpose, a mechanical polishing procedure was optimized in order to induce different, but well controlled, morphologies on Si(100) surfaces. The use of different abrasive papers and slurries enabled the formation of a wide spectrum of topographical irregularities (from the submicro- to the nano-scale) and a broad range of surface profiles. An AFM-based morphological and topographical campaign was carried out to characterize each silicon rough surface through a set of parameters. Samples were subsequently water lubricated and tribologically characterized through ball-on-disk tribometer measurements. Indeed, the wettability of each surface was investigated by measuring the water droplet contact angle, that revealed a hydrophilic character for all surfaces, even if no clear correlation with roughness emerged. Nevertheless, this observation brings input to the purpose, as it allows to exclude that the differences in surface profile affect lubrication. So it is possible to link the dynamic friction coefficient of rough Si samples exclusively to the opportune set of surface roughness parameters that can exhaustively describe both height amplitude variations (R_a, R_{dq}) and profile periodicity (R_{sk}, R_{ku}, l_c) that influence asperity-asperity interactions and hydrodynamic lift in different ways. For this main reason they cannot be treated separately, but with dependent approach through which it was possible to explain even counter intuitive results: the unexpected decreasing of friction coefficient with increasing R_a is justifiable by a more consistent increasing of kurtosis R_{ku}.

8.1. Introduction

Tribology is historically the science of rubbing and is deserved to be considered an ancient craft discipline with a quite modern scientific formulation, as the full interdisciplinary multi-scale description of the interaction between surfaces in relative motion and the involved mechanisms [1]. Motivations surge wherever and whenever friction, wear, lubrication and related topics assume a huge importance on human life and activities, and the control of such phenomena is required so as to provide strategies for improving item performances and allowing energy and raw material savings at all levels and ranges of applications.
In particular, for proper design of contact surfaces, it is crucial to understand the impact of surfaces roughness and topography on friction. As a matter of fact, engineered surfaces prepared by various machining processes, for both mesoscale objects and micro-nano devices, are not ideally smooth, but with surface irregularities whose amplitudes span from few nanometers to few microns [2, 3].
Early pioneering works have been shown that the friction between surfaces is substantially affected by the surface texture [4-6]: topography and density of peaks/valleys are expected to significantly influence tribological properties, especially when rough surfaces act as lubricated contacts. More recently, regular micro-scale surface texturing [7, 8] and nano-scale surface patterning [9] have been observed to affect sliding behaviours. Under hydrodynamic lubrication, surface roughness and topography guide the capacity to form the lubricant film that fully separates mating surfaces so as to behave as the major load carrying mechanism. Furthermore, under mixed lubrication regime, where the average film thickness is of the same order of magnitude as (or smaller than) surface profile peaks, asperity-asperity contacts alternate with fluid regions between irregularities. Thus, even regarding this scenario, an important role on frictional dissipation is played by peaks amplitude and periodicity, since they determine both the coexisting load supporting mechanisms: contacting performances and lubricant film formation/breakdown.
A still debated question concerns the set of parameters to be exploited for describing random surface textures. Average surface roughness (R_a) draws a very good overall description of profile heights variation and is usually studied together with the average slope of the asperities (R_{dq}). Plenty of published works assert that the load-carrying capacity decreases as R_a and

R_{dq} increase, inferring that the increasing of the coefficient of friction primarily depends on the overall shear stresses required to overcome the asperities during sliding [4, 5, 10-12].

However, this latest conclusion is still far to guarantee an exhaustive comprehension of the problem. R_a, R_{dq} (and other strictly interrelated twin parameters) are amplitude parameters that do not sufficiently describe the topography of the surface, because they are purely sensitive to the height deviation from the main profile, but they do not give any information about symmetry, waviness and periodicity. In this sense, recent researches suggest to make use of opportune topography-sensitive parameters: in particular, skewness (R_{sk}) and kurtosis (R_{ku}) were predicted and observed to be strictly related to the load bearing ratio, maximum contact pressure and effective average lubricant film thickness during sliding contact [3, 12]. Both R_{sk} and R_{ku} are linked to the autocorrelation length (l_c), that is widely recognized as one of the most effective parameter to describe the profile periodicity, since it indicates the statistical distance over which every couple of points can be treated as independent in a random profile [13]. R_{sk} is a pure number that statistically quantifies the degree of symmetry of a surface profile across the main line: $R_{sk} = 0$ describes symmetrical height distribution; positive values indicate the major presence of high peaks above broad valleys; on the contrary, negative values indicate the major presence of deep scratches with the loss of narrow asperities. R_{ku} is a pure number that statistically weights the probability density sharpness of a surface profile across the main line: $R_{ku} = 3$ indicates a Gaussian distribution; $R_{ku} < 3$ indicates the prevailing alternation of broad low peaks and valleys; on the contrary, $R_{ku} > 3$ indicates the prevailing alternation of sharp high peaks and scratches [14, 15].

The aim of the present paper is to give a contribution to the investigation on the not yet clearly defined influence between lubricated friction and surface roughness parameters, through AFM and ball-on-disk characterizations of rough silicon samples whose surface morphologies were modified with reliable and accurately controlled polishing procedures in order to induce various surface textures with different distributions and shapes of random nanoirregularities. In order to complete the study, contact angle measurements have also been performed for checking the wettability of the same samples, a property which also relates to surface roughness and lubrication. The contact angle measurement is a standard procedure in this context. Depositing a small drop, with size smaller than the liquid capillary length in order to neglect gravity, the angle formed between the tangent of

the liquid drop at the contact and the surface itself gives us quantitative information about the hydrophobic/hydrophilic surface behaviour.

8.2. Experimental procedures

For the purpose of this investigation, well accurate and reproducible mechanical polishing protocols were optimized in order to prepare a set of silicon samples, with different surface roughness and topographies. Commercial flat silicon samples were glued on a piston holder. The holder was loaded through a bound spring, whose elastic force could be calibrated in order to control the normal pressure applied to the sample during machining. In this way, the sample surface is perpendicularly secured to a rotating polishing disk covered by abrasive pads (SiC papers, or velvet rugs imbued by Al_2O_3 slurry). A further device, consisting in a radial arm equipped with a pair of pulleys, was coupled to the piston holder, so that the silicon sample also experienced the autorotation during its rubbing against the abrasive medium. Through this custom rig, reliability, isotropy and uniformity of the produced textures are ensured.
Three different sample were machined (labeled: “180”, “400”, “P3”) keeping constant the operative conditions (normal pressure, lapping speed, polishing time) but varying the abrasive medium. Table 8.1 summarizes the manufacturing conditions of each machined sample.
Samples were analysed through a three-step experimental protocol: microscope imaging, tribological testing, contact angle measurements. A flat unmachined reference silicon sample (labeled: “Flat”) was also characterized.
The tribological campaign was carried out by a ball-on-disk microtribometer (UMT2-CETR). Friction coefficient measurements were performed at constant normal load (250 mN), sliding speed (1.5 cm/s) and elapsed time (1 hour). Steel 100Cr6 balls (diameter: 1.6 mm) were chosen as static counterparts. A bath of distilled water (99 % pure) was continuously refilled to act as lubricant between sliding bodies. In order to get a statistically representative collection of friction coefficient data, each sample was tested three times under the same abovementioned conditions. Average friction coefficients with standard deviations as error bars were finally calculated.

Sample	Applied pressure (kPa)	Speed rotation (rpm)	Lapping time (min)	Abrasive medium
"180"	7	50	20	SiC paper (grit: 180)
"400"	7	50	20	SiC paper (grit: 400)
"P3"	7	50	20	Al_2O_3 slurry (grain size: 3 μm)
"FLAT"	Unmachined			

Table 8.1 Main processing parameters exploited during polishing procedure for silicon rough samples.

Topographical characterization was performed by atomic force microscope (AFM, Veeco Digital Instrument Enviroscope Nanoscope IV). AFM is the most powerful technique for the surface morphological characterization related to its in-plane and out-of-plane spatial resolution. The in-plane resolution is related to the radius of curvature of the tip, stated to be less than 10 nm. To exclude any tip shape influence on the morphological measurements, the results from two different AFM tips were compared and no differences were found. The vertical spatial resolution is mainly related to the instrumental noise, which has been measured to be ± 0.2 nm. For each sample three separate 100 × 100 μm^2 areas were scanned through a matrix of 256 × 256 columns by rows. Such a wide scan size was chosen to include and statistically weight also those structures with low spatial periodicity and taking into account of the value of the contact area explored in tribological tests (about 500 μm^2 in agreement to hertzian approximation). Indeed, the values of the measured roughness parameters do not change increasing the spatial density of the scan matrix, acquiring 512 × 512 pts images and comparing them to 256 × 256 pts ones. From AFM topographical images, five roughness parameters were monitored and averaged (with standard deviation as error bar) so as to show appreciable differences in dependence of the type of surface preparation. Two of them are height-amplitude parameters: R_a (absolute average height with respect to the midline) and R_{dq} (mean square of average profile slopes with respect to the midline); the other three are R_{sk} (skewness), R_{ku} (kurtosis), l_c (autocorrelation length) and they provide additional topographical information to the previously

published ones. Other roughness parameters were excluded from the dissertation since they did not show any significant trend, or they cannot be considered fully relevant for the average properties of the samples (for example: R_{max}, defined as the maximum height difference between the absolute higher peak and the absolute lower valley, is strongly affected by local defects).
Finally, hydrophobic/hydrophilic behaviours were quantified for each sample through contact angle measurements. A standard single use syringe was exploited to perform series of five drops of distilled water, deposited on random areas of each ethanol-cleaned sample. Drops volumes spare from 2 to 20 µl. Indeed, drops radii range from 0.8 to 1.6 mm. Hence, average drop sizes are significantly larger than typical dimension of the observed nanoirregularities. For this reason the selection of the sample area to be wetted could be considered almost irrelevant. The contact angle was recorded with a digital photocamera (OLYMPUS MJU 1010) and then measured and statistically analyzed with ImageJ 1.41o software.

8.3. Results and discussion

Fig. 8.1 highlights the main results carried out from AFM-based surface topography characterizations. The comparison among 2D maps and related average 1D profiles shows the peculiar differences of the textures induced by lapping with respect to the commercial flat ones.
Table 8.2 summarizes the statistical analysis of the campaign. Samples "180" and "400" exhibit similar values of almost all surface roughness parameters. Also samples "P3" and "Flat" shows similar values of the surface roughness parameters, although very different with respect of those of "180" and "400" samples. Going into details: R_a values attest an increasing of average amplitude variance by a factor 25 from flatter samples ("P3," "Flat") to rougher samples ("180," "400") which exhibit visible scratches randomly oriented accordingly to the almost isotropic lapping procedure (see Figs. 8.1a and 8.1b); on the other hand, topography sensitive parameters outline even more distinct differences between the couple of twin textures: "180" and "400" samples show negative skewness values and quasi-Gaussian density sharpness of peak/valleys ($R_{ku} \sim 3$). On the contrary, "P3" and "Flat" samples display an opposite type of waviness with smaller periodicity (since l_c values are lower with respect to "180" and "400" ones)

and prevalence of sharp peaks and broad valleys, since R_{sk} values are positive and density sharpness distribution is barely leptokurtic ($R_{ku} >> 3$).
All water lubricated ball-on-disk tests were nearly under "mixed" or almost "quasi-hydrodynamic lubrication", since only soft elastic deformations of the counterparts occurred during sliding; in fact, it was impossible to identify wear scars on all of the involved sliding counterparts (silicon disks and steel balls). This observation allows to conclude that original textures were not altered, but retained their influence on contact modes during all tests. Thus, the correlation between tribological behaviours and surface topography properties can be considered significant. "180" and "400" twin rougher samples exhibit nearly equal average friction coefficients (respectively: $\mu_{180} = 0.028 \pm 0.001$, $\mu_{400} = 0.031 \pm 0.003$) but lower with respect to "P3" and "Flat" twin flatter samples average friction coefficients (respectively: $\mu_{P3} = 0.067 \pm 0.003$, $\mu_{FLAT} = 0.069 \pm 0.003$).

	Height-amplitude parameters		**Topography-sensitive parameters**		
Sample	R_a **(nm)**	R_{dq}	R_{ku}	R_{sk}	l_c **(µm)**
"180"	38 ± 9	0.14 ± 0.05	8 ± 6	-1.5 ± 1.0	1.3 ± 0.5
"400"	77 ± 8	0.185 ± 0.014	5 ± 2	-1.2 ± 0.6	1.6 ± 0.3
"P3"	2.9 ± 0.3	0.030 ± 0.002	310 ± 90	11 ± 3	0.33 ± 0.05
"FLAT"	1.4 ± 0.3	0.012 ± 0.003	130 ± 80	7 ± 4	0.41 ± 0.14

Table 8.2 Main results from AFM-based surface characterization. Comparison of surface roughness parameters.

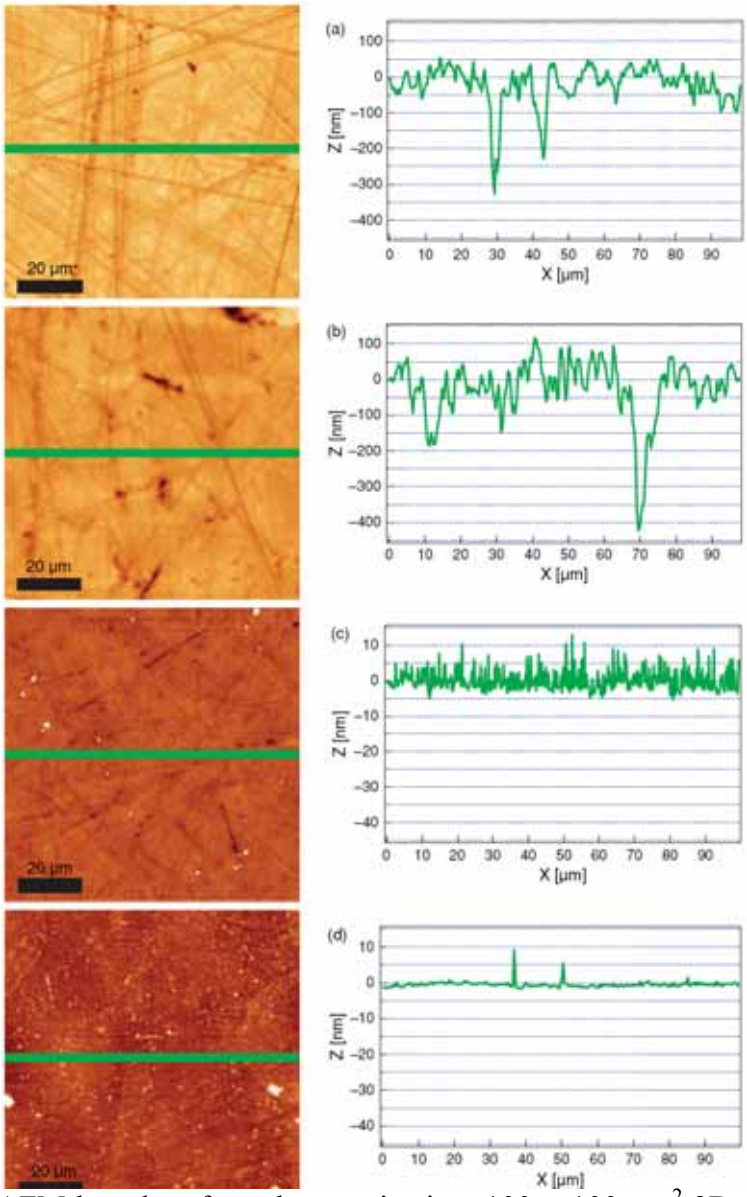

Fig. 8.1 AFM-based surface characterization. 100 × 100 µm^2 2D-maps and 1D-profiles averaged on a reduced area (see the stripe over the map). (a) sample "180"; (b) sample "400"; (c) sample "P3"; (d) sample "FLAT". Note that the Z-scale profile relative to "P3" (c) and "FLAT" (d) is reduced by a factor 10 with respect to the Z-scale profile relative to "180" (a) and "400" (b).

In Fig. 8.2, average friction coefficients are plotted against main surface roughness parameters. To rationalize these data distributions it is necessary, rather than useful, to take into account the competitive contact mechanisms that occur under "mixed" or "quasi-hydrodynamic" lubrication: friction force is the sum of two components since the total normal load is shared by the counterparts asperity interacting force and the lubricant hydrodynamic lifting force. Thus, the observed decreasing of friction coefficient with decreasing of R_{sk} and R_{ku} (see Figs. 8.2c and 8.2d) are in agreement with literature [3, 12]: lower values of skewness and kurtosis optimize maximum contact pressure and effective average lubricant film thickness, so as to favour the hydrodynamic support and minimize asperity-asperity interactions. The same considerations could be extended to l_c (Fig. 8.2e) reminding the inverse correlation that links periodicity to R_{sk} and R_{ku}. On the other hand, the decreasing of friction with increasing of R_a and R_{dq} (Figs. 8.2a and 8.2b) is in contrast to what expected, since previously reported conclusions [6, 10] infer that higher average profile amplitudes and more pronounced slopes require higher overall shear stresses to be overcome, thus justifying higher frictional dissipations. In order to explain these latest counter intuitive results, height-amplitude parameters and topography-sensitive parameters cannot be discussed separately, but with dependent approach. In fact they are linked to the two competitive components of friction force: R_a and R_{dq} quantify the asperities distribution, while R_{ku}, R_{sk} and l_c describe profile symmetry, waviness and periodicity, which guide lubrication film formation/breakdown and hydrodynamic lift effectiveness, as explained earlier. With the support of the available data, a preliminary model was theorized for a numeric interpretation of the discussed correlation between friction and roughness. For simplicity, the first approximation approach invokes only two of five parameters but no less than representative: R_{a} (height-amplitude sensitive) and R_{ku} (topography-sensitive).

R_a increases by increasing the peak heights, whereas R_{ku} increases by decreasing the autocorrelation length and thus the wavelength of the profile which lower values are predicted to optimized at least the effective average lubrication during sliding contact [3, 9].

Accordingly, it can be assumed:

$$\mu \propto R_a^{\alpha} R_{ku}^{\beta} \tag{1}$$

and thus:

$$\frac{d\mu}{\mu} = \alpha \frac{dR_a}{R_a} + \beta \frac{dR_{ku}}{R_{ku}} \tag{2}$$

Consequently positive or negative variations of the friction coefficient are expected according to:

$$\frac{d\mu}{\mu} \gtrless 0 \quad \alpha \frac{dR_a}{R_a} \gtrless -\beta \frac{dR_{ku}}{R_{ku}} \tag{3}$$

We can rationalize the experimental results with $\alpha \approx \beta \approx 0.2$. Thus Eq. (3) can explain the unexpected decreasing of friction coefficient with increasing R_a by a more consistent increasing of kurtosis R_{ku}. Contact angles measurement were further investigated in order to understand if friction variation are also linked to wettability behaviours, since it is well known that wettability affect lubrication [9, 16, 17]. No significant relationship between roughness parameters and contact angles have been observed (Fig. 8.3). In particular estimating the Wenzel [18, 19] roughness parameter r as $r \approx \left(\sqrt{4R_a^2 + (l_c/4)^2}\right) \Big/ (l_c/4)$ as geometrically suggested (and confirmed experimentally by the validity of $R_a \approx (l_c/4)R_{dq}$) the inequality $\cos\theta_{\exp} \neq r\cos\theta$ was found, in contrast to what one would expect according to the Wenzel model [18]. $\theta_{\exp}$ is here the measured contact angle, whereas θ is the intrinsic one. To rationalize this discrepancy further investigations are running, in particular to check the chemical state of the Si samples, that could also affect wettability.

In any case, this set of characterizations verified no correlation between wettability and tribological properties, as water affinity of the investigated surfaces is not consistently observed to be influenced by the different textures. This further conclusion allows to ascribe the observed friction coefficient behaviours exclusively to the differences in morphology and topography that affect load support mechanisms and thus frictional dissipations under “mixed” or “quasi-hydrodynamic” lubrication regimes.

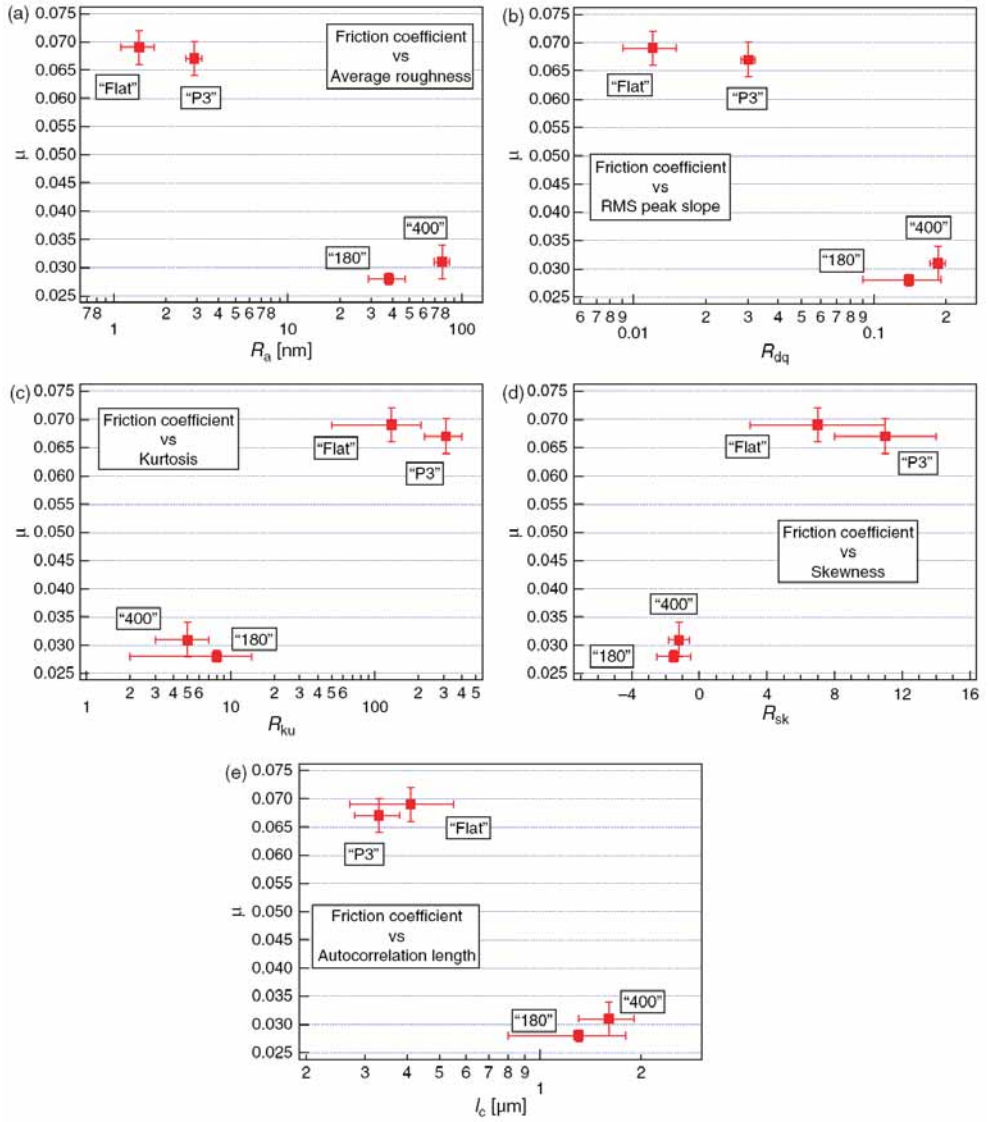

Fig. 8.2 Tribological characterization. Average friction coefficients of each sample are plotted against main roughness parameters: (a) R_a; (b) R_{dq}; (c) R_{ku}; (d) $R_{sk;}$ (e) l_c.

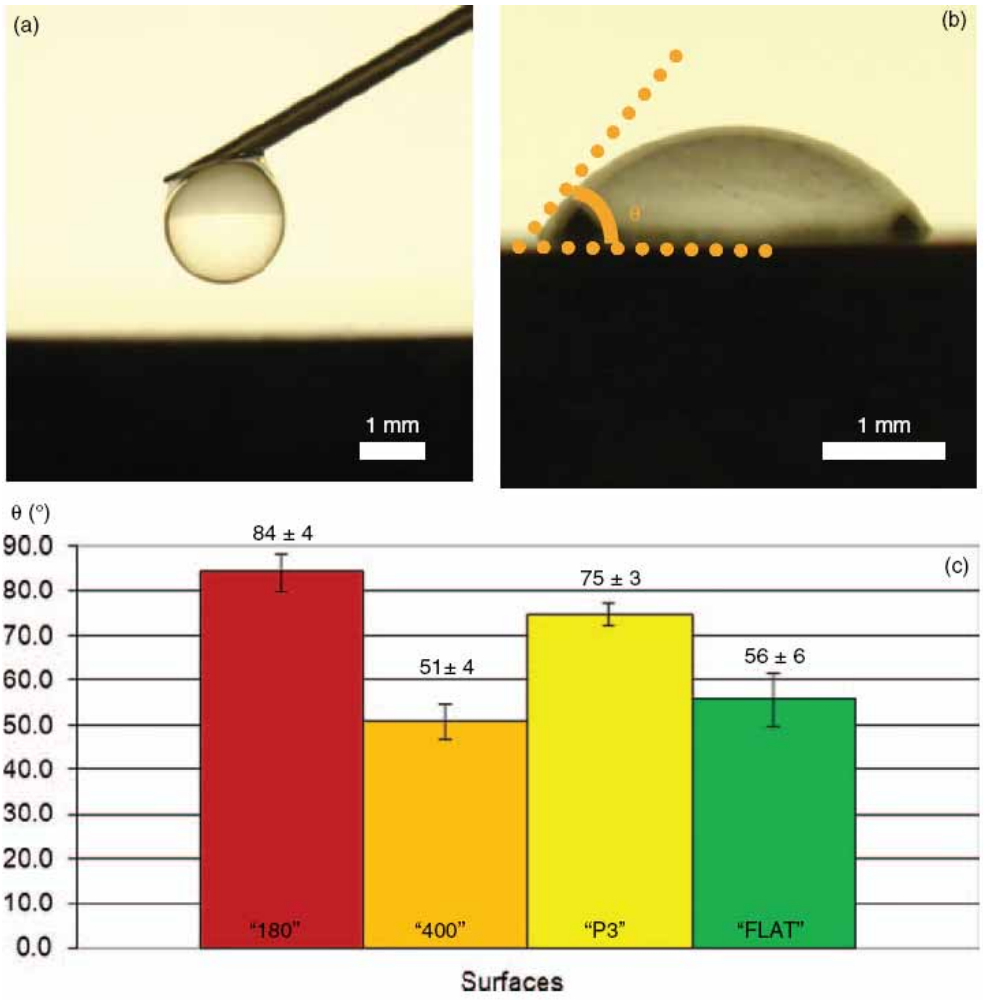

Fig. 8.3 Contact angle measurements. (a) A random-volume drop of distilled water is deposited with a standard single use syringe on the ethanol-cleaned samples. (b) The contact angle θ is recorded through a digital photocamera and gives quantitative information about the wettability surface behaviour: hydrophobic surfaces exhibit $\theta > 90°$, hydrophilic surfaces exhibit $\theta < 90°$. Results are shown in diagram (c).

8.4. Conclusions

A set of silicon surfaces with different surface nanotextures was prepared developing a well accurate and reproducible polishing procedure.
A reliable and highly resolved AFM-based surface characterization showed that isotropic method allowed the formation of a wide spectrum of isotropic and uniformly distributed topographical irregularities (from the submicro- to the nano-scale) and a broad range of surface profiles. Although gradual changes in both amplitude and topography parameters cannot be obtained through a random micro/nano-structuring process, at least one order of magnitude separated textures were realized, so that some consistent dissertations justified by the two-limits scenario can be argued.
As a matter of fact, ball-on-disk tests highlighted a significant correlation between roughness and "mixed" or "quasi-hydrodynamic" lubricated friction.
Furthermore, roughness and topography were not observed to consistently influence water drop contact angle. All samples revealed a hydrophilic character and no clear correlation with height-amplitude and topography-sensitive parameter emerged, allowing to suppose that, in this case, lubrication regimes were not affected by wettability. Thus the observed differences in friction coefficient can be exclusively ascribed to the differences in surface profile and topography that affect load support mechanisms.
Lower values of topography sensitive parameters (R_{ku}, R_{sk}) optimize maximum contact pressure and effective average lubricant film thickness, so as to favour the hydrodynamic support and minimize asperity-asperity interaction, thus validating previously published literature. The same considerations could be extended to l_c.
Apparent counter intuitive results in the correlation between friction coefficient and height-amplitude parameters (R_a, R_{dq}) can be rationalized invoking a dependent approach with topography-sensitive parameters. In agreement to the obtained data distribution, a first approximation model explain the unexpected decreasing of friction coefficient with increasing R_a by a more consistent increasing of R_{ku}.
In summary, this preliminary model confirm the main idea: for an exhaustive comprehension of the topic, the study of a representative set of surface roughness parameters is necessary. Height distribution (amplitude, slope) and topography (symmetry, waviness, periodicity) cannot be

discussed separately, as the former influence asperity-asperity interactions and the latter guide lubrication and hydrodynamic lift effectiveness.

ACKNOWLEDGMENTS

This research has been supported by PRRIITT (Regione Emilia Romagna) and Intermech Project. NMP is supported by METRAGEN.

REFERENCES

[1] Bhushan, B., Modern Tribology Handbook, CRC Press, **I** (2001).
[2] Zhu, D., *Tribol. Trans.* **46**, 44 (2003).
[3] Wang, W.-Z., Chen, H., Hu, Y.-Z., and Wang, H., *Tribol. Int.* **39**, 522 (2006).
[4] Gladman, C. A., *Microtecnic* **9**, 229 (1962).
[5] Myers, N. O., *Wear* **5**, 182 (1962).
[6] Koura, M. M., and Omar, M. A., *Wear* **73**, 235 (1981).
[7] Etsion, I., *J. Tribol.* **127**, 248 (2005).
[8] Borghi, A., Gualtieri, E., Marchetto, D., Moretti, L., and Valeri, S., *Wear* **265**, 1046 (2008).
[9] Marchetto, D., Rota, A., Calabri, L., Gazzadi, G. C., Menozzi, C., and Valeri, S., *Wear* **268**, 488 (2010).
[10] Bhushan, B., and Nosonovsky, M., *Nanotechnology* **15**, 749 (2004).
[11] Menezes, P. L., Kishore, and Kailas, S. V., *Sadhana* **33**, 181 (2008).
[12] Sedlacek, M., Podgornik, B., and Vizintin, J., *Wear* **266**, 482 (2009).
[13] Zhang, Y., and Sundararajan, S., *J. Appl. Phys.* **97**, 103526 (2005).
[14] Pugno, N. M., and Lepore, E., *J. Adhesion* **84**, 949-962 (2008).
[15] Pugno, N. M., and Lepore, E., *Biosystems* **94**, 218-222 (2008).
[16] Ando, Y., *Tribol. Lett.* **19**, 29 (2008).
[17] Wang, Y., Mo, Y., Zhu, M., and Bai, M., *Surf. Coat. Technol.* **203**, 137 (2008).
[18] Wenzel, R. N., *J. Phys. Chem.* **53**, 1466 (1949).
[19] Pugno, N. M., *J. Phys.: Condens. Matter* **19**, 395001, pp. 1-17 (2007).

STRONG MATERIALS

9. EVIDENCE OF THE MOST STRETCHABLE EGG SAC SILK STALK OF THE EUROPEAN SPIDER OF THE YEAR *META MENARDI*

Abstract

Spider silks display generally strong mechanical properties, even if differences between species and within the same species can be observed. While many different types of silks have been tested, the mechanical properties of stalks of silk taken from the egg sac of the cave spider *Meta menardi* have not yet been analyzed. *Meta menardi* has recently been chosen as the "European spider of the year 2012", from the European Society of Arachnology. Here we report a study where silk stalks were collected directly from several caves in the north-west of Italy. Field emission scanning electron microscope (FESEM) images showed that stalks are made up of a large number of threads, each of them with diameter of 6.03 ± 0.58 μm. The stalks were strained at the constant rate of 2 mm/min, using a tensile testing machine. The observed maximum stress, strain and toughness modulus, defined as the area under the stress-strain curve, are 0.64 GPa, 751 % and 130.7 MJ/m^3, respectively. To the best of our knowledge, such an observed huge elongation has never been reported for egg sac silk stalks and suggests a huge unrolling microscopic mechanism of the macroscopic stalk that, as a continuation of the protective egg sac, is expected to be composed by fibres very densely and randomly packed.
The Weibull statistics was used to analyze the results from mechanical testing, and an average value of Weibull modulus (m) is deduced to be in the range of 1.5 - 1.8 with a Weibull scale parameter (σ_0) in the range of 0.33 - 0.41 GPa, showing a high coefficient of correlation ($R^2 = 0.97$).

9.1. Introduction

Spider silks often display strong mechanical properties [1] and have been studied extensively during the last five decades. In particular, dragline silk is noted for its unique strength and toughness. Because of the complex structure of spider silk, large scale synthetic production still remains a challenge and can only be achieved through a controlled self-assembly of the macromolecular components with nanoscale precision [2].
Individual spiders spin 'toolkits' of seven to eight different types of silks, each of which comes from its own discrete gland(s) and spigot(s) [3]. Each type of spider silk has a unique chemical composition, molecular structure and material properties [4]. Orbwebs, for example, are composite structures built from multiple types of silks, each with its own unique molecular structure and mechanical function [4].
The best studied type of silk is the dragline silk, which is produced in the major ampullate gland. As the name itself suggests, dragline silk is used as a lifeline by most spiders moving through the environment and forms the backbone of most webs [4]. Minor ampullate glands produce threads that are sometimes added to major ampullate draglines or temporary spirals of the orbweb acting like a scaffolding for the construction of the web. Aciniform glands produce the silk used for prey wrapping and egg case construction and its fiber are more stretchable and tougher than dragline silk [5]. Flagelliform glands are unique to araneoid-orbweaving spiders and are used in the production of the catching spiral silk. In some derived taxa (like cobweb spinning theridiids) this type of silk is used to wrap preys [6]. Aggregate glands produce the glue coating on viscid capture threads and are unique to araneoid spiders, whilst piriform glands is used to cement threads to the substrate as well as to form silk junctions by forming attachment disks [4].
In line with state-of-the-art knowledge, it is widely accepted that a major role in the production of silk for egg sacs is played by the tubuliform (or cylindrical) glands [7-10], and it is likely that some spiders produce egg sac silk exclusively in these glands. Tubuliform silk is produced solely by adult orbweaving females. Egg sacs themselves are complex, layered structures containing fibres from several different glands [11-13]. This complexity creates confusion about how tubuliform silk is utilized. However, the morphology of the silk is quite distinctive because the glands produce large fibers with an irregular surface that is unlike any other silk. Moreover, the

left and right fibers are coated with a gluey secretion that causes them to adhere together [11]. The mechanical behaviour of the silk is quite distinct in displaying a very prominent yield followed by a long low modulus extension [3, 4, 14] .

In orbweb spiders, the spinnerets are three paired appendage-like organs on the abdomen, each of which contains dozens to hundreds of spigots connected to their own internal silk-producing glands (Fig. 9.1) [15]. A single spider is therefore capable of producing multiple silk threads of many kinds, and the arrangement of spigots on the spinnerets appears to relate functionally to how different silks are used together [6]. Dragline silk, flagelliform silk, aggregate silk and aciniform silk have been extensively characterized in *Argiope trifasciata* (Forsskål) [16-21], *Araneus diadematus* (Linnaeus) [22-31], *Argiope argentata* (Fabricius) [3, 32], *Argiope bruennichi* (Scopoli) [33], *Araneus gemmoides* Chamberlin & Ivie [32, 34], *Larinioides* (=*Araneus*) *sericatus* Clerck [35], *Nephila edulis* (Labillardière) [23, 25], *Nephila clavipes* (Linnaeus) [32, 34, 36-38], *Nephila pilipes* Fabricius [36], *Nephila madagascariensis* (= *N. inaurata madagascariensis*) (Vinson) [29], *Lactrodectus hesperus* Chamberlin & Ivie [32, 39], *Leucauge venusta* Walckenaer [32], *Plectreurys tristis* Simon [32], *Kukulcania hibernalis* Hentz [32] and *Salticus scenicus* (Clerck) [30]. These studies have shown that the various types of silks, produced by different glands, have very different mechanical properties [22, 24, 34], giving the thread different characteristics, depending on their respective function [8], that may vary according to different species. Variability in the mechanical properties of spider silk is very important. Spider silk is in fact central to many aspects of spider biology and ecology, from communication to prey capture. Spiders are the only animals which use silk in almost every part of their daily lives. Because silk is so important to spiders, it has presumably been subjected to strong selective pressures during the 400 million years of spider evolution and can be regarded as one of the key to spider's evolutionary success [40, 41].

It has been demonstrated that silk properties (in terms of different reeling methods [32, 42], environmental conditions [8, 20], types of silk [e.g. dragline, viscid or egg sac silk] [22, 24, 34]) are species-specific and lead to silk-based peptide fibrils or protein aggregates with different structural and mechanical properties. For example, different reeling speeds cause a variation in the diameter of the dragline thread [25] and so depending on the thickness of the thread the stress-strain curve varies. Spider dragline silk was tested in a wet environment to show that moisture induces

supercontraction in the threads for levels higher than 70 - 75 % of relative humidity, proving that when a thread is exposed to moisture, stresses quickly build up and tighten the thread [20]. By varying the conditions under which the spiders were kept (different reeling speeds, starvation periods), the species or the spiders inside the same species, it has been seen that dragline silk has different mechanical properties and varies on an interspecific, intraspecific and intra-individual level [23].

All silks are proteinaceous and belong to the general class of hierarchical protein materials. Each thread of spider silk is a composite of semi-amorphous α-chains and β-pleated nanocrystals [43]. In the orb web spider *Araneus diadematus* (the common European garden spider), the β-sheets are made up of a series of highly conserved poly-Ala repeats and are stacked up, thereby forming the protein crystals; these are embedded in a matrix of loosely arranged glycine-rich amino acids [26]. These protein crystals are held together by hydrogen bonds, one of the weakest chemical bonds, and have an important role in defining the mechanical properties of silk. When an external force is applied, the loose amino acids stretch and from a disordered position are straightened, whilst the β-sheets are subject to tensile force [44]. The β-sheet rich crystalline units are responsible for the toughness of the silk thread while the remaining, apparently amorphous regions, have a rubber like behavior [45]. One study used a simple coarse-grained model to simulate the mechanical deformation of silk in which the silk constitutive unit was a combination of two domains representing the α-chains and β-pleated sheets [46]. The stress-strain curve of their simulation had a similar shape to that of silk.

The studies on dragline silk have given us the opportunity to find a natural fiber with strong tensile properties in terms of large deformation [3, 8, 17-19, 21-30, 32-37, 39, 47]. A recent study has discovered a dragline silk which is twice as tough as any other previously described silk: this silk belongs to *Caerostris darwini* Kuntner & Agnarsson, which is a spider which constructs its orb web suspended above streams, rivers and lakes [47]. To be able to thoroughly understand all the various properties of spider silk we must be able to characterize all the different kind of silk.

The stress-strain behavior of the egg sac silk of *Araneus diadematus* [24] presents a logarithmic behavior, which is completely different to the behavior of dragline and viscid silk. The same can be said about the egg sac silk of *Argiope bruennichi* [33]. The stress-strain curves of the egg sac silk start with a small elastic region and then present an extremely flat plastic-hardening region [24]. The strain to break is roughly the same as that of the

dragline, but the tensile strength is about from 3 to 4 times lower. The egg case silk has an initial modulus, which is a measure of the stiffness of the fiber, significantly higher than that of the dragline thread. These differences are partly due to the different amino acid compositions in the silks. To our knowledge, few studies have been conducted on stalks of egg sac silk. In general, each egg sac consists of two major parts that can be distinguished by the naked eye, namely an egg sac case and a stalk. The egg sac case houses eggs, while the stalk attaches the cocoon to the substrate [12]. In the literature, the strain of spider egg sac silk is in the range from 19 % for *Araneus gemmoides* [34] to 29 % for *Argiope argentata* [3], showing an average value of ~26 %; while the average stress is of 1.1 GPa with a minimum value of 0.3 GPa for *Araneus diadematus* [24] and the maximum stress of 2.3 GPa for *Araneus gemmoides* [34].

One study took bundles of 100 dragline and minor ampullate silk threads respectively and pulled them at constant speeds [34]. They observed that physical interactions between the fibers influenced the elongation data and so increased the stretching capabilities of the bundle, compared to that of the single fiber. They saw that *Nephila clavipes* dragline silk had almost double the final stress value compared to the same silk of *Araneus gemmoides*, whilst the minor ampullate silk had roughly the same final stress value [34].

The cave spider *Meta menardi* (Latreille) is generally found in dark and humid places like caves and mines, throughout the northern hemisphere; and from northern Europe to Korea and northern Africa [16]. The cave spider *Meta menardi* has recently been chosen as the "European spider of the year 2012" from the European Society of Arachnology. Since no engineering studies of the egg sac of the cave spider *Meta menardi* yet exist and just few ones have been focused on egg sacs, we decided to conduct tensile tests on stalks of egg sac silk. We tested the stalk which connect the egg sacs of *Meta menardi* to the ceiling of the caves (the arrow, in Fig. 9.2, indicates such sample). In total 15 stalks were found and were pulled until they broke. Samples were viewed under FESEM to analyze the fracture surfaces and measure the diameter of the stalk. To be able to see how the threads were stacked in each stalk, a Focused Ion Beam (FIB) was used to cut the stalk. Using the FESEM micrographies of the cross-section of the FIB-cut stalk and the processing software ImageJ 1.41o, we were able to measure the real diameter and the exact number of single threads in each stalk, improving the accurateness [19]. Thus, the stress-strain curves and the Weibull shape and

scale parameters of the stalk of the egg sac silk of *Meta menardi* are here determined.

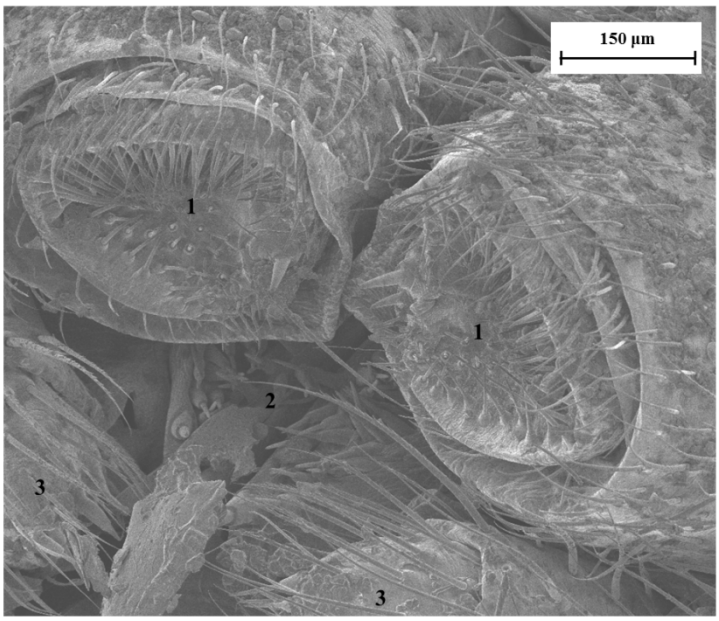

Fig. 9.1 FESEM image of the spinnerets of *Meta menardi* (1. Anterior lateral; 2. Posterior median; 3. Posterior lateral).

Fig. 9.2 Egg sac of the spider *Meta menardi*. Photo by Francesco Tomasinelli (2009).

9.2. Materials and methods

Note that: no specific permits were required for the described field studies, the location is not privately-owned, the field studies did not involve endangered or protected species.

9.2.1. Tensile testing

We identified different caves in Piedmont (a north-western region of Italy) to search for *Meta menardi* egg sacs. The egg sacs are generally spun at the end of summer and hatch in late winter. Fifteen stalks of the egg sacs were taken from the caves in which they were found (Table 9.1). Since the egg sacs were collected in their natural habitat, the measured mechanical stress-

strain behavior of the silk would probably better represent the real characteristics than that produced by lab-reared spiders.
We collected fifteen stalks of the egg sacs in three different caves: four in Grotta Inferiore del Pugnetto, three in Grotta del Bandito and eight in Grotta di Chiabrano. The spiders of this species are generally found in dark areas close to cave opening, where temperature and humidity are still influenced by the external conditions. The egg sacs hung from the ceiling of the cave with a bundle of threads (stalk) and are generally found in ventilated areas. The surveys were done on three separate days. When we found the egg sacs, we carefully took the stalks of the egg sacs from the ceiling of the caves and glued only the stalk ends to 30 x 50 mm^2 cardboard holders, which had a ~20 x 20 mm^2 hole in their center so that the stalk could be suspended to enable the whole to be transported maintaining the original tension of the stalk and mounted on the testing machine without being damaged. All tests were done in the Laboratory of Bio-inspired Nanomechanics "Giuseppe Maria Pugno" (Politecnico di Torino, Italy) with an air temperature of 22 ± 1 °C and 31 ± 2 % relative humidity.
Tensile tests were conducted on thirteen of the fifteen specimens, the remaining two specimens were representatives of the tested samples and examined under the FESEM and FIB. The tensile tests were conducted using a testing machine (Insight 1 kN, MTS, Minnesota, USA), equipped with a 10 N cell load with pneumatic clamps (closure pressure of 275.6 kPa). The cardboard holders were placed between the clamps with an additional double-sided tape defining an initial length l0 in the range from 18 to 19 mm. Once the holders were in place, the clamps were brought to zero tension and then the sides of the holders were cut, leaving the stalk loose between the clamps. The specimens were pulled until they completely broke at a constant rate of 2 mm/min, coherently with the parameter setting of previous studies [20, 23-25, 29, 33, 34, 48].

Cave name	Speleological cadastre number	Municipality	Province	Date	Number of samples
Grotta del Bandito	1002 Pi/CN	Roaschia	Cuneo	02/2011	3
Grotta inferiore del Pugnetto or Tana del lupo	1502 Pi/TO	Mezzenile	Torino	02/2011	4
Grotta di Chiabrano or Tuna del Diau	1621 Pi/TO	Perrero	Torino	02/2011	8

Table 9.1 List of the caves visited for the collection of the samples with collection date and number of samples.

The computer program TestWorks 4 (MTS, Minnesota, USA) recorded the experimental data of the applied tensile force and then the stress-strain curves were computed using the estimation of the real diameter and of the exact number n of single threads at the cross-section of each stalk. Stress σ, strain ε and modulus E, in order, were calculated using the following equations (1, 2, 3):

$$\sigma = \frac{F}{\sum_{i=1}^{n} A_i} = \frac{F}{A_b} \tag{1}$$

$$\varepsilon = \frac{\Delta l}{l_0} \tag{2}$$

$$E = \left.\frac{d\sigma}{d\varepsilon}\right|_0 \tag{3}$$

where F is the force measured by the testing machine, A_b is the initial cross-sectional area of the stalk (given as the initial cross-sectional area A_i of a single thread multiplied by the number n of threads of the stalk), l_0 is the initial length of the stalk and Δl is the change in stalk length during test. The area under the stress-strain curve gives the energy required to break the material, and this variable can be used to quantify toughness. The spider silk dissipates energy in the volume, thus the classical fracture toughness cannot be defined, suggesting intrinsic huge toughening mechanisms.
The stress results of the tensile tests are then treated with the Weibull statistics, which defines the probability of failure P for a stalk as:

$$P(\sigma) = 1 - e^{-\left(\frac{\sigma}{\sigma_0}\right)^m} \tag{4}$$

where σ is the applied stress, m is the Weibull's shape parameter, or Weibull modulus, and σ_0 is the Weibull's scale parameter. The cumulative probability $P_i(\sigma_i)$ can be obtained experimentally as:

$$P_i(\sigma_i) = \frac{i - 1/2}{N} \tag{5}$$

where N is the total number of measured fracture stresses σ_i, ranked in ascending order.

9.2.2. FESEM and FIB characterization

Each stalk was cut by FIB (FEI Quanta 3D FEG, at 5 kV). The real diameter and the exact number of single threads in each stalk was determined using the FESEM (FEI-Inspect™ F50, at 1 - 2 kV) micrographies of the cross-section of the FIB-cut stalk and the processing software ImageJ 1.41o.

9.3. Results

We performed tensile tests of the egg sac silk stalks of *Meta menardi*. The 13 stalks that we found were divided into two groups depending on the type of stalk. We were able to macroscopically distinguish two types of stalk "cable" type (group A) and "ropey" type (group B). The "cable" like stalk was made up of a series of threads tightly packed together forming a very compact structure (Fig. 9.3 a), meanwhile in the "ropey" stalk the threads were not very compacted (Fig. 9.3 b). Group A and B had 4 and 6 stalks, respectively. The remaining stalks did not give us concrete information in terms of tensile strength and were discarded. The tensile tests performed gave very different values in terms of stress, strain and modulus. This motivated us to interpret the results with Weibull statistics.

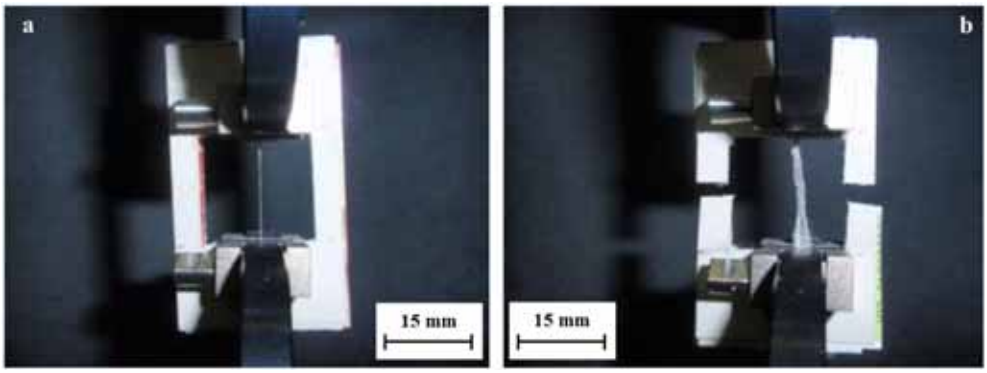

Fig. 9.3 Distinction of the stalk types: cable-like (Group A) (a) and ropey-like (Group B) (b).

The FESEM images showed that the threads that made up the stalks all had similar diameters and all are clearly parallel-oriented (Figs. 9.4 a, b, c). Thus, we were able to assess that each stalk was made up of a certain number of parallel threads, which are all with about the same diameter. In addition, their ends are clamped between the pneumatic clamps with an additional double-sided tape at the closure pressure of 275.6 kPa, which is a high pressure if compared to the testing forces. As a consequence, the macroscopic unraveling of the stalk as well as the slipping of the stalk or of the cardboard holders between the clamps become actually impossible due to the cooperative action of the high closure pressure and of the double-

sided tape, so just the right stretching of the bundle itself becomes allowed. Moreover, no additional length is available for sliding after the clamps so we can exclude artifacts in our observations.
The diameter of the single thread is 6.03 μm (Fig. 9.4 d), which is close to the upper value of the range from 1 to 6 μm indicated in [8], while the diameter of the bundles fell in the range from 200 to 300 μm. The FIB images gave us the opportunity to observe how many silk threads composed each stalk, thus allowing us to calculate the real thread cross-sectional area. Using the FESEM we saw that each stalkwas made up of an average of 150 single silk threads, corresponding to an effective cross section of 4283.67 μm^2.

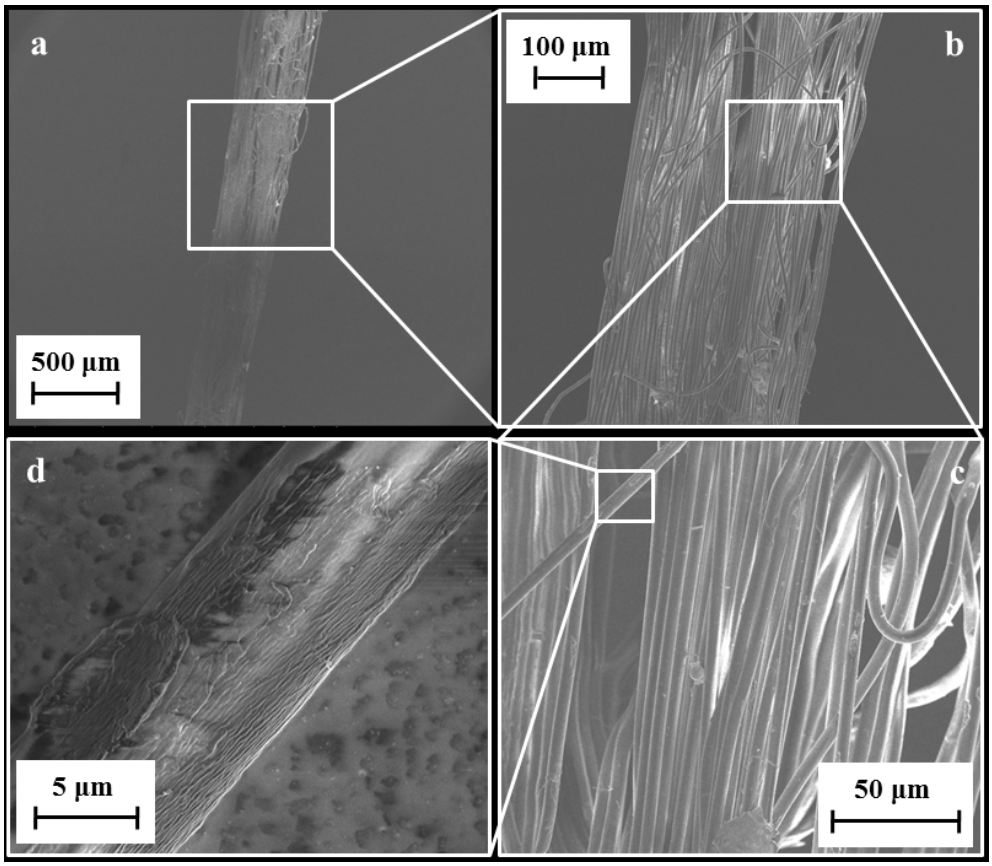

Fig 9.4 FESEM characterization of the silk stalk at different magnifications.

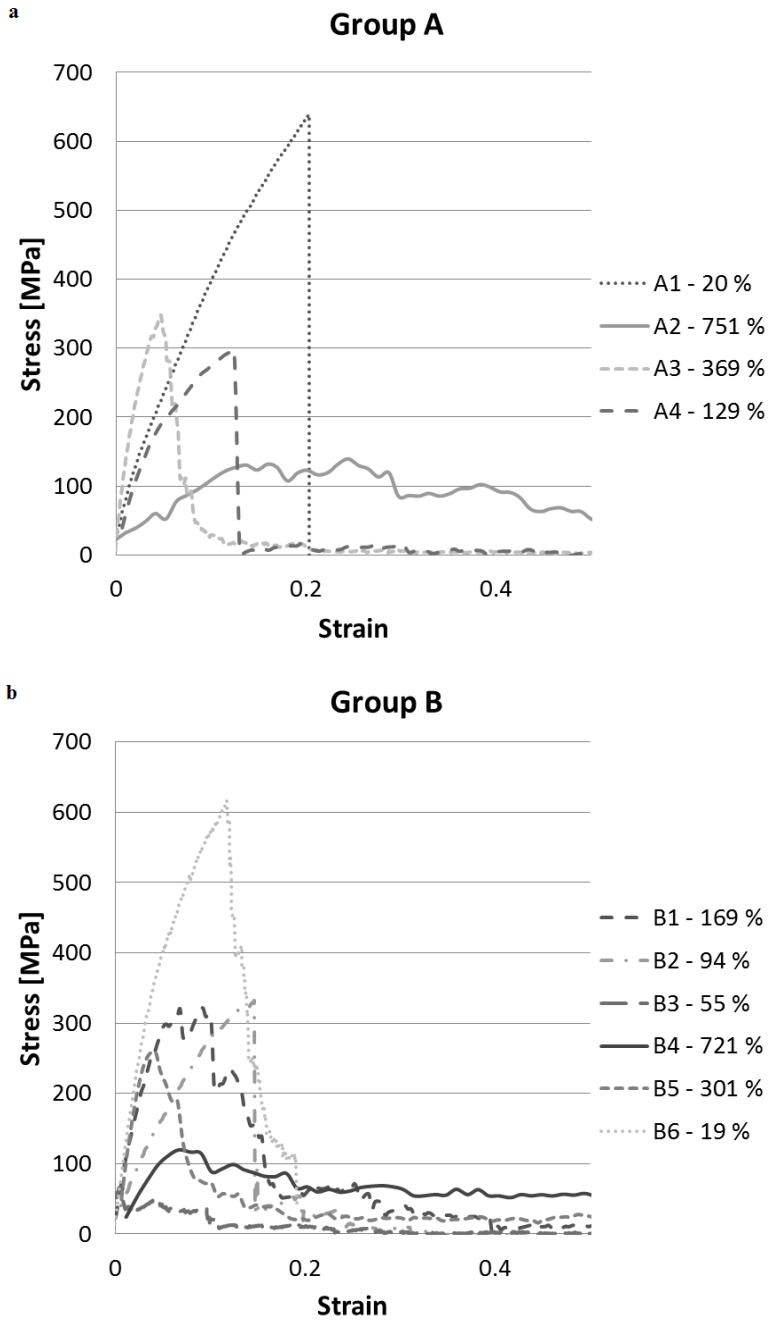

Fig. 9.5 Stress - strain curves of group A (a) or B (b) stalks.

From the various tensile tests, we calculated the average failure stress, which for group A was 0.355 GPa and for group B was 0.286 GPa, even if very scattered. The average failure strain was 318 % for group A and 227 % for group B. The average values of toughness were 76.5 MJ/m^3 for group A and 51.3 MJ/m^3 for group B. Young's modulus is calculated as the initial slope of the stress-strain curve and equal to 20.4 GPa for group A and 22.46 GPa for group B. Figs. 9.5 a, b shows the various stress-strain curves that were characterized.

The stress-strain curves showed different shapes, also caused by the varying number of threads that composed each stalk. The curves had a small initial elastic region which reached a maximum stress which then dropped quickly to very low values, but continuing to large strains until the failure was reached, in some cases through a series of peaks which were caused by the breaking of single or a small number of threads in the stalk. The strain values also differed, but were all above 20 %, with some stalks reaching 300 % strain or more before breaking. Two tests were pulled to an extraordinary length, the maximum strain that they were subject to was 751 % for stalk A2, corresponding to a toughness value of 130.7 MJ/m^3 (represented with solid line in Fig. 9.5 a), and 721 % for stalk B4, corresponding to a toughness value of 117.4 MJ/m^3 (represented with solid line in Fig. 9.5 b).

Following the Weibull statistics, we apply Eq. (4) to the set of fracture stresses of the egg sac silk stalks of *Meta menardi*, reported in Table 9.2. The Weibull modulus m, an index of the dispersion of the stress distribution, is 1.8 for group A (Fig. 9.6 a) and 1.5 for group B (Fig. 9.6 b), whereas σ_0, an index of the mean value of the stress distribution, is equal to 0.409 GPa for group A and 0.326 GPa for group B. Note that the correlation coefficient is high ($R^2 = 0.97$) for both the groups.

Group A		Group B	
Test n°	Stress (GPa)	Test n°	Stress (GPa)
1 (A2)	0.139	1 (B3)	0.067
2 (A3)	0.297	2 (B4)	0.120
3 (A4)	0.347	3 (B5)	0.259
4 (A1)	0.639	4 (B1)	0.322
		5 (B2)	0.332
		6 (B6)	0.617

Table 9.2 The measured stress of each stalk, in ascending order.

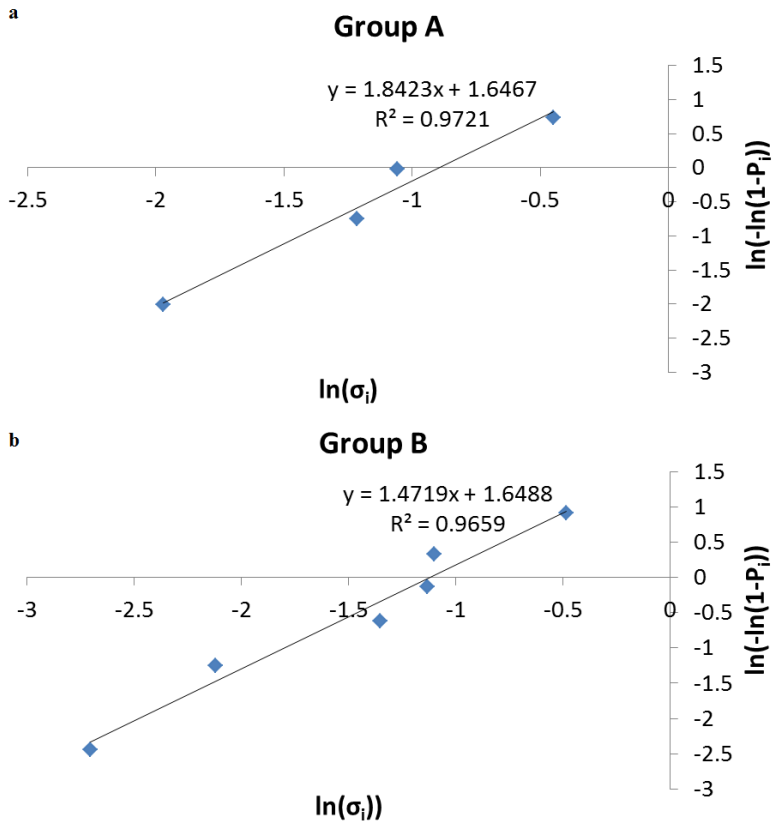

Fig. 9.6 Weibull statistics for stress of group A (a) or B (b) stalks.

9.4. Discussion

Referring to previous scientific studies, scientists focused their attention on different types of silk and mechanically characterized them. Limiting our analysis to tensile tests conducted on egg sac silk, only few studies have been carried out, particularly on *Argiope argentata* [3], *Araneus diadematus* [24], *Nephila madagascariensis* [29], *Argiope bruennichi* [33], *Araneus gemmoides* and *Nephila clavipes* [34]. In addition, the genuses Nephila, Araneus and Meta belong to three related families of orb web weavers (Nephilidae, Araneidae and Tetragnathidae, respectively [16]) and thus general conclusions could be drawn [49]. The shapes of the stress-strain curves that we observed have a similar shape of that for carbon nanotube (CNT) bundles [50, 51]. These curves present a series of kinks or load drops which are an indication of sub-bundle failures when a bundle is pulled in a direction parallel to its axis. As we can see in our data, we also have a series of kinks indicating that the failure of the bundle, once it has reached its peak load, occurs with the fracture of sub-bundles. Though our curves were similar to those of CNT bundles, they were completely different to those of the dragline silk bundles and egg sac silk stalks [34]. Comparing their results to ours, we see that their failure stresses and toughness are much higher.

The β-sheet nanocrystals are held together by hydrogen bonds, one of the weakest chemical bond. It was seen that when a thread is pulled, the force peaks in the force-displacement graph are a confirmation that the hydrogen bonds break and reform at an adjacent hydrogen bond ring. This occurs by preserving the initial side-chain orientation and shifting, or by rotating and forming an opposite side-chain orientation. This leads to a series of force peaks in the mechanical response and increases the total dissipated energy [2]. The size of the β-sheet nanocrystals influences the tensile response of a silk thread, consequently the smaller the crystals the greater the strength and toughness of the thread. As mentioned above, the fibers are made up of semi-amorphous α-chains and β-pleated sheets which are embedded in a rubber like matrix. Images from the FESEM further show that the fibers are made up of 2 layers [38], an inner layer and an outer coating. It seems that some fibers have a polymeric like fracture surface and some have a more regular surface. This second case is probably due to the different crystals that make up the fiber, in fact β-sheets are crystal-like, responsible for the toughness of the thread and have a more fragile rupture. On the other hand

we can assume that some fibers have a very ductile break, caused by the amorphous rubber-like region (Fig. 9.7 a, b).

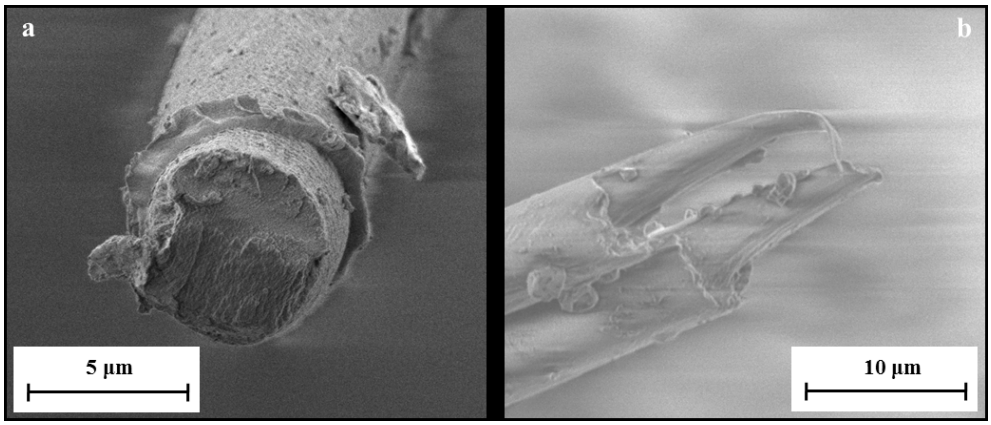

Fig 9.7 Detailed views of fracture surfaces of broken silk fibers.

Having cut our stalk with a FIB, we have been able to observe the cross section of our stalks at a SEM eye angle of 52° (Fig. 9.8 a, b, c) and from the top (Fig. 9.8 d) and thus calculate the stress-strain curves. Each stalk is made up of a series of single silk threads which, when pulled, stack up together to form what we initially hypothesized being a cylindrical cable. The diameters of our egg sac silk threads (~6 µm) were slightly smaller than those of egg sac silk of *Nephila clavipes* (~7 µm) [34] while equal to those of *Argiope bruennichi* [33], but much bigger than the dragline silk (~1.4 µm) of the same species. For comparison, the diameters of dragline silk and minor ampullate in *Nephila clavipes* or *Araneus gemmoides*, were estimated to be 3 and 2.5 µm [34], or 2.5 and 2 µm [33], respectively.

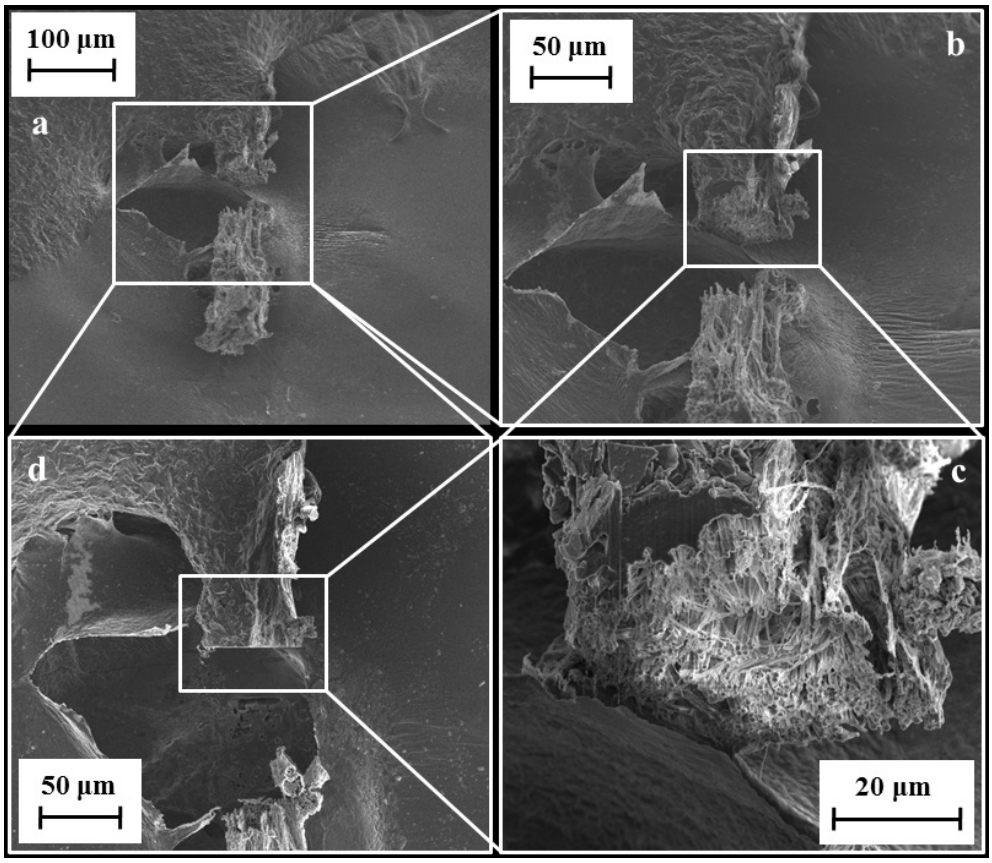

Fig. 9.8 FESEM characterization of the stalk cut with FIB: (a, b, c) at an eye angle of 52°, (d) from the top.

Surprisingly, the strains that our fibers sustained were impressively high, some stalks were pulled to more than 200 %, reaching values of 721 - 751 %, which have not been seen in any spider single thread or stalk of egg sac silk yet. Such enormous elongations suggest a huge unrolling mechanism in the stalk.

In Figs. 9.9-9.11, we report toughness, ultimate stress and ultimate strain respectively for different types of spider silks; specifically in Fig. 9.11 our record of ultimate strain clearly emerges. The reason for this very high strain is yet unknown but could be caused by an interaction and different disposition of the α-chains and β-pleated sheets within the fibers thus giving them the possibility to stretch to such high strain values. As stated in the

introduction, it has been observed that physical interactions between the fibers could influence the elongation data and so increased the stretching capabilities of the stalk, compared to that of the single fiber [34]. We saw that the extreme strain of the stalks could be caused by a macroscopic unraveling of the stalk it self. The failure strains of the egg sac silk of *Araneus diadematus* reached values of 30-40 %, much lower than our strains [24]. Egg sac threads from *Nephila clavipes* extended 24 ± 2 % their initial length and the maximum stress was 1.3 ± 0.2 GPa whereas for *Araneus gemmoides* these values were respectively 19 ± 2 % and 2.3 ± 0.2 GPa [34].

The failure stresses of our stalks were much inferior to these, but the strains sustained by them were much higher, probably due to physical interactions within the stalks and the type of deformation that occurred at the nanoscale. Bundles of dragline and minor ampullate silk made up of 100 threads were also tested [34] and showed a wide range over which they broke and thus these authors were not able to determine a useful value for the tensile strength of the fiber bundles due to the fact that there was a great variety in the diameters of the threads that made up the bundle [34]. We have here solved this problem using Weibull statistics and our results (m is in the range from 1.5 to 1.8 and σ_0 is in the range from 0.33 to 0.41 GPa) are in line with the values of the shape (m) and scale (σ_0) parameters of Weibull statistics which are equal to 3.4 and 0.6 GPa for the dragline of *Argiope trifasciata* [17] or equal to 5.7 and 0.4 GPa for the silkworm cocoons of *Bombyx mori* [52], respectively.

The great standard deviation in the values of our stress and strain results within the two groups of stalks could be due to the fact that they differed in terms of diameter, number of threads and the physical condition of the stalks that also may affect the performances, see Table 9.3. The stalks were all taken from the natural habitat of the spider where humidity and temperature play an important role. As it was seen moisture induces supercontraction in the threads thus causing them to tighten up [20], the temperature of the caves was roughly 9 ± 2 °C, while the tests were done in an environment where the temperature was much higher and could have caused the fibers to change their natural state. The tests were also done a couple of days after collecting the stalks and were kept in the laboratory in different conditions, causing the threads to lose or modify some properties.

We observed that the higher the stress that the stalk could sustain, the lower the maximum strain before breakage. If strain reached high values the peak stresses did not exceed 0.64 GPa. In this case, we assume that the thread

deformed in a rubber like way, extending to great values, due to physical interactions [54-57] between the threads composing the stalk.

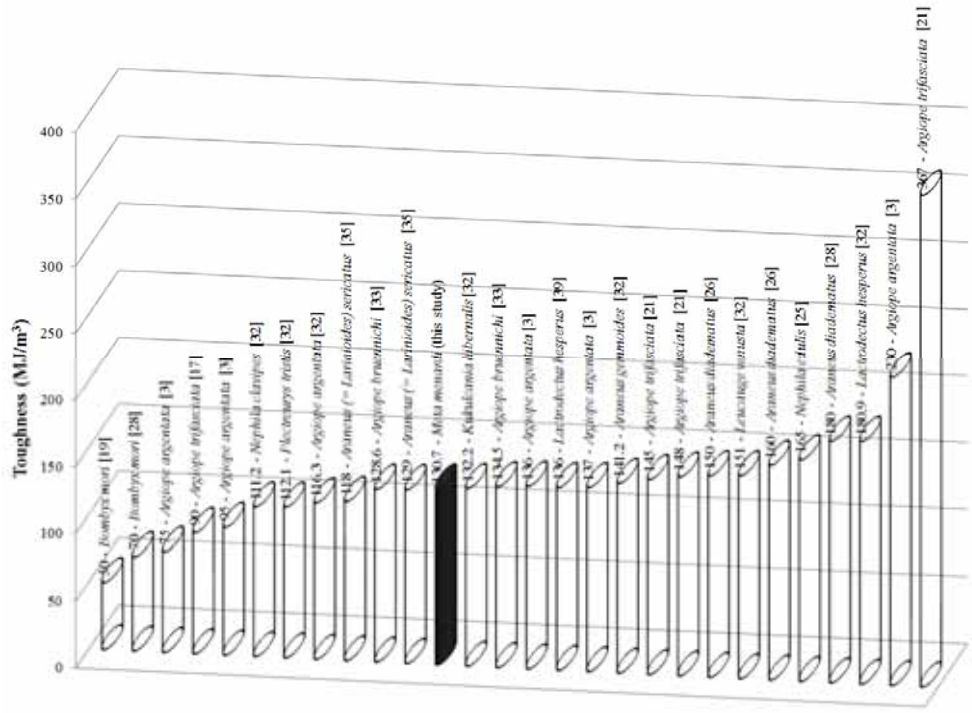

Fig. 9.9 The maximum toughness of different types of (mainly spider) silks.

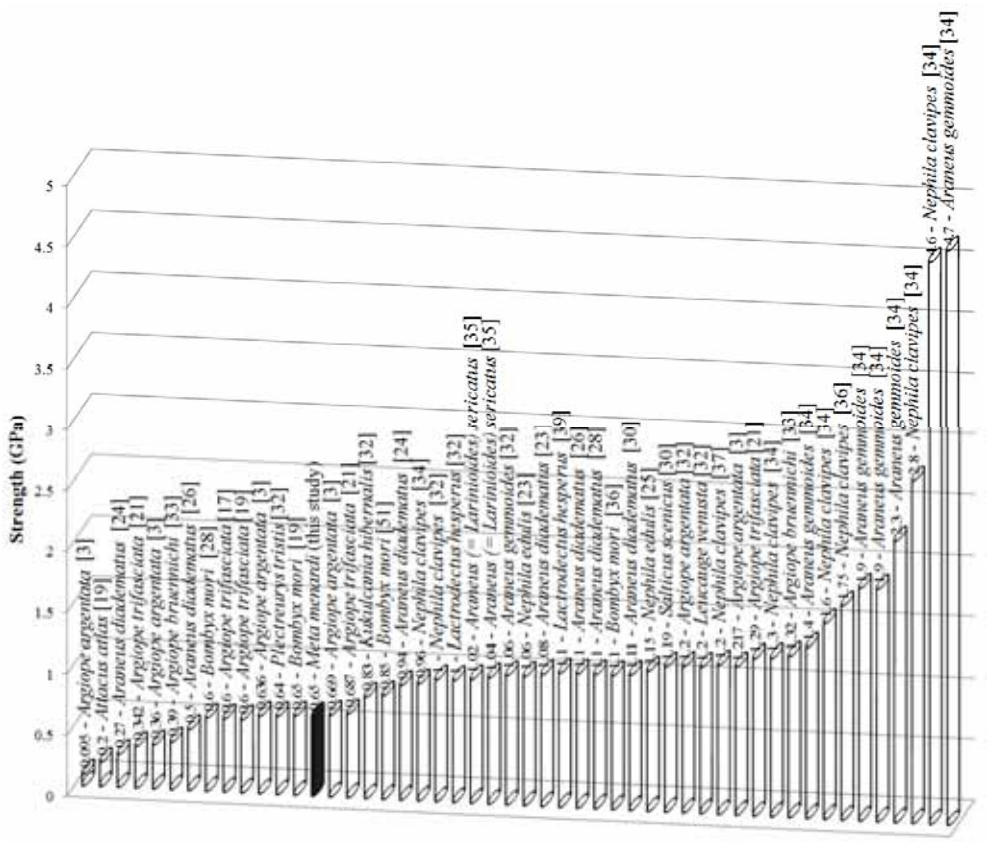

Fig. 9.10 The maximum strength of different types of (mainly spider) silks.

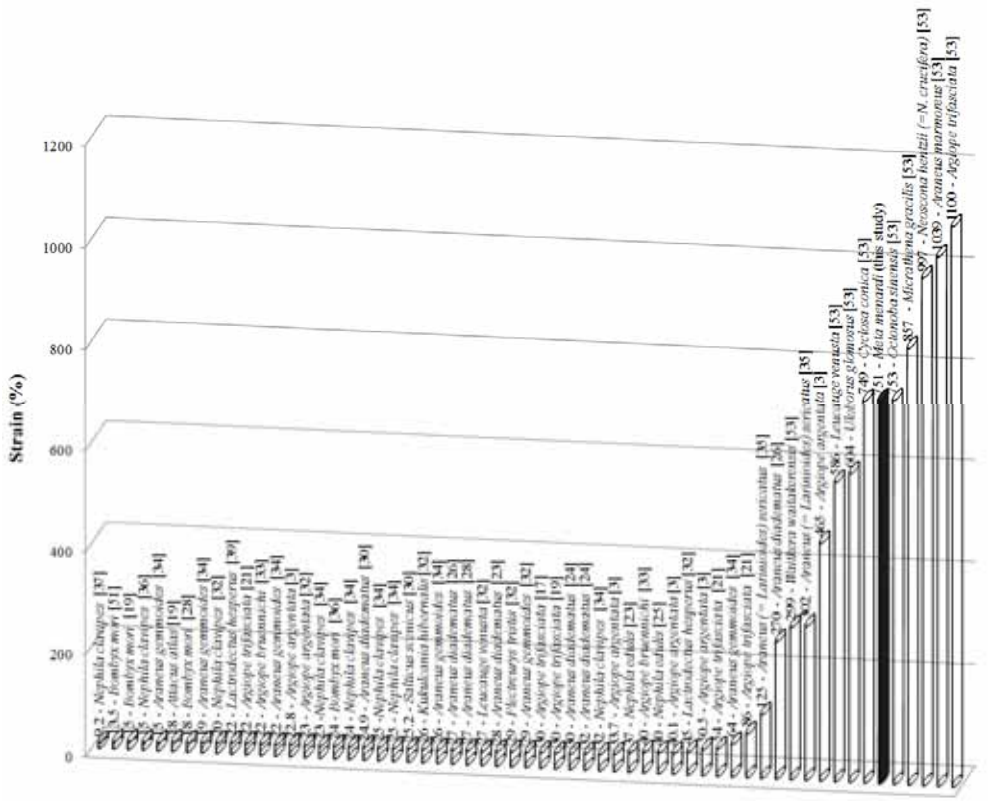

Fig. 9.11 The maximum strain of different types of (mainly spider) silks, showing the record for egg sac silk stalks observed in our experiments.

Ref.	Class, Order	Family	Species	Function	Glands	Experimental conditions (temperature and humidity)	l_0	Number of threads	Strain rate	Number of samples
[24]	Arachnida, Araneae	Araneidae	*Araneus diadematus*	egg sac	tubuliform (cylindrical)	wet (20 °C, 65 %)	20 mm	1	20 mm/min	398
[24]	Arachnida, Araneae	Araneidae	*Araneus diadematus*	structural threads and dragline	major ampullate	wet (20 °C, 65 %)	20 mm	1	20 mm/min	183
[26]	Arachnida, Araneae	Araneidae	*Araneus diadematus*	structural threads and dragline	major ampullate	not given	not given	not given	not given	not given
[28]	Arachnida, Araneae	Araneidae	*Araneus diadematus*	structural threads and dragline	major ampullate	not given	not given	not given	not given	not given
[23]	Arachnida, Araneae	Araneidae	*Araneus diadematus*	structural threads and dragline	major ampullate	wet (24 °C, 50 %)	6.9 mm	1	3 mm/min	30
[30]	Arachnida, Araneae	Araneidae	*Araneus diadematus*	structural threads and dragline	major ampullate	not given	not given	2	14-20 mm/min	16
[26]	Arachnida, Araneae	Araneidae	*Araneus diadematus*	glue coating on viscid capture threads	aggregate glands	not given	not given	not given	not given	not given
[34]	Arachnida, Araneae	Araneidae	*Araneus gemmoides*	auxiliary radial threads and temporary scaffolding	minor ampullate	not given	40 mm	1	5 mm/min	10
[34]	Arachnida, Araneae	Araneidae	*Araneus gemmoides*	egg sac	tubuliform (cylindrical)	not given	40 mm	1	5 mm/min	10
[34]	Arachnida, Araneae	Araneidae	*Araneus gemmoides*	structural threads and dragline	major ampullate	not given	40 mm	1	5 mm/min	10
[32]	Arachnida, Araneae	Araneidae	*Araneus gemmoides*	structural threads and dragline	major ampullate	not given	not given	1	1 % strain/s	23
[34]	Arachnida, Araneae	Araneidae	*Araneus gemmoides*	auxiliary radial threads and temporary scaffolding	minor ampullate	not given	40 mm	100	5 mm/min	10
[34]	Arachnida, Araneae	Araneidae	*Araneus gemmoides*	structural threads and dragline	major ampullate	not given	40 mm	100	5 mm/min	10
[35]	Arachnida, Araneae	Araneidae	*Araneus (= Larinioides) sericatus*	structural threads and dragline	major ampullate	wet (21 °C, 50 %)	25 mm	1	13.2 mm/min	60
[35]	Arachnida, Araneae	Araneidae	*Araneus (= Larinioides) sericatus*	glue coating on viscid capture threads	aggregate glands	wet (21 °C, 50 %)	25 mm	1	217.1 mm/min	41
[53]	Arachnida, Araneae	Araneidae	*Araneus marmoreus*	adhesive threads of the catching spiral	flagelliform glands	wet (23 °C, 60 %)	20 mm	1	0.017 mm/min	3
[3]	Arachnida, Araneae	Araneidae	*Argiope argentata*	structural threads and dragline	major ampullate	wet (21.5 °C, 45 %)	21 mm	1	12.6 mm/min (1 % strain/s)	13
[32]	Arachnida, Araneae	Araneidae	*Argiope argentata*	structural threads and dragline	major ampullate	not given	not given	1	1 % strain/s	62
[3]	Arachnida, Araneae	Araneidae	*Argiope argentata*	wrapping silk and packing silk	aciniform gland	wet (21.5 °C, 45 %)	10 mm	1	6 mm/min (1 % strain/s)	28
[3]	Arachnida, Araneae	Araneidae	*Argiope argentata*	adhesive capture threads of the catching spiral	flagelliform glands	wet (21.5 °C, 45 %)	21 mm	1	12.6 mm/min (1 % strain/s)	87
[3]	Arachnida, Araneae	Araneidae	*Argiope argentata*	auxiliary radial threads and temporary scaffolding	minor ampullate	wet (21.5 °C, 45 %)	21 mm	1	12.6 mm/min (1 % strain/s)	51
[3]	Arachnida, Araneae	Araneidae	*Argiope argentata*	egg sac	tubuliform (cylindrical)	wet (21.5 °C, 45 %)	21 mm	1	12.6 mm/min (1 % strain/s)	29
[33]	Arachnida, Araneae	Araneidae	*Argiope bruennichi*	egg sac	tubuliform (cylindrical)	wet (24 °C, 34 %)	20 mm	1	10 mm/min	4

[33]	Arachnida, Araneae	Araneidae	*Argiope bruennichi*	structural threads and dragline	major ampullate	wet (24 °C, 34 %)	20 mm	1	10 mm/min	4
[17]	Arachnida, Araneae	Araneidae	*Argiope trifasciata*	structural threads and dragline	major ampullate	wet (20 °C, 60 %)	20 mm	1	0.24 mm/min ($2*10^{-4}$ /s)	28
[21]	Arachnida, Araneae	Araneidae	*Argiope trifasciata*	structural threads and dragline	major ampullate	not given	21 mm	1	12.6 mm/min (1 % strain/s)	7
[19]	Arachnida, Araneae	Araneidae	*Argiope trifasciata*	structural threads and dragline	major ampullate	wet (20 °C, 60 %)	10 mm	1	0.12 mm/min ($2*10^{-4}$ /s)	10
[21]	Arachnida, Araneae	Araneidae	*Argiope trifasciata*	wrapping silk and packing silk	aciniform gland	not given	10 mm	2	6 mm/min (1 % strain/s)	14
[21]	Arachnida, Araneae	Araneidae	*Argiope trifasciata*	auxiliary radial threads and temporary scaffolding	minor ampullate	not given	21 mm	2	12.6 mm/min (1 % strain/s)	11
[53]	Arachnida, Araneae	Araneidae	*Argiope trifasciata*	adhesive threads of the catching spiral	flagelliform glands	wet (23 °C, 60 %)	20 mm	1	0.017 mm/min	3
[53]	Arachnida, Araneae	Araneidae	*Micrathena gracilis*	adhesive threads of the catching spiral	flagelliform glands	wet (24 °C, 60 %)	20 mm	1	0.017 mm/min	3
[53]	Arachnida, Araneae	Araneidae	*Neoscona hentzii (= N. crucifera)*	adhesive threads of the catching spiral	flagelliform glands	wet (23 °C, 60 %)	20 mm	1	0.017 mm/min	3
[53]	Arachnida, Araneae	Araneidae	*Cyclosa conica*	adhesive threads of the catching spiral	flagelliform glands	wet (25 °C, 61 %)	20 mm	1	0.017 mm/min	3
[53]	Arachnida, Araneae	Uloboridae	*Octonoba sinensis*	dry cribellar capture threads of the catching spiral	flagelliform glands	wet (23 °C, 61 %)	20 mm	1	0.017 mm/min	3
[53]	Arachnida, Araneae	Uloboridae	*Uloborus glomosus*	dry cribellar capture threads of the catching spiral	flagelliform glands	wet (24 °C, 62 %)	20 mm	1	0.017 mm/min	3
[53]	Arachnida, Araneae	Uloboridae	*Waitkera waitakerensis*	dry cribellar capture threads of the catching spiral	flagelliform glands	wet (25 °C, 70 %)	20 mm	1	0.017 mm/min	3
[32]	Arachnida, Araneae	Filistatidae	*Kukulcania hibernalis*	dragline	major ampullate	not given	not given	1	1 % strain/s	102
[32]	Arachnida, Araneae	Theridiidae	*Lactrodectus hesperus*	structural threads and dragline	major ampullate	not given	not given	1	1 % strain/s	70
[39]	Arachnida, Araneae	Theridiidae	*Lactrodectus hesperus*	auxiliary radial threads and temporary scaffolding	minor ampullate	not given	12 mm	30	12.6 mm/min	30
[32]	Arachnida, Araneae	Tetragnathidae	*Leucauge venusta*	structural threads and dragline	major ampullate	not given	not given	1	1 % strain/s	61
[53]	Arachnida, Araneae	Tetragnathidae	*Leucauge venusta*	adhesive threads of the catching spiral	flagelliform glands	wet (25 °C, 60 %)	20 mm	1	0.017 mm/min	3
this study	Arachnida, Araneae	Tetragnathidae	*Meta menardi*	egg sac	tubuliform (cylindrical)	wet (22 °C, 31 %)	18-19 mm	150	2 mm/min	10
[34]	Arachnida, Araneae	Nephiliidae	*Nephila clavipes*	auxiliary radial threads and temporary scaffolding	minor ampullate	not given	40 mm	1	5 mm/min	10
[34]	Arachnida, Araneae	Nephiliidae	*Nephila clavipes*	egg sac	tubuliform (cylindrical)	not given	40 mm	1	5 mm/min	10
[34]	Arachnida, Araneae	Nephiliidae	*Nephila clavipes*	structural threads and dragline	major ampullate	not given	40 mm	1	5 mm/min	10
[32]	Arachnida, Araneae	Nephiliidae	*Nephila clavipes*	structural threads and dragline	major ampullate	not given	not given	1	1 % strain/s	66
[36]	Arachnida, Araneae	Nephiliidae	*Nephila clavipes*	structural threads and dragline	major ampullate	wet (23 °C, 49 %)	12.7 mm	1	12.7 mm/min (100 %/min)	19

[37]	Arachnida, Araneae	Nephiliidae	*Nephila clavipes*	structural threads and dragline	major ampullate	wet (21 °C, 50 %)	50.8 mm	1	304.8 mm/min (10 % strain/s)	30
[34]	Arachnida, Araneae	Nephiliidae	*Nephila clavipes*	auxiliary radial threads and temporary scaffolding	minor ampullate	not given	40 mm	100	5 mm/min	10
[34]	Arachnida, Araneae	Nephiliidae	*Nephila clavipes*	structural threads and dragline	major ampullate	not given	40 mm	100	5 mm/min	10
[23]	Arachnida, Araneae	Nephiliidae	*Nephila edulis*	structural threads and dragline	major ampullate	wet (24 °C, 50 %)	6.9 mm	1	3 mm/min	30
[25]	Arachnida, Araneae	Nephiliidae	*Nephila edulis*	structural threads and dragline	major ampullate	wet (22 °C, 50 %)	12 mm	1	6 mm/min (50 % strain/min)	not given
[32]	Arachnida, Araneae	Plectreuridae	*Plectreurys tristis*	dragline	major ampullate	not given	not given	1	1 % strain/s	108
[30]	Arachnida, Araneae	Salticidae	*Salticus scenicus*	dragline	major ampullate	not given	not given	2	14-20 mm/min	5
[19]	Insecta, Lepidoptera	Saturniidae	*Attacus atlas*	cocoon	silk glands	wet (20 °C, 60 %)	30 mm	1	0.36 mm/min ($2*10^{-4}$ /s)	10
[28]	Insecta, Lepidoptera	Bombycidae	*Bombyx mori*	cocoon	silk glands	not given	not given	not given	not given	not given
[19]	Insecta, Lepidoptera	Bombycidae	*Bombyx mori*	cocoon	silk glands	wet (20 °C, 60 %)	30 mm	1	0.36 mm/min ($2*10^{-4}$ /s)	10
[51]	Insecta, Lepidoptera	Bombycidae	*Bombyx mori*	cocoon	silk glands	wet (20 °C, 60 %)	40 mm	1	0.48 mm/min (0.0002 /s)	10
[36]	Insecta, Lepidoptera	Bombycidae	*Bombyx mori*	cocoon	silk glands	wet (23 °C, 49 %)	12.7 mm	1	3.81 mm/min (30 %/min)	20

Table 9.3 The main parameters which may influence tensile testing results: systematics, function, silk-producing glands, temperature and humidity, initial length (l_0) of samples, number of tested threads, selected strain rate and number of tested samples. Spider nomenclature according to [16].

9.5. Conclusion

The tensile properties and the Weibull shape and scale parameters of stalks of egg sac silk of *Meta menardi*, obtained directly from their natural habitat, were here determined. The results that were gathered from the tests differed significantly when compared to other tensile tests on spider silk. Whether the comparison is done with egg sac silk from other species of orbweb weavers, dragline silk or minor ampullate silk, the results are much higher, up to 750 %, to those reported in all the previous studies in terms of maximum strain of egg sac silk, suggesting the discovery of the most stretchable egg sac silk stalk ever tested. Such enormous elongations suggests a huge unrolling microscopic mechanism of the macroscopic stalk that, as a continuation of the protective egg sac, is expected to be composed by fibres very densely and randomly packed.

ACKNOWLEDGMENTS

We thank the “Nanofacility Piemonte” for the FESEM imaging instruments and E. Enrico, INRIM Institute, for the fundamental help performing the FESEM micrographs.

REFERENCES

[1] Brunetta, L., and Craig, C. L., Spider Silk, Evolution and 400 Million Years of Spinning, Waiting, Snagging, and Mating. Csiro Publishing (2010).
[2] Keten, S., Xu, Z., Ihle, B., and Buelher, M. J., *Nature Materials* **9**, 359-367 (2010).
[3] Blackledge, T. A., and Hayashi, C. Y., *J. Exp. Biol.* **209**, 2452-2461 (2006).
[4] Blackledge, T. A., Kuntner, M., and Agnarsson, I., *Adv. Insect Physiol.* **41**, 175-262 (2011).
[5] Rousseau, M. E., Lefevre, T., and Pezolet, M., *Biomacromolecules* **10**, 2945-2953 (2009).
[6] Eberhard, W. G., *J. Arachnol.* **38**, 407-414 (2010).
[7] Kovoor, J., Ecophysiology of Spiders. Berlin: Springer-Verlag. 160-186 (1987).

[8] Foelix, R. F., Biology of Spiders. New York: Oxford University Press (1996).
[9] Foradori, M. J., Kovoor, J., Moon, M. J., and Tillinghast, K., *J. Morphol.* **252**, 218-226 (2002).
[10] Craig, C. L., Spider Webs and Silk: Tracing Evolution from Molecules to Genes to Phenotypes. New York: Oxford University Press (2003).
[11] Gheysens, T., Beladjal, L., Gellynck, K., Van Nimmen, E., Van Langenhove, L., and Mertens, J., *J. Arachnol.* **33**, 549-557 (2005).
[12] Hajer, J., Maly, J., Hruba, L., and Rehakova, D., *J. Morphol.* **270**, 1269-1283 (2009).
[13] Vasanthavada, K., Hu, X., Falick, A. M., La Mattina, C., Moore, A. M. F., Jones, P. R., Yee, R., Reza, R., Tuton, T., and Vierra, C., *J. Biol. Chem.* **282**, 35088-35097 (2007).
[14] Van Nimmen, E., Gellynck, K., Van Langenhove, L., and Mertens, J., *Text Res. J.* **76**, 619-628 (2006).
[15] Vehoff, T., Glišović, A., Schollmeyer, H., Zippelius, A., and Salditt, T., *Biophys. J.* **93**, 4425-4432 (2007).
[16] Platnick, N. I., The world spider catalogue. version 12.0. American Museum of Natural History (2011).
[17] Perez-Rigueiro, J., Elices, M., Llorca, J., and Viney, C., *J. Appl. Polym. Sci.* **82**, 2245-2251 (2001).
[18] Elices, M., Pérez-Rigueiro, J., Plaza, G. R., and Guinea, G. V., *J. Mineral Metals Materials Soc.* **57**, 60-66 (2005).
[19] Poza, P., Perez-Rigueiro, J., Elices, M., and Llorca, J., *Eng. Fract. Mech.* **69**: 1035-1048 (2002).
[20] Guinea, G. V., Elices, M., Perez-Rigueiro, J., and Plaza, G., *Polymer* **44**, 5785-5788 (2003).
[21] Hayashi, C. Y., Blackledge, T. A., and Lewis, R. V., *Mol. Biol. Evol.* **21**, 1950-1959 (2004).
[22] Van Nimmen, E., Gellynck, K., and Van Langenhove, L., *Autex Research Journal* **5**, 120-126 (2005).
[23] Madsen, B., Shao, Z. Z., and Vollrath, F., *Int. J. Biol. Macromol.* **24**, 301-306 (1999).
[24] Van Nimmen, E., Gellynck, K., Gheysens, T., Van Langenhove, L., and Mertens, J., *J. Arachnol.* **33**, 629-639 (2005).
[25] Vollrath, F., Madsen, B., and Shao, Z., Proc. R Soc. Lond. B **268**, 2339-2346 (2001).
[26] Gosline, J. M., Guerette, P. A., Ortlepp, C. S., and Savage, K. N., J. Exp. Biol. **202**, 3295-3303 (1999).

[27] Köhler, T., and Vollrath, F., *J. Exp. Zool.* **271**, 1-17 (1995).
[28] Römer, L., and Scheibel, T., *Prion* **4**, 154-161 (2008).
[29] Gosline, J. M., Demont, E. M., and Denny, M. W., *Endeavor* **10**, 37-44 (1986).
[30] Ortlepp, C., and Gosline, J. M., *J. Exp. Biol.* **211**, 2832-2840 (2008).
[31] Shao, Z., and Vollrath, F., *Polymer* **40**, 1799-1806 (2008).
[32] Swanson, B. O., Blackledge, T. A., Beltran, J., and Hayashi, C. Y., *Appl. Phys. A-Mater.* **82**, 213-218 (2006).
[33] Zhao, A. C., Zhao, T. F., Nakagaki, K., Zhang, Y. S., SiMa, Y. H., Miao, Y. G., Shiomi, K., Kajiura, Z., Nagata, Y., Takadera, M., and Nakagaki, M., *Biochemistry* **45**, 3348-3356 (2006).
[34] Stauffer, S. L., Coguill, S. L., and Lewis, R. V., *J. Arachnol.* **22**, 5-11 (1994).
[35] Denny, M., *J. Exp. Biol.* **65**, 483-506 (1976).
[36] Dunaway, D. L., Thiel, B. L., and Viney, C., *J. Appl. Polym. Sci.* **58**, 675-683 (1995).
[37] Cunniff, P. M., Fossey, S. A., Auerbach, M. A., Song, J. W., Kaplan, D. L., Adams, W. W., Eby, R. K., Mahoney, D., and Vezie, D. L., *Polym. Advan. Technol.* **5**, 401-410 (1994).
[38] Vollrath, F., Holtet, T., Thorgensen, H. C., and Frische, S., *Proc. Biol. Sciences* **263**, 147-151 (1996).
[39] Moore, A. M. F., and Tran, K., *Int. J. Biol. Macromol.* **24**, 277-282 (1999).
[40] Craig, C. L., Spiderwebs and silk: Tracing evolution from molecules to genes to phenotypes. New York: Oxford University Press (2003).
[41] Sensenig, A., Agnarsson, I., and Blackledge, T. A., *J. Evolution. Biol.* **23**, 1839-1856 (2010).
[42] Boutry, C., Řezáč, M., and Blackledge, T. A., *PLoS ONE* **6**, 1-8 (2011).
[43] Keten, S., and Buehler, M. J., *J. R. Soc. Interface* **7**, 1709-1721 (2010).
[44] Krasnov, I., Diddens, I., Hauptmann, N., Helms, G., Ogurreck, M., Seydel, T., Funari, S. S., and Müller, M., *Phys. Rev. Lett.* **100**, 1-4 (2008).
[45] Gosline, J. M., Denny, M. W., and Demont, M. E., *Nature* **309**, 551-552 (1984).
[46] Nova, A., Keten, S., Pugno, N. M., Redaelli, A., and Buehler, M. J., *Nano Letters* **10**, 2626-2634 (2010).
[47] Agnarsson, I., Kuntner, M., and Blackledge, T. A., *PLoS ONE* **5**, 1-8 (2010).

[48] Álvarez-Padilla, F., Dimitrov, D., Giribet, G., and Hormiga, G., *Cladistics* **25**, 109-146 (2009).
[49] Xiao, T., Ren, Y., Liao, K., Wu, P., Li, F., and Chen, H.M., *Compos. Sci. Technol.* **68**, 2937-2942 (2008).
[50] Bosia, F., Buelher, M. J., and Pugno, N. M., *Phys. Rev. E* **82**, 056103, 1-7 (2010).
[51] Perez-Rigueiro, J., Viney, C., Llorca, J., and Elices, M., *J. Appl. Polym. Sci.* **75**, 1270-1277 (2000).
[52] Perez-Rigueiro, J., Viney, C., Llorca, J., and Elices, M., *J. Appl. Polym. Sci.* **70**, 2439-2447 (1998).
[53] Opell, B. D., and Bond, J. E., *Biol. J. Linn. Soc.* **70**, 107-120 (2000).
[54] Pugno, N. M., *J. Mech. Phys. Solids* **58**, 1397-1410 (2010).
[55] Allmeling, C., Jokuszies, A., Reimers, K., Kall, S., and Vogt, P. M., *J. Cell. Mol. Med.* **10**, 770-777 (2006).
[56] Dal Pra, I., Freddi, G., Minic, J., Chiarini, A., and Armato, U., *Biomaterials* **26**, 1987-1999 (2005).
[57] Dal Pra, I., Chiarini, A., Boschi, A., Freddi, G., and Armato, U., *Int. J. Mol. Med.* **18**, 241-247 (2006).

APPENDIXES

Appendix I. TOPOLOGICAL AND STATISTICAL OBSERVATIONS ON THE SKIN OF TOKAY GECKOS AS AN INSPIRATION FOR AN ARTIFICIAL ADHESIVE HUMAN SUIT

Abstract

We report the experimental description of the entire (about 10 hours long) moulting process of a female tokay gecko (*Gekko gecko*) and the related observations on its skin topology. A statistical analysis on the skin tessellation has been performed. A detailed field emission scanning electron microscopy (FESEM) characterization of the complete adhesive system of the gecko's foot, discovering new peculiarities, as well as of four samples of skin taken from the gecko's back, upper tail, abdomen and upper head is carried out. The gecko's skin shows unexpected complexity, *e.g.* it is covered by nano-hooks (0.2-1.5 μm in length and ~30-50 nm in diameter) superimposed to the evident nearly circular tessellations (circularity ~0.9; area ~0.5 mm^2, perimeter ~3 mm). The skin of the eye seems to be fully anti-adhesive.

I.1. Introduction

After the pioneering observation by Aristotele [1], biologists and material scientists posed their attention on the adhesive abilities of geckos and similar creatures [2-17] and are nowadays renewing their interest on tokay gecko (*Gekko gecko*) [18-28], which displays the strongest dry adhesion known in nature. Technological applications are consequently envisioned and recently the feasibility of Spiderman Suits has been demonstrated [29, 30]. Fracture Mechanics approaches, able to solve problems in extremely different contexts [31-35], are expected to play a fundamental role in better understanding the animal's adhesion.
The epidermal adhesive layer, entirely covering the reptile, has a complex multi-structure: it consists of a new (inner) generation, formed beneath the

older (outer) generation and each of them is constituted by six distinct layers. In the period between two next moults, the formation of a new inner generation initiates and goes on, so that the older generation is shed during the next moult. As a consequence, the gecko replaces the outer generation with a complete new one at each shedding cycle [23].
Casual observations reveal little about the mechanism and time scale of the moulting process. We know that although geckos are not known to groom their feet yet retain their stickiness and clearness for all months between two next moulting processes: gecko setae become cleaner with repeated use, thus self-cleaning [24]. However, it was also showed that the gecko's adhesive ability of clinging to inclined surfaces decreased constantly over a period of one month after the molting process [12, 24]. Thus the mechanism of the moulting process remains partially unclear.
The aim of this paper is firstly to describe the entire moulting process of a female tokay gecko in terms of time and animal actions through a 16h-video recorded. Secondly, four pieces of the gecko's old skin were taken from four different parts of the gecko's body, FESEM-analysed and characterized *via* a topological statistical analysis. A unexpected complexity is observed. The eye skin seems to be fully anti-adhesive.

I.2. Materials and methods

I.2.1 Moulting process

The entire moulting process, about 10 hours long, of a 50 g female tokay gecko (here called G1) was experimentally video recorded. The animal was left in its terrarium (a Poly(methyl meth-acrylate), *i.e.* PMMA, box of sizes 32 x 32 x 38 cm^3), provided with several air inlets and with the bottom covered with a natural reptile bedding (Repti Bark).
The considered gecko had been maintained in captivity prior to the analysed moult and was in perfect health condition before, during and after the observation. Gecko was maintained in its terrarium at ~28 °C. The temperature of the room, in which the entire moulting process was observed, was ~22 °C. Gecko fed moths and water *ad libitum* and crickets two times per week. The gecko feeding was maintained always the same. The animal did not show any kind of discomfort, any symptoms of suffering or distress

and, in addition, any lasting physical damages for the absolutely natural conditions of our observations.

I.2.2. FESEM observations

We accurately performed detailed FESEM analyses of the gecko's skin topology, naturally shed during the moulting process. We observed different gecko's body parts: back and upper tail of G1 (Figs. I.1A, I.1C and I.1B, I.1D respectively before and after specimen removal), abdomen and eyes of a 64 g male adult tokay gecko (denoted by G2) (Figs. I.1E, I.1G and I.1F, I.1H respectively before and after specimen removal).
Referring to Figs. I.2-I.5, the investigations of the three dimensional structures of the skin surface were carried out only with FESEM (Zeiss SUPRA 40). To avoid alteration of the thin superficial structures, no fixation procedure was applied to the gecko's skin. Samples of about ~0.8 mm^2 were cut (see Fig. I.1) and fixed to aluminium stubs by double-sided adhesive carbon tape (Nisshin EM Co. Ltd.), 6h air-dried and chrome-coated (approx. 25 nm).

I.2.3. Statistical analysis

The gecko's skin was statistically analysed using the software ImageJ 1.41o. The number of the evident roughly circular structures, their area, perimeter and circularity were quantified considering statistically representative areas of 5 x 5 mm^2. The unit scales of area and perimeter are mm^2 and mm, respectively. The values of the circularity vary in the range from 0 (straight line) to 1 (perfect circle).

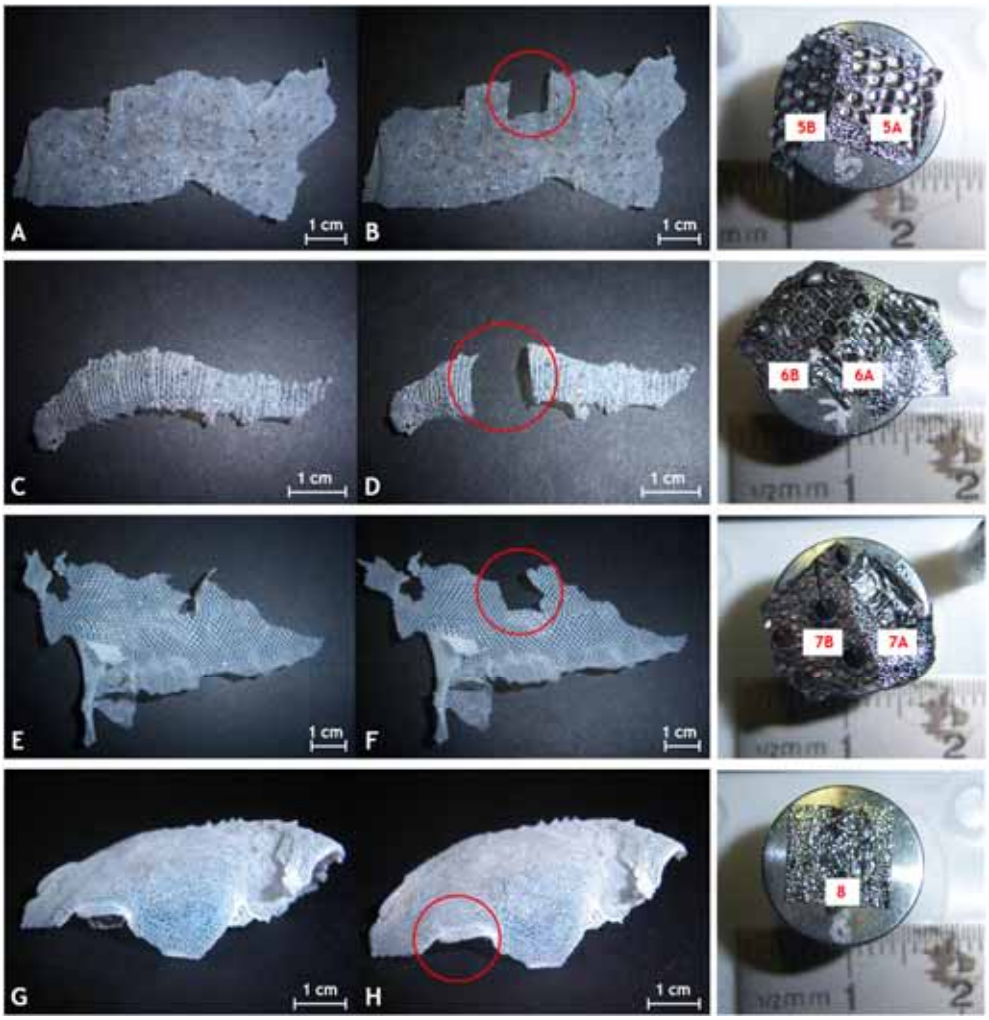

Fig. I.1 Details of the gecko's skin: back and upper tail of G1 (A, C and B, D respectively before and after specimen removal), abdomen and eyes of G2 (E, G and F, H respectively before and after specimen removal, photographed with Kodak V1003): the red circle individuates the specimen area. On the right, FESEM samples (photographed with Kodak V1003): the red letters mark the corresponding samples analysed in the next Figs. I.2-I.5.

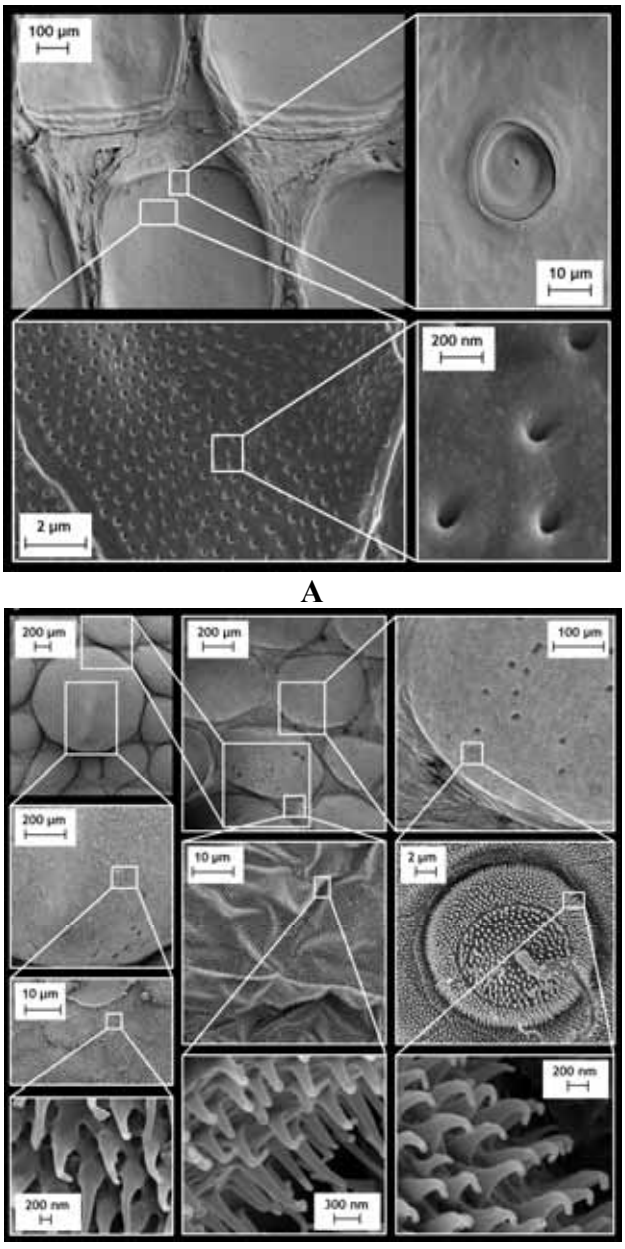

Fig. I.2 Details of the skin of the tokay gecko G1, back (see red circle in Fig. I.1B) showed by FESEM (Zeiss SUPRA 40): from down (A), from up (B).

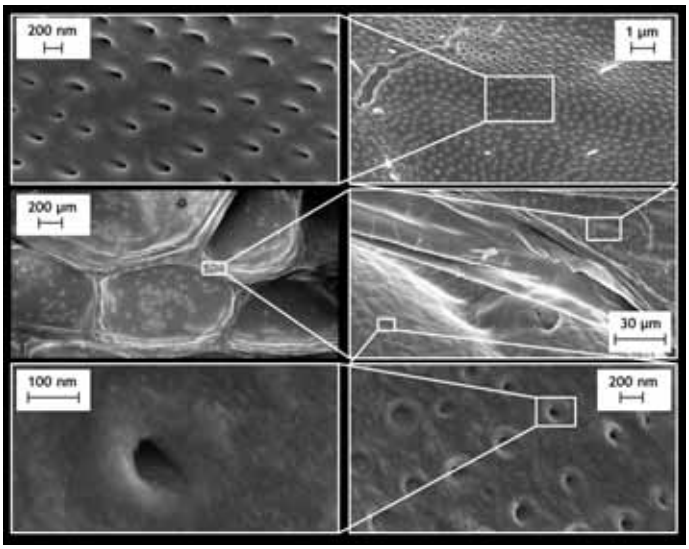

A

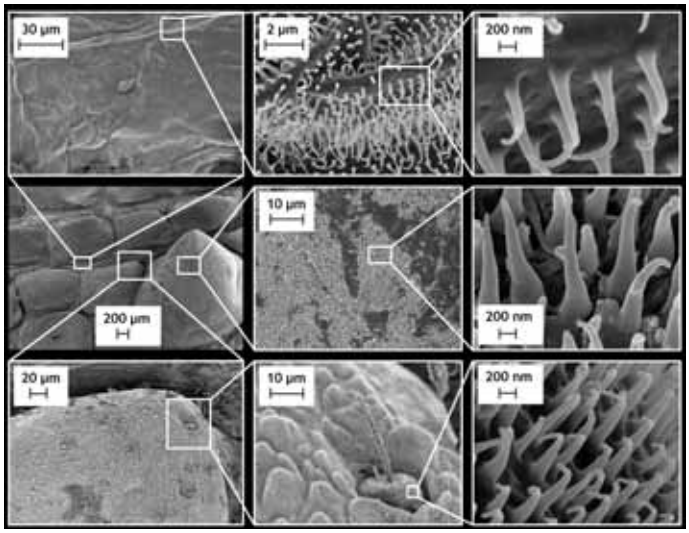

B

Fig. I.3 Details of the skin of Tokay gecko G1, upper tail (see red circle in Fig. I.1D) showed by FESEM (Zeiss SUPRA 40): from down (A), from up (B).

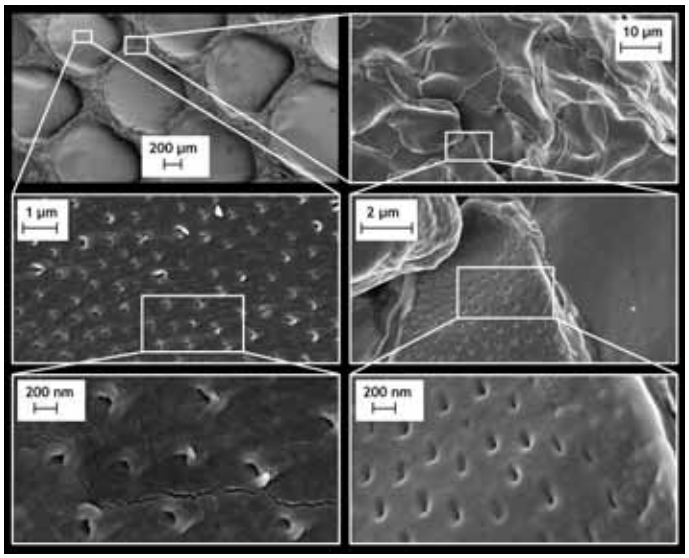

A

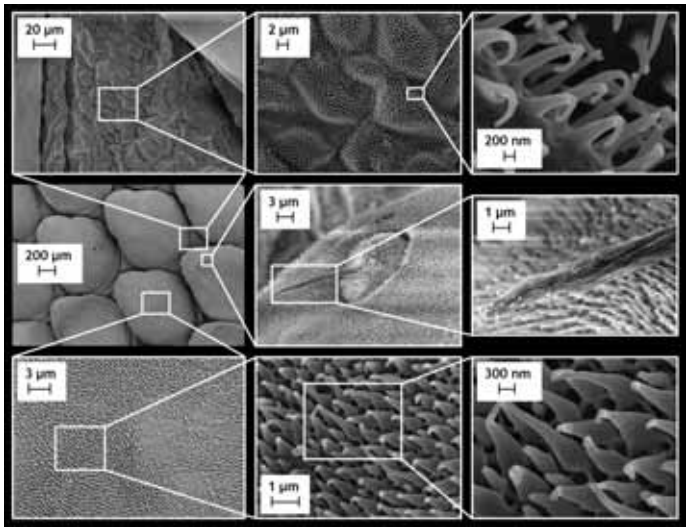

B

Fig. I.4 Details of the skin of Tokay gecko G2, abdomen (see red circle in Fig. I.1F) showed by FESEM (Zeiss SUPRA 40): from down (A), from up (B).

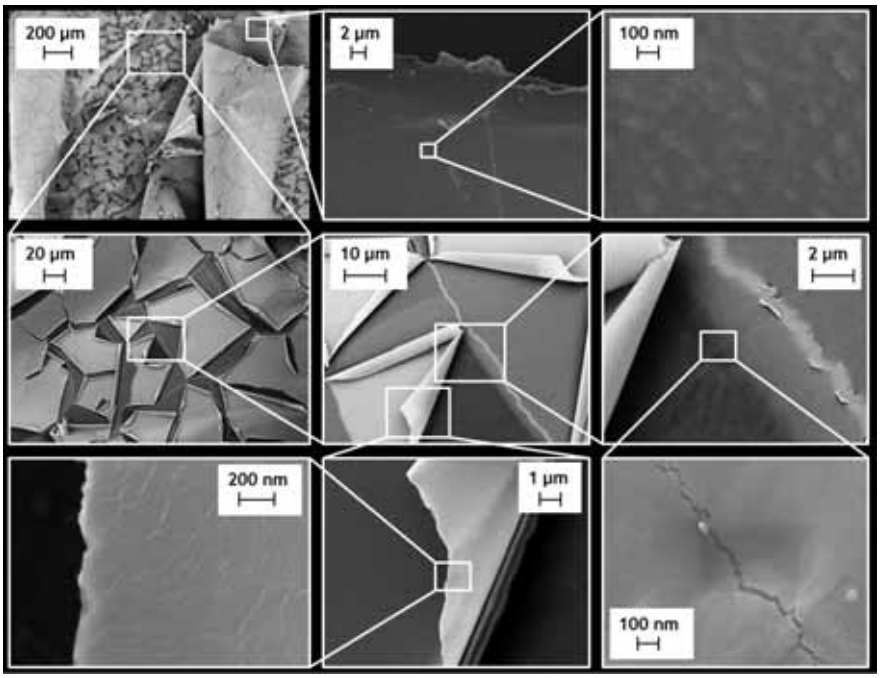

Fig. I.5 Details of the skin of Tokay gecko G2, eye (see red circle in Fig. I.1H) showed by FESEM (Zeiss SUPRA 40). The inability of the metallization to adhere on the eye skin seems to preliminary suggest an anti-adhesive and thus self-cleaning surface, perhaps developed for maximizing the visual ability in critical conditions (*e.g.* as anti-fogging mechanism, as observed in other animals).

I.3. Results

I.3.1. Moulting process

The entire moulting process was recorded for 16 consecutive hours by DCR SR55E SONY digital video camera. Gecko started its effective moulting process at 12:30 *a.m.* and finished it at 10:30 *p.m.* (after 10 hours; we continued to record its movements until 4:30 *a.m.* of the day after). Significant events were then extracted using Nero Vision software (Fig. I.6). The camera was located out of the terrarium and the gecko was left alone, with the exception of the short (few minutes) operator presence when the camera orientation was changed from the lateral prospective to the frontal

one (after 1h and 45 minutes from the beginning, see Fig. I.6, snapshots 17, 18) and when the samples of the back and upper tail skin were collected (see Fig. I.6, snapshots 35).

I.3.2. FESEM observations

SEM micrographs of the gecko's skin (Figs I.1-I.3) show that the skin of the back, upper tail and abdomen of the animal's body is covered with nanostructured hairy units. From the micrographs, we can distinguish hairy units of ~0.5-1 μm in length and ~50 nm in diameter for the back skin, ~0.5-1.5 μm in length and ~30-50 nm in diameter for the upper tail skin and ~0.2-1 μm in length and ~50nm in diameter for the abdomen skin. Thus, comparing these dimensions with those of the hairy units discovered in the toe (~2-5 μm in length and ~200 nm in diameter), we conclude that the two hairy units are similar, but scaled by a factor of about 3. The inability of the metallization to adhere on the eye skin seems to preliminary suggest an anti-adhesive and thus self-cleaning surface, perhaps developed for maximizing the visual ability in critical conditions (*e.g.* as anti-fogging mechanism, as observed in other animals).

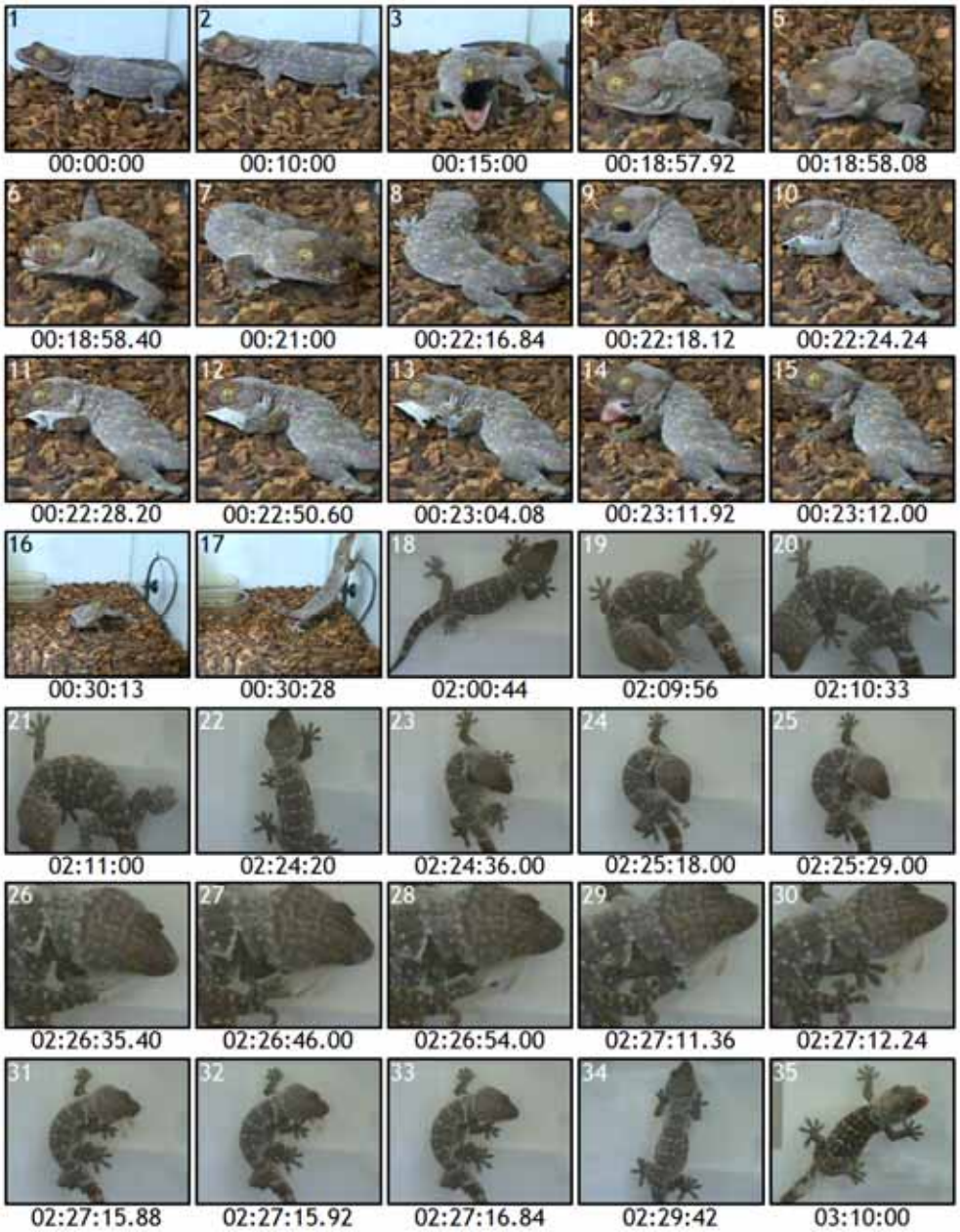

Fig. I.6 Snapshots (ss) of the entire moulting process of the gecko G1. Staying on the bottom of its terrarium, the gecko begun its moulting process using its tongue to try to remove the older generation skin from its head and eyes (ss 1-4): it opened wide its mouth in order to facilitate the detachment

of the old skin from the new one (ss 3). After almost 20 min, gecko started to remove its old skin from the fore right foot (ss 5÷7): it put the toes in its mouth in order to easily remove its old skin. The old skin generation of its fore right foot was entirely eaten and the result is shown in ss 7 (note the clean fore right foot). After only 1 min, gecko proceeded with its fore left foot following the same technique: this phase is accurately recorded and ss 8-15 show it step by step (note the clean fore left foot in ss 15). Afterwards, gecko left the bottom and came up to the vertical surface of the terrarium (ss 16, 17). The animal stayed on the vertical surface almost 45 min motionless and made only few steps on the bottom and again on the vertical surface during the following 45 min, reaching the position shown in ss 18. Thus, gecko tried to clean its hind left foot but its adhesion on vertical surface was not sufficient to guarantee the gecko's stability: instead gecko slowly slipped down (ss 19-21) and decided to clean its hind left foot positioning again on the bottom of the terrarium. Gecko spent less than 15 min for this operation and then returned on the vertical surface. The result is shown in ss 22 (note the clean hind left foot). After only few seconds, the procedure of removing the old skin from the last hind right foot was started: gecko begun with the skin of its right side (ss 23-24) and continued taking off the old skin from its hind right foot, as an adherent suit (ss 25-33). The technique of taking off the old skin from the toes of the hind right foot was highlighted in the snapshots 26-30. As usual, at the end the gecko had eaten the old generation of its skin (ss 31-33). The result is shown in ss 34 (note the clean hind right foot). After 3 hours, samples of the skin of the gecko's back and upper tail were taken and the result is shown in ss 35. No more snapshots were reported due to the inappropriate location of the digital video camera focus with respect the new position.

After making clean all its feet, gecko stayed almost motionless for 70 min on the vertical surface. At 4 h and 20 min from the beginning, it came down to the bottom of the box and made its tail completely clean in 3 min using only its mouth. After 110 min almost motionless (so at 6 h and 30 min), gecko begun the procedure of making its head completely clean rubbing its head against the small pieces of bark of which the bottom is covered. This procedure was stopped for about 145 min and then restarted (so 9 h from the beginning) following the same technique and with the final help of its hind foot in order to scratch out the last piece of old skin from its head (this happened after 10 h from the beginning). After making its body clean, removing the skin of the old generation, the animal maintained its last

position motionless on the bottom and nothing happens for the following 6 hours.

I.3.3. Statistical analysis

Tables I.1, I.2, I.3 and I.4 summarize the average parameters of area, perimeter, circularity of the skin structures. The standard deviation (SD), the maximum and minimum values are also reported. Note that samples A3 and B3 in Fig. I.7 were double-analysed: in Table I.1B and I.2B, we isolated the calculation of the above mentioned parameters for specific 3D conical structures (coloured in light yellow in Fig. I.7), found in the number of 2 within the 5 x 5 mm^2 analysed areas. The summary of the calculated parameters is shown in Fig. I.8.

n° = 29	Area (mm^2)	Perimeter (mm)	Circolarity
Average value	0.313	2.226	0.782
SD	0.0731	0.2615	0.0447
Max Value	0.435	2.636	0.856
Min Value	0.136	1.557	0.696

A

n° = 2	Area (mm^2)	Perimeter (mm)	Circolarity
Average value	1.840	5.164	0.867
SD	0.7710	0.1230	0.0050
Max Value	1.894	5.251	0.870
Min Value	1.785	5.077	0.863

B

Table I.1 Statistical topological analysis of the back skin (G1). These data refer to Fig. I.7, series A: (A) the parameters of the white almost-circular structures; (B) the parameters of the light yellow almost-conical structures.

n° = 21	Area (mm^2)	Perimeter (mm)	Circolarity
Average value	0.472	2.698	0.788
SD	0.1596	0.5062	0.0458
Max Value	0.686	3.281	0.826
Min Value	0.100	1.239	0.643

A

n° = 2	Area (mm^2)	Perimeter (mm)	Circolarity
Average value	1.832	5.259	0.833
SD	0.1146	0.0120	0.0488
Max Value	1.913	5.267	0.867
Min Value	1.751	5.250	0.798

B

Table I.2 Statistical topological analysis of the upper tail skin (G1). These data refer to Fig. I.7, series B: (A) the parameters of the white almost-circular structures; (B) the parameters of the light yellow almost-conical structures.

n° = 16	Area (mm^2)	Perimeter (mm)	Circolarity
Average value	0.874	3.553	0.870
SD	0.0477	0.1210	0.0168
Max Value	0.947	3.722	0.903
Min Value	0.799	3.367	0.839

Table I.3 Statistical topological analysis of the abdomen skin (G2). These data refer to Fig. I.7, series C.

n° = 75	Area (mm^2)	Perimeter (mm)	Circolarity
Average value	0.156	1.513	0.794
SD	0.0868	0.4608	0.1072
Max Value	0.474	3.038	0.902
Min Value	0.003	0.260	0.348

Table I.4 Statistical topological analysis of the upper head skin (G2). These data refer to Fig. I.7, series D.

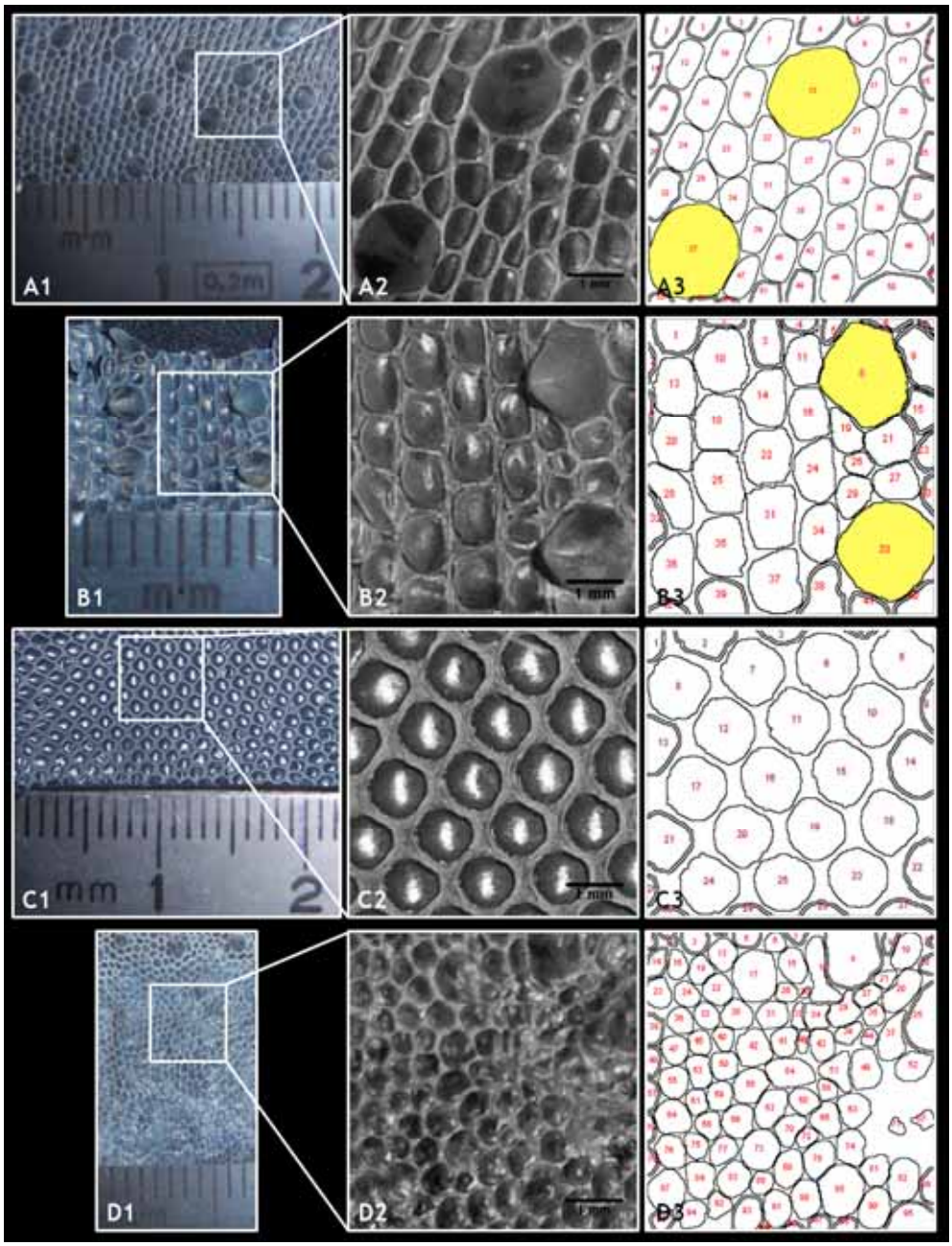

Fig. I.7 Statistical topological analysis of the gecko's skin (photographed with Kodak V1003 and acquired with the software ImageJ 1.41o): back (A1) and upper tail (B1) of G1, abdomen (C1) and head (D1) of G2. Photographs A1, B1, C1 and D1 refer to samples of Fig. I.1 (A, C, E and G

respectively). A2, B2, C2 and D2 insets show the grey scale image of the analysed 5 x 5 mm^2 areas. A3, B3, C3 and D3 insets present the final result of the image acquisition. Note that A2 and B2 insets show 3D conical structures, marked in light yellow in A3 and B3 insets and accordingly analysed separately (Tables I.1B and I.2B).

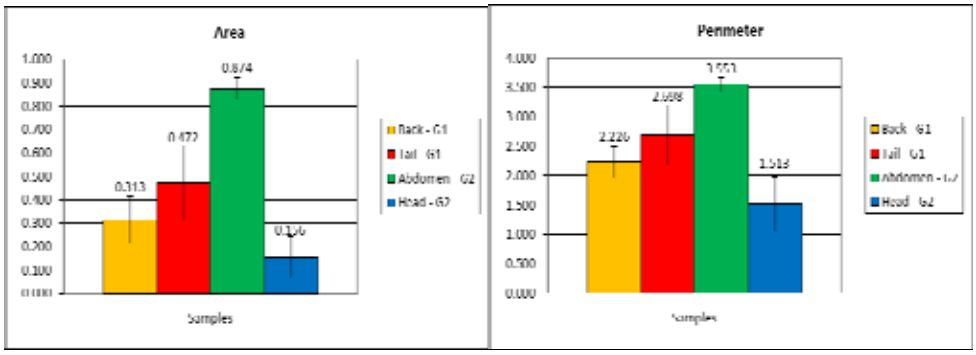

Fig. I.8 Summary of the statistical analysis for both area and perimeter skin structures (the conical structures are not here considered).

I.4. Adhesion and anti-adhesion

From one hand, it was demonstrated that the gecko's adhesive ability increased after the moult by a factor of about 10 (in terms of adhesion times) [22, 25]. Noting that the van der Waals forces F_{vdW}, mainly responsible for the gecko's adhesion, can be described as $F_{vdW} = k/s^3$, where k is a constant and s represents the contact separation, we roughly estimate here the role of the moult on the gecko's adhesion. Even if the contact separation has to be of the order of the nanometer in order to match the observed seta forces, we simply assume here a value for s of the order of the thickness t of the new skin for the configuration just after the moult and of the order of $2t$ (new plus old skin) before the moult. As a consequence, the ratio of the adhesive forces just after and before the moulting process is predicted to be $F_{vdW}(s=t)/F_{vdW}(s=2t) = 8$. Note that such a prediction is independent from the actual thickness t of the skin and suggests that the contact separation s is reduced by a factor of 2-3 after the moult.
On the other hand, we want here to stress again the inability of the metallization to adhere on the skin of the eye (Fig. I.5), which seems to

preliminary suggest an anti-adhesive and thus self-cleaning surface, perhaps developed for maximizing the visual ability in critical conditions.

I.5. Conclusions

We have reported the experimental description of the entire moulting process of a female tokay gecko and of the related observation on its skin topology. The gecko's skin shows unexpected complexity, *e.g.* it is covered by nanohooks (0.2-1.5 μm in length and ~30-50 nm in diameter) superimposed to the evident nearly circular tessellations (for them the statistical analysis suggests values of circularity of ~0.9, mean area of ~0.5 mm^2 and mean perimeter of ~3 mm). The moult, a well-documented complex process about 10 hours long, increases the adhesive ability by a factor of ~10. The inability of the metallization to adhere on the eye skin seems to preliminary suggest an anti-adhesive and thus self-cleaning surface, perhaps developed for maximizing the visual ability in critical conditions (*e.g.* as anti-fogging mechanism, as observed in other animals).

ACKNOWLEDGMENTS

The authors would like to thank the "2I3T Scarl - Incubatore dell'Università di Torino" for the SEM imaging instruments and M. G. Faga, CNR - ISTEC member, Chemical Department IFM and NIS Centre of Excellence, University of Torino for the help in performing the SEM micrographs.

REFERENCES

[1] Aristotle, *Historia Animalium*, 343 B.C. See Book IX, Part 9, translated by Thompson DAW, http://classics.mit.edu/Aristotle/history_anim.html.
[2] Cartier, O., *Verhandl. Würz Phys-med Gesell* **1**, 83-96 (1872).
[3] Haase, A., *Archiv. Naturgesch* **66**, 321-345 (1900).
[4] Gadow, H., Amphibia and Reptiles (Macmillan & Company, Ltd., London, 1902).
[5] Weitlaner, F., *Verhdl. Zool. Bot. Ges. Wien.* **52**, 328-332 (1902).
[6] Schmidt, H. R., *Jena. Z. Naturwiss* **39**, 551-580 (1904).

[7] Hora, S. L., *J. Proc. Asiat. Soc. Beng.* **9**, 137-145 (1923).
[8] Dellit, W. D., *Jena. Z. Naturwiss* **68**, 613-658 (1934).
[9] Mahendra, B. C., *Proc. Indian. Acad. Sci.* **13**, 288-306 (1941).
[10] Maderson, P. F. A., *Nature* **203**, 780-781 (1964).
[11] Ruibal, R., and Ernst, V., *J. Morph.* **117**, 271-294 (1965).
[12] Hiller, U., *Z. Morphol Tiere* **62**, 307-362 (1968).
[13] Hiller, U., *Forma et functio* **1**, 350-352 (1969).
[14] Gennaro, J. G. J., *Nat. Hist.* **78**, 36-43 (1969).
[15] Williams, E. E., and Peterson, J. A., *Science* **215**, 1509-1511 (1982).
[16] Stork, N. E., *J. Exp. Biol.* **88**, 91-107 (1980).
[17] Schleich,H. H., and Kästle, W., *Amphibia-Reptilia* **7**, 141-166 (1986).
[18] Irschick, D. J., Austin, C. C., Petren, K., Fisher, R., Losos, J. B., and Ellers, O., *Biol. J. Linn. Soc.* **59**, 21-35 (1996).
[19] Liang, Y. A., Autumn, K., Hsieh, S. T., Zesch, W., Chan, W.-P., Fearing, R., Full, R. J., and Kenny, T. W., Technical Digest of the 2000 Solid-State Sensor and Actuator Workshop., 33-38 (2000).
[20] Autumn K., Liang Y. A., Hsieh S. T., Zesch W., Chan W.-P., Kenny W. T., Fearing R., and Full R. J., *Nature* **405**, 681- 685 (2000).
[21] Autumn, K., Ryan, M. J., and Wake, D. B., *Q. Rev. Biol.* 77, 383-408 (2002).
[22] Lepore, E., Antoniolli, F., Brianza, S., Buono, M., Carpinteri, A., and Pugno, N., *J. Nanomat.* **194524**, pp. 1-5 (2008).
[23] Rizzo, N. W., Gardner, K. H., Walls, D. J., Keiper-Hrynko, N. M., Ganzke, T. S., and Hallahan, D. L., *J. R. Soc. Interface* **3**, 441-451 (2006).
[24] Hansen, W. R., and Autumn, K., *Proc. Natl. Acad. Sci. USA* **102**, 385-389 (2005).
[25] Pugno, N., and Lepore, E., J. *Adhesion* **84**, 949-962 (2008).
[26] Huber, G., Gorb, S. N., Spolenak, R., and Arzt, E., *Biol. Lett.* **1**, 2-4 (2005).
[27] Autumn, K., Sitti, M., Liang, Y. A., Peattie, A. M., Hansen, W. R., Sponberg, S., Kenny, T. W., Fearing, R., Israelachvili, J. N., and Full, R. J., *Proc. Natl. Acad. Sci. USA* **99**, 12252-6 (2002).
[28] Pugno, N., and Lepore, E., *Biosystems* **94**, 218-222 (2008).
[29] Pugno, N. M., *J. Phys.: Condens. Matter* **19**, 395001, pp. 1-17 (2007).
[30] Pugno, N.M., *Nano Today* **3**, 35-41 (2008).
[31] Pugno, N.M., *Int. J. Fracture* **140**, 159-168 (2006).
[32] Ippolito, M., Mattoni, A., Colombo, L., and Pugno, N., *Phys. Rev. B* **73**, 104111-1/6 (2006).

[33] Pugno, N., Peng B., and Espinosa H.D., *Int. J. Solid. Struct.* **42**, 647-661 (2004).
[34] Pugno, N., *Acta Materialia* **55**, 5269-5279 (2007).
[35] Pugno, N., *Acta Materialia* **55**, 1947-1953 (2007).

GENERAL CONCLUSIONS

Over most of the past 150 years, scientific researchers have examined the superadhesive abilities of insects, spiders, reptiles and geckos by looking at their adhesive systems, climbing abilities and adhesion mechanisms. Moreover, the superantiadhesive properties of some plants have attracted scientists which are interested in the understanding of such special properties, superhydrophobicity and self-cleaning, which are related to the antiadhesion of water and dirt. Finally, the superstrong behaviour of spider silk has revealed interesting applications thanks to its structural and mechanical properties.

In nature, the common key of adhesive (in Chapters 1, 2, 3, 4 and 5), antiadhesive (in Chapters 6, 7 and 8) and strong (in Chapter 9) properties of materials deals with nanoscale: from the superadhesive terminal unit contacts of geckos (spatulae, ~200 nm wide and 15-20 nm thick) to the finest superantiadhesive structure of lotus leaves (nanotubules, diameter of ~200 nm), to the fibroin protein of spider silks.

In Chapter 1, we demonstrate that living Tokay geckos (*Gekko gecko*) display adhesion times following the Weibull statistics. The Weibull shape (m) and scale (t_0) parameters describe quantitatively the statistics of the adhesion times of different geckos (male or female) and materials, glass or Poly(methyl meth-acrylate) (PMMA): $m_{PMMA} \approx 1$ and $t_{0PMMA} \approx 800$ s *versus* $m_{Glass} \approx 2$ and $t_{0Glass} \approx 23$ s.

Chapter 2 confirms that the Weibull modulus has a value in the restricted range of 1-1.2, when both the virgin and machined PMMA surfaces are considered.

Chapter 3 highlights the normal adhesive abilities of living Tokay geckos which adhere to PMMA or glass surfaces. The normal safety factor λ, which is the ratio between the maximum normal adhesive force and the body weight, was thus determined: the normal safety factor is $\lambda_{PMMA} = 10.23$ on PMMA surface and $\lambda_{Glass} = 9.13$ on glass surface. In addition, the self-renewal of the gecko's adhesive system after moulting was documented.

Chapter 4 investigates the adhesion angles of living Tokay geckos at two different hierarchical levels of the feet and toes. The adhesion angles between opposing front and rear feet (β_F) and between the first and fifth toe of each foot (β_T) on different inverted surfaces (steel, aluminium, copper, Poly(methyl meth-acrylate) and glass) have been experimentally measured.

The resulting angle α was computed as $\alpha = (180° - \beta)/2$ and found equal to 28° ($\alpha_{F\_FR\text{-}RL}$) and 30° ($\alpha_{F\_FL\text{-}RR}$) for the opposing front and rear feet or equal to 26° (α_{T_FR}), 29° (α_{T_FL}), 28° (α_{T_RR}) and 26° (α_{T_RL}) between the first and fifth toe of each foot. Such results are in line with the new multiple peeling theory: as the number of hierarchical level n increases, the dimensionless adhesion strength parameter λ decreases and determines a decrease of the adhesion angle α.

Chapter 5 ends the first section of this thesis on adhesive materials. In particular, in this chapter the shear adhesive force of four non-climbing living cockroaches (*Blatta Orientalis* Linnaeus) was investigated using a centrifuge machine on six surfaces (steel, aluminium, copper, two sand papers (Sp 50, Sp150) and a common paper sheet). The shear safety factor was thus determined as the ratio between the maximum shear adhesive force and the body weight: the cockroach's maximum shear adhesive factor is 12.1 on Sp150, while the minimum shear adhesive factor is 1.9 on steel surface.

Chapter 6 displays the effects of two superficial industrial processes (plasma and thermoforming) on the surface wettability. Such an analysis was developed in collaboration with the Indesit Company and clearly suggests that plasma or thermoforming are ideal treatments to tune the wettability and enhance the hydrophilic or hydrophobic behaviour of PS surfaces, respectively.

Chapter 7 shows how an artificial biomimetic superhydrophobic polystyrene (PS) surface can be performed by coping a natural lotus leaf with a simple template method at room temperature and atmospheric pressure. Two parameters were used to compare the artificial PS surface *vs* the natural lotus leaf: the contact angle is 149° *vs* 153° and the drop sliding speed is 417 mm/s *vs* 319.4 mm/s, respectively.

Chapter 8 stresses the necessity of a representative set of surface roughness parameters in order to understand the tribological properties of lubricated surfaces: a low value of topography sensitive roughness parameter (R_{ku}, R_{sk}) optimizes the contact pressure and the effective lubricant film thickness, so as to favour the hydrodynamic support and minimize the asperity-asperity interaction.

Chapter 9 is about a natural stretchable material: the bundles of about 150 threads (each of ~6 μm in diameter), which connect the egg sac (cocoon) of the cave spider *Meta menardi* to the ceiling of the caves, were tested to determine the stress-strain curves, and the stress results were analysed with

the Weibull statistics. The maximum stress, strain and toughness modulus reach the value of 0.64 GPa, 750 % and 130.7 MJ/m^3, respectively. The average value of the Weibull modulus (m) is in the range of 1.5-1.8 and of the Weibull scale parameter (σ_0) in the range of 0.33-0.41 GPa with a high correlation coefficient ($R^2 = 0.97$).

When the adhesive, anti-adhesive or strong mechanisms in nature become completely understood, the transfer-into-technology operation of a superadhesive and reusable material or a stable superhydrophobic and self-cleaning material or a stretchable material will be the next forced step to industrialization. The industrial application of a superadhesive and reusable material could be mainly for space applications (*i.e.* connections between space components or suits and gloves for astronauts, which allow them to remain attached to the external side of a space shuttle without awkward cables); the industrial application of a superhydrophobic and self-cleaning material may be for civil engineering applications (*i.e.* the glass windows of skyscrapers, the external building coverings) or air transport security (*i.e.* a superficial pattern to realize an anti-ice wings for airplanes) or home technology (*i.e.* the internal faces of refrigerators or freezers, the surfaces of bathroom fittings or tiles). Finally, the industrial application of a super-stretchable material might be for air transport security (*i.e.* security systems to decrease the velocity of an airplane or large webs to stop hijacked airplanes).

Although the effort to industrialize a product like the above-mentioned ones is considerable, only few patents have been duly deposited at the European Patent Office in these fields of research. In particular, the number of patents with the words “super adhesive reusable” as title keywords is equal to zero, while there are eight patents for inventions with the words “self cleaning super hydrophobic” as title keywords during the last eight years, i.e. a current rate of one European patent per year, and only one patent with the word “super stretchable” as keyword in the title has been deposited in 1987.

In our opinion, if we take a look to the current cutting-edge technology, we understand how many great possibilities exist to become Innovators able to develop new products in these fields of scientific research. Nevertheless, only a deep and detailed knowledge of what happens in nature, of how nature have optimized each process, mechanism and animal which is strictly related to its own habitat will lead to a reasonable starting base to develop a new good engineered product.